

Pool Fire Burning Facilitated by Subcooled Nucleate Boiling Heat and Mass Transfer Processes

by
Xiaoyue Pi

A Dissertation
Submitted to the Faculty
of the
Worcester Polytechnic Institute
in partial fulfillment of the requirements for the
Degree of Doctor of Philosophy
in
Fire Protection Engineering
January 2022

Approved:

Dr. Ali S. Rangwala, Worcester Polytechnic Institute, USA, Advisor.

Dr. Vasudevan Raghavan, Indian Institute of Technology Madras, India, Co-Advisor.

Dr. Elaine S. Oran, Texas A&M University, USA, Committee Member.

Dr. Albert Simeoni, Worcester Polytechnic Institute, USA, Committee Member.

Dr. Chih-Jen (Jackie) Sung, University of Connecticut, USA, Committee Member.

.....*page intentionally left blank*.....

Preface

This dissertation was submitted for the degree of Doctor of Philosophy at the Worcester Polytechnic Institute (WPI). The Ph.D. study was conducted between August 2016 and January 2022 at the Department of Fire Protection Engineering, under the supervision of:

- **Ali S. Rangwala**, advisor, Professor, Department of Fire Protection Engineering, Worcester Polytechnic Institute, USA.
- **Vasudevan Raghavan**, co-advisor, Professor, Department of Mechanical Engineering, Indian Institute of Technology Madras, India.

The following articles have been published or presented at the time of submitting this Ph.D. dissertation:

- **X. Pi**, A.S. Rangwala, The influence of wire orientation during nucleate pool boiling in subcooled dodecane, *International Journal of Heat and Mass Transfer* 137 (2019) 1247-1257. (Presented in Chapters 2-3).
- **X. Pi**, L. Chang, A.S. Rangwala, The influence of an immersed heater on pool fire burning behaviors, 11th US National Combustion Meeting, 2019, Pasadena, CA, United States. (Presented in Chapters 2-3).
- **X. Pi**, K. Twarog, L. Chang, C.J. Sung, A.S. Rangwala, The influence of surface configuration of an immersed metal element to pool fire burning, 35th American Society for Gravitational and Space Research (ASGSR) Meeting, 2019, Denver, CO, United States. (Presented in Chapters 2-3).
- **X. Pi**, L. Chang, A.S. Rangwala, The burning rate of a pool fire increased by bubble behaviors during nucleate boiling, *Fire Safety Journal* 120 (2021) 103097. (Presented in Chapters 2-3).

.....page intentionally left blank.....

Acknowledgments

This project is supported by the Bureau of Safety and Environmental Enforcement, U.S. Department of the Interior, Washington, D.C., and the Teaching Assistantship from the Department of Fire Protection Engineering (FPE) at WPI. Meanwhile, the candidate would like to express her sincere gratitude for the SFPE Chapter Scholarships and the NFPA Fellowship.

First and foremost, the candidate would like to thank her incredible advisors. To Professor Rangwala for his supervision of this unique and meaningful project and his open mind to various possibilities and opportunities. To Professor Raghavan for his impressive wisdom and expertise in handling challenges, as well as his excellent guidance, support, and trust in the candidate's ideas. It is more than a miracle to be advised by such superb professors.

The candidate would also like to thank her marvelous Ph.D. committee members. To Professor Oran for her profound knowledge of clarifying problems and procedures, beautiful personality, and enthusiasm, which are sources of inspiration. To Professor Simeoni for his dedication to helping the candidate overcome obstacles, together with his willingness to share valuable ideas with others. To Professor Chih-Jen (Jackie) Sung for his generosity to provide help from multiple aspects, deep insight into the project, great patience with the candidate, and attentiveness to detail. It is the candidate's fortune to be taken care of by such brilliant professors.

The candidate would like to express her special thanks to Sharanya Nair, who devotes significant time and effort to making the numerical works possible and helping with the dissertation preparation. More importantly, she is such a perfect teammate. Special thanks go to Li Chang and Kyle Twarog, who are professional and great researchers ensuring the conduction of experiments. And special thanks are also owed to Thomas Partington, Trevor J. Borth, and Russell G. Lang, who are experts in handling intractable technician difficulties.

Sincere thanks go to the colleagues in the WPI Combustion Lab for their generous help with experiments. Special thanks to Kemal S. Arsava, Mahesh Kotalgi, Veronica M. Kimmerly, Suhas Lakkundi, Cong Li, Nadia Mofidi, Marine Roux, and Nathaniel G. Sauer (alphabetical sequence).

Further thanks are owed to numerous colleagues and friends at WPI, who help and encourage the candidate during her Ph.D. study. Special thanks to Statia M. Canning, Professor Nicholas A. Dembsey, Professor Rudra P. Kafle, Praveen Kamath, Yu Liu, Yuting Liu, Professor Kathy A. Notarianni, Diane R. Poirier, Professor Milosh T. Puchovsky, Professor John M. Sullivan, Jr., Douglas C. White, Bo Yang, Qing Yin, and Young-Geun You (alphabetical sequence).

The author would like to extend her gratitude to thank the colleagues and friends from multiple institutions and organizations during her study and internship associating with the FPE. Special thanks to Weiyuan Chen, Yan Ding, Stephen D’Aniello, Yanyun Fu, Professor Junhui Gong, Haiqing Guo, Professor Jie Ji, Professor Juncheng Jiang, Lin Jiang, Man Li, Professor Xuhai Pan, Xingyu Ren, Denise Staplins, Wei Tang, Professor Arnaud C. Trouvé, Salman Verma, Huaxian Wan, Professor Jinghong Wang, Yi Wang, Raquel Hakes Weston-Dawkes (and her family), James P. White, Yibing Xing, Cong Zhang, and Professor Kuibin Zhou (alphabetical sequence).

Sincere gratitude is owed to the candidate’s gorgeous friends, who devote their time and energy to assisting from different aspects. Special thanks to Ruolei Ji, Ting Li, Yi Liu, Xiaoyun Ni, Mengting Pan, Yingxing Qian, Yue Shao, Hui Shi, and Yunqiu Sun (alphabetical sequence).

Finally, and most importantly, the candidate would like to thank her family. Special and sincere thanks to her parents and her brother Lingling, who are the light in the candidate’s life.

Because of the page limit, it is impossible to include all important names. Therefore, to those who love the candidate and/or who are loved by the candidate: thank you very much for showing up in her life, and hope she will always be beyond your expectations.

Table of Contents

Preface	iii
Acknowledgments	v
List of Figures	xiii
List of Tables	xx
Nomenclature	xxi
Abstract	xxvi
1 Introduction	1
1.1 Background and motivation.....	1
1.2 Literature review	4
1.3 Objectives	9
1.4 Layout	10
2 Experimental setup and procedure	12
2.1 Overview.....	12
2.2 First-stage experiment.....	13
2.2.1 Introduction.....	13
2.2.2 Experimental setup and procedure.....	14
2.2.3 Data processing.....	16
2.3 Second-stage experiment	16
2.3.1 Introduction.....	16

2.3.2	Experimental setup and procedure.....	18
2.3.3	Data processing.....	20
2.4	Third-stage experiment.....	21
2.4.1	Introduction.....	21
2.4.2	Experimental setup and procedure.....	22
2.4.3	Data processing.....	26
3	Experimental results.....	29
3.1	First-stage experiment.....	29
3.1.1	Boiling process.....	29
3.1.2	Influence of the wire inclination.....	33
3.1.2.1	ONB and CHF.....	33
3.1.2.2	The influence of φ on the number of bubbles.....	37
3.1.2.3	The influence of φ on the velocity of bubbles.....	43
3.1.2.4	The influence of φ on the size of bubbles.....	46
3.1.3	Summary.....	48
3.2	Second-stage experiment.....	48
3.2.1	Flame height.....	48
3.2.2	Mass loss rate.....	50
3.2.2.1	The influence of an immersed object.....	50
3.2.2.2	The influence of initial immersion depth, l	54
3.2.3	Summary.....	58
3.3	Third-stage experiment.....	59
3.3.1	Mass loss rate.....	59

3.3.2	Bubble visualization.....	60
3.3.3	Bubble quantification.....	65
3.3.3.1	Manual method	65
3.3.3.2	Gray-scale method	67
3.3.4	Summary.....	72
4	Numerical model setup and procedure.....	74
4.1	Overview.....	74
4.2	Description.....	75
4.2.1	Assumption and simplification	76
4.2.2	Flame modeling	78
4.2.2.1	Flame height.....	78
4.2.2.2	Temperature distribution.....	79
4.2.2.3	Heat flux.....	81
4.2.3	Governing equations, initial and boundary conditions	84
4.3	Discretization	86
4.3.1	Discretization using FDM.....	87
4.3.1.1	Object region (CV ₁ and CV ₂)	87
4.3.1.2	Liquid region (CV ₃)	90
4.3.2	Initial condition.....	93
4.3.3	Boundary conditions	93
4.3.3.1	Object region (CV ₁ and CV ₂)	93
4.3.3.2	Liquid region (CV ₃)	94
4.3.3.3	Interfaces.....	95

4.4	Mass loss rate.....	96
4.5	Energy imbalance at interfaces.....	100
4.5.1	Solid side.....	100
4.5.2	Liquid side.....	102
4.6	Energy imbalance in interior cells.....	104
4.6.1	Maximum of a single cell.....	104
4.6.2	Whole CV.....	106
4.7	Validation.....	108
4.7.1	First-stage validation.....	109
4.7.2	Second-stage validation.....	111
4.7.3	Third-stage validation.....	113
5	Numerical model results.....	116
5.1	First-stage validation.....	116
5.1.1	Mass loss rate.....	116
5.1.2	Temperature.....	122
5.2	Second-stage validation.....	123
5.2.1	Model verification.....	124
5.2.2	Mass loss rate.....	126
5.2.3	Temperature.....	128
5.3	Third-stage validation.....	130
5.3.1	Model verification.....	131
5.3.2	Mass loss rate.....	133
5.3.3	Temperature.....	135

5.3.4	Flame height.....	138
5.4	First-stage parametric study (L_C)	139
5.4.1	Model verification.....	140
5.4.2	Mass loss rate.....	142
5.4.3	Temperature	144
5.5	Second-stage parametric study (L_C and D_o).....	147
5.5.1	Model verification.....	148
5.5.2	Mass loss rate.....	152
5.5.3	Mass loss rate prediction.....	154
5.5.3.1	2D plot method	155
5.5.3.2	3D plot method	156
5.5.4	Temperature	160
5.5.5	Heat flux from the hot gas	165
5.6	Summary.....	168
6	Conclusions.....	169
6.1	Summary.....	169
6.2	Future works	172
	Appendices.....	174
	Appendix A temperature-resistance calibration.....	174
	Appendix B Energy imbalance at interfaces.....	176
	B.1 Solid side.....	176
	B.2 Liquid side.....	178

Bibliography 182

List of Figures

Figure 1.1: Illustration of a liquid pool fire with an immersed object, where the heat transfer mechanisms (blue) and important experimental configurations with phenomena (yellow) are labeled. 2

Figure 1.2: A sketch (LHS) shows a liquid pool fire with an object immersed at the center, and a corresponding diagram (RHS) depicts the formation of the thermal feedback loop..... 3

Figure 2.1: Experimental setup of the first-stage experiment (not to scale), where an electrically heated wire-shaped nichrome object is immersed in a dodecane pool with subcooling at different wire inclinations, φ , and $\varphi = 0^\circ$ (horizontal), 22° , 33° , 44° , 49.5° , 74° , and 90° (vertical). 15

Figure 2.2: Schematic showing the setup of the second-stage experiment (not to scale). A composite-shaped aluminum object is immersed in an ethanol pool fire maintained at a constant liquid level. The immersion depths, l , are adjusted between 0 mm, 2.5 mm, 4.5 mm, and 7.0 mm. 19

Figure 2.3: Schematic of the setup of the third-stage experiment (not to scale). A composite-shaped copper object is immersed in the liquid ethanol maintaining at a constant liquid level, where the immersion depths are $l = 0$ mm, 3.0 mm, 6.0 mm, and 9.0 mm at a steady state, and diameters of holes (through the disk) are $D_{\text{hole}} = 0$ mm (“no holes”), 1.09 mm (“small holes”), and 2.06 mm (“big holes”)..... 23

Figure 2.4: Schematic showing an exemplary bubble distribution in a single image. The solid blue circle denotes the contour of a bubble around its nucleation site, and the bubble’s departure to the liquid surface is depicted by the blue arrow and the dashed blue circle..... 27

Figure 3.1: A boiling curve depicting a heated nichrome wire horizontally ($\varphi = 0^\circ$) immersed in a subcooled dodecane pool, where the wire diameter, $D = 1.27 \times 10^{-4}$ m and the subcooled temperature of the liquid, $T_{\text{sub}} \approx 25$ °C. 30

Figure 3.2: Images (taken at an elevated plane) and the corresponding sketches describing characteristic bubble phenomena at different heat flux values, where $\varphi = 0^\circ$ 31

Figure 3.3: Boiling curves showing the variation of q'' along ΔT at different φ , where $\varphi = 0^\circ$, 22° , 33° , 44° , 74° , and 90° 35

Figure 3.4: Images (taken at an elevated plane) showing the process of a thermal crisis, where $q'' \approx \text{CHF}$, $\varphi = 44^\circ$, and the total time duration is about 1.36 s. Images are taken by a video camera (left) and a high-speed camera (right)..... 37

Figure 3.5: Representative locations in the boiling process, where A: $q'' \approx 0.2 \times 10^3 \text{ kW/m}^2$, point B: ONB, point C: $q'' \approx 0.5 \times 10^3 \text{ kW/m}^2$, denoting the end of hysteresis, point D: $q'' \approx 1.6 \times 10^3 \text{ kW/m}^2$, point E: CHF, and point F: wire glowing..... 38

Figure 3.6: Images (taken at an elevated plane) showing the bubble phenomena at points A-F, where φ is adjusted from 0° to 74° 41

Figure 3.7: Images (taken at an elevated plane) showing the bubble motion, where $\varphi = 49.5^\circ$ 44

Figure 3.8: The variation of q'' along ν at different φ , where φ is varied from 0° to 49.5° . 45

Figure 3.9: A sketch showing bubble phenomena at different φ , where $q'' \approx 1.6 \times 10^3 \text{ kW/m}^2$ and $\varphi = 0^\circ, 22^\circ, \text{ and } 44^\circ$ 47

Figure 3.10: The variation of flame height as a function of time, where magenta triangles denote a baseline experiment without immersed objects, and black squares denote an object experiment at $l = 0 \text{ mm}$ 49

Figure 3.11: Images comparing the flame height between a baseline experiment and an object experiment at $l = 0 \text{ mm}$, where $t = 100 \text{ s}$ 50

Figure 3.12: The variation of liquid ethanol mass loss rate as a function of time, where magenta down-pointing triangles and the dotted curve denote the baseline experiment, black squares and the solid curve denote the object experiment at $l = 0 \text{ mm}$, red circles and the dashed curve denote the object experiment at $l = 2.5 \text{ mm}$, blue up-pointing triangles and the short dashed curve denote the object experiment at $l = 4.5 \text{ mm}$, and green left-pointing triangles and the dotted curve denote the object experiment at $l = 7.0 \text{ mm}$ 51

Figure 3.13: Bubble phenomena on the surface of the immersed object, which are in accordance with the mass loss rate curve for a single experiment, where $l = 7.0 \text{ mm}$ 53

Figure 3.14: Mean mass loss rate and temperature measurement at steady state at different l , where $l = 0\text{-}7.0 \text{ mm}$ 55

Figure 3.15: Bubble phenomena at steady state at different l , including (a) (inclined) top view, as well as (b) front view, where $l = 0\text{-}7.0 \text{ mm}$ 56

Figure 3.16: Mean mass loss rate at steady state for different scenarios. In the x-axis, “No”, “Small”, and “Big” represent the scenarios of the no holes, small holes having diameters of 1.09 mm, and big holes having diameters of 2.06 mm through the disk, respectively. “0”, “3”, “6”, and “9” in parentheses denote the immersion depths (mm) of the object at steady state, individually, and “baseline” represents the baseline experiment. 60

Figure 3.17: Images (front view) showing bubble phenomena for different cases, where the immersion depth at steady state, $l = 0$ mm, 3.0 mm, 6.0 mm, and 9.0 mm. Images in the first, second, and third rows represent the “no holes”, “small holes”, and “big holes” cases, representatively. 61

Figure 3.18: Images (bottom view) showing bubble phenomena for different cases, where the immersion depth at steady state, $l = 0$ mm, 3.0 mm, 6.0 mm, and 9.0 mm. Images in the first, second, and third rows represent the “no holes”, “small holes”, and “big holes” cases, representatively. 62

Figure 3.19: Images (side view) showing bubble phenomena for different cases, where time interval $\Delta t = 1/3$ s, and immersion depths at steady state, $l = 0$ mm, 3.0 mm, 6.0 mm, and 9.0 mm. 64

Figure 3.20: Schematic describing the bubble categorization in different regions, where regions A, B, C, and D represent the bubbles on the immersed rod, in the fuel, on the bottom disk, and at the liquid surface, respectively. 65

Figure 3.21: An example showing the procedure to obtain region A and the immersed object region using the gray-scale method. The example case is the “small holes” at $l = 3$ mm, and 200 images are used for the averaging process. 68

Figure 3.22: Schematic showing the dimensions used for the calculation of region A. 69

Figure 3.23: The influence of the number of images, N , on the volume of the region A, V_A , where $N = 5, 15, 50, 100, 150, 200$, and 250. 70

Figure 3.24: Mean mass loss rate (black diamond), individual mass loss rate (blue triangle), and volume of the region A (red circle) at steady state for the different cases, where the x-axis shows different experimental cases, the left y-axis denotes mean mass loss rate, and the right y-axis denotes the volume of the region A, V_A 71

Figure 4.1: Axisymmetric computational domain for the numerical simulation of an object immersed in a liquid pool fire, consisting of CVs 1 (collector), 2 (heater), and 3 (liquid). 76

Figure 4.2: Variation of air properties as a function of temperature.	84
Figure 4.3: Axisymmetric computational domain with discretized cells, where interfaces and boundary points, as well as (i, j) are labeled (not to scale).	87
Figure 4.4: Schematic of mass loss rate representing the heat into a cell at the solid-liquid interface (red) and inside of the liquid (blue).	97
Figure 4.5: Calculations of the heat in/out of a cell, \dot{q}_e , at the solid-liquid interface (red) and in the liquid (blue).	99
Figure 4.6: Schematic of the energy imbalance check applied to a single cell, which consists of the external heat (green), the heat required to vaporize liquid at the saturation temperature (blue), and the sensible heat to raise the temperature of object and liquid (magenta) in time Δt	105
Figure 4.7: Schematic of the energy imbalance check applied to the whole CV, which consists of the external heat (green), the heat required to vaporize liquid at the saturation temperature (blue), and the sensible heat to raise the temperature of object and liquid (magenta) in time Δt	107
Figure 4.8: Schematic of the first-stage validation (not to scale), where no objects are immersed in a water pool having a constant height. The domain is heated by a radiant heat panel having a constant heat flux, \dot{q}_g'' , from the top.	110
Figure 4.9: Schematic of the second-stage validation (not to scale), where a copper cylinder object is immersed in a water pool having a constant height. The domain is heated by a radiant heat panel having a constant heat flux, \dot{q}_g'' , from the top.	112
Figure 4.10: Schematic of the third-stage validation (not to scale), where an aluminum cylinder object is immersed in a hexane pool having a constant height. The domain is heated by the pool fire.	114
Figure 5.1: The influence of grid spacing on the model convergence, where the x-axis (in log10 scale) denotes the decreasing grid spacing, the left y-axis and blue square notations denote the mass loss rate, and the right y-axis and red circle notations denote the energy imbalance ratio applied to the whole CV.	118
Figure 5.2: The influence of time step on the model convergence, where the x-axis denotes the decreasing time step (in log10 scale), the left y-axis and blue square notations denote the mass loss rate, and the right y-axis and red circle notations denote the energy imbalance ratio applied to the whole CV.	119

Figure 5.3: The variation of MLR with time, where heat input coefficient, $\zeta = 0.45$ (red dashed), 0.55 (blue dash-dotted), and 0.65 (green dotted). The experimental data (black solid) is digitized [75] by removing the initial 250 s with fluctuations..... 121

Figure 5.4: Liquid temperature along height at steady state, where the temperature is reported at $r = 0.03$ m, the black square denotes the experimental data from measurements, the blue dashed curve denotes the numerical results, and the red dotted line labels the liquid level. 122

Figure 5.5: Temperature contour in liquid at $t = 2000$ s, where the temperature ranges from 298.15 K to 373.15 K..... 123

Figure 5.6: Maximum residues at interfaces 1 (red solid and black dashed) and 2 (green dotted and blue dash-dotted) calculated at the object and liquid sides as a function of time, whose locations (at $t = 2000$ s) are labeled. 125

Figure 5.7: Energy imbalance ratio as a function of time, consisting of the maximum value among individual cells (red solid) and the one applied to the whole CV (blue dashed). 126

Figure 5.8: The variation of MLR as a function of time, consisting of the experimental data (black solid) digitized [75] by removing the initial 250 s with fluctuations and numerical data from the model..... 127

Figure 5.9: The variation of the MLR from interfaces as a function of time. For subscripts, “i0” denotes interface 0 representing the liquid surface (black solid), “i1” denotes interface 1 (red dashed), and “i2” denotes interface 2 (blue dotted)..... 128

Figure 5.10: Liquid temperature along height at steady state, where the temperature is reported at $r = 0.03$ m, the black square denotes the experimental data from measurements, the blue dashed curve denotes the numerical results, and the red dotted line labels the liquid level. 129

Figure 5.11: Temperature contour in liquid and object at $t = 2000$ s, where the temperature ranges from 298.15 K to 570.0 K. 130

Figure 5.12: Maximum residue at different L_C at $t = 600$ s, which are calculated from object (red circle) and liquid (black square) sides. 132

Figure 5.13: Energy imbalance ratio at different L_C at $t = 600$ s, including the maximum value among individual cells (red circle) and the one applied to the whole CV (black square). 133

Figure 5.14: MLR at different L_C at $t = 600$ s, including the experimental data (red circle) from the reference [17] and numerical data (black square) from the model. 134

Figure 5.15: The variation of the MLR from interfaces at different L_C at $t = 600$ s. For subscripts, “i0” denotes interface 0 representing the liquid surface (red circle), and “i1” denotes interface 1 (black square)..... 135

Figure 5.16: Temperature of the object surface ($r = 0.05$ m) and flame along the height, where $t = 600$ s, the length of the heater is $L_H = 0.035$ m, and the length of the object is $L_C = 0.14$ m. 136

Figure 5.17: Temperature contour in liquid and object at $t = 600$ s, where $L_C = 0.04$ m, 0.05 m, 0.09 m, 0.12 m, 0.14 m, and 0.16 m, and the temperature bar ranges from 298.15 K to 1000.0 K..... 138

Figure 5.18: Flame height at different L_C , where the numerical data is obtained at $t = 600$ s, and the corresponding images are taken during experiments. 139

Figure 5.19: Maximum residue at different L_C at $t = 600$ s, where values of residue are calculated from object (red circle) and liquid (black square) sides, respectively, and $L_C = 0.04$ m, 0.05 m, 0.09 m, 0.12 m, 0.14 m, 0.16 m, 0.2 m, 0.25 m, 0.3 m, 0.4 m, 0.5 m, 0.6 m, 0.7 m, 0.8 m, 0.9 m, and 1 m..... 141

Figure 5.20: Energy imbalance ratio at different L_C at $t = 600$ s, including the maximum value among individual cells (red circle) and the one applied to the whole CV (black square). 142

Figure 5.21: MLR at different L_C at $t = 600$ s, including the experimental data (red circle) from the reference [17] and numerical data (black square) from the model. 143

Figure 5.22: A bar plot showing the MLR from interfaces at different L_C at $t = 600$ s, where the x-axis represents L_C , and the y-axis represents MLR. For subscripts, “i0” denotes interface 0 representing the liquid surface (blank box with blue words), and “i1” denotes interface 1 (shaded box with red words) representing the solid-liquid interface. The percentage denotes the ratio of the MLR from the corresponding interface to the total MLR..... 144

Figure 5.23: Temperature of the object surface ($r = 0.05$ m) (solid) and flame (dotted) along height, where $t = 600$ s, and the lengths of collectors are: $L_C = 0.04$ m, 0.14 m, 0.25 m, 0.5 m, and 1 m. 145

Figure 5.24: Temperature contour in liquid and object at $t = 600$ s, where $L_C = 0.04$ m (a), 0.25 m (b), and 1 m (c), and the temperature bar ranges from 298.15 K to 1150.0 K. 147

Figure 5.25: Maximum residue at different L_C and D_o at $t = 3000$ s, including the values calculated from object (a, red) and liquid (b, blue) sides, where $D_o = 0.0025\text{--}0.04$ m and $L_C = 0.04\text{--}1$ m. 150

Figure 5.26: Energy imbalance ratio at $t = 3000$ s, including the maximum value among individual cells (a, red) and the one applied to the whole CV (b, blue) sides, where $D_o = 0.0025\text{--}0.04$ m and $L_C = 0.04\text{--}1$ m. 152

Figure 5.27: The ratio of MLR to MLR_b at $t = 3000$ s, where $D_o = 0.0025\text{--}0.04$ m and $L_C = 0.04\text{--}1$ m. MLR_b denotes the MLR from the baseline experiment, whose value is 0.11 g/s. 153

Figure 5.28: The ratio of MLR_{i1} to MLR at $t = 3000$ s, where $D_o = 0.0025\text{--}0.04$ m and $L_C = 0.04\text{--}1$ m. MLR consists of MLR_{i0} and MLR_{i1} , which denotes the mass vaporization coming from interface 0 and 1, respectively. The black dashed line points out the situation when $MLR_{i0} = MLR_{i1}$ 154

Figure 5.29: Relationship between \dot{m}'' and P_c/A_c depicted by numerical data (black circle) and a non-linear curve fitting plot (red dashed), where adjusted $R^2 \approx 0.98148$ 156

Figure 5.30: The variation of \dot{m}'' along L_C^* and D_o^* , denoted by (a) numerical data (red sphere) and (b) a non-linear surface fitting plot (rainbow palette), where adjusted $R^2 \approx 0.99528$ 159

Figure 5.31: Temperature of the object surface (solid) and flame (dotted) at different L_C and D_o , where $t = 3000$ s, L_C is (a) 0.14 m and (b) 1 m, and $D_o = 0.0025$ m, 0.005 m, 0.01 m, 0.02 m, and 0.04 m. 162

Figure 5.32: Temperature contour in liquid and object at $t = 3000$ s, where $L_C = 0.14$ m and 1 m, $D_o = 0.0025$ m, 0.005 m, 0.01 m, 0.02 m, and 0.04 m, and the temperature bar ranges from 298.15 K to 1150.0 K. 165

Figure 5.33: Temperature of the object surface (solid) and flame (dotted) at different L_C and D_o , where $t = 3000$ s, L_C is (a) 0.14 m and (b) 1 m, and $D_o = 0.0025$ m, 0.01 m, and 0.04 m. .. 167

Figure A.1: The temperature-resistance calibration, where circular symbols denote experimental data, and lines represent their corresponding linear fitting. The liquid temperature ranges from 50 to 150 °C. 175

List of Tables

Table 2.1: The experimental matrix of the third-stage experiment.	24
Table 3.1: The number of bubbles at points D and E and the motion direction of bubbles, where φ is adjusted from 0° to 90°	43
Table 3.2: The count-up (N_D) and measurement (D_D) of bubbles at the point D, where φ is adjusted from 0° to 74°	46
Table 3.3: The departure frequency and the distribution of bubbles at steady state at different l , where $l = 0-7.0$ mm.	57
Table 3.4: The critical volume and the number of bubbles at steady state at different l	58
Table 3.5: The bubble quantification using the manual method.	66
Table 4.1: Coefficients used by McCaffrey's Correlation for the centerline data [21].	80
Table 4.2: Expressions of $T_{i,j}^{n+1} \Big _{GE}$ calculated at the solid side.	102
Table 4.3: Expressions of $T_{i,j}^{n+1} \Big _{GE}$ calculated at the liquid side.	103
Table 4.4: Properties of the liquid and objects (at 1 atm) [72,82,85-88].	109
Table 4.5: Detailed information of the setup for the first-stage validation.	111
Table 4.6: Detailed information of the setup for the second-stage validation.	113
Table 4.7: Detailed information of the setup for the third-stage validation.	115
Table 5.1: Model inputs for the first-stage validation.	121
Table 5.2: Model inputs for the second-stage validation.	124
Table 5.3: Model inputs for the third-stage validation.	131
Table 5.4: Model inputs for the second-stage parametric study.	148

Nomenclature

Acronyms

CHF	Critical heat flux
CV	Control volume
FDM	Finite Difference Method
LHS	Left-hand side
MLR	Mass loss rate
ONB	The onset of nucleate boiling
RHS	Right-hand side

Symbols, Roman

A	Area	m^2
c	Specific heat	$J/kg \cdot K$
C	Coefficient (in the McCaffrey's Correlation)	
d	differential	
D	Diameter	m
g	Gravitational acceleration	m/s^2
Gr	Grashof number	
h	Convective heat transfer coefficient	$W/m^2 \cdot K$
h_{fg}	Latent heat of vaporization	J/kg

i, j	Unit vectors in a cylindrical polar coordinate system	
I	Current	A
k	Thermal conductivity	W/m · K
l	Immersion depth	m
L	Length	m
max	Maximum	
min	Minimum	
M, N	Points	
N	Number	
Nu	Nusselt number	
Pr	Prandtl number	
q	Heat	W
r, z	Cylindrical polar coordinate	
R	Electrical resistance	Ω
Ra	Rayleigh number	
t	Time	s
T	Temperature	K or °C
U	Voltage	V
v	Volumetric rate, velocity	m ³ /s
V	Volume	m ³

Symbols, Greek

α	Thermal diffusivity	m^2/s
β	Thermal expansion coefficient	K^{-1}
Δ	Difference	
ΔH_c	Heat of combustion	J/kg
ΔH_{vap}	Heat of vaporization	J/kg
ε	Emissivity	
φ	Inclination	$^\circ$
Φ	Energy imbalance ratio	
γ	Residue	
η, θ	Coefficients (in the McCaffrey's Correlation)	
λ	Grid Fourier number	
ν	Kinematic viscosity	m^2/s
π	$\approx 3.14\dots$	
ρ	Density	kg/m^3
σ	Stefan-Boltzmann constant $\approx 5.67 \times 10^{-8} \text{ W}/\text{m}^2 \text{ K}^4$, standard deviation	$\text{W}/\text{m}^2 \cdot \text{K}^4$
ω	Temperature-resistance coefficient	$\Omega/^\circ\text{C}$
ζ	Heat input coefficient	

Subscripts

amb	Ambient
avg	Average

b	Baseline
c	Combustion
C	Collector
conv	Convection
D	Disk
e	Net
exp	Experiment
FP	Flat plate
g	Gas
GE	Governing equation
H	Heater
i	Interface
l, L	Liquid
num	Numerical model
o	Object
R	Rod
rad	Radiation
s	Surface
sat	Saturation
sen	Sensible (heat)
sub	Subcooled
vap	Vaporization
w	Wire

0 Initial

Superscripts

n Index in marching direction

” Per unit area

Overbars

– Denotes averaged quantity or time-averaged quantity

· Rate

Abstract

Keywords: Boiling, bubble visualization, Finite Difference Method, heat and mass transfer, oil spill, pool fire.

In-situ burning of oil spills has been one of the most effective methods to clean up oil leaks in offshore areas. However, it is highly challenging to efficiently burn a thin layer of oil floating on the water surface. A novel technique for oil spill burning developed at WPI in 2014, named Flame RefluxerTM, is further analyzed in this dissertation to obtain controlling parameters. Unlike the conventional heat transfer from the flame to the fuel surface, the Flame RefluxerTM creates an additional thermal loop to collect heat and transfer it to the liquid fuel. As a result, the *in-situ* burning rate improves notably. Furthermore, subcooled nucleate boiling phenomena on the surface of the immersed object significantly improve both boiling and burning rates. The nucleate boiling is analyzed in depth in this dissertation.

Several existing works have reported the positive impact of the immersed object. However, the mechanisms and interactions remain unclear, and further investigations are desired. This dissertation performs three phases of experiments, followed by a comprehensive numerical model development.

The first-stage experiments are performed in a subcooled dodecane pool, where an electrically heated wire-shaped nichrome object is immersed. Various bubble phenomena are characterized to analyze the boiling process. The inclination of the object, φ , is varied as the variable, where $\varphi = 0^\circ$ (horizontal), 22° , 33° , 44° , 49.5° , 74° and 90° (vertical).

The second-stage experiments are performed by immersing a composite-shaped aluminum object in a burning liquid ethanol pool with refilling. The heated object, bulk liquid, and fire

interactions are analyzed and coupled to various bubble phenomena observed with different immersion depths. The initial immersion depth, l , is varied as the variable, where $l = 0$ mm, 2.5 mm, 4.5 mm, and 7.0 mm. Further analyses state the inconsistency in mass loss rate as a function of depth from the processed data and bubble visualization perspectives.

The third-stage experiments are performed by immersing a composite-shaped copper object in a burning liquid ethanol pool with refilling. The difference between the second and third stage experiments is the inclusion of regularly spaced holes added to the immersed object serving as active nucleate boiling sites. Three cases are analyzed: “no holes”, “small holes” ($D = 1.09$ mm), and “big holes” ($D = 2.06$ mm) cases. In all experiments (stages 1, 2, and 3), unique photography techniques are employed to capture various bubble phenomena allowing qualitative and quantitative analysis.

Using the Finite Difference Method (FDM) and an explicit time marching scheme, a numerical model is developed to discretize the governing equations and boundary conditions on the C programming platform. The convergence is verified by checking the residue at interfaces and the energy imbalance for the domain. The simulation results are validated by comparing the results with the experimental data from the literature. After the model is verified and validated, two parametric studies are conducted to explore the influence of the object configurations on the pool fire for potential optimal designs.

Ultimately, this dissertation provides a framework to seek and examine potential designs while using the Flame RefluxerTM technique, with a long-term goal of providing solutions to clean up oil spills at sea effectively.

1 Introduction

This chapter systematically presents the background of the research topic, literature related to the topic, motivation for the present work, broad scope, and specific objectives.

1.1 Background and motivation

Accidental oil spills into the environment have brought intractable issues and addressed public concerns for decades by harming the vulnerable ecosystem and the sensitive social economy [1-2]. Damages of oil spills at sea are usually much worse than those on land because the oil contaminant can spread on the water surface and move for miles, which may penetrate the ecosystem in the form of the oil slick, toxic volatile components, etc. [3-5]. Meanwhile, it is challenging and costly to attenuate, remove, and clean up oil spills [6]. Especially amid the recent COVID-19 pandemic, the situation has exacerbated the oil industry. The cost of oil production, storage, and transportation has increased, while the budget to understand and handle the oil spills disasters has shrunk due to the economic crisis [7-8]. Therefore, the techniques that effectively manage the spilled pollutants are essential.

Multiple strategies have been implemented to mitigate oil spills hazards; for example, *in-situ* burning (ISB) - to burn the oil in place, is recognized as one of the most traditional and effective methods [9-10]. But even though the ISB method has been frequently utilized on land, it has been challenging and counterintuitive to burn the thin oil slick over water directly [11]. This is because of considerable thermal dissipation through the underlying cold water. Furthermore, there is only around 1-5% of thermal feedback from the flame to the oil surface to vaporize the liquid oil [12]. At the same time, the remaining heat is lost to the ambient via plume convection and radiation, which causes the vaporization rate not sufficient to sustain the complete burning [13]. Fortunately,

by taking advantage of a design proposed by the researchers from Worcester Polytechnic Institute [13- 18], the ISB technique has been significantly improved, manifesting an increase in the oil burning rate. The idea is illustrated in Figure 1.1, where a thermally conductive object is immersed in an oil pool such that it interacts with both flame and liquid fuel. Under the circumstances, an additional thermal feedback loop is formed, as illustrated in Figure 1.2, enabling increased heat and mass transfer processes within the regions.

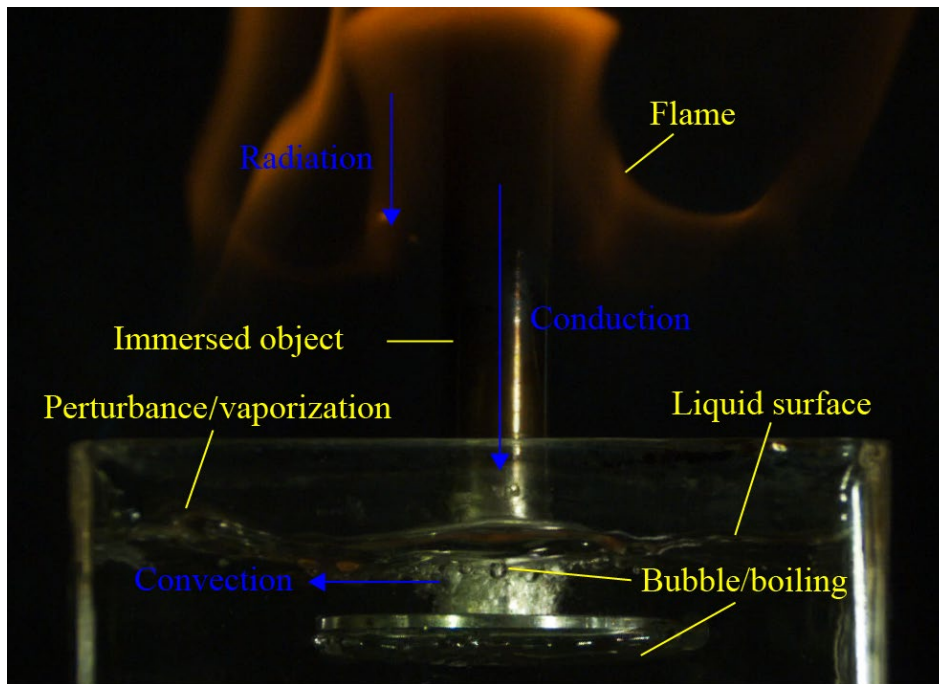


Figure 1.1: Illustration of a liquid pool fire with an immersed object, where the heat transfer mechanisms (blue) and important experimental configurations with phenomena (yellow) are labeled.

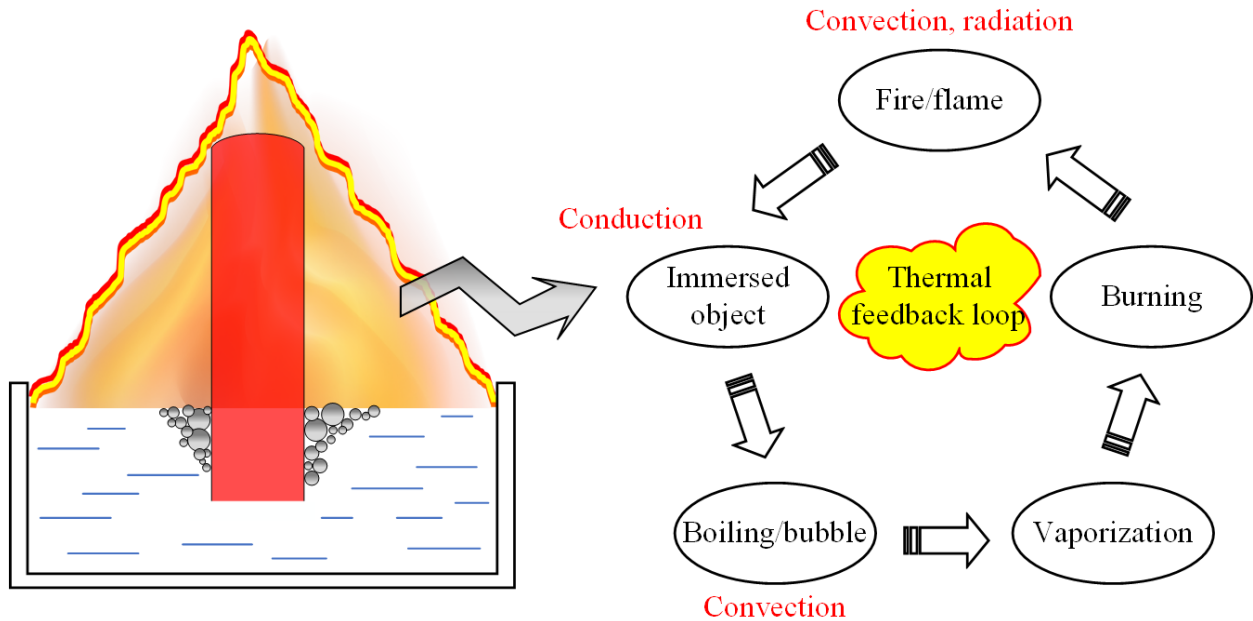


Figure 1.2: A sketch (LHS) shows a liquid pool fire with an object immersed at the center, and a corresponding diagram (RHS) depicts the formation of the thermal feedback loop.

Two fundamental mechanisms are believed to contribute the most to the enhancement in the burning rate. Firstly, the integrated interactions among gas, liquid, and solid regions in this configuration. Considerable heat is efficiently collected from the flame by a high thermal conductivity material and is transferred to the liquid pool through the immersed portion via conduction. The liquid pool surface receives heat by conduction, convection, and radiation. Therefore, when compared to traditional pool fires, there is an additional heat transfer to the core of the liquid by the immersed object conducting heat.

Additionally, as the immersed object's temperature exceeds the liquid fuel's saturation temperature, the boiling heat and mass transfer processes initiate at the solid-liquid interface. Depending on the degree of superheat, boiling occurs on its surface in contact with liquid. Subsequently, bubbles form at the solid-liquid interface displaying vigorous behaviors, including

nucleation, growth, transport, and breakup, which facilitate heat and mass transfer primarily through convection. As a result, an enhancement in liquid fuel vaporization occurs, the burning rate increases, and the pool fire with a higher burning rate is sustained.

Improvement in the design requires exploring two fundamental mechanisms using systematic stages of investigations. Based on this requirement, the primary motivation for this dissertation includes obtaining a relationship between the pool fire burning and nucleate boiling heat and mass transfer due to the presence of the immersed object. Furthermore, by following this methodology, multiple configurations of the immersed object have to be studied and analyzed to understand the effect of configurational parameters of the immersed object on burning rate, which benefits the practical design solving real-world oil spills issues.

1.2 Literature review

Before detailed explorations, some important concepts and studies associated with this design are reviewed from existing literature, including the pool fire, heat and mass transfer process, and subcooled boiling.

For liquid pool fires, the variables of interest include pool diameter, thermal properties of liquid, absorption of flame radiation by the liquid surface, etc. [19-21]. *In-situ* burning belongs to them and is a method to clean up oil spills at sea, where the oil floats on the water surface. However, sustaining the burning of a thin oil layer over water is challenging. Therefore, the method needs improvements in increasing the burning rate and efficiency. Accordingly, some researchers proved that liquid fuel's vaporization and burning rates could be significantly improved, by immersing thermally conductive objects passing through both flame and liquid regions via experimental and numerical strategies [13-22]. If this concept can be analyzed comprehensively, the corresponding applications will be simple, feasible, and efficient to treat oil spills at sea.

Experiments were conducted to study different aspects of pool fires [23- 28], but few of them investigated non-combustible objects immersed in the flame and the liquid to collect the heat from the flame. Some studies [29-31] investigated the thermal response of objects engulfed in fires, but they mostly focused on the interactions between the solid and gas regions from a structural fire safety point of view. Recently, Rangwala et al. [13] conducted pool fire experiments of different scales in hexane and oil-water emulsion. As a result, around 280-1250% increase in the burning rate was reported, compared to the baseline cases without such immersed objects, because of the nucleate boiling facilitated by the immersed objects. It was also found that pool fire burning rate varied with the height of the immersed object, and the maximum burning rate was obtained when the object was fully exposed to the flame. However, clear bubble visualization was not possible during the experiments because of the use of opaque containers or fuels. Further analyses [17] were conducted to a series of bench-scale experiments, where a thin metal cylinder was used as the immersed object. The results showed that such a design could be utilized to clear up oil spills efficiently. Arsava et al. [18] proposed an empirical-based integral model to predict the temperature profile in the liquid region, which was validated by the experiments performed in the crude oil slick over saline water. Fang et al. [22] analyzed the pool fire with the thermal feedback from embedded plates by including the variable Spalding B number and nucleate boiling correlation in the calculation.

Regarding the numerical works, Sezer et al. [15] studied the burning rate of a pool fire composed of three layers: metal wool immersed in fuel, fuel, and water. Parametric studies showed an optimal metal wool thickness according to the mass burning rate. Sezer et al. [16] also developed a one-dimensional model for solving the transient heat transfer in an immersed aluminum cylinder and combined that with a two-dimensional model for solving the temperature

field within the fuel. Validated results indicated that the mass burning rate was enhanced by the thermal loop and the boiling occurring at the cylinder-fuel interface. Parametric studies were conducted towards the optimal cylinder length in the flame.

As indicated in preceding discussions, the heat and mass transfer process in the liquid region of the loop played an important role, causing rapid vaporization at the solid-liquid interface after the ambient liquid was heated to its saturation point [32]. While boiling occurs under various circumstances depending on the liquid status, this dissertation focuses on pool boiling, which corresponds to the pool fire having comparatively quiescent liquid [33]. Meanwhile, based on bulk liquid temperature, boiling can be further categorized as subcooled and saturated [33]. It is termed subcooled boiling when the bulk liquid temperature is below its saturation temperature. In contrast, when the temperature is at or slightly exceeds the saturation temperature, it is termed saturated boiling. This dissertation focuses on subcooled boiling because the practical application is applied to open water, where the temperature of the bulk liquid is not saturated.

Four regimes can be identified throughout a pool boiling process, namely, free convection, nucleate, transition, and film boiling [34-35], which may be delineated according to the excess temperature at the solid-liquid interface. Transitions between the regimes can be sensitive and critical. For example, a significant change of heat and mass transfer at the interface is sometimes associated with a slight variation of the excess temperature. Such behavior reveals the discrepancy between a traditional pool fire and a novel one with an immersed object. The temperature variation of the container wall mostly has a negligible impact on the flame compared to the case of a conductive object placed at the center of the pool. The significant temperature difference between the immersed solid and surrounding liquid leads to distinct regimes of pool boiling. For a novel pool fire with a submerged object, subsequent boiling regimes can be reached through the object

surface with noticeable excess temperature. This is different from a traditional pool fire, where heat transfer is dominated by free convection in the liquid region. As a result, the convective heat and mass transfer process is significantly improved, facilitating the burning rate.

Besides excess temperature via thermal measurements, the boiling process can also be depicted by the vapor bubbles generating from the crevices on the solid surface with various behaviors [36-37]. In general, bubbles can hardly be observed in the free convection regime. Isolated bubbles begin to grow from active nucleation sites in the nucleate boiling regime. As the rate of bubble formation increases in the transition boiling regime, bubbles coalesce and start forming a vapor film. Finally, the solid surface is fully covered by a vapor film in the film boiling regime [33].

Furthermore, bubble phenomena, as well as heat and mass transfer processes, are influenced by the conditions of the subcooling [38-40], liquid property [41- 46], configurations of the immersed object [47 -58], etc. Lee and Singh [38] reported that when the subcooling condition was applied, the boiling heat transfer could vary because of the variation of the micro-convection adjacent to the heating surface. When the liquid was different, the heat transfer coefficient varied, because of discrepancies in liquid properties, including thermal conductivity, density, and specific heat [43]. Addoms [47] pointed out that the diameter significantly affected the heat flux throughout boiling regimes. He also indicated the critical heat flux (CHF) decreased as wire diameter got smaller because of non-negligible flaws in wires. Siegel and Howell [49] studied the CHF at saturation conditions from electrically heated platinum wires in horizontal and vertical orientations at different gravity levels. They reported that a vertically mounted wire gave lower values of CHF than a horizontal one due to the direction of the buoyancy vector.

Further studies also showed that the difference of CHF became small as gravity reduced. Wang et al. [54] performed a series of subcooled pool boiling experiments on the platinum wires with different inclinations and noticed that the interfacial effects and buoyancy took turns to dominate the bubble movement when the wire was not horizontal. Zhang et al. [55] conducted experiments in liquid nitrogen, where CHF was noticed to monotonously decrease as the wire inclination angle increased from 0° to 90°. Jones et al. [57] investigated solids having a wide range of roughness values in water and Fluorinert™ FC-77 and found a stronger dependence on surface roughness for Fluorinert™ FC-77 than water.

Even though bubble visualization may be helpful, it is challenging to capture vigorous bubbles via unaided eyes because of their tiny size and fast motion. Early researchers set normal exposure time for the photography, and the images were too blurred to read. Later, advanced photography techniques were employed to ensure a better image quality [59- 64]. For example, Westwater and Santangelo [59] successfully captured clear bubbles by implementing 10^{-6} second exposure time for still photographs and 4000 frames per second for high-speed motion pictures. Qiu et al. [62] studied the boiling under low gravity conditions, where bubble shape and lift-off progress were analyzed using high-speed images.

Despite the progress existing works have made towards understanding the technique of enhancing the burning rate using immersed objects, some mechanisms and integrated interactions remain unclear, and further investigations are required. For instance, even though the increased convective heat transfer in the liquid region facilitated the burning rate [13-22], analysis at the solid-liquid interface is still missing. Heat and mass transfer processes and bubble behavior can be unique, especially for the scenarios of an immersed cylinder heated up by a subcooled liquid pool

fire. Furthermore, even though individual mechanisms have been thoroughly studied, the integrated ones have never been unveiled due to comprehensive interactions.

1.3 Objectives

The primary goal of the present research is to investigate the unique phenomena and mechanisms at the solid-liquid interface due to the subcooled nucleate boiling, together with the integrated interactions among gas, liquid, and solid regions in the novel pool fire. Detailed objectives are described below, including the strategies of the experiment and numerical model.

1. Experimental objectives: (1) To experimentally study the heat and mass transfer processes, as well as accompanying bubble visualization, especially for scenarios occurring at the solid-liquid interface. (2) To examine different configurations (inclination, immersion depth, and surface condition) of the immersed object to understand the design from diverse perspectives. (3) To study the unique bubble phenomena during the subcooled nucleate pool boiling by taking advantage of high-speed photography and image processing techniques.

2. Numerical model objectives: (1) To develop a numerical model where primary mechanisms in three phases (gas, liquid, and solid) are modeled by solving the energy equations for a cylindrical object immersed in a liquid-fuel pool fire. (2) To ascertain the temperature distribution for object and liquid regions and predict the mass loss rate of the liquid. (3) To carry out the validation of the numerical model using experimental data from the literature. (4) To perform parametric studies, explore the object configurations' influence on the pool fire with an immersed object.

The primary **deliverables** from the present work include:

1. The unveiling of the unique phenomena occurring at the heated solid-liquid interface in a subcooled liquid pool.

2. The analysis of the thermal feedback loop, including the mechanisms of pool fire and nucleate boiling heat and mass transfer.
3. The build-up and development of a model capable of including major mechanisms in all regions.
4. The demonstration of the effect of geometrical parameters of the immersed object on burning rate, based on the analyses of experimental measurements, phenomena, and parametric studies from the model.

Ultimately, the present work's long-term **purpose** is to provide solutions to effectively clean up oil spills at sea after filling the void in the understanding of the novel pool fire burning facilitated by nucleate boiling heat and mass transfer processes. The results from the present works enable comprehensive cognition of the integrated physical mechanisms behind the design. The strategies provide a framework to seek and examine potential optimal designs, from the perspectives of effectiveness, efficiency, and implementation feasibility. The methodology to evaluate the integrated mechanisms of pool fire and nucleate boiling heat and mass transfer would provide references to solve problems with similar concerns.

1.4 Layout

The main body of the dissertation consists of six chapters:

- Chapter 1: introduces the general problem of a novel pool fire facilitated by nucleate boiling heat and mass transfer after immersing objects to interact with fire and liquid. An additional thermal feedback loop is formed, whose details require researchers' attention. A comprehensive understanding of the idea contributes to solving oil spills issues at seas.
- Chapter 2: describes the setup, procedure, as well as data collection and analysis for three stages of experiments, consisting of a wire-shaped object immersed in a liquid pool without

fire, a composite-shaped object immersed in a liquid pool fire, and a composite-shaped object (with holes) immersed in a liquid pool fire.

- Chapter 3: presents the results of stages of experiments via processed data, images, and discusses the effect of configurations of the immersed objects.
- Chapter 4: explains the methodology to build up a numerical model, which couples the heat transfer in the liquid fuel and immersed object to the hot gas regions.
- Chapter 5: shows the results of model verification, validation, and parametric studies that explore the effects of geometrical parameters of the immersed object on the burning rate.
- Chapter 6: summarizes the current study and states future works.

2 Experimental setup and procedure

This chapter introduces three stages of experiments [65-68], consisting of a wire-shaped object immersed in a liquid pool without fire, a composite-shaped object immersed in a liquid pool fire, and a composite-shaped object (with holes) immersed in a liquid pool fire. Studies are elaborated from the aspects of experimental setup and procedure, as well as data processing.

2.1 Overview

Experiments are conducted by immersing a heated object in a subcooled liquid pool, whose purpose is to study the mechanisms of a pool fire burning facilitated by subcooled nucleate boiling heat and mass transfer process and examine the object design. Three stages of experiments are carried out.

The first-stage experiment [65] is conducted in a subcooled dodecane pool, where an electrically energized wire-shaped nichrome cylinder is immersed. In this stage, the object's inclination is varied, and the main focus is to investigate the impact on the liquid vaporization process. Instead of using fire as a self-coupling heat input method, an electrical power supply is implemented in a controllable manner. Details are discussed in Section 2.2.

The second-stage experiment [66-67] is conducted in a burning liquid ethanol pool with continuous fuel refilling, where a composite-shaped aluminum cylinder is immersed in the pool. In this stage, the immersion depth of the object is varied, and the main focus is to investigate the liquid pool burning enhancement by immersed objects. The experimental setup is updated comparing the previous stage, such as methods of heat input and subcooling, object and container configurations, object's material, liquid's type, etc. Details are discussed in Section 2.3.

The third-stage experiment [68] is conducted in a burning liquid ethanol pool with continuous fuel refilling. A composite-shaped copper cylindrical cylinder with holes at its base is immersed in the pool. In this stage, the immersion depth and the surface condition (holes) of the object are varied, and the main focus is to investigate the liquid pool burning enhancement caused by immersed objects. Similarly, the experimental setup is updated compared to previous stages, such as object and container configurations, the object's material, etc. Details are discussed in Section 2.4.

In each stage, multiple photographs are captured to visualize the process characterized by unique bubble behaviors, liquid perturbation, flame, etc. These phenomena are expected to associate with data carefully measured from experiments.

2.2 First-stage experiment

2.2.1 Introduction

The first-stage experiment [65] is conducted in a subcooled dodecane pool, where an electrically heated nichrome wire is immersed. The setup idea originates from Nukiyama [34], who has immersed an electrically heated nichrome wire in boiling water to study the boiling process. When a heated object is immersed in liquid, heat is transferred from the object's surface to adjacent liquid layers because of the temperature gradient. After the object's surface temperature surpasses the saturation temperature of the liquid, boiling occurs at the solid-liquid interface. Nukiyama [34] has elaborated on the relationship between heat flux and excess temperature, whose values are calculated from current and voltage measurements. Depending on the magnitude of the excess temperature at the interface, different boiling regimes are identified. Therefore, similar methodologies are implemented to initiate the study on the liquid impacted by the boiling process.

Considering the practical application of this study as applied to the oil slick floating on the water surface, a subcooled dodecane pool is utilized.

Furthermore, even though multiple variables [38-58] can be studied for the boiling heat process, configurations of the object are focused in this dissertation to figure out potential optimal designs. For example, the object's inclination can influence the boiling process. However, there are unknowns specific to the interactions between a cylindrical object immersed at various inclinations and the ambient subcooled liquid. Therefore, the object's inclination is selected as the variable to be studied in the first-stage experiment.

Besides data measurements, various bubble motions and growth can also depict the boiling process. Therefore, advanced photography techniques are employed to record the experimental phenomena.

2.2.2 Experimental setup and procedure

The experimental setup of the first-stage experiment is illustrated in Figure 2.1, where a nichrome wire ($L = 1.27 \times 10^{-4}$ m) is immersed in dodecane and energized by a controllable electrical power supply (Mastech HY5005E-2 DC power supply, dual adjustable outputs: 0-50 V and 0-5 A). Two multimeters are employed to measure the voltage and current and are further used to calculate the heat flux from the wire to ambient liquid \dot{q}'' , and the electrical resistance of the wire, R . To control the variables, the size of the wire is maintained the same before each experiment. Also, as a wire's parameters are sensitive to ambient temperature and the manufacturing process, the initial wire resistance is measured before each experiment. Furthermore, the wire is carefully cleaned before each experiment. A subcooled condition is provided for the dodecane pool by placing the glass container in a vat filled with a mixture of ice and water. Thermocouples are used to track the

temperature in both the glass container and the vat, and the subcooled temperature of the bulk dodecane, T_{sub} , is maintained at about 25 °C.

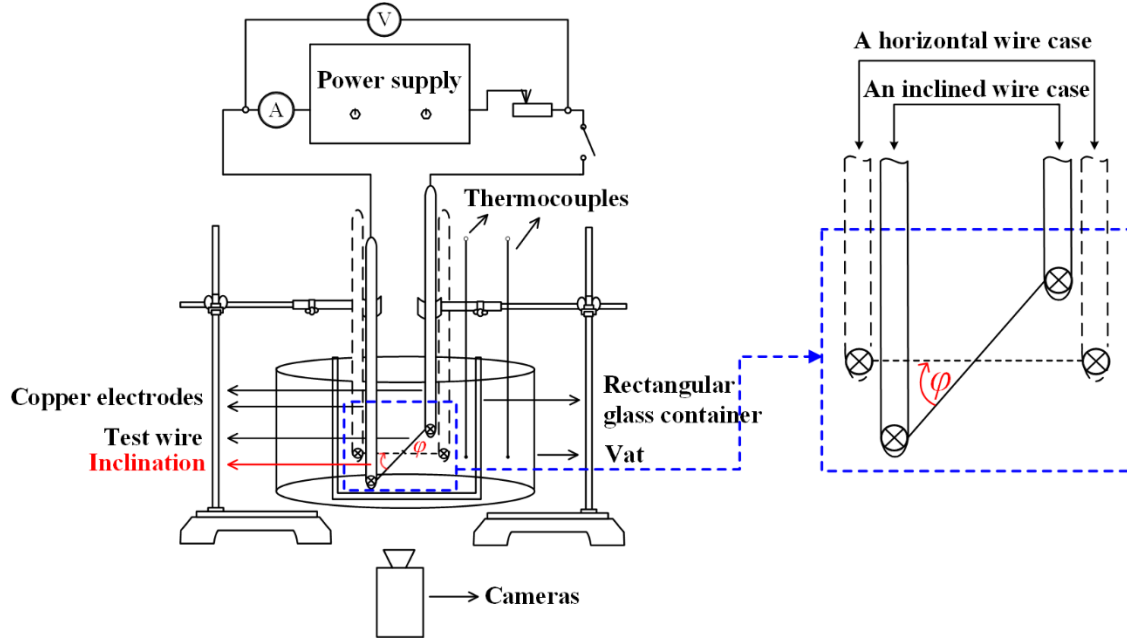


Figure 2.1: Experimental setup of the first-stage experiment (not to scale), where an electrically heated wire-shaped nichrome object is immersed in a dodecane pool with subcooling at different wire inclinations, φ , and $\varphi = 0^\circ$ (horizontal), 22° , 33° , 44° , 49.5° , 74° , and 90° (vertical).

Two thick copper cylindrical electrodes ($D = 1.28 \times 10^{-2}$ m) are connected in the loop to hold the wire and adjust the wire inclination. Because of the lower electrical resistivity and the larger cross-sectional area of thick copper electrodes, their resistance is negligible compared to the thin nichrome wire. After obtaining R , the wire temperature, T , is further calculated by using the temperature-resistance calibration (Appendix A) obtained before the experiments.

As shown in the enlarged sketch on the RHS of Figure 2.1, the wire inclination, φ , is selected as the variable and adjusted from 0° (horizontal), 22° , 33° , 44° , 49.5° , 74° , and 90° (vertical). The

adjustment is realized by moving two electrodes up and down, by maintaining the midpoint of the wire at a constant height.

Cameras (Photron FASTCAM SA1.1 high-speed video system and Sony HDR-PJ790 HD video camera) are equipped at appropriate locations to capture bubble phenomena along the wire at an elevated height compared to the reaction plane container. It is because the unclear view of bubbles restricts the front-view photography through layers of container walls.

Each experiment starts from electrically energizing the wire and ends with the wire glowing or burn-out. Each trial is repeated two to three times to ensure reliability.

2.2.3 Data processing

The heat flux from the wire to the ambient liquid, \dot{q}'' , is calculated from the measurements of the voltage and current, which is given by:

$$\dot{q}'' = \frac{UI}{\pi DL}, \quad (2.1)$$

where U is voltage, I is current, D is wire diameter, and $L \approx 7 \times 10^{-2}$ m is wire length.

Furthermore, by using the measurements of U and I , the electrical resistance of the wire, R , is calculated according to the Ohms Law, which is expressed as:

$$R = \frac{U}{I}. \quad (2.2)$$

2.3 Second-stage experiment

2.3.1 Introduction

The second-stage experiment [66-67] uses fire as the heat input to the liquid fuel to evaluate the interactions among gas (fire), liquid (fuel), and solid (object) regions. The interactions between

any of the two regions have been studied from different aspects in literature. For example, the relationship between a heated object and subcooled liquid fuel is discussed in Section 2.2, the connection between liquid fuel vaporization and pool fire burning is explored in many traditional pool fire studies [23-28], and there are also investigations [29-31] discussing the thermal response of objects engulfed in fires.

The experiment is conducted in a burning liquid ethanol pool with refilling by following some methodologies used in the first-stage experiment. However, some updates need to be mentioned:

1. Fire is used as the heat input to study the mechanisms interacting among all three regions.
2. A composite-shaped cylinder is utilized as the immersed object, enabling horizontal and vertical bubble motions. Its diameter is increased from a wire-shaped cylinder, as it is more feasible to be utilized in fire scenarios. Also, aluminum is used due to its better thermal conductivity and easier processing.
3. Ethanol is chosen as the liquid because it is a comparatively cleaner hydrocarbon with low soot generation and is suitable for long-duration experiments. The liquid level in the reaction container is kept constant, realized by a fuel refilling system.
4. A quartz cuboid tray is used as the reaction container due to changes in the methods of heating and subcooling.

Furthermore, according to the discussions in recent studies [13-18,22], the object's length is noticed to be vital to the boiling process and pool fire burning. Therefore, the immersion depth of the object is selected as the variable to be studied in the second-stage experiment.

Similarly, advanced photography techniques are utilized to record the experimental phenomena, as various bubble motions and growth can depict the boiling process, and the burning process can be characterized by flame height.

2.3.2 Experimental setup and procedure

The experimental setup of the second-stage experiment is demonstrated in Figure 2.2, where a composite-shaped aluminum cylinder is partially immersed in a burning ethanol pool. The object comprises of a cylindrical rod (diameter, $D_R = 11$ mm, length, $L_R = 240$ mm), and horizontally attached with a thin cylindrical disk ($D_D = 34$ mm, $L_D = 0.75$ mm) at the bottom, which is capable of displaying bubble phenomena along with different directions. The idea of the composite-shaped design comes from practical applications [13-18,22] and the results of the first-stage experiment [65]. Furthermore, to ensure a constant surface condition and repeatability, one object is used throughout experiments. The object is carefully cleaned with heptane and then rinsed with ethanol before each experiment. Ethanol is configured in a quartz cuboid tray (inside dimensions: 70 mm \times 70 mm \times 40 mm), and its level is maintained constant via a gravity feedback refilling system. The refilling system consists of a communicating pipe, a feed container (to maintain the liquid level), a pump (Omega FPU5MT peristaltic pump), and a reservoir being placed on a digital load cell (Sartorius ED6202S-CW load cell). Ethanol is constantly supplied to the feed container by a pump at a constant rate, to ensure that ethanol continually spills over into the reservoir return hose. This also eliminates considerable fluctuations in the liquid level in the reaction chamber. The openings of the feed container and reservoir are loosely covered by a thin tinfoil sheet so that the mass loss caused by ethanol evaporation is negligible.

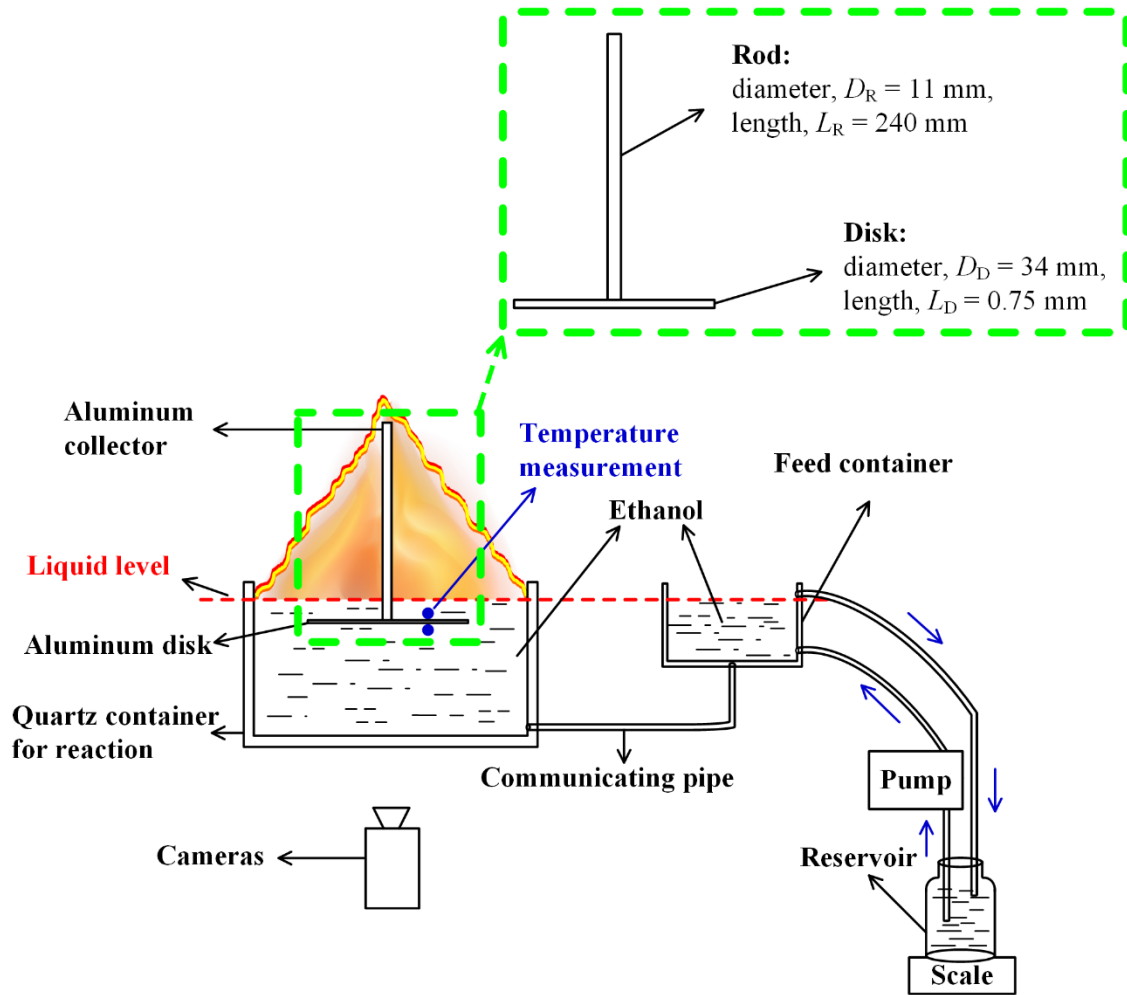


Figure 2.2: Schematic showing the setup of the second-stage experiment (not to scale). A composite-shaped aluminum object is immersed in an ethanol pool fire maintained at a constant liquid level. The immersion depths, l , are adjusted between 0 mm, 2.5 mm, 4.5 mm, and 7.0 mm.

The temperature of the disk's surfaces is measured via a K-type thermocouple. The measurement is applied to its upper and lower surfaces, and the locations are at the center loop between exterior edges of the rod and the disk. Because the boiling process is closely associated with surface conditions, the thermocouple is thus attached to the disk surfaces temporarily at the

end of the experiment, without interfering with the mass loss rate measurement, the photography, or future experiments.

The initial immersion depth, l , is used as the variable, which is defined as the distance between the upper disk surface and liquid level before experiments. It is varied as 0 mm, 2.5 mm, 4.5 mm, and 7.0 mm. The temperature of the setup is maintained at ambient temperature (23 ± 2 °C) before experiments.

Two DSLR cameras (Canon EOS 5D and Canon EOS 7D), a video camera (Sony HDR-PJ790 HD), and a high-speed camera (Chronos 1.4) are placed at appropriate locations to record phenomena of bubbles and flame. Images are recorded as MTS video files for the video camera, whose individual frames are extracted for post-processing.

Each experiment starts from the ignition of a pool fire and lasts for about 900 s (670 s for the baseline experiment). Each trial is repeated three times to ensure reliability.

2.3.3 Data processing

1. Flame height

Flame images are used to analyze the flame dynamics qualitatively and quantitatively. For example, a visible flame region in an image can be used to determine the instantaneous flame height by implementing image processing techniques.

During experiments, a video camera is employed to record the flame at the frame rate of 29 fps. The focus and exposure settings are fixed at the lower part of the flaming region, where the luminosity is fairly steady, to ensure stability and reduce the negative impact from the background. Images are first extracted from MTS video files and then cropped to concentrate on the flame region during the processing. Next, one of the images (taken in the middle of the whole video) is

utilized to set up a gray-scale threshold based on visual observation. The same threshold is applied to all other images from the video. After that, pixels in the images are binarized, where white pixels denote the flame region and black pixels denote the ambient region. The distribution of white pixels is used to evaluate the instantaneous flame extents (height and width). The corresponding instantaneous flame heights are time-averaged to further evaluate the mean flame height within a specific time.

2. Mass loss rate

The mass loss rate of ethanol is calculated based on the variation of mass of the reservoir with time. The mass of the reservoir is measured by a load cell, whose sample rate is set to 5 samples per second. The mean mass loss rate within a certain time is calculated by averaging the corresponding instantaneous mass loss rates.

2.4 Third-stage experiment

2.4.1 Introduction

The third-stage experiment [68] is conducted in a burning liquid ethanol pool with continuous refilling, and it is similar to the second-stage experiment. However, some changes are pointed out:

1. The material of the immersed object is changed to copper because of its higher melting point and better thermal conductivity.
2. The size of the reaction container is increased to ensure ambient conditions at boundaries, as well as to avoid the perturbation caused by the refilling via the bottom.
3. The size of the immersed object is decreased.

Furthermore, literature [47-58] shows that multiple surface configurations influence the boiling process. Therefore, the object's immersion depth and surface condition are selected as variables to be studied in the third-stage experiment.

Similarly, advanced photography techniques are utilized to record the experimental phenomena, as miscellaneous bubble motion and growth can depict the boiling process, and the burning process can be characterized by flame height. A laser system is added, which captures clear images of vigorous bubbles by providing brightness and short pulse time.

2.4.2 Experimental setup and procedure

The experimental setup of the third-stage experiment is demonstrated in Figure 2.3, which is developed based on that used in the second-stage experiment as discussed in Section 2.3. A composite-shaped aluminum cylinder is utilized as the immersed object, consisting of a cylindrical rod (diameter, $D_R = 6.79$ mm, length, $L_R = 68.5$ mm) and a thin cylindrical disk ($D_D = 34.5$ mm, $L_D = 1$ mm). The object is partially immersed in a liquid ethanol pool kept in a quartz cuboid tray (inside dimensions: 100 mm \times 100 mm \times 200 mm). The container is filled with liquid ethanol, whose liquid level is maintained via a gravity feed container through a communicating pipe. Ethanol is constantly supplied to the feed container by a pump (Omega FPU5MT peristaltic pump) at a constant rate of 40 RPM to ensure that ethanol constantly spills over into the reservoir return hose. The fuel reservoir is mounted on a load cell (Sartorius ED6202S-CW load cell) to record the mass variation and obtain the ethanol burning rate. A thin tinfoil sheet loosely covers the feed container and reservoir openings, and the mass loss caused by ethanol evaporation is thus negligible.

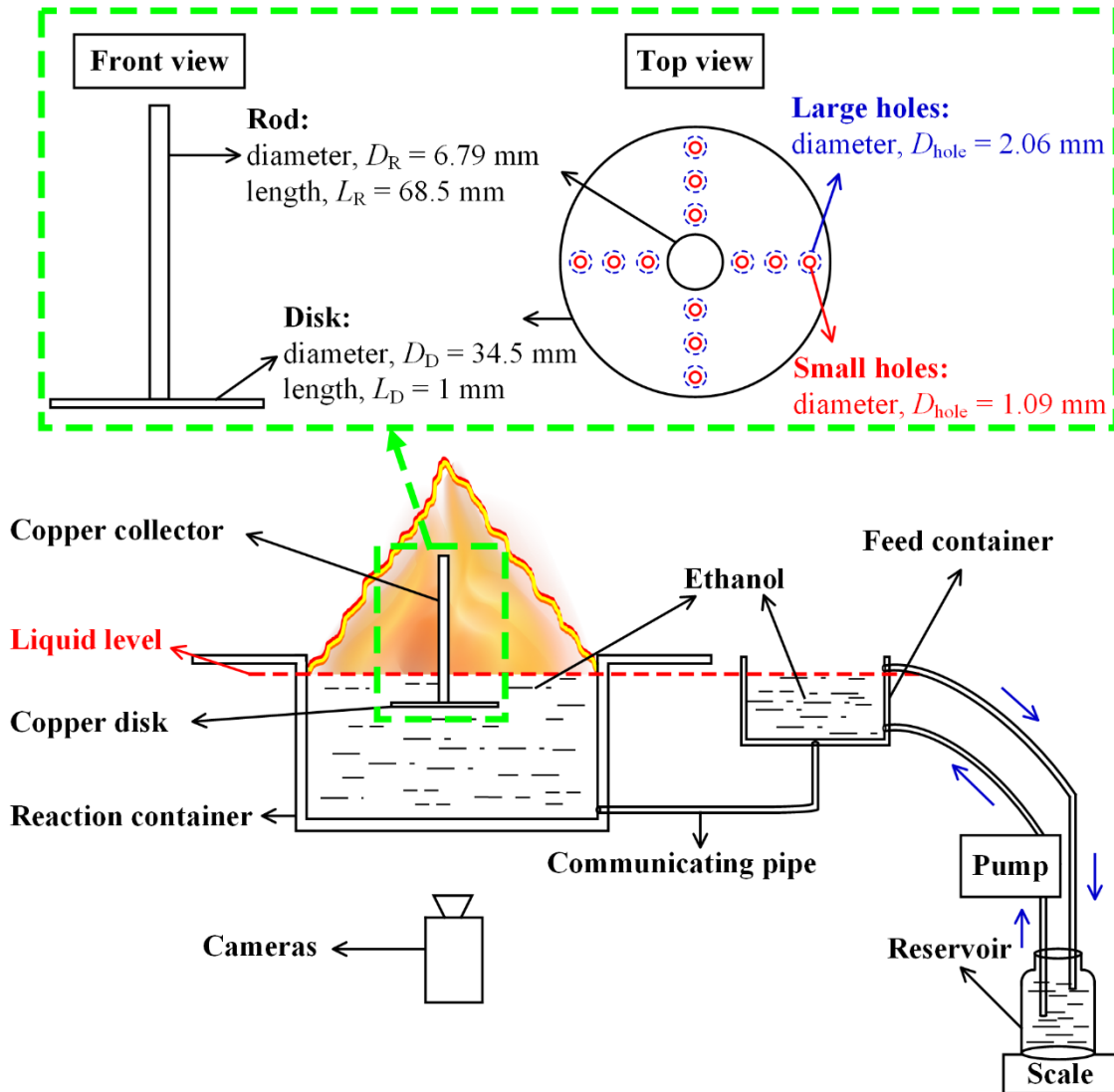


Figure 2.3: Schematic of the setup of the third-stage experiment (not to scale). A composite-shaped copper object is immersed in the liquid ethanol maintaining at a constant liquid level, where the immersion depths are $l = 0$ mm, 3.0 mm, 6.0 mm, and 9.0 mm at a steady state, and diameters of holes (through the disk) are $D_{hole} = 0$ mm (“no holes”), 1.09 mm (“small holes”), and 2.06 mm (“big holes”).

Experiments conducted in this stage are summarized in Table 2.1, which includes two variables: the immersion depth, l , and the surface condition (holes). The immersion depth is

defined as the distance between the upper disk surface and the lower liquid surface at a steady state, which is adjusted between 0 mm, 3 mm, 6 mm, and 9 mm. It is noted that l here denotes the distance at steady state during experiments, which differs from the initial distance defined in the second-stage experiment. Drilling holes vary the surface condition of the copper disk with the diameters of $D_{\text{hole}} = 1.09$ mm and $D_{\text{hole}} = 2.06$ mm through the disk. In both cases, twelve holes are aligned in groups of four as shown in the top view of Figure 2.3.

Table 2.1: The experimental matrix of the third-stage experiment.

Case	1	2	3	4	5	6	7	8	9	10	11	12	13
Immersion distance l (mm)	0	3	6	9	0	3	6	9	0	3	6	9	Baseline
Disk's surface condition*	N	N	N	N	S	S	S	S	B	B	B	B	--

* N: No holes, S: small holes, B: big holes, and --: not applicable.

Several cameras are utilized to visualize experimental phenomena:

1. To depict the bubble formation and distribution in the liquid (side view), high-contrast backlit imaging is taken using a digital camera (Dantec FlowSense 4M MkII 12-bit CCD camera paired with a Nikon Micro-NIKKOR 55mm lens). Simultaneously, a laser system (Litron Nano L 200-15 Nd: YAG 532nm laser is pulsed at its full single-cavity output of 200 MJ per pulse into a vial of Rhodamine 590 dye and methanol, thus causing the Rhodamine solution to fluoresce at 566 nm, and the resultant diffuse light pulse is further diffused via a glass diffuser plate) is introduced, which provides short pulse time of the fluorescent backlight, and allows for clear images capturing bubble behaviors. The camera is set to a frame rate of 12 fps and an aperture of $f/8$ is utilized to ensure that all bubbles within the field of view are within the depth of field of the camera system.

Images captured by the FlowSense camera are dewarped utilizing a polynomial dewarping function, calibrated formed from a dewarping grid imaged before the testing commenced.

2. A high-speed camera (Chronos 1.4 high-speed camera) and a DSLR camera (Canon EOS 7D DSLR) are utilized to record the bubble formation and distribution in the liquid (front view). The frame rate of the high-speed camera is set to around 1500 fps to capture the rapid motion of bubbles. The DSLR is utilized to image bubbles on a ‘snapshot’ basis, therefore, a far lower frame rate at about 1/3 fps is sufficient. Meanwhile, the imaging is illuminated with an LED light source to ensure brightness.

3. To capture the bubble development along the bottom surface, a video camera (Sony HDR-PJ790 video camera) is equipped at an approximate 30-degree angle lower than the plane of the reaction container (bottom view). Videos are recorded at a resolution of 1440×1080 pixels and a frame rate of 29 fps. All images are recorded as MTS video files, and frames from those are extracted for post-processing.

4. To obtain the flame height of the pool fire (side view), a camera (Thorlabs DCC1240C 8-bit color CCD camera paired with a Tamron 35mm C-mount lens) is utilized (side view). The flame is imaged with a resolution of 1280×1024 pixels and a frame rate of 15 fps. All images are recorded as AVI video files, and frames from those are extracted for post-processing.

Each experiment starts with igniting a pool fire; the fire is allowed to burn for 20 min to establish a quasi-steady state before diagnostics are performed. After that, the immersion depth is adjusted as $l = 0$ mm, 3 mm, 6 mm, and 9 mm, and each case has a duration of about 10 min. The diagnostics are implemented after 2 min after each adjustment. Each trial is repeated four times to ensure reliability.

2.4.3 Data processing

1. Mass loss rate

Methodologies of obtaining the mass loss rate are similar to those described in Section 2.3.3.

2. Bubble quantification

Furthermore, with the implementation of multiple cameras, high-quality images capable of capturing clear bubble phenomena can be obtained. Therefore, it would be even more meaningful if the bubble information can be quantified from images besides visualization. In terms of this, two methods are considered to quantify bubbles, which are termed as manual method and the gray-scale method.

(1) Manual method

The manual method focuses on individual bubbles captured from a single image. By taking advantage of a high-speed video camera, the images extracted from the neighboring frames can depict the bubble motion within a short time interval. Therefore, sequential images allow the possibility to track the motion of individual bubbles from nucleation sites to the liquid surface, as shown in Figure 2.4. Meanwhile, the information of individual bubbles is measurable in images, whose calculation depends on the shape of bubbles. Furthermore, the volumetric rate of bubbles, v , is calculated as:

$$v = \frac{V}{t} = \frac{N \times V_0}{t}, \quad (2.3)$$

where V , N , and V_0 are the average values of the total volume of bubbles, the number of bubbles, and the volume of individual bubbles obtained from repeated measurements in different regions,

respectively; and t is the mean time interval which bubbles travel from nucleation sites to liquid surface.

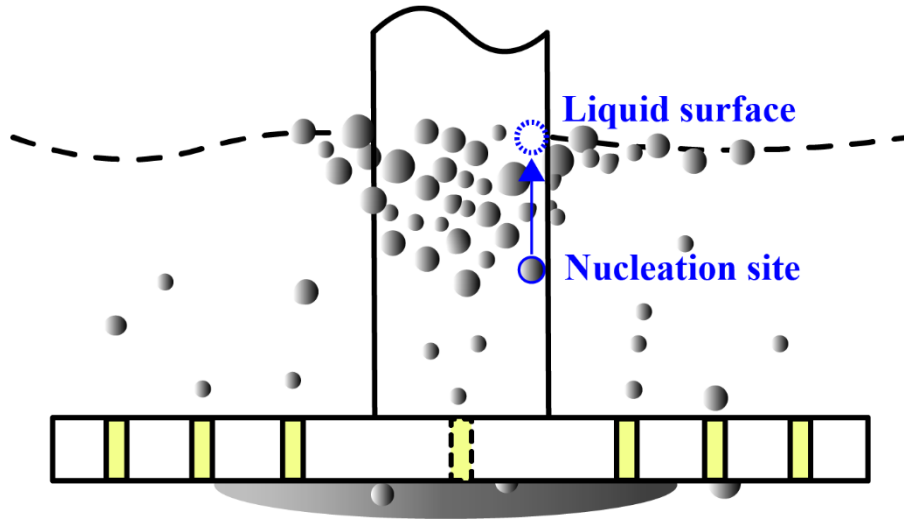


Figure 2.4: Schematic showing an exemplary bubble distribution in a single image. The solid blue circle denotes the contour of a bubble around its nucleation site, and the bubble's departure to the liquid surface is depicted by the blue arrow and the dashed blue circle.

Furthermore, the uncertainty of v during bubble quantification analyses can be determined by considering the propagation of uncertainty [69-70], which is expressed as:

$$\frac{\sigma_v}{v} \approx \sqrt{\left(\frac{\sigma_V}{V}\right)^2 + \left(\frac{\sigma_t}{t}\right)^2}, \quad (2.4)$$

where σ_v represents the standard deviation of v .

(2) Gray-scale method

The gray-scale method focuses on the bubbles around the immersed object captured from the average of multiple images. The dewarped high-contrast photos are utilized for analyses because of the precision in size and the explicit edge. At first, an averaged image is obtained by averaging the corresponding pixels from numbers of images. Next, a gray-scale threshold is applied to the

averaged image, and pixels are hence binarized. White pixels denote the region of the object and the attached bubbles, while black pixels denote the region of the ambient liquid. The distribution of white pixels is used to evaluate the volume of bubbles that are attached to the surface of the immersed object.

3 Experimental results

This chapter shows the results of stages of experiments via processed data and images. The effects of configurations of the immersed objects are meanwhile explored, including the inclination (Section 3.1), the immersion depth (Sections 3.2-3.3), and the surface condition (Section 3.3).

3.1 First-stage experiment

3.1.1 Boiling process

Figure 3.1 shows the variation of the heat flux, \dot{q}'' , as a function of the excess temperature difference between the wire surface and bulk liquid, ΔT , where the wire is horizontally ($\varphi = 0^\circ$) immersed in a subcooled dodecane pool. The x-axis represents ΔT , where $\Delta T = T_s - T_{\text{sub}}$, determinations of the wire surface temperature, T_s , and subcooled temperature of liquid, T_{sub} , are explained in Section 2.2 and Appendix A. The y-axis represents \dot{q}'' , as calculated from Eq. (2.1).

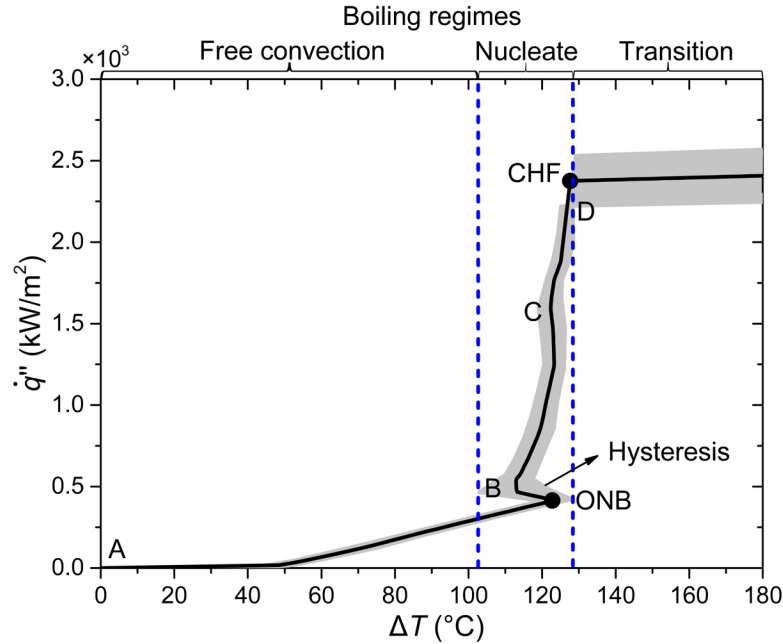


Figure 3.1: A boiling curve depicting a heated nichrome wire horizontally ($\varphi = 0^\circ$) immersed in a subcooled dodecane pool, where the wire diameter, $D = 1.27 \times 10^{-4}$ m and the subcooled temperature of the liquid, $T_{\text{sub}} \approx 25$ °C.

Different regimes can be recognized in the boiling curve. Especially in the nucleate boiling regime, the heat transfer coefficient is found to significantly increase, indicating that the heat transfer rapidly increases even with a slight increase in the temperature of the wire. Similar findings are also mentioned in related studies [13-18], where the regime is believed to be vital to practical applications. Therefore, the process requires further exploration. For example, points denoting the nucleate boiling regime's start and end need special attention, termed ONB and CHF [33]. ONB (onset of nucleate boiling) locates between the free convection and the nucleate boiling regimes. CHF (critical heat flux) locates around the end of the nucleate boiling regime, associated with the upcoming thermal crisis.

Some specific points on the boiling curve are selected for further analyses: points A, ONB, B, C, D, and CHF, as labeled in Figure 3.1. The corresponding images and sketches are presented in Figure 3.2, which allows for the visual analysis of the unique phenomena occurring at each point.

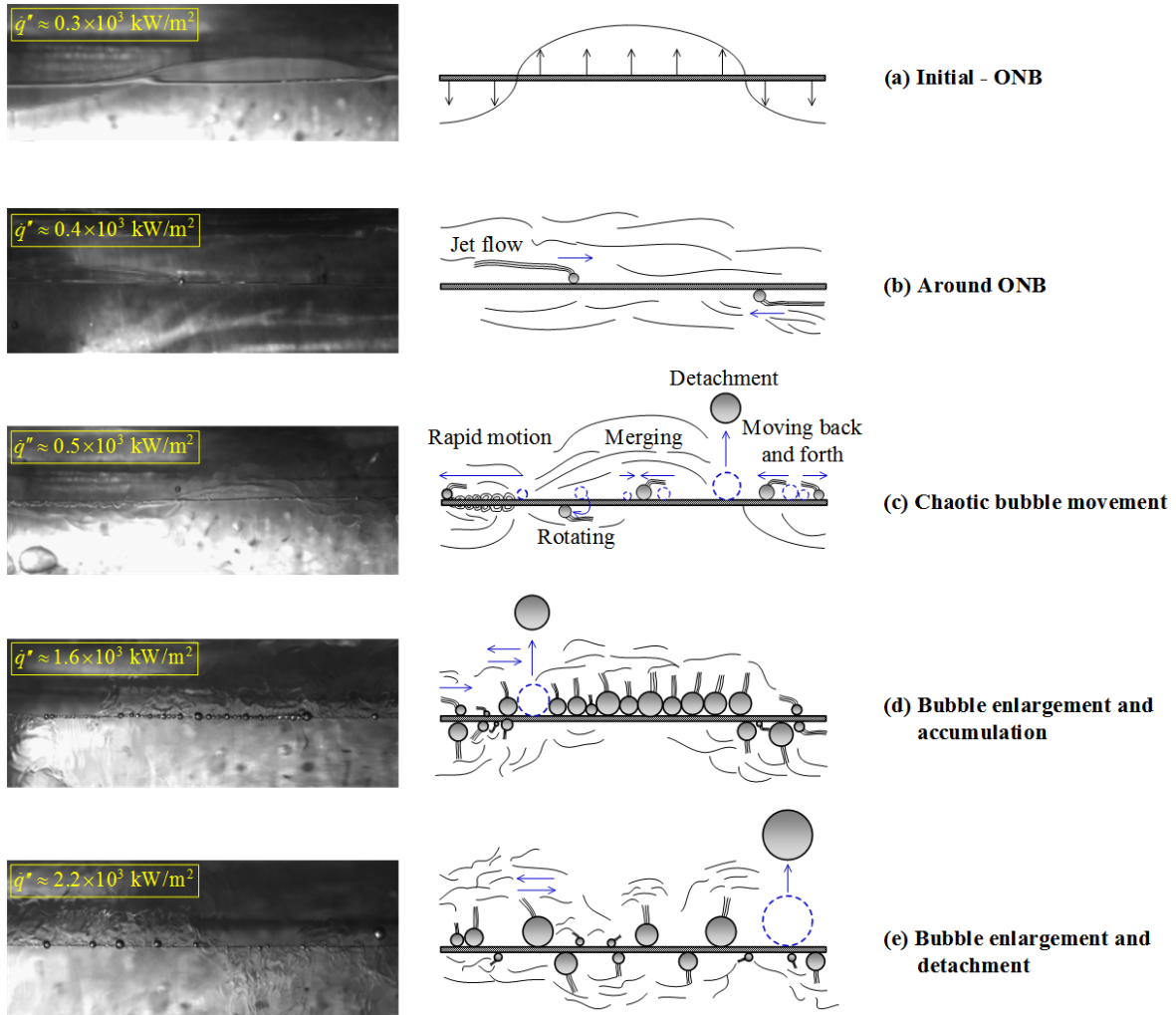


Figure 3.2: Images (taken at an elevated plane) and the corresponding sketches describing characteristic bubble phenomena at different heat flux values, where $\phi = 0^\circ$.

From A to B, \dot{q}'' increases slowly from 0 to $0.4 \times 10^3 \text{ kW/m}^2$, as ΔT increases from 0 to 122 °C as shown in Figure 3.1, where heat is transferred from the heated wire to subcooled dodecane via natural convection. Accordingly, no bubbles are observed on the initial heating plane, as shown

in Figure 3.2(a). Later, when ΔT reaches ONB, a hysteresis phenomenon is presented in Figure 3.1, which denotes the initiation of the nucleate boiling regime. The hysteresis ranges from ONB to B, where ΔT is decreased from 122 to 113 °C, while \dot{q}'' is increased from 0.4×10^3 to 0.5×10^3 kW/m². The hysteresis can be explained by the experimental phenomena as shown in Figure 3.2 (b), where evident perturbation appears in the vicinity of the wire suddenly. Such perturbation is caused by incipient bubbles sweeping along the wire and having jet flows on the top. Immediately after the hysteresis, \dot{q}'' increases sharply from 0.5×10^3 kW/m² at B to 2.4×10^3 kW/m² at CHF, for a small increase of ΔT from 114 to 129 °C during the nucleate boiling regime as shown in 2. The corresponding phenomena are presented in Figure 3.2(c)-Figure 3.2 (e), where the overall bubble size is observed to increase gradually. When the bubble size is large enough, bubbles depart from the wire due to buoyancy. For the number of bubbles staying on the wire surface, it reaches the maximum at C, when $\dot{q}'' \approx 1.6 \times 10^3$ kW/m². After that, comparatively larger bubbles hardly stay on the wire from C to D, where $\dot{q}'' \approx 2.2 \times 10^3$ kW/m² at D. Such phenomena are caused by the increasingly more vigorous bubble behaviors (for example, bubble collision and coalescence) with an increase in \dot{q}'' . Meanwhile, the enhanced heat flux accelerates the bubble growth rate, and hence, the bubble departure becomes more frequent. Finally, when ΔT is further increased to around CHF, the wire glows or burns out.

Furthermore, besides bubble nucleation and departure, there are also various phenomena of bubbles interacting. These include bubble sweeping, chasing, rotating, merging, etc. These behaviors further contribute to the increase of CHF and heat transfer for several reasons:

1. A wider microlayer forms during the boiling process, promoting more thermal absorption from the wire [39].
2. The vaporization at the bubble base helps remove the wire's heat.

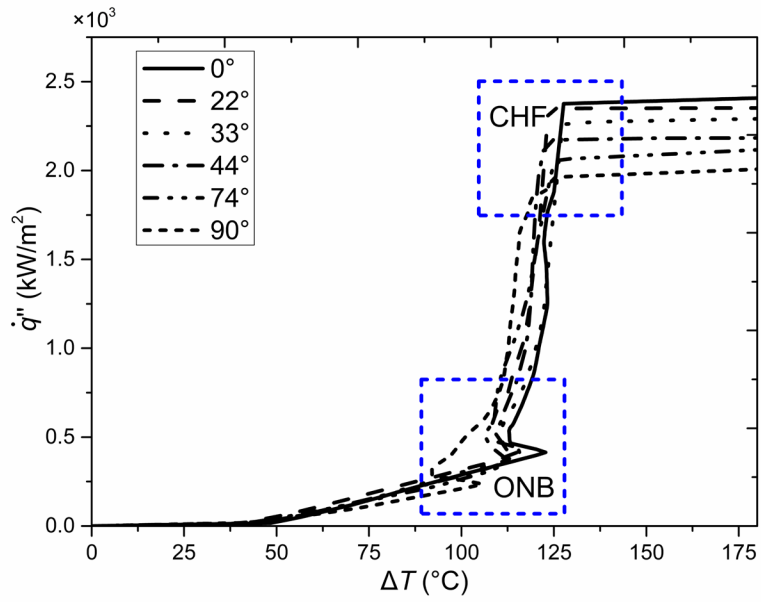
3. Due to the bubble motion, the bulk liquid is introduced to cool the vicinity of the hot wire surface.
4. Jet flows, caused by the bottom-to-top Marangoni effect, appear in regions around the bubble edge and facilitate heat transfer [71].

3.1.2 Influence of the wire inclination

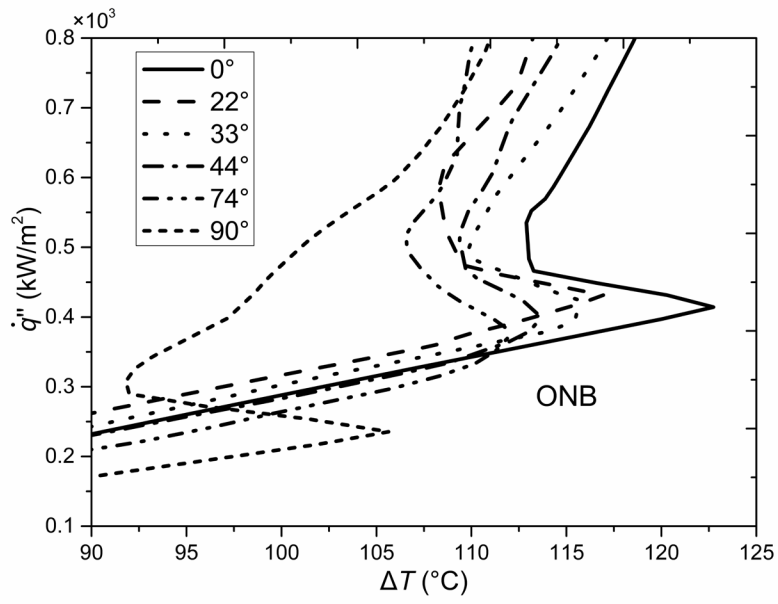
The influence of the wire inclination on the subcooled boiling process is investigated from perspectives of the boiling curve (ONB and CHF) and bubble phenomena (number, velocity, and size), where φ is adjusted from 0° (horizontal) to 90° (vertical).

3.1.2.1 ONB and CHF

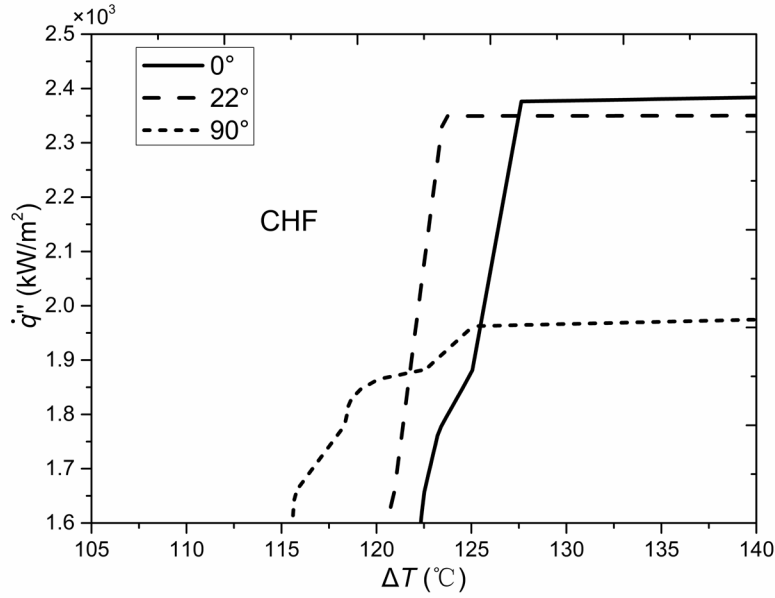
Boiling curves at different φ are presented in Figure 3.3, whose data are averaged from repeated experiments. The influence of φ on ONB is illustrated in Figure 3.3(a) and Figure 3.3(b), where the excess temperature at ONB, ΔT_{ONB} , is found to decrease as φ increases from 0° to 90° monotonically. However, the heat flux at ONB, \dot{q}''_{ONB} , increases as φ is increased from 0° to 22° , and then it decreases as φ is increased further from 22° to 90° . Therefore, the heat transfer coefficient at ONB is the maximum at $\varphi = 22^\circ$. Also, the hysteresis is found around ONB in all cases investigated, and it is especially noticeable at $\varphi = 90^\circ$.



(a)



(b)



(c)

Figure 3.3: Boiling curves showing the variation of \dot{q}'' along ΔT at different ϕ , where $\phi = 0^\circ$, 22° , 33° , 44° , 74° , and 90° .

The influence of ϕ on CHF is depicted in Figure 3.3(a) and Figure 3.3(c). In Figure 3.3(c), when ϕ is increased from 0° to 22° , it is noticed that the decrease in the heat flux at CHF, \dot{q}''_{CHF} , is relatively small (1.1%), while the decrease in the excess temperature at CHF, ΔT_{CHF} , is comparatively more significant (3.2%). This indicates that the heat transfer coefficient increases when ϕ is increased from 0° to 22° , though it decreases as ϕ further increases.

Therefore, the heat transfer coefficient reaches the maximum at $\phi = 22^\circ$ at both ONB and CHF, because of comparative higher \dot{q}'' and lower ΔT . If such inconsistency can be explained, it would be meaningful to future studies and practical applications.

Taking scenarios at CHF as an example, a thermal crisis is initiated from a weak point (an active nucleation site) on the wire and then spread rapidly along the wire, as presented in Figure

3.4. Therefore, it is reasonable to propose that the phenomenon of wire glowing starts at some weak points, where more bubbles stack and coalesce. At some moment, as the heat can only be transferred through vapor, a sharp temperature increase is obtained. Therefore, the reason that CHF reaches the maximum at $\varphi = 0^\circ$, while the heat transfer coefficient reaches the maximum at $\varphi = 22^\circ$ can be explained as follows. For inclined cases, the continuous bottom-to-top motion of bubbles is mainly driven by buoyancy, which actively causes the perturbation of liquid around it. It facilitates the cooling effect on the whole wire. Therefore, the heat transfer coefficient of a fire can be benefited by buoyancy, when $\varphi \neq 0^\circ$. While for a horizontal case, the bubble motion is dominated by the interfacial effects. Thus, the cooling effect is more effective in eliminating weak points but not for the whole wire. Therefore, the maximum CHF can be obtained when $\varphi = 0^\circ$. As $\varphi = 22^\circ$ is the smallest inclination in the cases investigated, it takes advantage of both aspects, and therefore, comparatively larger heat transfer coefficient and CHF are obtained at $\varphi = 22^\circ$.

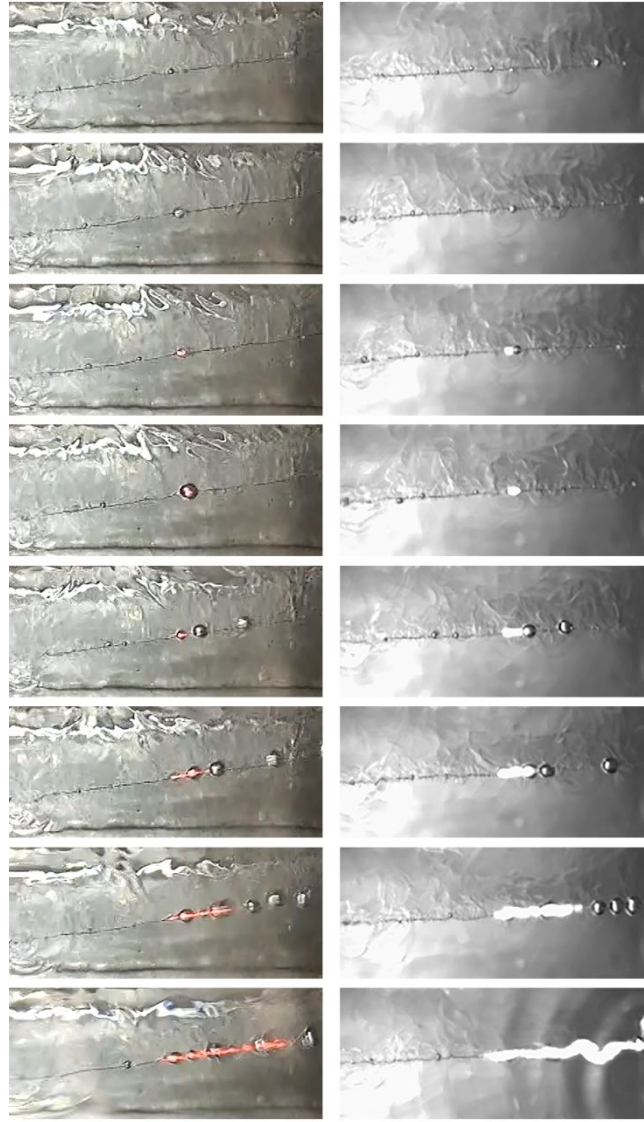


Figure 3.4: Images (taken at an elevated plane) showing the process of a thermal crisis, where $\dot{q}'' \approx \text{CHF}$, $\varphi = 44^\circ$, and the total time duration is about 1.36 s. Images are taken by a video camera (left) and a high-speed camera (right).

3.1.2.2 The influence of φ on the number of bubbles

Figure 3.5 shows an exemplary boiling curve at $\varphi = 0^\circ$, together with six points (A-F) representing different \dot{q}'' . In accordance with this, the bubble phenomena at points A-F are shown in Figure 3.6(a)-Figure 3.6(f), where φ is adjusted from 0° to 74° .

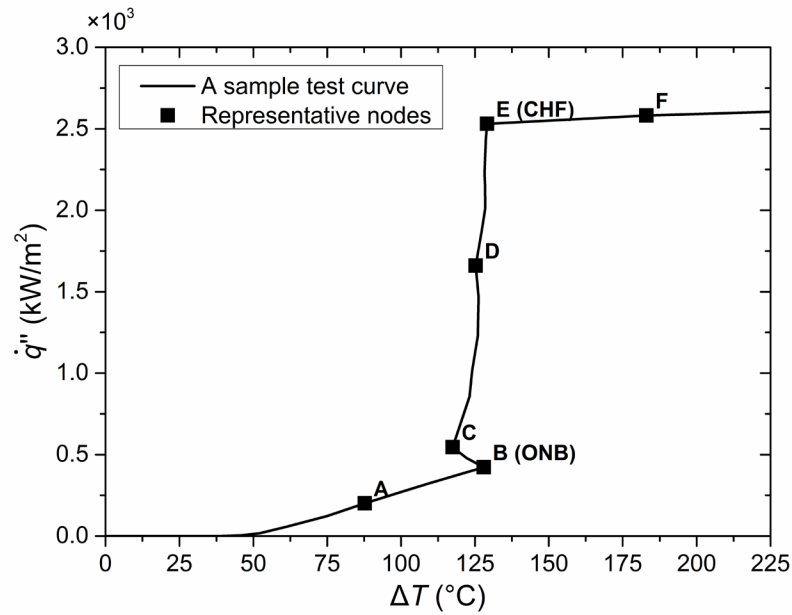
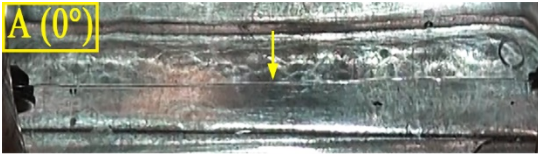


Figure 3.5: Representative locations in the boiling process, where A: $\dot{q}'' \approx 0.2 \times 10^3 \text{ kW/m}^2$, point B: ONB, point C: $\dot{q}'' \approx 0.5 \times 10^3 \text{ kW/m}^2$, denoting the end of hysteresis, point D: $\dot{q}'' \approx 1.6 \times 10^3 \text{ kW/m}^2$, point E: CHF, and point F: wire glowing.



$$\dot{q}'' \approx 0.216 \times 10^3 \text{ kW/m}^2$$



$$\dot{q}'' \approx 0.368 \times 10^3 \text{ kW/m}^2$$



$$\dot{q}'' \approx 0.425 \times 10^3 \text{ kW/m}^2$$



$$\dot{q}'' \approx 1.628 \times 10^3 \text{ kW/m}^2$$

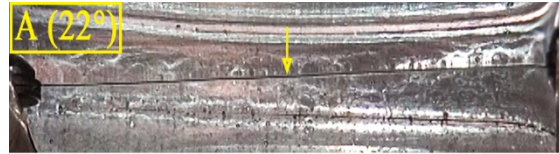


$$\dot{q}'' \approx 2.358 \times 10^3 \text{ kW/m}^2$$



$$\dot{q}'' > 2.358 \times 10^3 \text{ kW/m}^2$$

(a) $\varphi = 0^\circ$ (horizontal).



$$\dot{q}'' \approx 0.186 \times 10^3 \text{ kW/m}^2$$



$$\dot{q}'' \approx 0.431 \times 10^3 \text{ kW/m}^2$$



$$\dot{q}'' \approx 0.554 \times 10^3 \text{ kW/m}^2$$



$$\dot{q}'' \approx 1.590 \times 10^3 \text{ kW/m}^2$$

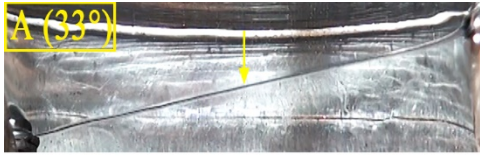


$$\dot{q}'' \approx 2.425 \times 10^3 \text{ kW/m}^2$$



$$\dot{q}'' > 2.425 \times 10^3 \text{ kW/m}^2$$

(b) $\varphi = 22^\circ$.



$$\dot{q}'' \approx 0.224 \times 10^3 \text{ kW/m}^2$$



$$\dot{q}'' \approx 0.424 \times 10^3 \text{ kW/m}^2$$



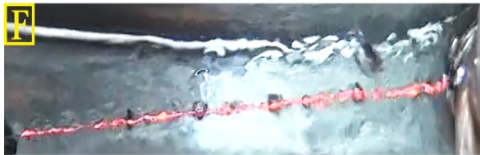
$$\dot{q}'' \approx 0.484 \times 10^3 \text{ kW/m}^2$$



$$\dot{q}'' \approx 1.596 \times 10^3 \text{ kW/m}^2$$



$$\dot{q}'' \approx 2.344 \times 10^3 \text{ kW/m}^2$$



$$\dot{q}'' > 2.344 \times 10^3 \text{ kW/m}^2$$

(c) $\varphi = 33^\circ$.



$$\dot{q}'' \approx 0.225 \times 10^3 \text{ kW/m}^2$$



$$\dot{q}'' \approx 0.370 \times 10^3 \text{ kW/m}^2$$



$$\dot{q}'' \approx 0.545 \times 10^3 \text{ kW/m}^2$$



$$\dot{q}'' \approx 1.582 \times 10^3 \text{ kW/m}^2$$

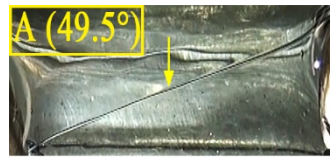


$$\dot{q}'' \approx 2.235 \times 10^3 \text{ kW/m}^2$$



$$\dot{q}'' > 2.235 \times 10^3 \text{ kW/m}^2$$

(d) $\varphi = 44^\circ$.



$$\dot{q}'' \approx 0.238 \times 10^3 \text{ kW/m}^2$$



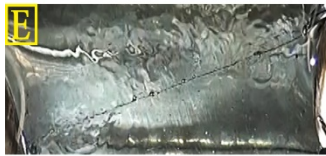
$$\dot{q}'' \approx 0.372 \times 10^3 \text{ kW/m}^2$$



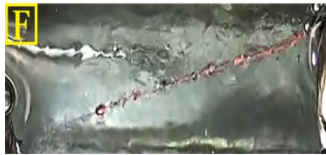
$$\dot{q}'' \approx 0.486 \times 10^3 \text{ kW/m}^2$$



$$\dot{q}'' \approx 1.617 \times 10^3 \text{ kW/m}^2$$



$$\dot{q}'' \approx 2.175 \times 10^3 \text{ kW/m}^2$$



$$\dot{q}'' > 2.175 \times 10^3 \text{ kW/m}^2$$

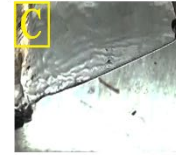
(e) $\varphi = 49.5^\circ$.



$$\dot{q}'' \approx 0.217 \times 10^3 \text{ kW/m}^2$$



$$\dot{q}'' \approx 0.324 \times 10^3 \text{ kW/m}^2$$



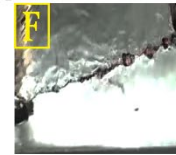
$$\dot{q}'' \approx 0.526 \times 10^3 \text{ kW/m}^2$$



$$\dot{q}'' \approx 1.613 \times 10^3 \text{ kW/m}^2$$



$$\dot{q}'' \approx 2.020 \times 10^3 \text{ kW/m}^2$$



$$\dot{q}'' > 2.020 \times 10^3 \text{ kW/m}^2$$

(a) $\varphi = 74^\circ$.

Figure 3.6: Images (taken at an elevated plane) showing the bubble phenomena at points A-F, where φ is adjusted from 0° to 74° .

As shown in Figure 3.6, no bubbles are observed before reaching B (ONB). Later, bubbles initiate, whose motion causes the hysteresis and changes the natural convective flow right after B. This process starts abruptly and results in a slight decrease in the wire temperature. From C to E, it is in the nucleate boiling regime, where the bubble generation rate, bubble size, and the liquid perturbation increase along the increase of \dot{q}'' . Phenomena of wire glowing and burn-out are observed at F, where \dot{q}'' exceeds CHF and there is a steep increase in the wire temperature.

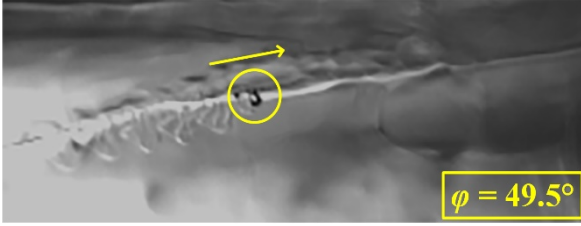
The number of bubbles at D and E is presented in Table 3.1. It should be noted that the number of tiny bubbles whose diameter is less than the wire diameter is not considered in Table 3.1. It is intuitive to find that bubbles do not stay on the wire surface with inclinations. The number of bubbles generally decreases as φ increases, as demonstrated in Figure 3.6 and Table 3.1. As φ is increased from 0° to 22° , the number of bubbles is found to decrease significantly at D. However, the decrease is not that much at E. It is probably because of more vigorous bubble generation and departure at E that has larger \dot{q}'' .

Table 3.1: The number of bubbles at points D and E and the motion direction of bubbles, where φ is adjusted from 0° to 90° .

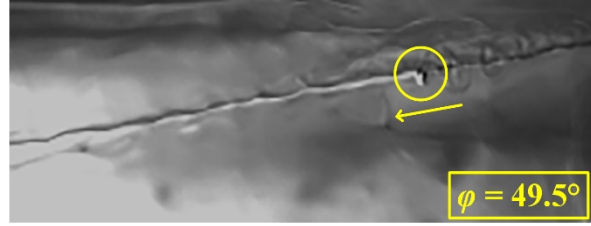
Figure 3.6	Inclination, φ	Number of bubbles at D	Number of bubbles at E	The direction of the bubble motion
(a)	0°	25	12	Back and forth
(b)	22°	6	11	Upward
(c)	33°	6 ± 1	10 ± 1	Upward
(d)	44°	6	10 ± 2	Upward
(e)	49.5°	6 ± 3	8 ± 3	Upward
(f)	74°	6 ± 3	7 ± 3	Upward
--	90°	--	--	Upward

3.1.2.3 The influence of φ on the velocity of bubbles

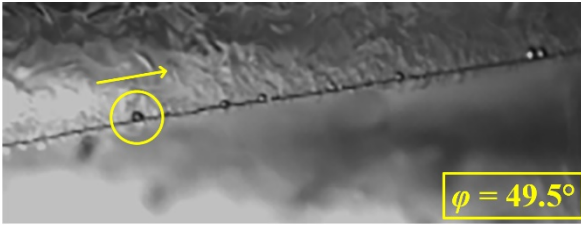
Figure 3.7(a)-Figure 3.7 (d) illustrate the velocity, v , and the moving direction of bubbles at different \dot{q}'' , where $\varphi = 49.5^\circ$. When \dot{q}'' is small, bubbles can move both upward and downward, because the interfacial effects and buoyancy take turns to control the direction of the bubble motion for inclined wire cases [54]. But when \dot{q}'' is further increased, the upward buoyancy becomes dominant, and bubbles solely move upward along the inclined wire. Also, both \dot{q}'' and v can be characterized by the flow pattern. For example, the flow intensity increases as the increase of \dot{q}'' .



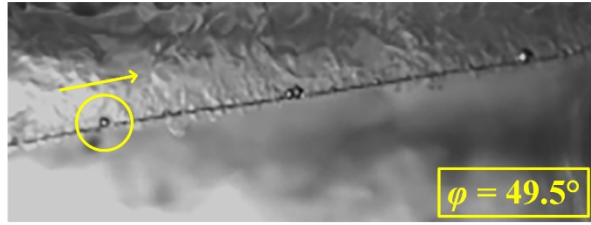
(a) $\dot{q}'' \approx 0.4 \times 10^3 \text{ kW/m}^2$,
 $v = 180.30 \text{ mm/s}$, upward.



(b) $\dot{q}'' \approx 0.4 \times 10^3 \text{ kW/m}^2$,
 $v = -148.18 \text{ mm/s}$, downward.



(c) $\dot{q}'' \approx 1.4 \times 10^3 \text{ kW/m}^2$,
 $v = 66.55 \text{ mm/s}$, upward.



(d) $\dot{q}'' \approx 1.9 \times 10^3 \text{ kW/m}^2$,
 $v = 53.45 \text{ mm/s}$, upward.

Figure 3.7: Images (taken at an elevated plane) showing the bubble motion, where $\varphi = 49.5^\circ$.

The velocity of bubbles is found to change during the boiling process, as presented in Figure 3.7 and Figure 3.8, where the absolute value of v generally decreases as \dot{q}'' increases at $\varphi = 0^\circ$, 22° , 44° and 49.5° . Furthermore, provided with a similar \dot{q}'' , v for inclined wire cases is generally larger than that for $\varphi = 0^\circ$ because of buoyancy. Immediately after reaching CHF, the glowing phenomenon may be observed, together with a dramatic velocity increase.

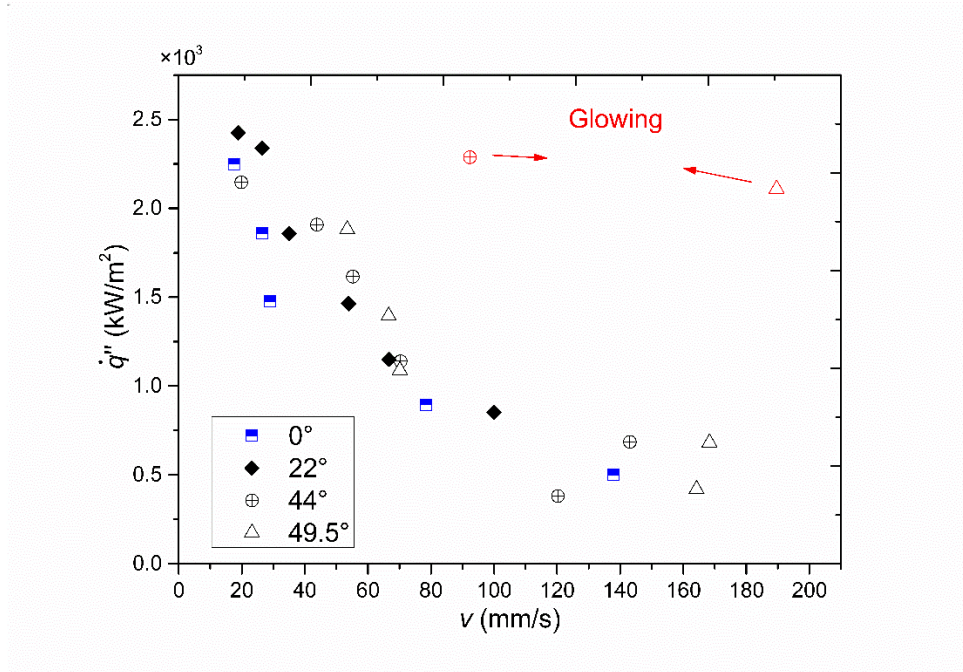


Figure 3.8: The variation of \dot{q}'' along v at different φ , where φ is varied from 0° to 49.5° .

To better examine the bubble velocity, the count-up of the number of bubbles passing through a measurement location (at about 3/4 height of the wire) at D in a time duration of 30 s, N_D , is shown in Table 3.2, where $\dot{q}'' \approx 1.6 \times 10^3 \text{ kW/m}^2$. N_D is noticed to increase as φ increases. Such increase is evident when φ is increased from 22° to 33° , and from 49.5° to 74° , however, the increase is not noticeable from 33° to 49.5° .

Table 3.2: The count-up (N_D) and measurement (D_D) of bubbles at the point D, where φ is adjusted from 0° to 74° .

Inclination, φ	The number of bubbles passing through a measurement location at D, $N_D (\pm 10)$	The average diameter of individual bubbles at D, D_D (m), $\times 10^{-3}$	$N_D \times D_D^3$ (m ³), $\times 10^{-9}$
0°	--	0.529	--
22°	86	0.415	6.145
33°	126	0.331	4.569
44°	132	0.294	3.354
49.5°	134	0.240	1.852
74°	202	0.167	0.941

3.1.2.4 The influence of φ on the size of bubbles

As shown in Table 3.2, the average diameter of individual bubbles, D_D , decreases as φ increases. Furthermore, it is also interesting to evaluate the influence of φ on the total bubble volume at D, by calculating $N_D \times D_D^3$, whose value is found to decrease as φ increases from 22° to 74° .

Among all the inclined cases investigated, the bubble detachment is only found at the top end of the wire, determined by the bubble growth rate and the wire length. Specifically, the individual bubbles arrive at the top end of the wire before reaching the critical bubble detachment size. While for the horizontal case, the bubble detachment is mainly dependent on the bubble size, which may occur at any location on the wire.

Bubble phenomena at different φ are depicted in Figure 3.9, where the heat flux $\dot{q}'' \approx 1.6 \times 10^3$ kW/m² and $\varphi = 0^\circ$, 22° and 44° . Sketches are based on the images taken at an elevated plane. As φ is increased from 0° to 44° , both the number and the size of bubbles decrease. Moreover, for

the horizontal case, the liquid perturbation is found in the regions above and below the wire; while it is mostly above the wire for the inclined cases.

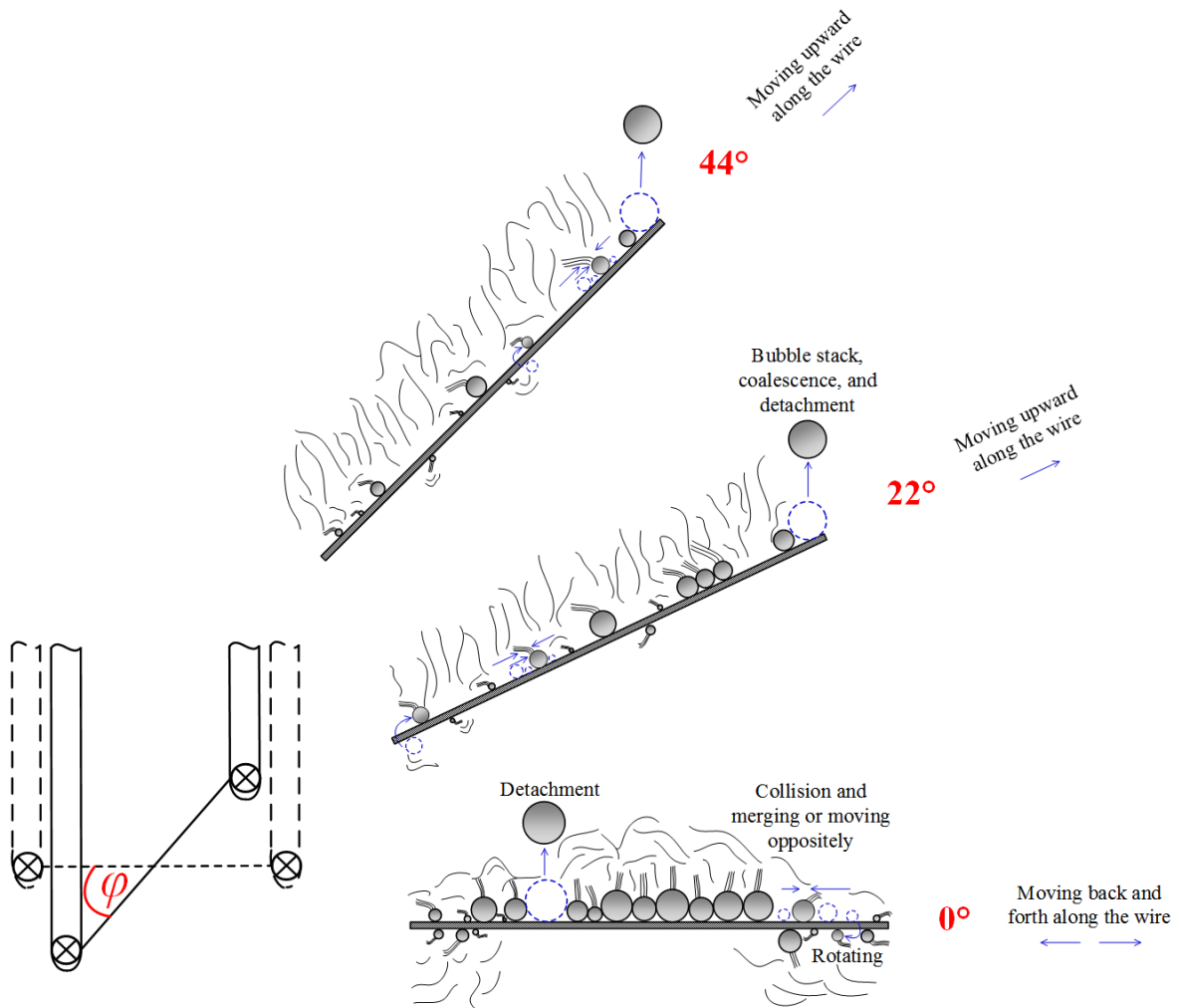


Figure 3.9: A sketch showing bubble phenomena at different ϕ , where $\dot{q}'' \approx 1.6 \times 10^3 \text{ kW/m}^2$ and $\phi = 0^\circ, 22^\circ, \text{ and } 44^\circ$.

Moreover, as shown in Figure 3.4 and Figure 3.6, a significant increase in the size of bubbles is observed after \dot{q}'' exceeds CHF, accompanied by a steep temperature jump as shown in Figure 3.5.

3.1.3 Summary

Experiments are performed by immersing an electrically heated wire-shaped nichrome cylinder in a subcooled dodecane pool. The wire inclination, φ , is varied as $\varphi = 0^\circ$ (horizontal), 22° , 33° , 44° , 49.5° , 74° and 90° (vertical). Interactions between the heated wire and bulk liquid are found to be influenced by the boiling process, and various bubble phenomena can characterize such a process.

Results show that as φ increases, the velocity of bubbles increases, while the number and size of bubbles and CHF decreases. Further analyses show that $\varphi = 22^\circ$ is the optimal inclination from the perspective of heat transfer coefficient because of the comparative higher \dot{q}'' and lower ΔT at both ONB and CHF. Various bubble phenomena, including sweeping, chasing, rotating, merging, etc., are observed during boiling regimes. Such bubble behaviors are considered to facilitate the heat and mass transfer processes.

3.2 Second-stage experiment

3.2.1 Flame height

Figure 3.10 shows the variation of flame height as a function of time for two experimental cases, where magenta triangles denote a baseline experiment, and black squares denote an object immersed in the pool to a depth of 0 mm. The addition of an aluminum object is noticed to increase the flame height by about 150%. The flame height in each image is defined as the distance between the fire source and the top of the flame based on visualizing the flame image. An image processing technique is implemented for analyses as described in Section 2.3.3. During analyses, instantaneous flame heights are averaged every 6 s and used as the average flame height reported in Figure 3.10.

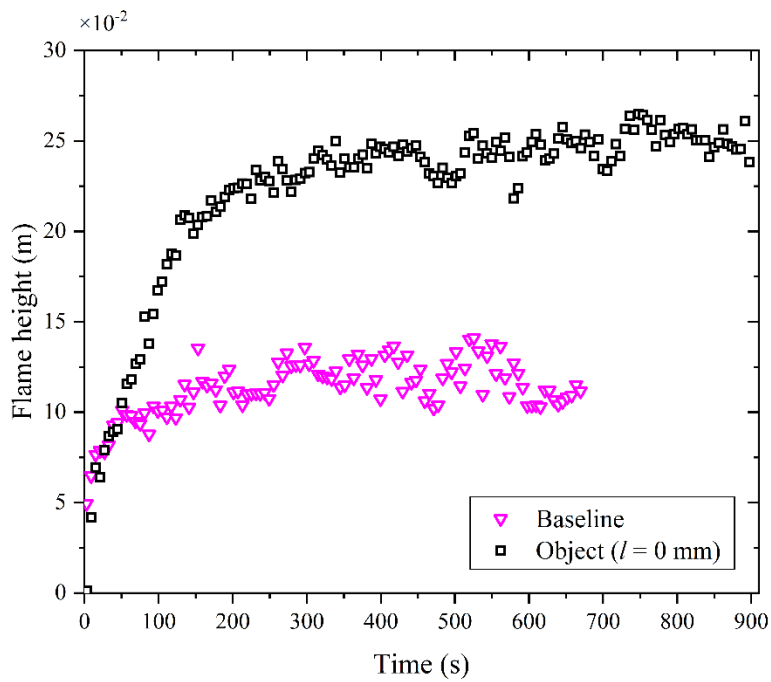


Figure 3.10: The variation of flame height as a function of time, where magenta triangles denote a baseline experiment without immersed objects, and black squares denote an object experiment at $l = 0$ mm.

Images from the corresponding experiments that compare the flame height are shown in Figure 3.11, where $t = 100$ s. The instantaneous flame heights labeled in images are noticed to be slightly higher than those reported in Figure 3.10. It is reasonable for such a small discrepancy because the fire is fluctuating. The data in Figure 3.10 is averaged every 6 s, while it is an instantaneous value in Figure 3.11. More importantly, a similar increase in the flame height is found after introducing an immersed object from images, as shown in Figure 3.11.

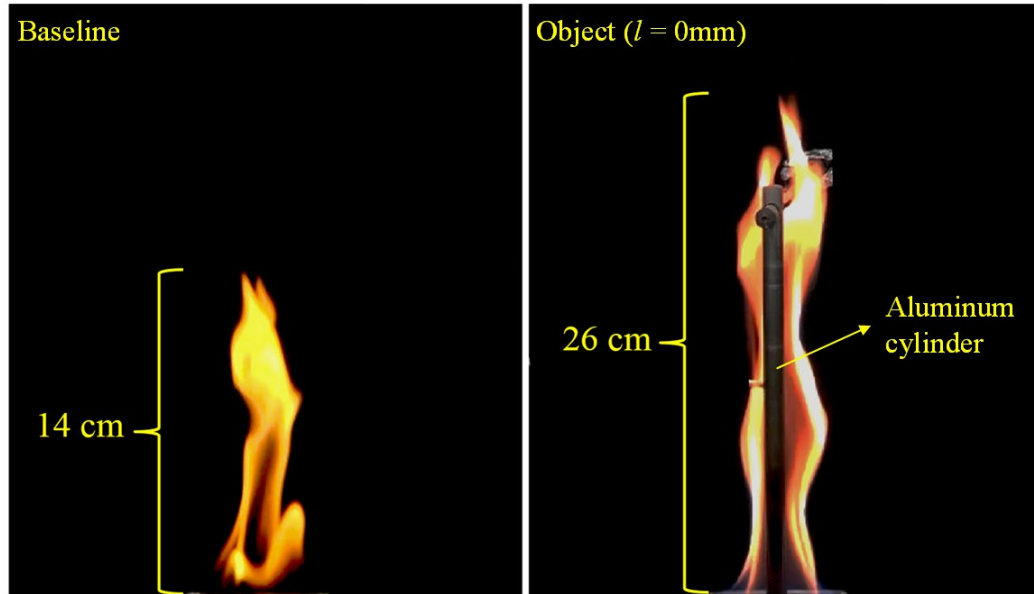


Figure 3.11: Images comparing the flame height between a baseline experiment and an object experiment at $l = 0$ mm, where $t = 100$ s.

3.2.2 Mass loss rate

This section discusses mass loss rate influenced by the addition of an immersed object, as well as the object's initial immersion depth, l .

3.2.2.1 The influence of an immersed object

Figure 3.12 depicts the influence of an immersed object on mass loss rate, where the initial immersion depth is varied as $l = 0$ mm, 2.5 mm, 4.5 mm, and 7.0 mm. Sketches and images are attached to the RHS to explain the setup. Raw data is sampled every 0.2 s for 900 s (670 s for baseline experiment) during experiments. Data is at first averaged per repeated experiments at each time during the data processing, and it is further averaged every 6 s to obtain an averaged mass loss rate. The processed data is denoted by symbols, as shown in Figure 3.12. Additionally, a fifth-

order polynomial fit is applied to depict the corresponding trends, denoted by curves as shown in Figure 3.12.

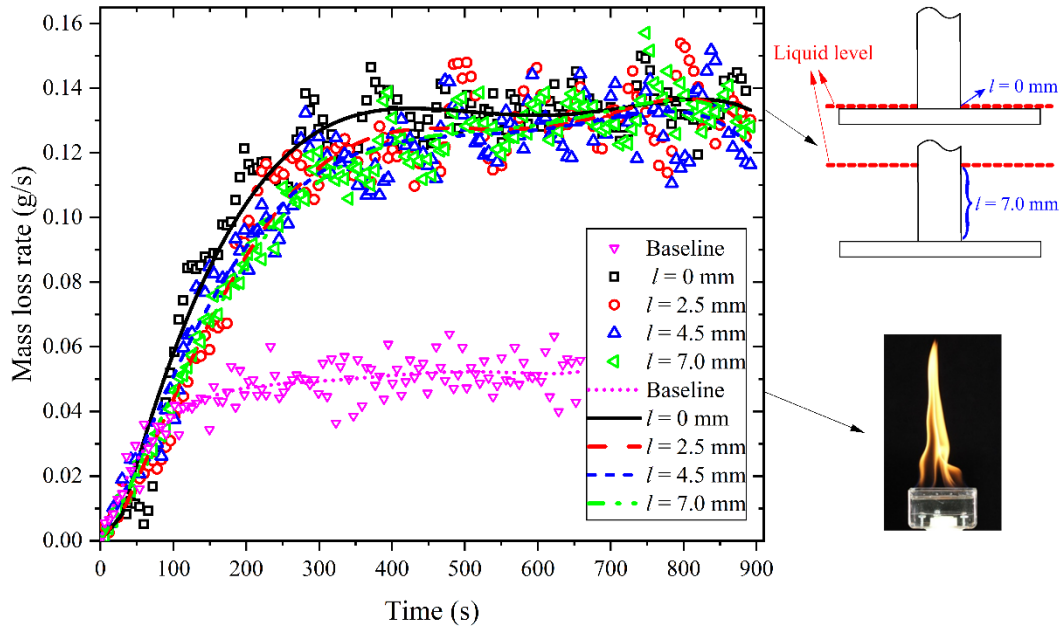


Figure 3.12: The variation of liquid ethanol mass loss rate as a function of time, where magenta down-pointing triangles and the dotted curve denote the baseline experiment, black squares and the solid curve denote the object experiment at $l = 0$ mm, red circles and the dashed curve denote the object experiment at $l = 2.5$ mm, blue up-pointing triangles and the short dashed curve denote the object experiment at $l = 4.5$ mm, and green left-pointing triangles and the dotted curve denote the object experiment at $l = 7.0$ mm.

Figure 3.12 shows that the mass loss rate increases sharply initially and ultimately reaches a steady state for all cases. For the baseline experiment, the steady state is reached earlier at about 150 s, with the corresponding mass loss rate at about 0.05 g/s. For experiments with an immersed object, the steady state is reached at about 300-400 s, with the corresponding mass loss rates reaching about 0.12-0.15 g/s, which is around 2.5 times more than the mass loss rate of the baseline

experiment. Such an increase is because of the formation of a thermal feedback loop induced by the immersed object. Heat is transferred by the rod in the flame and then transferred by conduction to its lower part and the disk immersed in the pool. The subcooled nucleate boiling subsequently occurs on the surface of the heated immersed object, thereby resulting in an enhancement in the ethanol vaporization rate and its burning rate. Such an enhancement in return further facilitates the heating of the rod in the flame.

According to the first-stage experiment, bubble behaviors, such as bubble nucleation, growth, and motion, interact with the liquid actively. Therefore, time-varied bubble behaviors captured at different instants are depicted in Figure 3.13, together with the mass loss rate curve from an experiment. Before the ignition, no bubbles and flow perturbation are observed at $t = 0$ s. Soon after, at $t = 25$ s, incipient nucleation starts after the temperature of the immersed object surface exceeds the saturation temperature of bulk liquid ethanol. Bubbles grow and move around the object with multiple behaviors, such as chase, collision, coalescence, etc., driven by buoyancy and surface tension gradient. At the same time, a significant increase in mass loss rate is observed.

Furthermore, two types of bubbles are observed - small spherical bubbles appear on the surface of the immersed rod, and a flat hemispherical large bubble is attached on the bottom surface of the disk. The large bubble forms by merging tiny bubbles as shown at $t = 118$ s. Bubble behaviors become increasingly vigorous as the combustion reaction continues, which transfers additional heat from the flame. It can be revealed by the increasing number of small bubbles and the growing size of the large bubble. As the bubble size increases, the large bubble departure imitates at around $t = 400$ s.

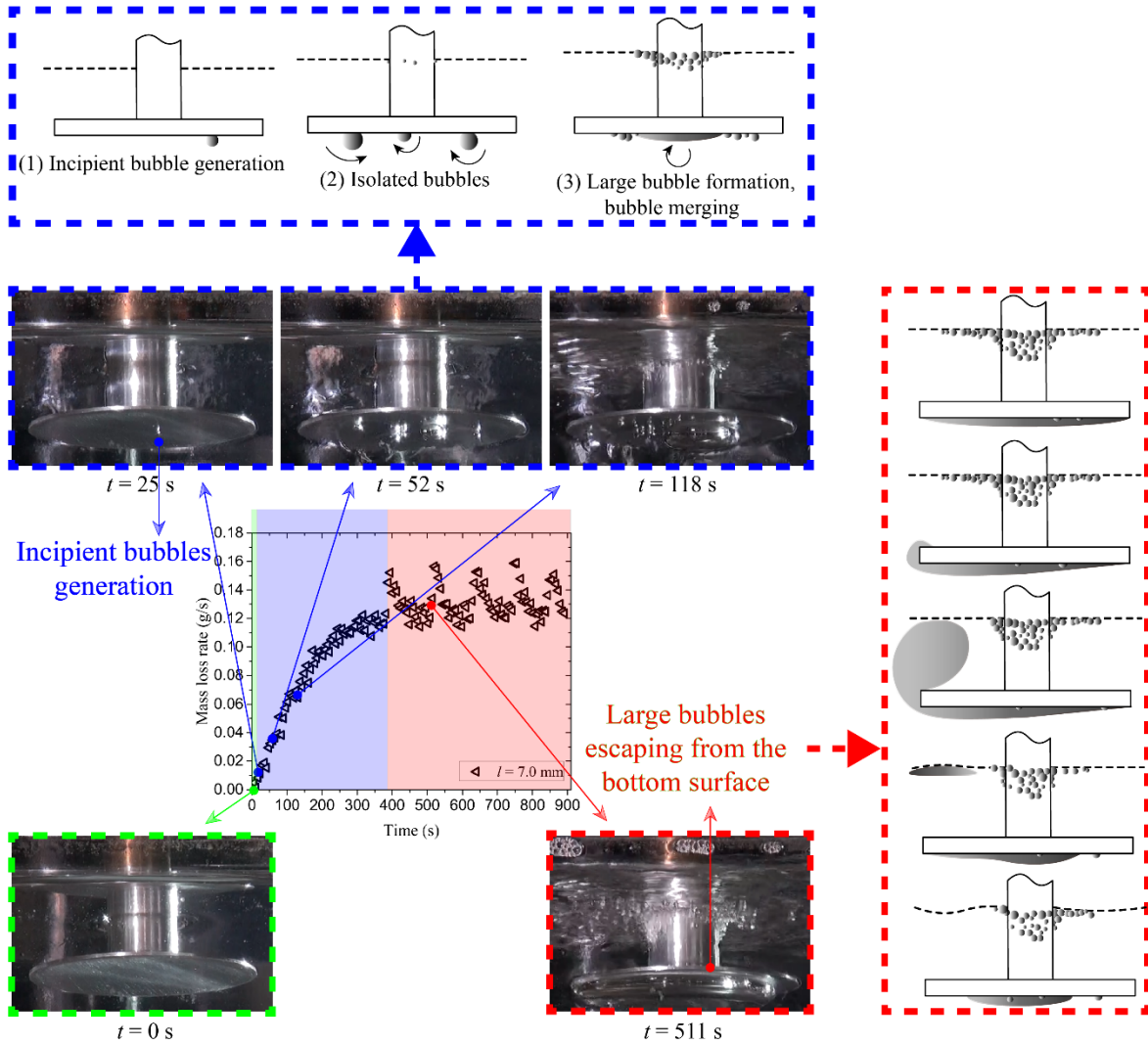


Figure 3.13: Bubble phenomena on the surface of the immersed object, which are in accordance with the mass loss rate curve for a single experiment, where $l = 7.0 \text{ mm}$.

As shown in sketches in Figure 3.13, the expansion of the large bubble ceases, when it reaches the edge of the disk. After that, it escapes from the bottom disk because of buoyancy, resulting in an evident perturbation in ethanol, as well as a conspicuous fluctuation of mass loss rate. The approximate frequency of the large bubble departure ranges from 8×10^{-3} to $1.2 \times 10^{-2} \text{ Hz}$. Small

bubbles' distribution on the immersed rod does not further expand after $t = 400$ s. The departure frequency for small bubbles is much higher, which is over 100 Hz for the cases investigated.

3.2.2.2 The influence of initial immersion depth, l

Recalling Figure 3.12, discrepancies in mass loss rate can be observed at different l . To better analyze differences at the steady state, the mean mass loss rate at different l is shown in Figure 3.14, where $l = 0$ mm, 2.5 mm, 4.5 mm, and 7.0 mm, and a steady state is obtained at $t = 400$ -900 s. Meanwhile, the corresponding temperature measured at both the top and bottom surfaces of the disk is presented. Intuitively, both temperatures decrease as l increases because of the cooling effect of bulk ethanol. However, the mean mass loss rate first decreases and then increases, showing a non-linear behavior. Error bars are included in Figure 3.14 by calculating the standard deviation from repeated experiments. The tendency of mass loss rate at different l remains the same after considering errors. To explain the inconsistency at $l = 4.5$ mm, analyses on the bubble phenomena are expected.

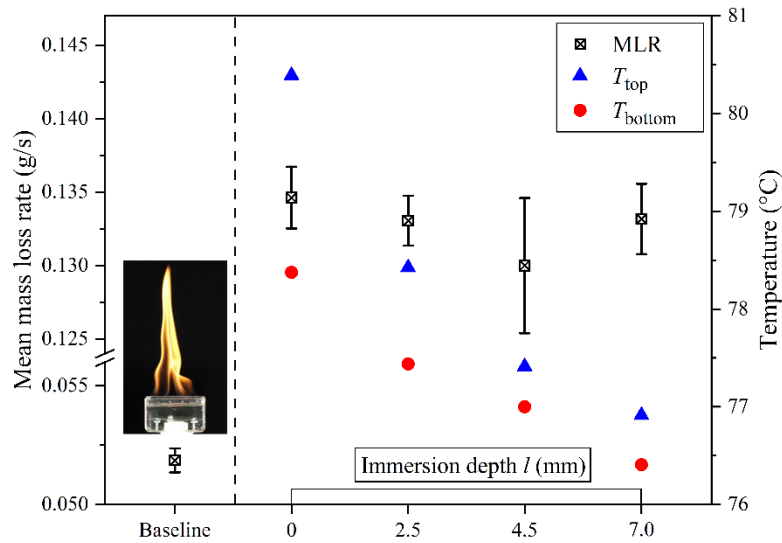


Figure 3.14: Mean mass loss rate and temperature measurement at steady state at different l , where $l = 0-7.0$ mm.

Figure 3.15(a)-Figure 3.15(b) depict bubble phenomena at different l from the (inclined) top and front views, including both large and small bubbles. For the large bubble attached to the bottom surface of the disk, both size and distribution do not vary too much at different l . While for small bubbles, as depicted in Figure 7(a), their amount at the liquid-gas interface significantly decreases as l is increased from 2.5 to 7.0 mm. Especially in Figure 3.15(a-4), noticeable ripples are found at the liquid surface. Phenomena at the fluid surface interface are considered to be dominated by small bubble behaviors because of their much more frequent departure, as shown in Table 3.3.

Further observations in Figure 7(b) suggest that the distribution of small bubbles along the immersed rod has similar inconsistency to that of mass loss rate at $l = 4.5$ mm. The length of distribution first increases as l is increased from 0 to 4.5 mm, where the immersed rod surface is fully covered with small bubbles; however, when l is further increased from 4.5 to 7.0 mm, the

lower immersed rod is no longer covered with bubbles. Moreover, no bubbles are observed on the top disk surface when l is adjusted from 2.5 to 7.0 mm, which matches the temperature reported in Figure 3.14 (the atmospheric boiling point of ethanol is 78.5 °C [72]).

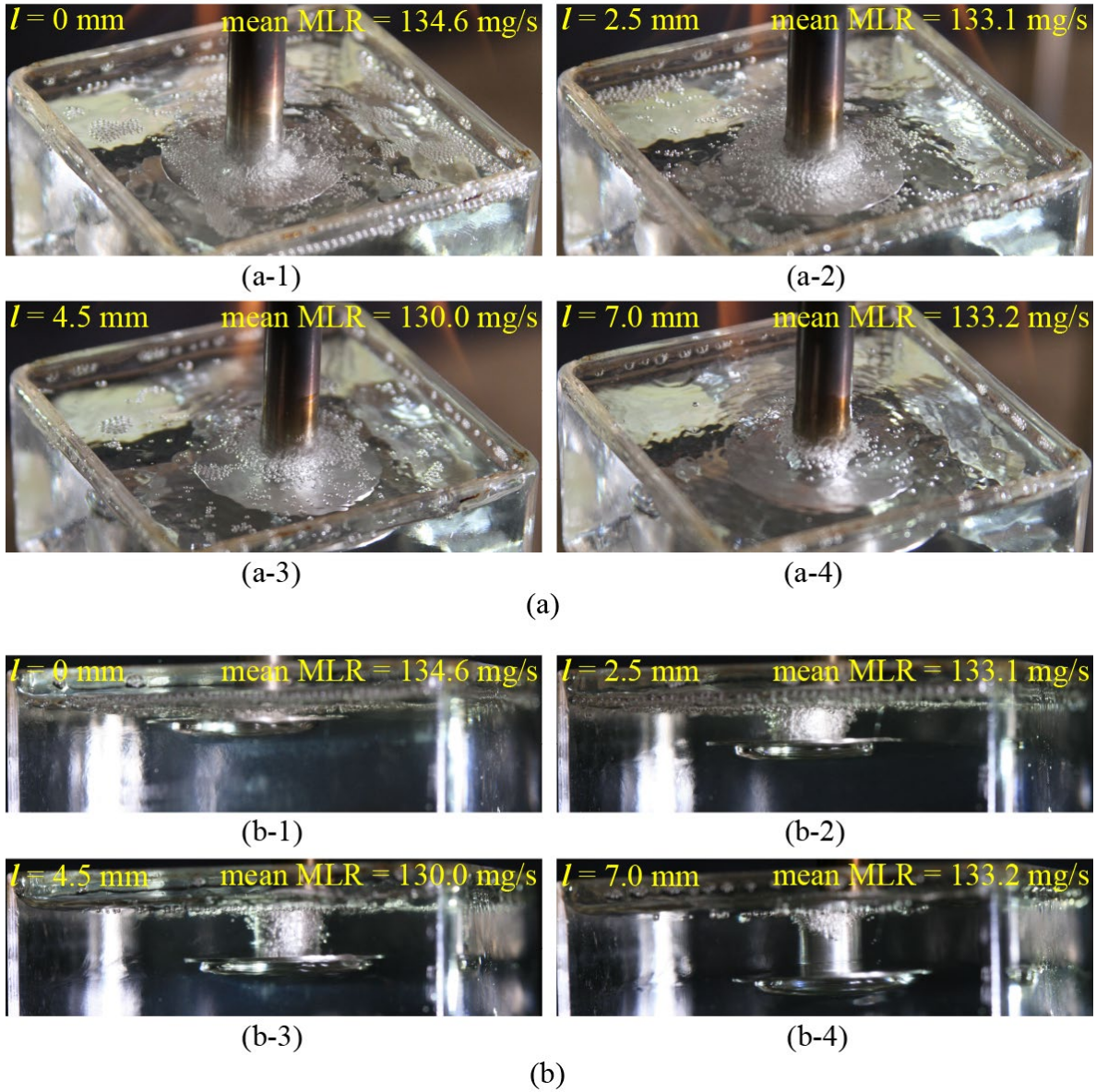


Figure 3.15: Bubble phenomena at steady state at different l , including (a) (inclined) top view, as well as (b) front view, where $l = 0-7.0$ mm.

Table 3.3: The departure frequency and the distribution of bubbles at steady state at different l , where $l = 0-7.0$ mm.

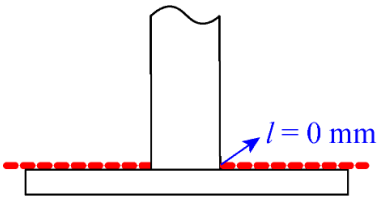
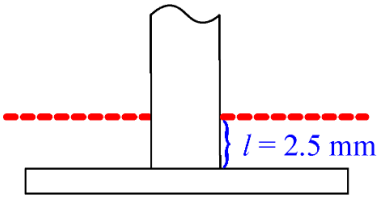
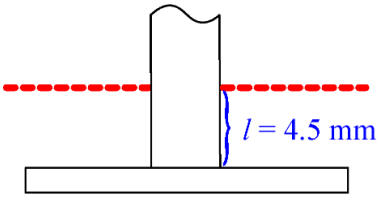
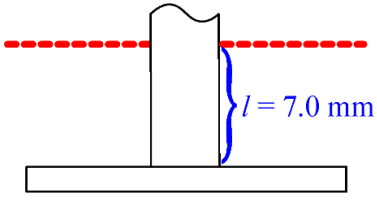
Initial immersion depth, l (mm)	Departure frequency (large bubble) (Hz), $\times 10^{-3}$	Departure frequency (small bubble) (Hz), $\times 10^{-3}$	Distribution on the immersed object
	10	--	100 %
	12	$> 10^5$	100 %
	8	$> 10^5$	100 %
	8	$> 10^5$	≈ 30 %

Table 3.3 shows the departure frequency of both types of bubbles at a steady state at different l . The variation of bubble departure frequency is found not strongly dependent on l for both bubbles; however, the departure frequency of large bubbles is almost four orders of magnitude lower than that of small bubbles. Consequently, even though the departure of a large bubble brings evident fluctuations to the liquid surface, as shown in Figure 3.13, its impact on the average mass loss rate is temporary. The overall influence of large bubbles may probably be negligible compared to that of the small bubbles having a much higher departure frequency.

Table 3.4 shows the critical volume of a single bubble, where measurements are applied to the images right before the large bubble departure and during the small bubble departure. Meanwhile, the number of bubbles is also included. Analyses show that the bubble amount does not vary much during the corresponding bubble departure. For large bubbles, even though the instantaneous impact of an individual bubble is noticeable, the overall effect on average mass loss rate may be negligible because of its much smaller number compared to small ones. Furthermore, when l is increased from 2.5 to 7.0 mm, the variation of the critical volume of small bubbles matches well with the mass loss rate, as reported in Figure 3.14.

Table 3.4: The critical volume and the number of bubbles at steady state at different l .

Initial immersion depth, l (mm)	Critical volume (large bubble) (mm^3)	Amount (large bubble)	Critical volume (small bubble) (mm^3)	Amount (small bubble)
0	< 2000	1	--	--
2.5	< 2000	1	0.079	> 100
4.5	< 2000	1	0.028	> 100
7.0	< 2000	1	0.041	> 100

The findings above indicate that the small bubble behaviors are the dominant controlling parameters to facilitate the ethanol burning rate because of their higher departure frequency and larger amount. The inconsistency in the mass loss rate at $l = 4.5$ mm also corresponds to small bubble behaviors.

3.2.3 Summary

Experiments are performed by immersing a composite-shaped aluminum cylinder in a burning liquid ethanol pool with refilling. The initial immersion depth, l , is varied as $l = 0\text{mm}$, 2.5 mm, 4.5

mm, and 7.0 mm. Comparing baseline experiments, the pool fire burning rate of object experiments has a noticeable increase because of the formation of the thermal feedback loop by introducing the immersed object. Such a process corresponds to comprehensive bubble behaviors.

Two different bubbles are observed on the surface of the immersed object - large bubbles escaping from the bottom surface of the disk and small bubbles departing from the immersed rod. Both bubble behaviors bring considerable perturbations to the ethanol surface. Even though the influence of the individual large bubble is noticeable, the overall impact on the average mass loss rate throughout the steady state may be negligible because of much lower departure frequency and number. Analyses show that as l increases, the mass loss rate first decreases and then increases, displaying a non-linear behavior, while the disk surfaces' temperature monotonically decreases. Such inconsistency corresponds to the variation of small bubble behaviors. Therefore, small bubble behaviors are the dominating controlling parameters that facilitate fuel vaporization and pool fire burning.

3.3 Third-stage experiment

3.3.1 Mass loss rate

At the steady state, the mean mass loss rate and its corresponding error in different scenarios are depicted in Figure 3.16, whose calculations are similar to those used for Figure 3.14. The x-axis denotes different scenarios (the immersion depth at the steady state and the surface condition) as summarized in Table 2.1, and the y-axis denotes the corresponding mean mass loss rate at the steady state. Error bars are included in Figure 3.16 by calculating the standard deviation from repeated experiments. It can be noticed that the mean mass loss rate increases (about 110%) after an object is immersed in the fuel. However, the variation in the mass loss rate at different scenarios

does not follow a clear trend. Therefore, bubble visualization techniques are implemented to figure out explanations.

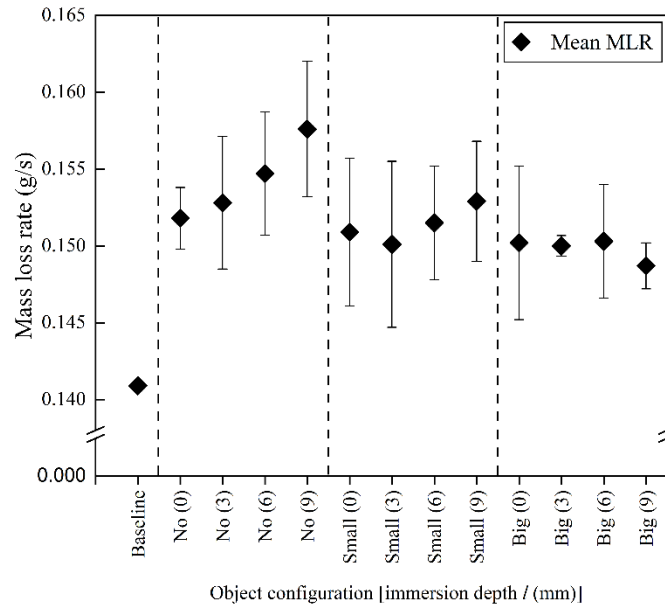


Figure 3.16: Mean mass loss rate at steady state for different scenarios. In the x-axis, “No”, “Small”, and “Big” represent the scenarios of the no holes, small holes having diameters of 1.09 mm, and big holes having diameters of 2.06 mm through the disk, respectively. “0”, “3”, “6”, and “9” in parentheses denote the immersion depths (mm) of the object at steady state, individually, and “baseline” represents the baseline experiment.

3.3.2 Bubble visualization

Using multiple cameras, bubbles around the immersed object have been visualized from different aspects. According to discussions in Sections 3.1-3.2, such visualization is informative because bubble phenomena characterize the processes of boiling heat and mass transfer and pool fire burning.

First, images (front view) taken by a DSLR are displayed in Figure 3.17. Similar to the phenomenon reported in the second-stage experiment, isolated small bubbles are found on the surface of the immersed object, and large hemispherical bubbles are located on the bottom surface of the disk. Also, as l increases, small bubbles cannot cover the whole surface of the immersed rod, which indicates the possible inconsistency in mass loss rate as l is increased. Furthermore, in the “big holes” case, small bubbles are found in the liquid region, departing from the holes - such a phenomenon results in an extra liquid perturbation above the disk.

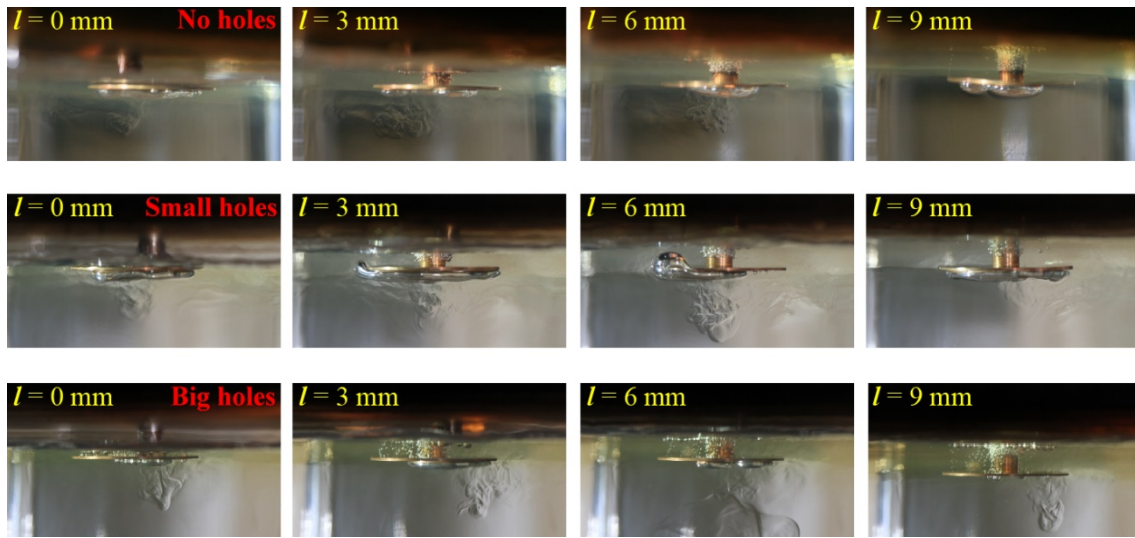


Figure 3.17: Images (front view) showing bubble phenomena for different cases, where the immersion depth at steady state, $l = 0$ mm, 3.0 mm, 6.0 mm, and 9.0 mm. Images in the first, second, and third rows represent the “no holes”, “small holes”, and “big holes” cases, representatively.

Moreover, since shapes of individual bubbles are visible in these images, the manual method discussed in Section 2.4.3 may be utilized to obtain the bubble size. Similarly, the evaluations of the bubble size and the bubble motion are possible by using high-speed images. Therefore, analyses are performed, which are presented in Section 3.3.3.

Furthermore, images (bottom view) taken by a video camera are displayed in Figure 3.18, where large hemispherical bubbles are found on the bottom surface of the disk. For the cases with holes, bubbles on the disk surface are found to initiate at the center of both disk (having comparatively higher temperature) and holes.

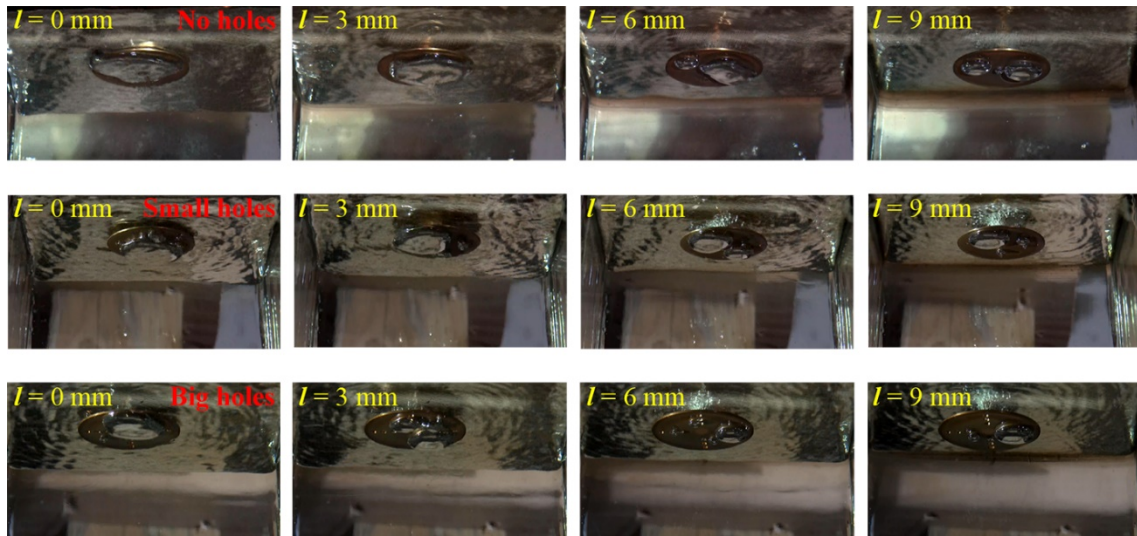
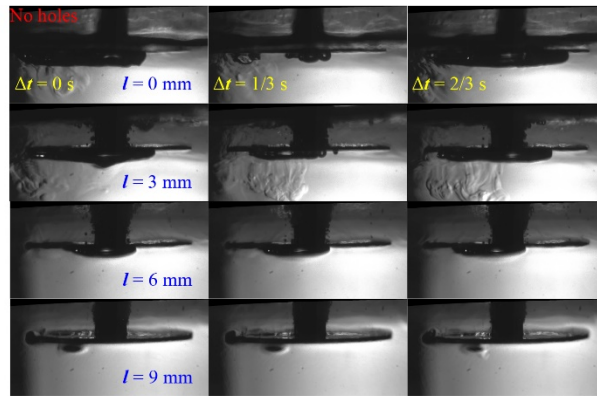


Figure 3.18: Images (bottom view) showing bubble phenomena for different cases, where the immersion depth at steady state, $l = 0$ mm, 3.0 mm, 6.0 mm, and 9.0 mm. Images in the first, second, and third rows represent the “no holes”, “small holes”, and “big holes” cases, representatively.

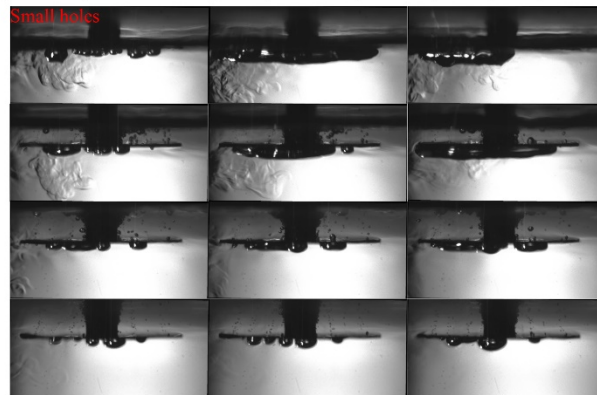
According to Figure 3.17, both generation and departure of the bubbles on the bottom surface of the disk are facilitated by the presence of the holes. It is also possible that the critical bubble departure size decreases for the cases with holes because bubbles can more easily travel to the edge for the departure, as the new active nucleation sites are not at the center. Also, bubbles on the bottom disk can depart through holes. Therefore, holes change the behavior of bubbles on the disk, which facilitates the heat removal from the object. However, it is also possible that the temperature

of an object decreases because of the heat removal on its surface, which corresponds to a decrease in the mass loss rate for the cases with holes as shown in Figure 3.16.

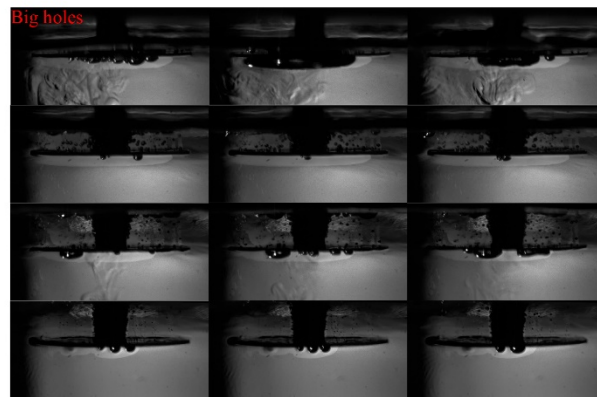
High-contrast backlit images (side view) taken by a digital camera and laser technique are displayed in Figure 3.19, where (a), (b), and (c) denote “no holes”, “small holes” ($D_{\text{hole}} = 1.09$ mm), and “big holes” ($D_{\text{hole}} = 2.06$ mm) cases, respectively. Three continuous-captured images are shown for each case, whose time interval is $1/3$ s, which are utilized to depict the bubble motion. For example, when l is small, the bubble motion becomes more vigorous, manifested by the distinct differences for the bubbles on the bottom surface of the disk. However, the difference is not that apparent for the small bubbles on the surface of the immersed rod, which is caused by their rapid and repeated motion, having a period much shorter than $1/3$ s. However, the bubble’s distribution on the surface of the rod is found to vary among different cases. Recalling the results of the second-stage experiment, small bubble behaviors are found to dominate the process. Therefore, it is reasonable to have each case characterized by the small bubbles attached to the surface of the rod. Moreover, as l increases, the thickness of bubbles attached to the bottom surface of the disk is found to reduce. Also, bubbles are noticed to appear in the fuel region above the disk for the hole cases.



(a) No holes, where $\Delta t = 0$ s, $4/15$ s, and $8/15$ s, $l = 0$ mm, 3 mm, 6mm, and 9 mm.



(b) Small holes.



(c) Large holes.

Figure 3.19: Images (side view) showing bubble phenomena for different cases, where time interval $\Delta t = 1/3$ s, and immersion depths at steady state, $l = 0$ mm, 3.0 mm, 6.0 mm, and 9.0 mm.

It can be noticed that, instead of showing individual bubbles, Figure 3.19 depicts clear shapes and edges of each region. Therefore, the gray-scale method is suitable to be used, for example, to

quantify the bubbles attached to the surface of the immersed rod. The corresponding analysis is discussed in Section 3.3.3.

3.3.3 Bubble quantification

3.3.3.1 Manual method

Bubbles are found to possess characteristic behaviors in different regions. Therefore, Figure 3.20 illustrates a possible approach to categorize the chaotic bubbles based on their locations. The bubble quantification is then applied to regions A, B, and C by using the manual method, whose results are shown in Table 3.5.

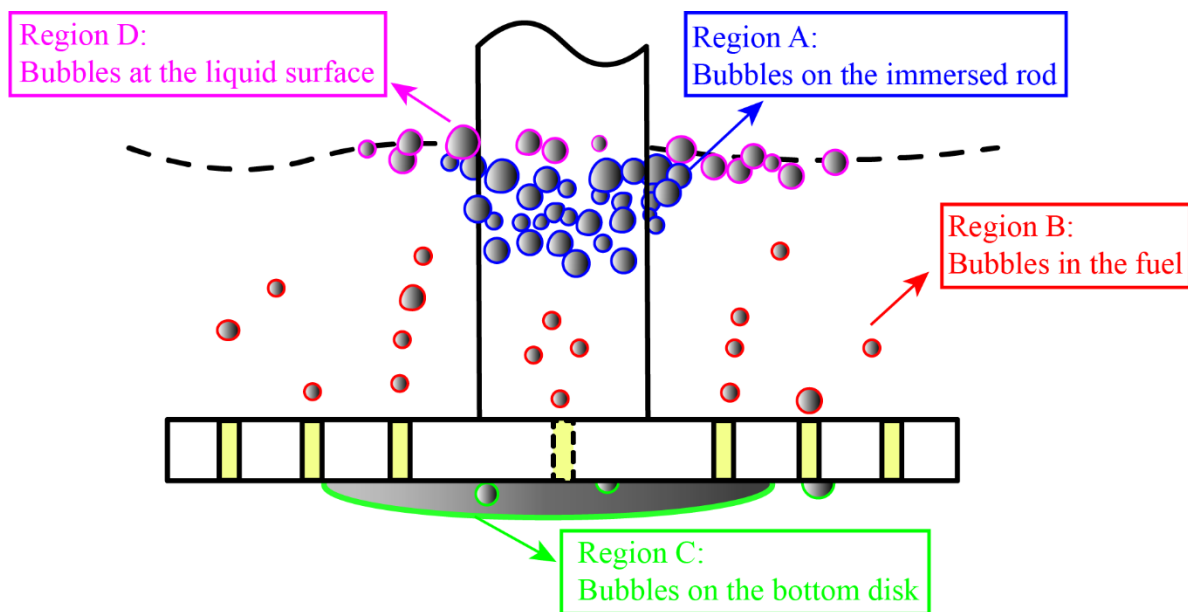


Figure 3.20: Schematic describing the bubble categorization in different regions, where regions A, B, C, and D represent the bubbles on the immersed rod, in the fuel, on the bottom disk, and at the liquid surface, respectively.

Table 3.5: The bubble quantification using the manual method.

Initial immersion depth, l (mm)	Disk's surface condition*	Enhanced volumetric regression rate, v_r (mm ³ /s)	Volumetric rate in A, v_A (mm ³ /s)	Volumetric rate in B, v_B (mm ³ /s)	Volumetric rate in C, v_C (mm ³ /s)
3	N	15.08	270.71 ± 103.13	0.00	1329.85 ± 384.34
6	N	17.49	565.71 ± 110.47	0.00	1197.37 ± 355.18
9	N	21.17	582.76 ± 177.35	3.38 ± 4.04	17.36 ± 5.60
3	S	11.66	138.42 ± 104.37	112.59 ± 25.37	1692.00 ± 1211.01
6	S	13.44	298.42 ± 106.15	14.04 ± 8.50	573.61 ± 161.25
9	S	15.21	353.88 ± 58.24	8.84 ± 1.77	37.00 ± 13.44
3	B	11.53	308.63 ± 92.69	122.29 ± 83.25	729.92 ± 457.89
6	B	11.91	216.46 ± 39.88	47.61 ± 12.60	67.89 ± 31.11
9	B	9.89	130.88 ± 30.19	5.76 ± 1.42	3.39 ± 0.71

* N: No holes, S: small holes, and B: big holes,.

Results of the bubble quantification using the manual method are shown in Table 3.5, where the enhanced volumetric regression rate, v_r is given by:

$$v_r = \frac{\dot{m} - \dot{m}_b}{\rho}, \quad (3.1)$$

where \dot{m} denotes mean mass loss rate at steady state obtained from object experiments, \dot{m}_b is the mean mass loss rate at steady state obtained from baseline experiments, ρ represents the density of liquid ethanol, whose value is constant because of the refilling process. The calculation of

volumetric rates at different regions and the corresponding uncertainties are discussed in Section 2.4.3.

The variation of v_r is noticed to associate with that of v_A , which indicates the importance of region A. After adding holes, significant changes are found for v_B , which correspond to the bubble visualization in the liquid area above the disk for the cases with holes. Furthermore, the increase of v_B seems to relate to the decrease of v_A and v_r , which corresponds to the conjecture made in Section 3.3.2. The introduction of holes reduces the mass loss rate by removing the heat from the heated object.

3.3.3.2 Gray-scale method

Furthermore, as introduced in Section 2.4.3, the gray-scale method can be implemented to study the bubbles around the immersed rod (the region A as depicted in Figure 3.20). To be more explicit, an example is shown in Figure 3.21, which illustrates procedures to obtain a target image depicting region A and the immersed rod region. Procedures consist of image collection, averaging, applying thresholds, and cropping.

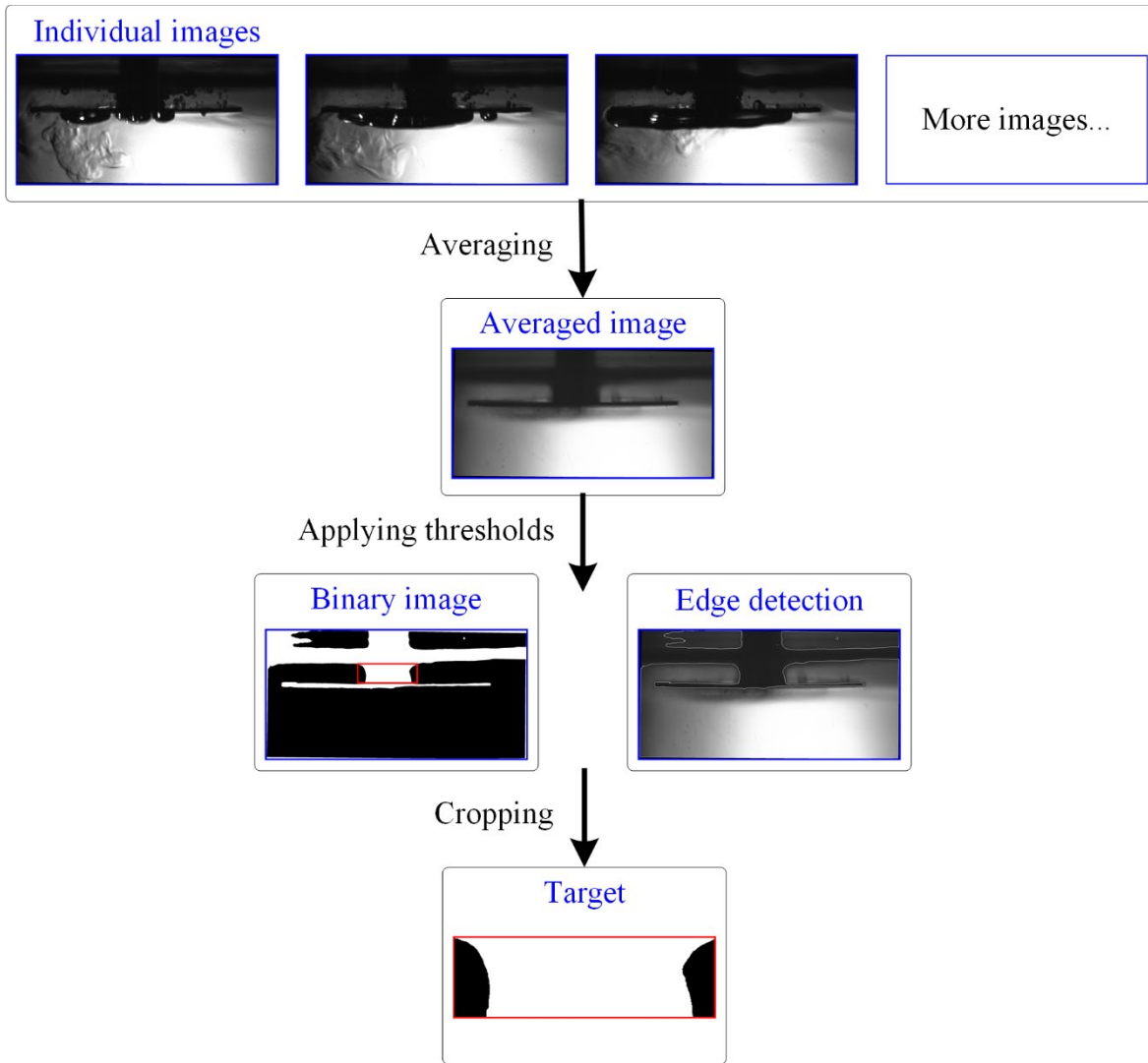


Figure 3.21: An example showing the procedure to obtain region A and the immersed object region using the gray-scale method. The example case is the “small holes” at $l = 3$ mm, and 200 images are used for the averaging process.

Next, as shown in Figure 3.22, to calculate the volume of region A, the region of the immersed rod is removed (dashed region). By assuming the configuration to be symmetrical, the calculation of the volume of region A, V_A , is given by:

$$V_A = \int_0^{L_A} \frac{\pi (D_{A,z}^2 - D_o^2)}{4} dz, \quad (3.2)$$

where $D_{A,z}$ denotes the diameter of the region A, which varies along the height, z , D_0 is the diameter of the rod, L_A is the length of the region A, and dz is the distance of a unit pixel. $D_{A,z}$, L_A , and dz are obtained by recognizing the white pixels, and the determination of D_0 requires a manual check because bubbles may or may not cover the whole surface of the entire immersed object.

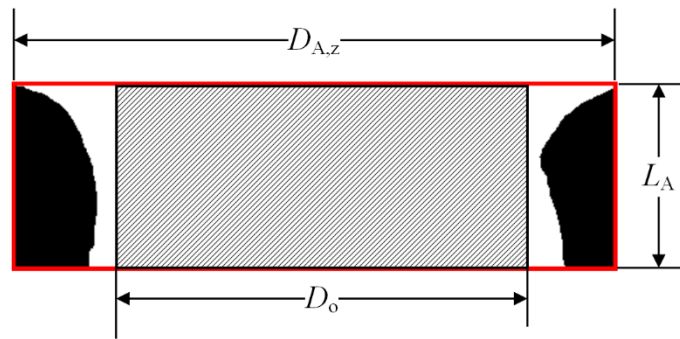


Figure 3.22: Schematic showing the dimensions used for the calculation of region A.

Another important parameter to be examined is the number of images used for the averaging process, N . For each case, 250 images are continuously captured at a steady state. Therefore, $N = 5, 15, 50, 150,$ and 250 are used for the evaluation, whose results are shown in Figure 3.23(a)-Figure 3.23(f).

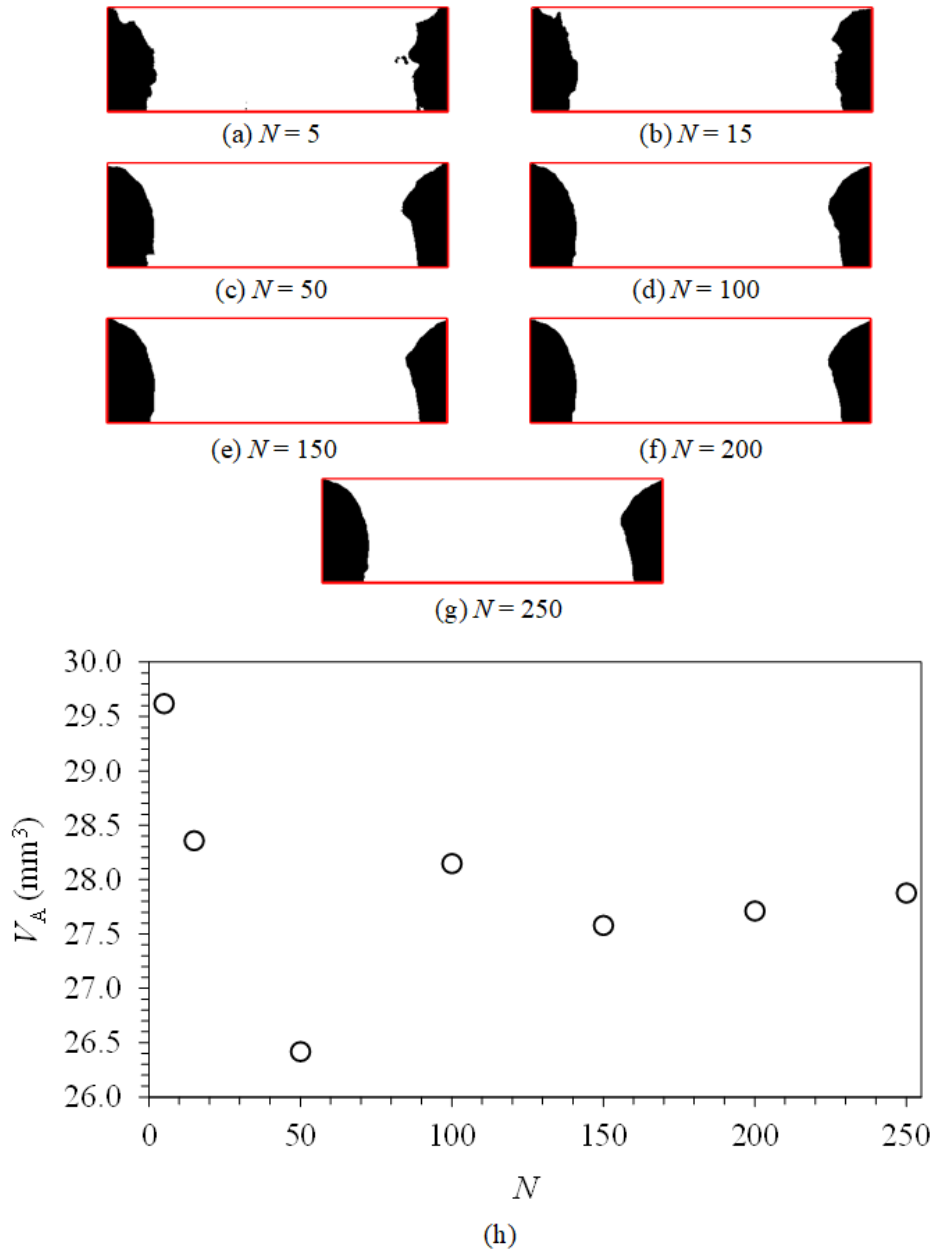


Figure 3.23: The influence of the number of images, N , on the volume of the region A, V_A , where $N = 5, 15, 50, 100, 150, 200$, and 250 .

As depicted in Figure 3.23(a)-Figure 3.23(e), the edges generally become smoother as N increases. V_A initially fluctuates and then tends to flat, as shown in Figure 3.23(f). When N is

increased from 150 to 250, the shape of the white pixel region and the value of V_A do not vary too much. Therefore, $N = 200$ is selected for further analyses.

By applying the gray-scale method and the parameters discussed above to image analyses, the results of V_A are shown in Figure 3.24, together with the corresponding mean mass loss rate from repeated and individual experiments, respectively. It is noted that the analysis of V_A is applied to individual experiments, and thus, the corresponding mass loss rate from individual experiments is reported for better comparisons.

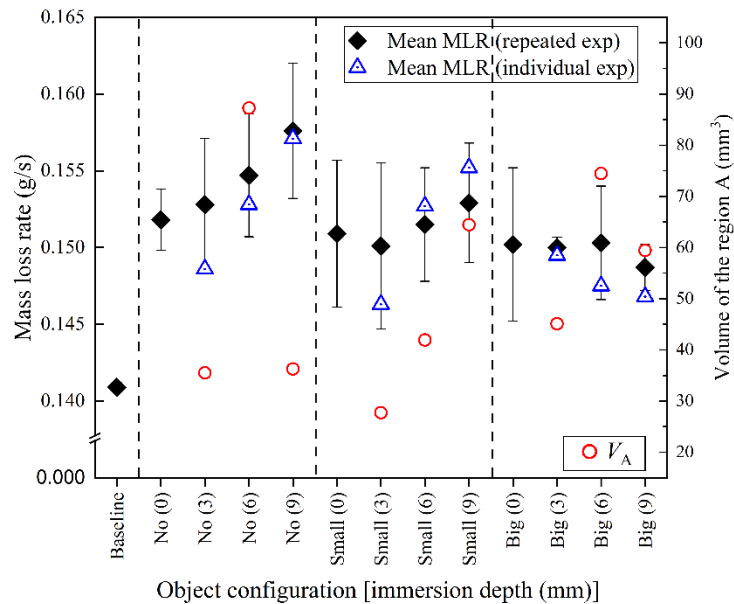


Figure 3.24: Mean mass loss rate (black diamond), individual mass loss rate (blue triangle), and volume of the region A (red circle) at steady state for the different cases, where the x-axis shows different experimental cases, the left y-axis denotes mean mass loss rate, and the right y-axis denotes the volume of the region A, V_A .

As presented in Figure 3.24, the range of V_A is reasonable for all the cases investigated. For the “small holes” case, the tendency of V_A matches well with that of the mean mass loss rate.

However, there are discrepancies for the “no holes” and “big holes” cases. For the “no holes” case, by checking the images presented in Figure 3.19 (a), those captured for the $l = 9$ mm case seem not completed, probably caused by the soot generation blocking the sight at the liquid level. For the “big hole” case, the slight discrepancy may result from the impact from other regions; for example, the bubble behaviors in region B are more noticeable for the “big holes” case, as shown in Figure 3.17 and Figure 3.19. Therefore, the bubble behaviors in other regions may be necessary if the object configuration is further varied.

3.3.4 Summary

Experiments conducted by immersing a composite-shaped copper cylinder in a burning liquid ethanol pool with refilling are analyzed. The immersion depth at steady state, l , and the surface condition are varied, where $l = 0$ mm, 2.5 mm, 4.5 mm, and 7.0 mm, and the surface condition includes “no holes”, “small holes”, and “big holes” cases. Comparing the baseline experiments, the pool fire burning rate increases due to the formation of a thermal feedback loop by immersing an object. Such a process corresponds to comprehensive bubble behaviors.

The bubble visualization is initially implemented qualitatively, where bubbles are found to have similar behaviors dependent on locations. Therefore, chaotic bubbles are categorized into four regions based on their locations. Furthermore, two methods are implemented to quantify bubble phenomena. It is noticed that similar results are obtained from qualitative and quantitative analyses. For example, bubbles in region A are found to dominate the process. Also, the introduction of the holes changes the bubble behaviors, resulting in more bubbles in region B, facilitating the bubble generation and departure on the bottom disk, which removes the heat from the heated object and undesirably reduces the ethanol mass loss rate. Accordingly, the impact of the bubbles in region A reduces after introducing holes.

Such findings are helpful to improve the practical design. Also, two methods are validated by the experimental data, which may be beneficial in future diagnostics. However, future works are needed, for example, to include the analyses to other regions in the gray-scale method.

4 Numerical model setup and procedure

This chapter explains the methodology involved in developing a numerical model, which analyzes the effect of a highly conducting immersed object on the mass burning rate of a liquid pool fire. The heat transfer from the flame to the liquid surface and that from the immersed object to the interior of liquid fuel are modeled. This heat transfer is coupled to the mass transfer from the liquid surface and at the solid-liquid interface. This chapter methodically reports the simplifications made in the model, the initial and boundary conditions, the discretization schemes, and the solution methods in detail.

4.1 Overview

Besides the stages of experiments unveiling the unique phenomena caused by the thermal feedback loop on the mass burning rate of a liquid pool, a computational model including all heat transfer mechanisms in three phases (gas, liquid, and solid) will be useful to couple their relationship. Due to the complexity of interactions between the phases, the expected solution is non-trivial. And commercial software, such as ANSYS [73] and FDS [74], that may handle the scenario seems to be complicated. Therefore, a simplified numerical model is developed to solve energy equations in an immersed object and liquid pool to understand the heat and mass transfer mechanisms. The governing equations are solved for a solid cylindrical object and the liquid fuel by considering a hot gas phase representing the flame. The model solution includes the determination of the temperature distribution for object and liquid regions and the prediction of the mass loss rate of the liquid.

Experiments in literature have shown a considerable increase in the burning rate in the presence of objects in pool fires [17]. To complement these, a simplified model is constructed

based on the experimental data from literature invoking necessary assumptions [17,75]. These assumptions are used to establish the geometric, boundary, and initial conditions that model the experiments physically (Section 4.2). To obtain a numerical solution of the energy equations in the model, the Finite Difference Method (FDM) is used to discretize the governing equations and boundary conditions (Section 4.3). Subsequently, the discretized equations are solved with an explicit time marching scheme on the C programming platform. The convergence is verified by checking the residue at interfaces (Section 4.5) and the energy imbalance for the domain (Section 4.6). The simulation results are validated by using experimental data from the literature (Section 4.7), from the perspectives of temperature and mass loss/burning rate (Section 4.4). Parametric studies exploring the influence of the object configurations on the pool fire with an immersed object are further conducted.

4.2 Description

A schematic of the model design is shown in Figure 4.1, where a cylindrical object is immersed in a cylindrical liquid pool. This configuration is inspired by the experimental setup of Arsava et al. [17], where heat is efficiently collected from the gas region and transmitted to the liquid region via the immersed object. For modeling this scenario, the domain is considered to be axisymmetric, following the cylindrical polar coordinate (r - z), with origin at the center of the liquid pool. The heat transfer from the flame is modeled considering suitable correlations for flame height and its temperature and assuming that convection and radiation are the predominant modes involved. The computational domain consists of three control volumes (CV). The immersed object (cylinder of diameter D_o) has been modeled as two regions: 1. the collector section, which is the upper portion of the object being heated by the flame, and 2. the heater section, which is the lower portion of the object in contact with the liquid phase. In Figure 4.1, CV_1 depicts the collector section of length

L_C , CV_2 depicts the domain for the heater section of length L_H , and CV_3 represents the liquid of diameter D and depth L_L . Three interfaces can be identified: interface 0 is the gas-liquid interface, interfaces 1 and 2 are the solid-liquid interfaces at the side and bottom surfaces of the heater in contact with the liquid, respectively. When the object is immersed up to the bottom of the liquid pool, interface 2 would be absent.

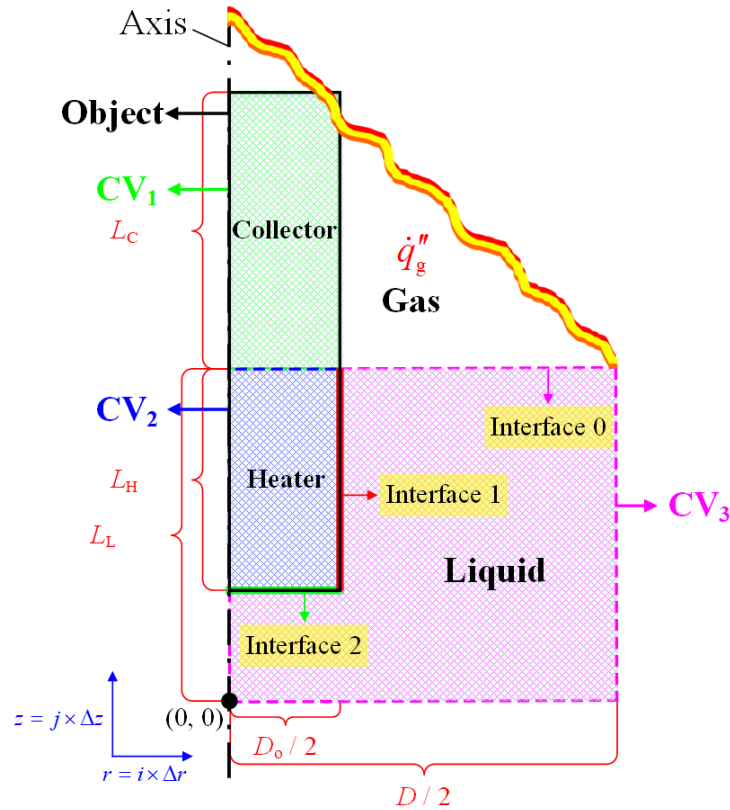


Figure 4.1: Axisymmetric computational domain for the numerical simulation of an object immersed in a liquid pool fire, consisting of CVs 1 (collector), 2 (heater), and 3 (liquid).

4.2.1 Assumption and simplification

For transient simulations to be carried out for solving the unsteady governing equations for CV_1 , CV_2 , and CV_3 , the following assumptions have been invoked while developing the model:

1. The domain is assumed to be axisymmetric, considering temperature variations only along r and z directions while neglecting those in the azimuthal direction.
2. The side ($r = D/2$) and bottom ($z = 0$) walls bounding the liquid fuel are assumed to be adiabatic.
3. The flame zone is modeled as a high-temperature gas phase region that heats the collector and the liquid's top surface. Empirical correlations for temperature profiles are used to model the temperature variation in the gas phase. These correlations are based on the heat release rate, which depends on the mass burning rate.
4. The liquid surface is considered non-regressing to simulate the experiments carried out with a constant liquid level, achieved by using a gravity feedback system. As the heat is transferred from the gas phase, the surface temperature of the liquid increases towards its saturation temperature at atmospheric pressure. Moreover, the temperature in the liquid region is confined by its saturation temperature.
5. The flame temperature variation in the z -direction is assumed to be more significant than that in the r -direction for the heat transfer to the object.
6. Air properties are evaluated at film temperature, which is the average of object surface temperature and flame temperature, as the gas phase temperature. This is reasonable as the air properties used for evaluating the heat transfer coefficient are in the boundary layer.
7. Thermal properties of the liquid, such as density, specific heat, and thermal conductivity, can be assumed constant if the variation of liquid temperature is small. To be more precise, as the liquid temperature varies from ambient to saturation temperature, its properties are evaluated at an average temperature between these two temperatures.
8. The convection inside the fuel and in-depth radiation is neglected.

9. The object properties are assumed constant, as their variations along the temperature are quite small. For the cases having fire as the heat input, it is reasonable to use property values at an average temperature between the ambient and estimated flame temperature

4.2.2 Flame modeling

When an object is placed in a pool fire, heat is transferred from the flame to the object through convection and radiation. Realistic modeling of flame is non-trivial and would potentially include solving the Navier-Stokes equations along with chemical kinetics models incorporated in equations for conservation of species. As discussed above, in this simplified model, the flame is simulated as a hot gas phase region by specifying a temperature distribution based on empirical correlations. This would thus act as a heat source for the immersed object and the liquid fuel. It is well known that the temperature variation in a pool fire is highly dependent on the flame height and the heat release rate [19]. These two parameters are calculated in the model using suitable empirical correlations.

4.2.2.1 Flame height

It is necessary to know the flame height, L_f , in order to estimate the gas phase temperature variation. The flame height depends upon the fire size, which is impacted by the pool diameter and the type of fuel burnt. For an object engulfed by a flame, the heating pattern on the object is determined by comparing the flame height and the object length. Heskestad [76] has correlated various data from pool fire experiments and has provided an empirical expression for the flame height, given by:

$$L_f = 0.235\dot{q}^{\frac{2}{5}} - 1.02D, \quad (4.1)$$

where \dot{q} is the heat release rate of the pool fire (kW) and D is the pool diameter. \dot{q} is dependent on the mass loss (or burning) rate, \dot{m} , and it is calculated as:

$$\dot{q} = \dot{m}\Delta H_c. \quad (4.2)$$

The mass burning rate, \dot{m} , is coupled with the net heat transfer to the fuel. This is discussed in Section 4.4. In the Eq. (4.2), ΔH_c is the heat of combustion, which is a fuel-dependent value [77].

4.2.2.2 Temperature distribution

For a pool fire, which is a buoyant diffusion flame, McCaffrey [77] has delineated three regions: 1. the persistent luminous flame, 2. the intermittent flame, and 3. the buoyant plume (hot gas) region. The correlation [21] that relates the temperature, location above the pool, and heat release rate is expressed as:

$$\frac{2g\Delta T_{\text{amb}}}{T_{\text{amb}}} = \left(\frac{\theta}{C}\right)^2 \left(\frac{z}{\frac{z}{2}}\right)^{2\eta-1}, \quad (4.3)$$

where g is the gravitational acceleration, ΔT_{amb} is the centerline temperature minus the ambient temperature, T_{amb} , z is the specific axial location above the pool surface, and θ , C , and η are coefficients as presented in Table 4.1.

Table 4.1: Coefficients used by McCaffrey's Correlation for the centerline data [21].

Region	θ	C	$z^* = \frac{z}{2} \left(\frac{\text{m}}{\text{kW}^{\frac{2}{5}}} \right)$	η
Flame	$6.8 \frac{\text{m}^{\frac{1}{2}}}{\text{s}}$	0.9	0.026-0.08	$\frac{1}{2}$
Intermittent	$1.9 \frac{\text{m}}{\text{kW}^{\frac{1}{5}} \cdot \text{s}}$	0.9	0.08-0.2	0
Plume	$1.1 \frac{\text{m}^{\frac{4}{3}}}{\text{kW}^{\frac{1}{5}} \cdot \text{s}}$	0.9	> 0.2	$-\frac{1}{3}$

There are three points of importance:

1. The maximum gas temperature, $T_{g,\max}$, is obtained in the flame region.
2. When $z / \dot{q}^{\frac{2}{5}}$ is very small ($< 0.026 \text{ m/kW}^{\frac{2}{5}}$) in the flame region, there are considerable discrepancies between the experimental data and values calculated using Eq. (4.3). Therefore, the temperature in this region is evaluated based on the experimental data by Sudheer and Prabhu [78-79], where experimental studies have been performed in both circular and square pool fires of different sizes, by implementing the infrared thermography to measure the temperature. Accordingly, the centerline temperature along height z has been reported. It can be noticed that when z is very small, the centerline temperature almost linearly increases along the increase of z . Meanwhile, the centerline temperature at $z = 0$ is found to associate with the pool configuration and liquid properties. Therefore, the gas temperature in the model is set as 555 K at $z^* = 0$ and $T_{g,\max}$ at $z^* = 0.026$ as shown in the Eq. (4.3), together with a linear fit representing the temperature in between:

$$T_g = \begin{cases} 555 \text{ K}, & \text{at } z^* = 0 \\ T_{g,\max}, & \text{at } z^* = 0.026 \end{cases}, \quad (4.4)$$

3. In cases with the length of the object being much larger than the flame height, the limit of $\Delta T_{\text{amb}} \geq 0$ needs to be ensured for the Eq. (4.3) and Table 4.1.

4.2.2.3 Heat flux

After prescribing the temperature profile, the heat flux from the gas to the object considering both convection and radiation, \dot{q}_g'' , is calculated as:

$$\dot{q}_g'' = \dot{q}_{g,\text{conv}}'' + \dot{q}_{g,\text{rad}}'' = \bar{h}_{\text{conv}} (T_g - T_{o,s}) + \varepsilon \sigma (T_g^4 - T_{o,s}^4), \quad (4.5)$$

where $\dot{q}_{g,\text{conv}}''$ is the heat flux via convection, $\dot{q}_{g,\text{rad}}''$ is the heat flux via radiation, \bar{h}_{conv} is the average convective heat transfer coefficient based on the average film temperature, ε is the emissivity, σ is the Stefan-Boltzmann constant, and $T_{o,s}$ is the temperature of the object surface, which is solved in Section 4.2.3.

The convection term, \bar{h}_{conv} , is calculated using the Nusselt number correlation for a vertical cylinder of height L_C [80-81], which is given by:

$$\bar{h}_{\text{conv}} = \frac{Nu_{L_C} k_g}{L_C}, \quad (4.6)$$

The average Nusselt number is defined in terms of the average Grashof number, Gr_{L_C} , and object dimensions, which is given by:

$$Nu_{L_C} = \left\{ 1 + 0.300 \left[32^{0.5} (Gr_{L_C})^{-0.25} \left(\frac{L_C}{D_o} \right)^{0.909} \right] \right\} \times Nu_{L_C\text{-FP}}, \quad (4.7)$$

where

$$Gr_{L_c} = \frac{g\beta_g |\bar{T}_g - \bar{T}_{o,s}| (L_c)^3}{(\nu_g)^2}, \quad (4.8)$$

In Eq. (4.7), the average local Nusselt number for a flat plate configuration, Nu_{L_c-FP} , is given by:

$$Nu_{L_c-FP} = \left\{ 0.825 + \frac{0.387 Ra_{L_c}^{\frac{1}{6}}}{\left[1 + \left(\frac{0.492}{Pr_g} \right)^{\frac{9}{16}} \right]^{\frac{8}{27}}} \right\}^2, \text{ where } 0.1 < Ra_{L_c} < 10^{12}, \quad (4.9)$$

where

$$Ra_{L_c} = Gr_{L_c} \times Pr_g, \quad (4.10)$$

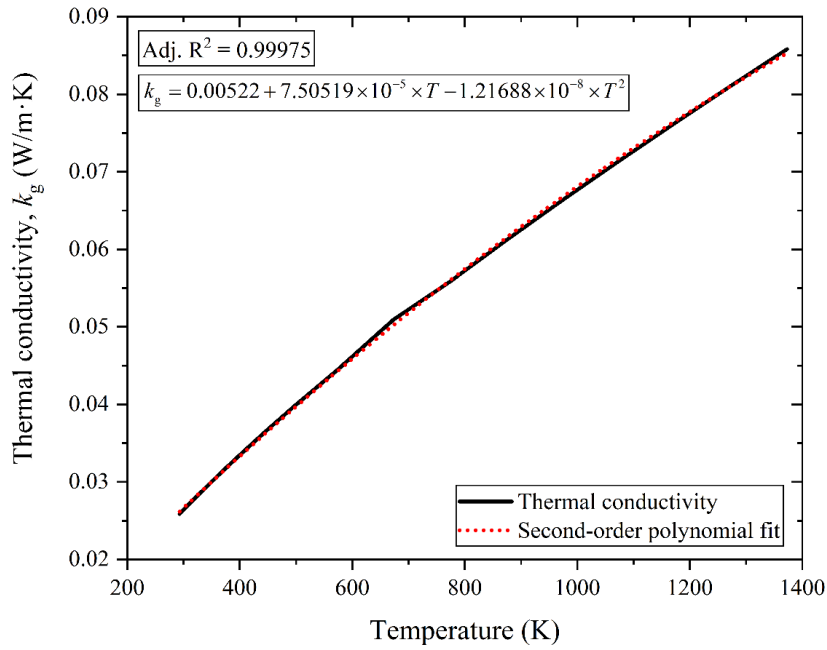
Ra_{L_c} is the Rayleigh number, Pr_g is the Prandtl number for the gas phase, and Pr_g is taken as 0.72.

In the above equations, k_g , β_g , and ν_g are the gas phase thermal conductivity, thermal expansion coefficient, and kinematic viscosity, respectively, which are air properties evaluated as a function of the film temperature, \bar{T}_{film} , given by,

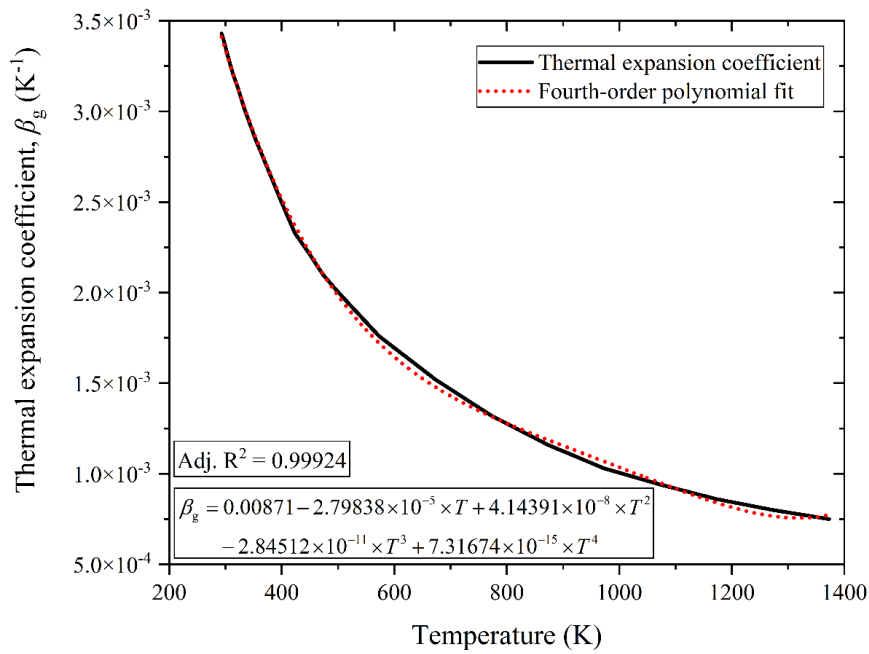
$$\bar{T}_{film} = \frac{\bar{T}_g + \bar{T}_{o,s}}{2}. \quad (4.11)$$

Here, \bar{T}_g and $\bar{T}_{o,s}$ are the average gas and average object surface temperature, respectively.

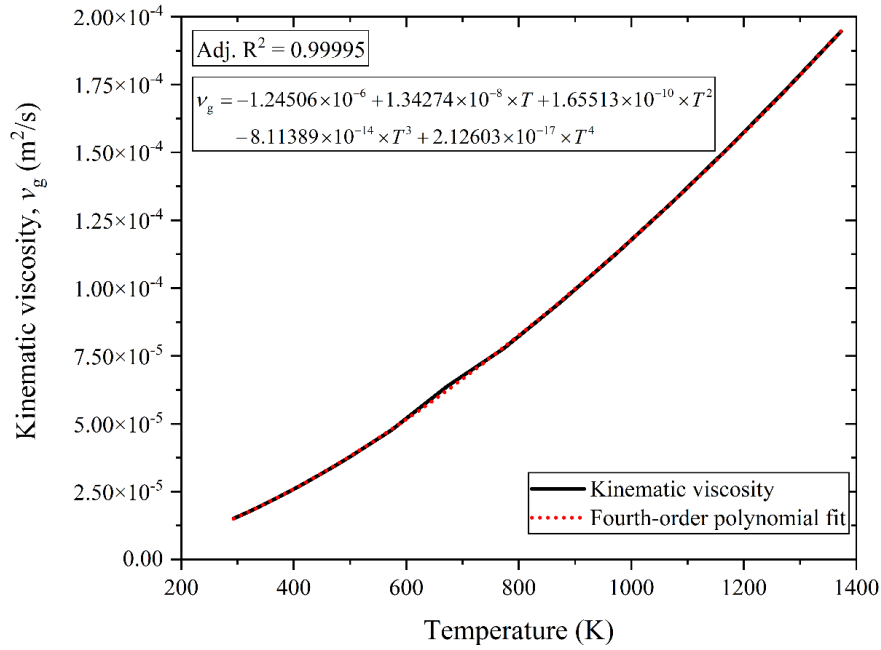
k_g is calculated by using a second-order polynomial fit as shown in Figure 4.2 (a), β_g and ν_g are calculated by using fourth-order polynomial fits shown in Figure 4.2(b) and Figure 4.2 (c) [82].



(a) Thermal conductivity of air, k_g .



(b) Thermal expansion coefficient of air, β_g .



(c) Kinematic viscosity of air, v_g .

Figure 4.2: Variation of air properties as a function of temperature.

For the radiation term, the determination of ε is based on literature [21,79-83]. Here, results vary in the range of 0.2 to 0.6 depending on the pool configuration and liquid properties. Keeping these in mind that $\varepsilon = 0.35$ is used in the present model.

4.2.3 Governing equations, initial and boundary conditions

For carrying out transient simulations, unsteady energy equations in cylindrical polar coordinates are solved in the computational domain as shown in Figure 4.1, along with appropriate boundary conditions to obtain the temperature distribution in the object and liquid fuel regions.

The governing equations are given as follows:

$$\text{For the **object**: } \rho_o c_o \frac{\partial T}{\partial t} = \frac{1}{r} \frac{\partial}{\partial r} \left(r k_o \frac{\partial T}{\partial r} \right) + \frac{\partial}{\partial z} \left(k_o \frac{\partial T}{\partial z} \right), \quad (4.12)$$

$$\text{For the **liquid**: } \rho_l c_l \frac{\partial T}{\partial t} = \frac{1}{r} \frac{\partial}{\partial r} \left(r k_l \frac{\partial T}{\partial r} \right) + \frac{\partial}{\partial z} \left(k_l \frac{\partial T}{\partial z} \right), \quad (4.13)$$

where ρ , c , T , and k are density, specific heat, temperature, and thermal conductivity, respectively; and subscripts o and l represent the immersed object and liquid, respectively.

The initial temperature is prescribed as the ambient temperature, T_{amb} :

$$\text{At } t = 0, \quad T(r, z, t = 0) = T_{\text{amb}}. \quad (4.14)$$

For solving a second-order differential equation, two boundary conditions are required for each direction (r and z), which are given as:

1. For the **object**:

$$\begin{aligned} \text{a. } & (r, z = L_L + L_C), \quad k_o \left. \frac{\partial T}{\partial z} \right|_o = \dot{q}_g'', \text{ [top]} \\ \text{b. } & (r = 0, z), \quad \frac{\partial T}{\partial r} = 0, \text{ [axis]} \\ \text{c. } & \left(r = \frac{D_R}{2}, z > L_L \right), \quad k_o \left. \frac{\partial T}{\partial r} \right|_o = \dot{q}_g'', \text{ [side]} \end{aligned} \quad (4.15)$$

where $\dot{q}_g'' = \bar{h}_{\text{conv}} (T_g - T_{o,s}) + \varepsilon \sigma (T_g^4 - T_{o,s}^4)$,

2. For the **liquid**:

$$\begin{aligned} \text{a. } & (r, z = L_L), \quad k_l \left. \frac{\partial T}{\partial z} \right|_l = \dot{q}_g'', \text{ [fuel surface]} \\ \text{b. } & (r = 0, z), \quad \frac{\partial T}{\partial r} = 0, \text{ [axis]} \\ \text{c. } & \left(r = \frac{D}{2}, z \right), \quad \frac{\partial T}{\partial r} = 0, \text{ [adiabatic side wall]} \\ \text{d. } & (r, z = 0), \quad \frac{\partial T}{\partial z} = 0, \text{ [adiabatic bottom]} \end{aligned} \quad (4.16)$$

3. For the **interfaces**:

$$\begin{aligned}
& \text{a. } \left(r = \frac{D_R}{2}, z \right), k_o \left. \frac{\partial T}{\partial r} \right|_o = k_1 \left. \frac{\partial T}{\partial r} \right|_l, \text{ [interface 1]} \\
& \text{b. } (r, z = L_L - L_H), k_o \left. \frac{\partial T}{\partial z} \right|_o = k_1 \left. \frac{\partial T}{\partial z} \right|_l, \text{ [interface 2]}
\end{aligned} \tag{4.17}$$

Here are some points that cannot be overlooked: The liquid fuel temperature is limited by the saturation temperature, T_{sat} , such that in the liquid region, $T(r, z, t) = \min(T_{\text{sat}}, T)$. Additionally, it should also be noted that the boundary conditions on the walls bounding the liquid can be modified according to the experimental configuration to isothermal or convective boundaries instead of the adiabatic condition as shown in the Eq. (4.16).

4.3 Discretization

The governing equations, initial and boundary conditions are discretized using the Finite Difference Method (FDM) [84]. The domain is divided into a uniform mesh as shown in Figure 4.3, where Δr and Δz represent the grid spacing in radial and axial directions, respectively. The radial location (r) in the domain is represented using increments in i , such that $r = i \times \Delta r$. Similarly, axial distance is represented by $z = j \times \Delta z$. Consequently, (i, j) represents a given node in the domain. The variables $M, N, M0, N0, M1$, and $N1$ denote the boundaries of the domain and interfaces. The discretized equations are discussed in detail for the liquid and the object regions, which are then solved with an explicit time marching scheme on the C programming platform.

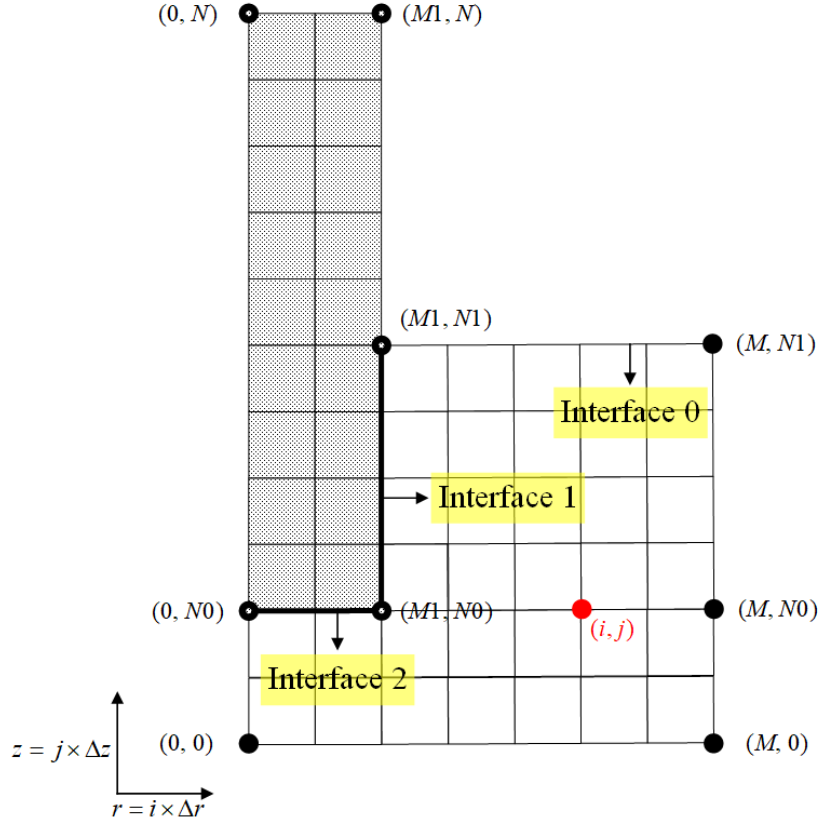


Figure 4.3: Axisymmetric computational domain with discretized cells, where interfaces and boundary points, as well as (i, j) are labeled (not to scale).

4.3.1 Discretization using FDM

4.3.1.1 Object region (CV_1 and CV_2)

The forward difference method is used to discretize the first-order time derivative. The central difference method is used to discretize the second-order space derivatives with second-order accuracy. The governing equation for the object region is shown in the Eq. (4.12). This consists of terms I, II, and III shown as:

$$\underbrace{\rho_o c_o \frac{\partial T}{\partial t}}_{\text{I. Time evolution}} = \underbrace{\frac{1}{r} \frac{\partial}{\partial r} \left(r k_o \frac{\partial T}{\partial r} \right)}_{\text{II. Radial conduction}} + \underbrace{\frac{\partial}{\partial z} \left(k_o \frac{\partial T}{\partial z} \right)}_{\text{III. Axial conduction}}, \quad (4.18)$$

where the time derivative (term I) on the LHS represents the energy storage in the CV, the diffusion terms on the RHS are expressions for the heat conduction in both radial (r) (term II) and axial (z) (term III) directions. The discretization process for this governing equation is shown below.

1. When $r > 0$

(1) Discretization of term I using the forward difference method at node (i, j) :

$$\rho_o c_o \left. \frac{\partial T}{\partial t} \right|_{i,j} = \rho_o c_o \frac{T_{i,j}^{n+1} - T_{i,j}^n}{\Delta t} + O(\Delta t), \quad (4.19)$$

where superscripts n and $n + 1$ represent the present (available) and the next (to be calculated) time step, respectively, and O represents the order of the error in using the difference method.

(2) Discretization of radial conduction (term II) using the central difference method:

$$\begin{aligned} \left. \frac{1}{r} \frac{\partial}{\partial r} \left(r k_o \frac{\partial T}{\partial r} \right) \right|_{i,j} &= \frac{k_o}{r} \left. \frac{\partial}{\partial r} \left(r \frac{\partial T}{\partial r} \right) \right|_{i,j} = \frac{k_o}{r} \frac{\partial T}{\partial r} + \frac{k_o}{r} r \frac{\partial^2 T}{\partial r^2} \\ &= \frac{k_o}{r} \left(\frac{T_{i+1,j}^n - T_{i-1,j}^n}{2\Delta r} \right) + k_o \left[\frac{T_{i+1,j}^n - 2T_{i,j}^n + T_{i-1,j}^n}{(\Delta r)^2} \right] + O([\Delta r]^2) \\ &= \frac{k_o}{2i \cdot (\Delta r)^2} (T_{i+1,j}^n - T_{i-1,j}^n) + \frac{k_o}{(\Delta r)^2} (T_{i+1,j}^n - 2T_{i,j}^n + T_{i-1,j}^n) + O([\Delta r]^2) \end{aligned} \quad (4.20)$$

It can be noted that an explicit scheme is used, where the temperatures at different nodes in the discretized equation are evaluated based on the values available at the n^{th} time step.

(3) Discretization of axial conduction (Term III) using the central difference method:

$$\left. \frac{\partial}{\partial z} \left(k_o \frac{\partial T}{\partial z} \right) \right|_{i,j} = k_o \left. \frac{\partial^2 T}{\partial z^2} \right|_{i,j} = \frac{k_o}{(\Delta z)^2} (T_{i,j+1}^n - 2T_{i,j}^n + T_{i,j-1}^n) + O([\Delta z]^2), \quad (4.21)$$

(4) Final expression:

By combining Eqs. (4.12) and (4.19)-(4.21), the discretized governing equation when $r > 0$ is expressed as:

$$T_{i,j}^{n+1} = (1 - 4\lambda_o) T_{i,j}^n + \left[\lambda_o \left(1 + \frac{1}{2i} \right) \right] T_{i+1,j}^n + \left[\lambda_o \left(1 - \frac{1}{2i} \right) \right] T_{i-1,j}^n + \lambda_o T_{i,j+1}^n + \lambda_o T_{i,j-1}^n, \text{ when } r > 0, \quad (4.22)$$

where the thermal diffusivity of the object is expressed as, $\alpha_o = \frac{k_o}{\rho_o c_o}$, and the grid Fourier number

is defined as, $\lambda_o = \frac{\alpha_o \Delta t}{(\Delta r)^2} = \frac{\alpha_o \Delta t}{(\Delta z)^2}$, by taking $\Delta r = \Delta z$.

2. When $r \rightarrow 0$

As $r \rightarrow 0$, the term II becomes undefined as the denominator has r as seen in Eq. (4.12). To overcome this difficulty, the term is further processed as:

$$\begin{aligned} \lim_{r \rightarrow 0} \frac{1}{r} \frac{\partial}{\partial r} \left(r k_o \frac{\partial T}{\partial r} \right) &= \lim_{r \rightarrow 0} \left(\frac{k_o}{r} \frac{\partial T}{\partial r} + \frac{k_o}{r} r \frac{\partial^2 T}{\partial r^2} \right) \\ &= \lim_{r \rightarrow 0} \left(\frac{k_o}{r} \frac{\partial T}{\partial r} + k_o \frac{\partial^2 T}{\partial r^2} \right), \quad (4.23) \\ &= \lim_{r \rightarrow 0} k_o \left(\frac{\partial T}{\partial r} \right) + k_o \frac{\partial^2 T}{\partial r^2} \Big|_{r=0} \end{aligned}$$

By applying the L'Hospital rule [84], the limit can be evaluated as:

$$\lim_{r \rightarrow 0} k_o \left(\frac{\partial T}{\partial r} \right) + k_o \frac{\partial^2 T}{\partial r^2} \Big|_{r=0} = 2k_o \frac{\partial^2 T}{\partial r^2} \Big|_{r=0}, \quad (4.24)$$

Therefore, the Eq. (4.12) is modified as:

$$\rho_o c_o \frac{\partial T}{\partial t} = 2k_o \frac{\partial^2 T}{\partial r^2} + \frac{\partial}{\partial z} \left(k_o \frac{\partial T}{\partial z} \right), \text{ when } r \rightarrow 0, \quad (4.25)$$

By combining the Eqs. (4.19), (4.21), and (4.25), the discretized governing equation when $r = 0$ is given by:

$$T_{0,j}^{n+1} = T_{0,j}^n + \lambda_o \left[2(T_{1,j}^n - 2T_{0,j}^n + T_{-1,j}^n) + (T_{0,j+1}^n - 2T_{0,j}^n + T_{0,j-1}^n) \right], \text{ at } r = 0, \quad (4.26)$$

The Eq. (4.26) is further re-written as:

$$T_{0,j}^{n+1} = (1 - 6\lambda_o)T_{0,j}^n + (2\lambda_o)T_{1,j}^n + (2\lambda_o)T_{-1,j}^n + \lambda_o T_{0,j+1}^n + \lambda_o T_{0,j-1}^n, \quad (4.27)$$

It should be noted that $T_{-1,j}^n$ is a ghost node defined outside the computational region, where the temperature has to be evaluated. By considering the axial symmetry at $r = 0$, this ghost node can be expressed in terms of temperature at nodes within the domain as:

$$\frac{\partial T}{\partial r} = 0 \Rightarrow \frac{T_{1,j}^n - T_{-1,j}^n}{\Delta r} = 0 \Rightarrow T_{1,j}^n = T_{-1,j}^n, \quad (4.28)$$

The Eq. (4.27) is then re-written as:

$$\begin{aligned} T_{0,j}^{n+1} &= (1 - 6\lambda_o)T_{0,j}^n + (2\lambda_o)T_{1,j}^n + (2\lambda_o)T_{-1,j}^n + \lambda_o T_{0,j+1}^n + \lambda_o T_{0,j-1}^n \\ &= (1 - 6\lambda_o)T_{0,j}^n + (4\lambda_o)T_{1,j}^n + \lambda_o T_{0,j+1}^n + \lambda_o T_{0,j-1}^n \end{aligned}, \quad (4.29)$$

4.3.1.2 Liquid region (CV3)

Similarly, for governing equations, the forward difference method is used to discretize time, and a similar procedure is applied to the Eq. (4.13) in the liquid region for the time evolution and conduction terms:

$$\underbrace{\rho_o c_1 \frac{\partial T}{\partial t}}_{\text{I. Time evolution}} = \underbrace{\frac{1}{r} \frac{\partial}{\partial r} \left(r k_1 \frac{\partial T}{\partial r} \right)}_{\text{II. Radial conduction}} + \underbrace{\frac{\partial}{\partial z} \left(k_1 \frac{\partial T}{\partial z} \right)}_{\text{III. Axial conduction}}, \quad (4.30)$$

1. When $r > 0$

(1) Discretization of time evolution (term I) using the forward difference method:

$$\rho_o c_1 \left. \frac{\partial T}{\partial t} \right|_{i,j} = \rho_o c_1 \frac{T_{i,j}^{n+1} - T_{i,j}^n}{\Delta t} + O(\Delta t), \quad (4.31)$$

(2) Discretization of radial conduction (term II) using the central difference method:

$$\begin{aligned}
\left. \frac{1}{r} \frac{\partial}{\partial r} \left(r k_1 \frac{\partial T}{\partial r} \right) \right|_{i,j} &= \left. \frac{k_1}{r} \frac{\partial}{\partial r} \left(r \frac{\partial T}{\partial r} \right) \right|_{i,j} = \frac{k_1}{r} \frac{\partial T}{\partial r} + \frac{k_1}{r} r \frac{\partial^2 T}{\partial r^2} \\
&= \frac{k_1}{r} \left(\frac{T_{i+1,j}^n - T_{i-1,j}^n}{2\Delta r} \right) + k_1 \left[\frac{T_{i+1,j}^n - 2T_{i,j}^n + T_{i-1,j}^n}{(\Delta r)^2} \right] + O\left[(\Delta z)^2\right], \quad (4.32) \\
&= \frac{k_1}{2i \cdot (\Delta r)^2} (T_{i+1,j}^n - T_{i-1,j}^n) + \frac{k_1}{(\Delta r)^2} (T_{i+1,j}^n - 2T_{i,j}^n + T_{i-1,j}^n) + O\left[(\Delta z)^2\right]
\end{aligned}$$

(3) Discretization of axial direction (term III) using the central difference method:

$$\left. \frac{\partial}{\partial z} \left(k_1 \frac{\partial T}{\partial z} \right) \right|_{i,j} = k_1 \left. \frac{\partial^2 T}{\partial z^2} \right|_{i,j} = \frac{k_1}{(\Delta z)^2} (T_{i,j+1}^n - 2T_{i,j}^n + T_{i,j-1}^n) + O\left[(\Delta z)^2\right], \quad (4.33)$$

(4) Final expression:

By combining Eqs. (4.13) and (4.31)-(4.33), the discretized governing equation when $r > 0$ is expressed as:

$$T_{i,j}^{n+1} = (1 - 4\lambda_1) T_{i,j}^n + \left[\lambda_1 \left(1 + \frac{1}{2i} \right) \right] T_{i+1,j}^n + \left[\lambda_1 \left(1 - \frac{1}{2i} \right) \right] T_{i-1,j}^n + \lambda_1 T_{i,j+1}^n + \lambda_1 T_{i,j-1}^n, \text{ when } r > 0, \quad (4.34)$$

where the thermal diffusivity of the liquid is expressed as, $\alpha_1 = \frac{k_1}{\rho_1 c_1}$, and the grid Fourier number

is defined as, $\lambda_1 = \frac{\alpha_1 \Delta t}{(\Delta r)^2} = \frac{\alpha_1 \Delta t}{(\Delta z)^2}$, by taking $\Delta r = \Delta z$.

2. When $r \rightarrow 0$

A similar procedure is followed when $r \rightarrow 0$ for the term II, which is given by:

$$\begin{aligned}
\lim_{r \rightarrow 0} \frac{1}{r} \frac{\partial}{\partial r} \left(r k_1 \frac{\partial T}{\partial r} \right) &= \lim_{r \rightarrow 0} \left(\frac{k_1}{r} \frac{\partial T}{\partial r} + \frac{k_1}{r} r \frac{\partial^2 T}{\partial r^2} \right) \\
&= \lim_{r \rightarrow 0} \left(\frac{k_1}{r} \frac{\partial T}{\partial r} + k_1 \frac{\partial^2 T}{\partial r^2} \right) , \\
&= \lim_{r \rightarrow 0} k_1 \left(\frac{\partial T}{\partial r} \right) + k_1 \frac{\partial^2 T}{\partial r^2} \Big|_{r=0}
\end{aligned} \tag{4.35}$$

By applying the L'Hospital rule [84], the limit can be evaluated as:

$$\lim_{r \rightarrow 0} k_1 \left(\frac{\partial T}{\partial r} \right) + k_1 \frac{\partial^2 T}{\partial r^2} \Big|_{r=0} = 2k_1 \frac{\partial^2 T}{\partial r^2} \Big|_{r=0} , \tag{4.36}$$

Therefore, the Eq. (4.12) is modified as:

$$\rho_1 c_1 \frac{\partial T}{\partial t} = 2k_1 \frac{\partial^2 T}{\partial r^2} + \frac{\partial}{\partial z} \left(k_1 \frac{\partial T}{\partial z} \right), \text{ at } r = 0, \tag{4.37}$$

By combining the Eqs. (4.19), (4.21), and (4.25), the discretized governing equation when $r = 0$ is given by:

$$T_{0,j}^{n+1} = T_{0,j}^n + \lambda_1 \left[2(T_{1,j}^n - 2T_{0,j}^n + T_{-1,j}^n) + (T_{0,j+1}^n - 2T_{0,j}^n + T_{0,j-1}^n) \right], \text{ at } r = 0, \tag{4.38}$$

The Eq. (4.26) is further re-written as:

$$T_{0,j}^{n+1} = (1 - 6\lambda_1)T_{0,j}^n + (2\lambda_1)T_{1,j}^n + (2\lambda_1)T_{-1,j}^n + \lambda_1 T_{0,j+1}^n + \lambda_1 T_{0,j-1}^n, \tag{4.39}$$

As before, $T_{-1,j}^n$ is expressed in terms of temperature at nodes within the domain as:

$$\frac{\partial T}{\partial r} = 0 \Rightarrow \frac{T_{1,j}^n - T_{-1,j}^n}{\Delta r} = 0 \Rightarrow T_{1,j}^n = T_{-1,j}^n, \tag{4.40}$$

The Eq. (4.27) is further simplified as:

$$\begin{aligned}
T_{0,j}^{n+1} &= (1 - 6\lambda_1)T_{0,j}^n + (2\lambda_1)T_{1,j}^n + (2\lambda_1)T_{-1,j}^n + \lambda_1 T_{0,j+1}^n + \lambda_1 T_{0,j-1}^n \\
&= (1 - 6\lambda_1)T_{0,j}^n + (4\lambda_1)T_{1,j}^n + \lambda_1 T_{0,j+1}^n + \lambda_1 T_{0,j-1}^n ,
\end{aligned} \tag{4.41}$$

4.3.2 Initial condition

As shown in Eq. (4.14), the entire domain is initialized to the value of the ambient temperature, T_{amb} . The expression at the node (i, j) is given as:

$$T_{i,j}^0 = T_{\text{amb}}, \quad (4.42)$$

4.3.3 Boundary conditions

According to Figure 4.3, boundary conditions of the object, liquid, and interfaces are discretized by following the procedures given below.

4.3.3.1 Object region (CV₁ and CV₂)

1. By discretizing Eq. (4.15), the condition at the top surface of the object is given by:

$$\begin{aligned} k_o \frac{\partial T}{\partial z} \Big|_o = \dot{q}_g'' &\Rightarrow k_o \left(\frac{T_{i,N+1}^n - T_{i,N-1}^n}{2\Delta z} \right) = \bar{h}_{\text{conv}} (T_g - T_{i,N}^n) + \varepsilon\sigma \left[T_g^4 - (T_{i,N}^n)^4 \right], \\ \Rightarrow T_{i,N+1}^n &= T_{i,N-1}^n + \frac{2\Delta z}{k_o} \left\{ \bar{h}_{\text{conv}} (T_g - T_{i,N}^n) + \varepsilon\sigma \left[T_g^4 - (T_{i,N}^n)^4 \right] \right\} \end{aligned} \quad (4.43)$$

The boundary condition is used to evaluate the temperature at the ghost node $(i, N + 1)$. After this, it is used in the discretized expression of the governing equation for node (i, N) based on Eq. (4.22), given by:

$$T_{i,N}^{n+1} = (1 - 4\lambda_o) T_{i,N}^n + \left[\lambda_o \left(1 + \frac{1}{2i} \right) \right] T_{i+1,N}^n + \left[\lambda_o \left(1 - \frac{1}{2i} \right) \right] T_{i-1,N}^n + \lambda_o T_{i,N+1}^n + \lambda_o T_{i,N-1}^n, \quad (4.44)$$

2. The axis condition is used for evaluating ghost nodes as shown in Eqs. (4.28) and (4.29).

3. The side condition is given by:

$$\begin{aligned} k_o \frac{\partial T}{\partial r} \Big|_o = \dot{q}_g'' &\Rightarrow k_o \left(\frac{T_{M+1,j}^n - T_{M-1,j}^n}{2\Delta r} \right) = \bar{h}_{\text{conv}} (T_g - T_{M,j}^n) + \varepsilon\sigma \left[T_g^4 - (T_{M,j}^n)^4 \right], \\ \Rightarrow T_{M+1,j}^n &= T_{M-1,j}^n + \frac{2\Delta r}{k_o} \left\{ \bar{h}_{\text{conv}} (T_g - T_{M,j}^n) + \varepsilon\sigma \left[T_g^4 - (T_{M,j}^n)^4 \right] \right\} \end{aligned} \quad (4.45)$$

where the ghost node at $(M + 1, j)$ is evaluated to be used in the discretized equation of the node at (M, j) .

4.3.3.2 Liquid region (CV3)

1. By discretizing the Eq. (4.16), the surface condition of liquid is given by:

$$\begin{aligned} k_1 \frac{\partial T}{\partial z} \Big|_{\parallel} = \dot{q}_g'' \Rightarrow k_1 \left(\frac{T_{i,N1+1}^n - T_{i,N1-1}^n}{2\Delta z} \right) &= \bar{h}_{\text{conv}} (T_g - T_{i,N1}^n) + \varepsilon\sigma \left[T_g^4 - (T_{i,N1}^n)^4 \right] \\ \Rightarrow T_{i,N1+1}^n = T_{i,N1-1}^n + \frac{2\Delta z}{k_1} \left\{ \bar{h}_{\text{conv}} (T_g - T_{i,N1}^n) + \varepsilon\sigma \left[T_g^4 - (T_{i,N1}^n)^4 \right] \right\} \end{aligned} \quad (4.46)$$

Using the data at node $(i, N1 + 1)$, the temperature at $j = N1$ is calculated based on the discretization of the governing equation Eq. (4.34), which is expressed as:

$$T_{i,N1}^{n+1} = (1 - 4\lambda_1) T_{i,N1}^n + \left[\lambda_1 \left(1 + \frac{1}{2i} \right) \right] T_{i+1,N1}^n + \left[\lambda_1 \left(1 - \frac{1}{2i} \right) \right] T_{i-1,N1}^n + \lambda_1 T_{i,N1+1}^n + \lambda_1 T_{i,N1-1}^n, \quad (4.47)$$

2. The axis condition is used for evaluating ghost nodes as shown in Eqs. (4.40) and (4.41).

3. The boundary condition at the adiabatic side wall condition is given by:

$$\begin{aligned} \frac{\partial T}{\partial r} = 0 \Rightarrow \left(\frac{T_{M+1,j}^n - T_{M-1,j}^n}{2\Delta r} \right) &= 0, \\ \Rightarrow T_{M+1,j}^n = T_{M-1,j}^n \end{aligned} \quad (4.48)$$

By applying Eq. (4.34), the temperature at node (M, j) is evaluated in terms of ghost nodes temperature, which is expressed as:

$$T_{M,j}^{n+1} = (1 - 4\lambda_1) T_{M,j}^n + \left[\lambda_1 \left(1 + \frac{1}{2i} \right) \right] T_{M+1,j}^n + \left[\lambda_1 \left(1 - \frac{1}{2i} \right) \right] T_{M-1,j}^n + \lambda_1 T_{M,j+1}^n + \lambda_1 T_{M,j-1}^n, \quad (4.49)$$

4. Similarly, the adiabatic condition at the bottom is given by:

$$\begin{aligned} \frac{\partial T}{\partial z} = 0 \Rightarrow \left(\frac{T_{i,1}^n - T_{i,-1}^n}{2\Delta z} \right) &= 0, \\ \Rightarrow T_{i,-1}^n = T_{i,1}^n \end{aligned} \quad (4.50)$$

By applying this to Eq. (4.34), the temperature is evaluated as:

$$T_{i,0}^{n+1} = (1 - 4\lambda_1)T_{i,0}^n + \left[\lambda_1 \left(1 + \frac{1}{2i} \right) \right] T_{i+1,0}^n + \left[\lambda_1 \left(1 - \frac{1}{2i} \right) \right] T_{i-1,0}^n + \lambda_1 T_{i,1}^n + \lambda_1 T_{i,-1}^n, \quad (4.51)$$

4.3.3.3 Interfaces

1. For interface 1, by discretizing the Eq. (4.17) with the $O([\Delta z]^2)$ accuracy, a three-point backward difference method is implemented for the solid side and a three-point forward difference method is implemented for the liquid side, given as:

$$\begin{aligned} k_o \frac{\partial T}{\partial r} \Big|_o &= k_1 \frac{\partial T}{\partial r} \Big|_l \\ \Rightarrow k_o \left(\frac{3T_{M1,j}^n - 4T_{M1-1,j}^n + T_{M1-2,j}^n}{2\Delta r} \right)_o &= k_1 \left(\frac{-3T_{M1,j}^n + 4T_{M1+1,j}^n - T_{M1+2,j}^n}{2\Delta r} \right)_l, \\ \Rightarrow (T_{M1,j}^n) &= \frac{(4T_{M1-1,j}^n - T_{M1-2,j}^n) + \frac{k_1}{k_o} (4T_{M1+1,j}^n - T_{M1+2,j}^n)}{3 \left(1 + \frac{k_1}{k_o} \right)} \end{aligned} \quad (4.52)$$

2. Similarly, for interface 2, by discretizing the Eq. (4.17) with the $O([\Delta z]^2)$ accuracy, a three-point forward difference method is implemented for the solid side and a three-point backward difference method is implemented for the liquid side, given as:

$$\begin{aligned} k_o \frac{\partial T}{\partial z} \Big|_o &= k_1 \frac{\partial T}{\partial z} \Big|_l \\ k_o \left(\frac{-3T_{i,N0}^n + 4T_{i,N0+1}^n - T_{i,N0+2}^n}{2\Delta z} \right)_o &= k_1 \left(\frac{3T_{i,N0}^n - 4T_{i,N0-1}^n + T_{i,N0-2}^n}{2\Delta z} \right)_l, \\ (T_{i,N0}^{n+1}) &= \frac{\frac{k_o}{k_1} (4T_{i,N0+1}^n - T_{i,N0+2}^n) + (4T_{i,N0-1}^n - T_{i,N0-2}^n)}{3 \left(1 + \frac{k_o}{k_1} \right)} \end{aligned} \quad (4.53)$$

Thus, the interface node is evaluated as a function of the nodes surrounding it. It should be noted that the governing equation is not solved at interfaces. Instead, the energy balance of the governing equation is checked from the evaluated interface temperature for the model, which is discussed in Section 4.5.

4.4 Mass loss rate

The fundamental idea of the model is to predict the mass loss rate of liquid in the presence of the immersed object. As discussed previously, the hot gas phase, representing the flame, transfers heat to the liquid as well as the collector through convection and radiation. Further, the collector transfers heat to the heater via conduction. The heater ensures the transfer of sensible and latent heat to the liquid fuel. As a result, as the liquid temperature attains the saturation temperature by sensible heating, the additional heat is used for vaporization. It is given by:

$$\dot{m} = \frac{\dot{q}_e}{h_{fg}}, \quad (4.54)$$

where \dot{q}_e represents the net heat transferred into a liquid volume, and h_{fg} is the latent heat of vaporization of the liquid.

For the discretized domain as shown in Figure 4.4, the determination of \dot{q}_e is dependent on the cell location, where the heat transfer is through a half cell at the solid-liquid interface (red), while it is through a full cell within the liquid (blue). As it is further illustrated in Figure 4.5(a), the heat is transferred from the heater to the liquid at the interface via a half cell. The evaluation of heat flux at interface 1, \dot{q}_{i1}'' , is discussed in Section 4.3. As illustrated in Figure 4.5(b), the heat is transferred inside of the liquid via a full cell. The coordinates M , N , $M0$, $N0$, $M1$, and $N1$ denote the boundaries of the domain and interfaces.

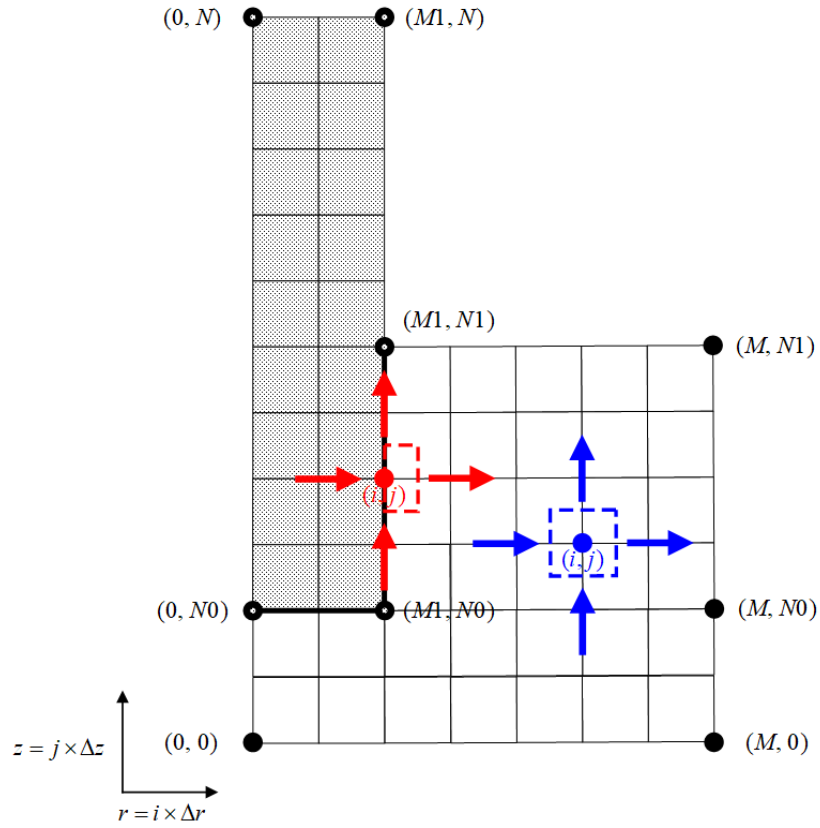
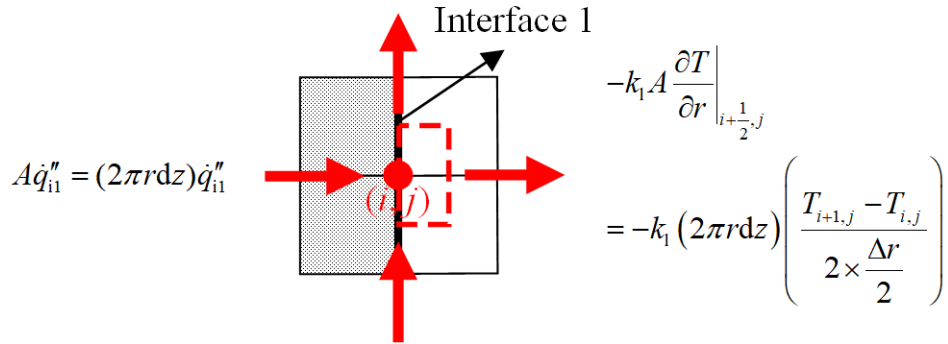


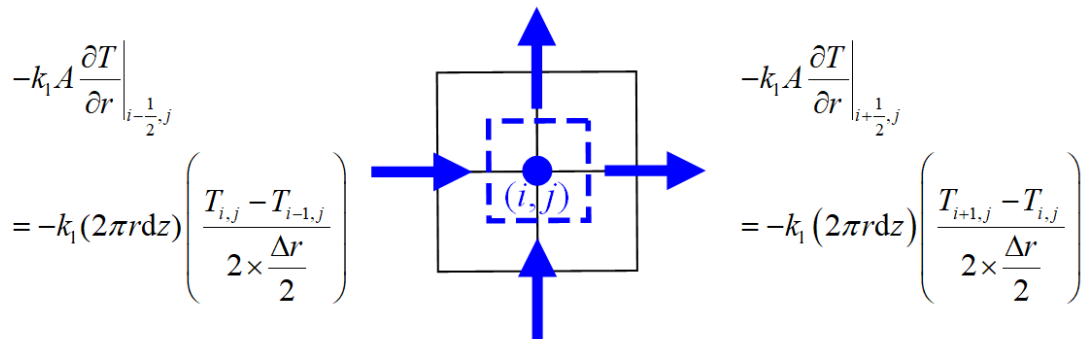
Figure 4.4: Schematic of mass loss rate representing the heat into a cell at the solid-liquid interface (red) and inside of the liquid (blue).

$$-\frac{(k_o + k_l)}{2} A \frac{\partial T}{\partial z} \Big|_{i,j+\frac{1}{2}} = -\frac{(k_o + k_l)}{2} (\pi r dr) \left(\frac{T_{i,j+1} - T_{i,j}}{2 \times \frac{\Delta z}{2}} \right)$$



$$-\frac{(k_o + k_l)}{2} A \frac{\partial T}{\partial z} \Big|_{i,j-\frac{1}{2}} = -\frac{(k_o + k_l)}{2} (\pi r dr) \left(\frac{T_{i,j} - T_{i,j-1}}{2 \times \frac{\Delta z}{2}} \right)$$

(a) At the solid-liquid interface 1 (half cell).

$$\begin{aligned}
& -k_1 A \frac{\partial T}{\partial z} \Big|_{i,j+\frac{1}{2}} = -k_1 (2\pi r dr) \left(\frac{T_{i,j+1} - T_{i,j}}{2 \times \frac{\Delta z}{2}} \right) \\
& -k_1 A \frac{\partial T}{\partial r} \Big|_{i-\frac{1}{2},j} = -k_1 (2\pi r dz) \left(\frac{T_{i,j} - T_{i-1,j}}{2 \times \frac{\Delta r}{2}} \right) \\
& -k_1 A \frac{\partial T}{\partial r} \Big|_{i+\frac{1}{2},j} = -k_1 (2\pi r dz) \left(\frac{T_{i+1,j} - T_{i,j}}{2 \times \frac{\Delta r}{2}} \right) \\
& -k_1 A \frac{\partial T}{\partial z} \Big|_{i,j-\frac{1}{2}} = -k_1 (2\pi r dr) \left(\frac{T_{i,j} - T_{i,j-1}}{2 \times \frac{\Delta z}{2}} \right)
\end{aligned}$$


(b) In the liquid (full cell).

Figure 4.5: Calculations of the heat in/out of a cell, \dot{q}_e , at the solid-liquid interface (red) and in the liquid (blue).

Equation (4.54) is valid when the liquid temperature reaches the saturation temperature, and $\dot{q}_e > 0$. When the liquid temperature is below the saturation temperature or $\dot{q}_e \leq 0$, the result is used to calculate the energy imbalance, which is discussed in Section 4.6.

Furthermore, the net heat into a cell is calculated by integrating the heat transfer through four faces of a cell. In a liquid cell (full cell), the Eq. (4.54) is further expressed as:

$$\dot{m} = \frac{\sum \left(-k_1 A \frac{\partial T}{\partial r} \Big|_{i-\frac{1}{2},j} - k_1 A \frac{\partial T}{\partial r} \Big|_{i+\frac{1}{2},j} - k_1 A \frac{\partial T}{\partial z} \Big|_{i,j+\frac{1}{2}} - k_1 A \frac{\partial T}{\partial z} \Big|_{i,j-\frac{1}{2}} \right)}{h_{fg}}, \quad (4.55)$$

4.5 Energy imbalance at interfaces

To evaluate the conditions at interfaces dictated by the temperature limit to the liquid saturation temperature, energy imbalance is checked using the temperature at interfaces. The procedure is applied to the solid and liquid sides, because of distinct discrepancies between their thermal properties.

4.5.1 Solid side

Based on the Eq. (4.12), the governing equation of solid is re-written as:

$$\frac{\partial T}{\partial t} = \frac{\alpha_o}{r} \frac{\partial T}{\partial r} + \alpha_o \frac{\partial^2 T}{\partial r^2} + \alpha_o \frac{\partial^2 T}{\partial z^2}, \quad (4.56)$$

Next, the Eq. (4.56) is discretized at different locations (as labeled in Figure 4.3). For the discretization at interface 1, where $i = M1, j = N0 + 1$ to $N1$, the backward difference method is implemented in the radial direction, and the central difference method is implemented in the axial direction. The temperature at node (i, j) is given by:

$$\begin{aligned} \left. \frac{T_{i,j}^{n+1} - T_{i,j}^n}{\Delta t} \right|_{\text{GE}} &= \frac{\alpha_o}{i(\Delta r)} \frac{3T_{i,j}^n - 4T_{i-1,j}^n + T_{i-2,j}^n}{2(\Delta r)} + \alpha_o \frac{2T_{i,j}^n - 5T_{i-1,j}^n + 4T_{i-2,j}^n - T_{i-3,j}^n}{(\Delta r)^2} + \alpha_o \frac{T_{i,j+1}^n - 2T_{i,j}^n + T_{i,j-1}^n}{(\Delta z)^2} \\ \Rightarrow T_{i,j}^{n+1} \Big|_{\text{GE}} &= T_{i,j}^n + \lambda_o \left(\frac{3T_{i,j}^n - 4T_{i-1,j}^n + T_{i-2,j}^n}{2i} \right) + \lambda_o \left(2T_{i,j}^n - 5T_{i-1,j}^n + 4T_{i-2,j}^n - T_{i-3,j}^n \right) + \lambda_o \left(T_{i,j+1}^n - 2T_{i,j}^n + T_{i,j-1}^n \right) \\ &= \left(1 + \frac{3}{2i} \lambda_o + 2\lambda_o - 2\lambda_o \right) T_{i,j}^n + \lambda_o \left(\frac{-4T_{i-1,j}^n + T_{i-2,j}^n}{2i} \right) + \lambda_o \left(-5T_{i-1,j}^n + 4T_{i-2,j}^n - T_{i-3,j}^n \right) + \lambda_o \left(T_{i,j+1}^n + T_{i,j-1}^n \right) \\ &= \left(1 + \frac{3}{2i} \lambda_o \right) T_{i,j}^n + \lambda_o \left(\frac{-4T_{i-1,j}^n + T_{i-2,j}^n}{2i} \right) + \lambda_o \left(-5T_{i-1,j}^n + 4T_{i-2,j}^n - T_{i-3,j}^n + T_{i,j+1}^n + T_{i,j-1}^n \right) \end{aligned} \quad (4.57)$$

where $T_{i,j}^{n+1} \Big|_{\text{GE}}$ is evaluated by using the governing equation.

Furthermore, to evaluate the difference between the implementation of the governing equation and the boundary condition, the ratio of the residue calculated at the solid side, γ_o , is expressed as:

$$\gamma_o = \frac{T_{i,j}^{n+1}|_{\text{GE}} - T_{i,j}^{n+1}}{T_{i,j}^{n+1}} \times 100\%, \quad (4.58)$$

where $T_{i,j}^{n+1}$ is the value calculated by using the interface boundary condition where heat flux balance is considered.

Similar calculations are applied to evaluate the temperature at interface 2, (M1, N0), and (0, N0) by using the governing equation, whose expressions are summarized in Table 4.2.

Table 4.2: Expressions of $T_{i,j}^{n+1}|_{\text{GE}}$ calculated at the solid side.

Interface node	Equation for $T_{i,j}^{n+1} _{\text{GE}}$	Eq.
Interface 1: $i = M1, j = N0 + 1$ to $N1$	$\left(1 + \frac{3}{2i} \lambda_o\right) T_{i,j}^n + \lambda_o \left(\frac{-4T_{i-1,j}^n + T_{i-2,j}^n}{2i}\right)$ $+ \lambda_o \left(-5T_{i-1,j}^n + 4T_{i-2,j}^n - T_{i-3,j}^n + T_{i,j+1}^n + T_{i,j-1}^n\right)$	(4.57)
Interface 2: $i = 1$ to $M1 - 1, j = N0$	$T_{i,j}^n + \lambda_o \left(\frac{T_{i+1,j}^n - T_{i-1,j}^n}{2i}\right)$ $+ \lambda_o \left(T_{i+1,j}^n + T_{i-1,j}^n - 5T_{i,j+1}^n + 4T_{i,j+2}^n - T_{i,j+3}^n\right)$	(4.59)
Node ($M1, N0$)	$\left(1 + \frac{3}{2i} \lambda_o + 4\lambda_o\right) T_{i,j}^n + \lambda_o \left(\frac{-4T_{i-1,j}^n + T_{i-2,j}^n}{2i}\right)$ $+ \lambda_o \left(-5T_{i-1,j}^n + 4T_{i-2,j}^n - T_{i-3,j}^n - 5T_{i,j+1}^n + 4T_{i,j+2}^n - T_{i,j+3}^n\right)$	(4.60)
Node ($0, N0$)	$(1 - 2\lambda_o) T_{i,j}^n + 4\lambda_o \left(T_{i+1,j}^n\right)$ $+ \lambda_o \left(-5T_{i,j+1}^n + 4T_{i,j+2}^n - T_{i,j+3}^n\right)$	(4.61)

4.5.2 Liquid side

Similarly, based on the Eq. (4.13), the governing equation of liquid for the temperature is re-written as:

$$\frac{\partial T}{\partial t} = \frac{\alpha_1}{r} \frac{\partial T}{\partial r} + \alpha_1 \frac{\partial^2 T}{\partial r^2} + \alpha_1 \frac{\partial^2 T}{\partial z^2}, \quad (4.62)$$

The ratio of the residue calculated at the solid side, γ_1 , is expressed as:

$$\gamma_1 = \frac{T_{i,j}^{n+1}|_{\text{GE}} - T_{i,j}^{n+1}}{T_{i,j}^{n+1}} \times 100\%, \quad (4.63)$$

Calculations are applied to interface 1, interface 2, ($M1, N0$), and ($0, N0$), whose expressions are summarized in Table 4.3.

Table 4.3: Expressions of $T_{i,j}^{n+1}|_{GE}$ calculated at the liquid side.

Interface node	Equation for $T_{i,j}^{n+1} _{GE}$	Eq.
Interface 1: $i = M1, j = N0 + 1$ to $N1$	$\left(1 - \frac{3}{2i}\lambda_1\right)T_{i,j}^n + \lambda_1\left(\frac{4T_{i+1,j}^n - T_{i+2,j}^n}{2i}\right)$ $+ \lambda_1\left(-5T_{i+1,j}^n + 4T_{i+2,j}^n - T_{i+3,j}^n + T_{i,j+1}^n + T_{i,j-1}^n\right)$	(4.64)
Interface 2: $i = 1$ to $M1 - 1, j = N0$	$T_{i,j}^n + \lambda_1\left(\frac{T_{i+1,j}^n - T_{i-1,j}^n}{2i}\right)$ $+ \lambda_1\left(T_{i+1,j}^n + T_{i-1,j}^n - 5T_{i,j-1}^n + 4T_{i,j-2}^n - T_{i,j-3}^n\right)$	(4.65)
Node ($M1, N0$)	$\left(1 - \frac{3}{2i}\lambda_1 + 4\lambda_1\right)T_{i,j}^n + \lambda_1\left(\frac{4T_{i+1,j}^n - T_{i+2,j}^n}{2i}\right)$ $+ \lambda_1\left(-5T_{i+1,j}^n + 4T_{i+2,j}^n - T_{i+3,j}^n - 5T_{i,j-1}^n + 4T_{i,j-2}^n - T_{i,j-3}^n\right)$	(4.66)
Node ($0, N0$)	$(1 - 2\lambda_1)T_{i,j}^n + 4\lambda_1\left(T_{i+1,j}^n\right)$ $+ \lambda_1\left(-5T_{i,j-1}^n + 4T_{i,j-2}^n - T_{i,j-3}^n\right)$	(4.67)

Detailed derivations of $T_{i,j}^{n+1}|_{GE}$ can be found in Appendix B.

4.6 Energy imbalance in interior cells

The convergence of the calculations is verified by checking the energy imbalance in interior cells.

Two methods are implemented: 1. finding out the maximum value of energy imbalance through a single cell, and 2. calculating the energy imbalance for the whole CV.

4.6.1 Maximum of a single cell

Figure 4.6 illustrates the energy imbalance check applied to a single cell, whose result, $I_{\text{cell,max}}$, is given by:

$$\begin{aligned} I_{\text{cell}} &= (\dot{q}_{\text{cell,e}}) - (\dot{q}_{\text{cell,vap}}) - (\dot{q}_{\text{cell,sen}}) \\ &= (-\dot{q}_{\text{cell,top}} + \dot{q}_{\text{cell,bottom}} + \dot{q}_{\text{cell,left}} - \dot{q}_{\text{cell,right}}) - (\dot{m}_{\text{cell}} h_{\text{fg}}) - \left[\rho V_{\text{cell}} c \left(\frac{T_{i,j}^n - T_{i,j}^{n-1}}{\Delta t} \right) \right]_{\text{cell}}, \end{aligned} \quad (4.68)$$

$$I_{\text{cell,max}} = \max(|I_{\text{cell}}|). \quad (4.69)$$

where Eq. (4.69) denotes the maximum of $|I_{\text{cell}}|$ among all the cells in the domain.

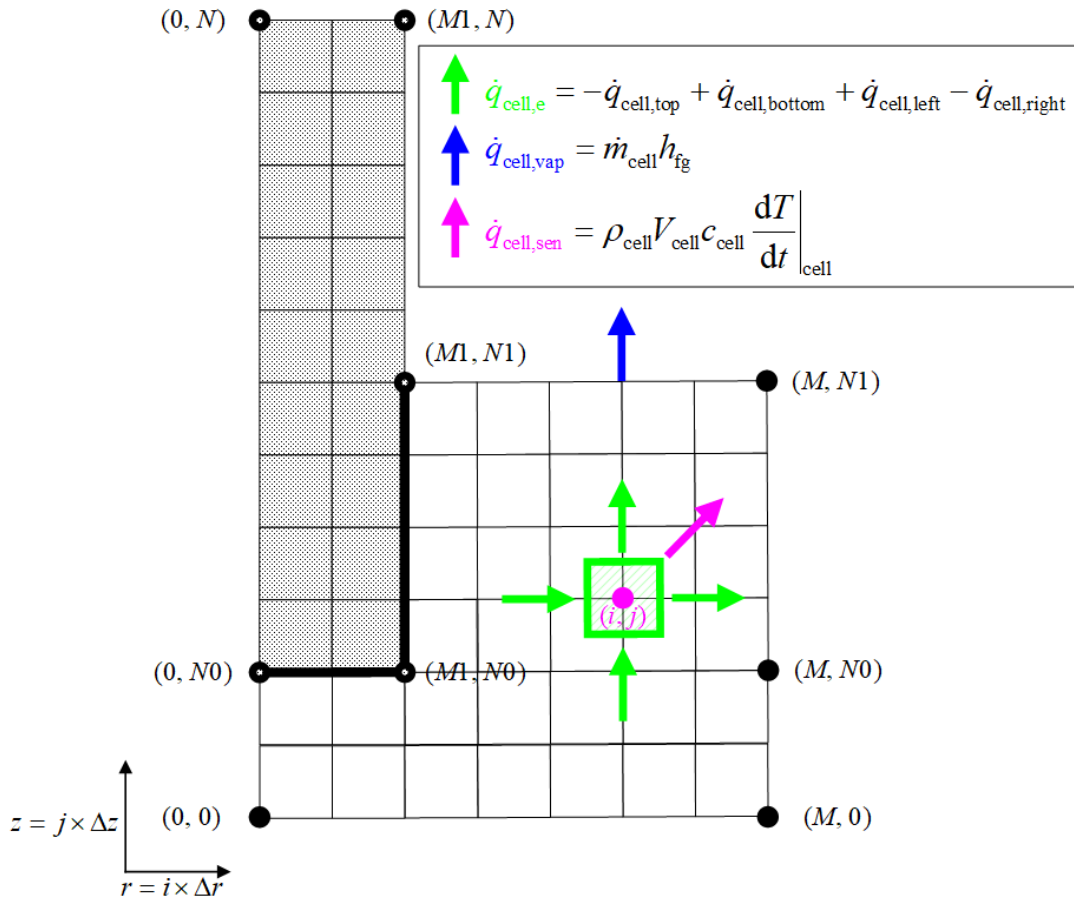


Figure 4.6: Schematic of the energy imbalance check applied to a single cell, which consists of the external heat (green), the heat required to vaporize liquid at the saturation temperature (blue), and the sensible heat to raise the temperature of object and liquid (magenta) in time Δt .

In Eq. (4.68), $\dot{q}_{\text{cell},e}$ is the external heat, $\dot{q}_{\text{cell},\text{vap}}$ is the heat required to vaporize the liquid at the saturation temperature T_{sat} , $\dot{q}_{\text{cell},\text{sen}}$ is the sensible heat needed to raise the temperature of object and liquid in time Δt , ρ and c are density and specific heat respectively, and V is volume. In the subscript, cell denotes a single cell, l is the liquid, and o is the object.

The volume of a cell, V_{cell} , is dependent on the configuration of the cell at different locations, which is similar to those discussed in Section 4.4.

Furthermore, the ratio of the energy imbalance to the total energy input is evaluated for further discussions, which is given by:

$$\begin{aligned}
\Phi_{\text{cell,max}} &= \frac{|I_{\text{cell,max}}|}{\dot{q}_{\text{total}}} \times 100\% = \frac{|I_{\text{cell,max}}|}{\dot{q}_o + \dot{q}_l} \times 100\% \\
&= \frac{|I_{\text{cell,max}}|}{\dot{q}_g''|_{j=N} \times A_{\text{o,top}} + \dot{q}_g''|_{j=N1} \times A_{\text{l,top}}} \times 100\% , \\
&= \frac{|I_{\text{cell,max}}|}{\dot{q}_g''|_{j=N} \times \left[\frac{\pi(D_o)^2}{4} \right] + \dot{q}_g''|_{j=N1} \times \left\{ \frac{\pi[D^2 - (D_o)^2]}{4} \right\}} \times 100\%
\end{aligned} \tag{4.70}$$

where the total heat rate, \dot{q}_{total} , consists of the heat rate from the heat source to the object, \dot{q}_o , and the liquid, \dot{q}_l .

4.6.2 Whole CV

Figure 4.7 illustrates the energy imbalance check applied to the whole CV, I_{cv} , given by:

$$\begin{aligned}
I_{\text{cv}} &= (\dot{q}_{\text{cv,e}}) - (\dot{q}_{\text{cv,vap}}) - (\dot{q}_{\text{cv,sen}}) \\
&= \dot{q}_g''|_{z=L_C+L_L} \times \left[\frac{\pi(D_o)^2}{4} \right] + \dot{q}_g''|_{z=L_L} \times \left\{ \frac{\pi[D^2 - (D_o)^2]}{4} \right\} - (\dot{m}_{\text{cv}} h_{\text{fg}}), \\
&\quad - \left[\rho_l V_l c_l \left(\frac{T_{\text{avg}}^n - T_{\text{avg}}^{n-1}}{\Delta t} \right) \right]_l + \rho_o V_o c_o \left(\frac{T_{\text{avg}}^n - T_{\text{avg}}^{n-1}}{\Delta t} \right) \Big|_o
\end{aligned} \tag{4.71}$$

where $\dot{q}_{\text{cv,e}}$ is the external heat, $\dot{q}_{\text{cv,vap}}$ is the heat required to vaporize liquid at the saturation temperature T_{sat} , $\dot{q}_{\text{cv,sen}}$ is the sensible heat needed to raise the spatial average temperature of CV

in time Δt , A is surface area, and V is volume. In the subscript, cv denotes the control volume, l is the liquid, o is the object, and avg denotes the average.

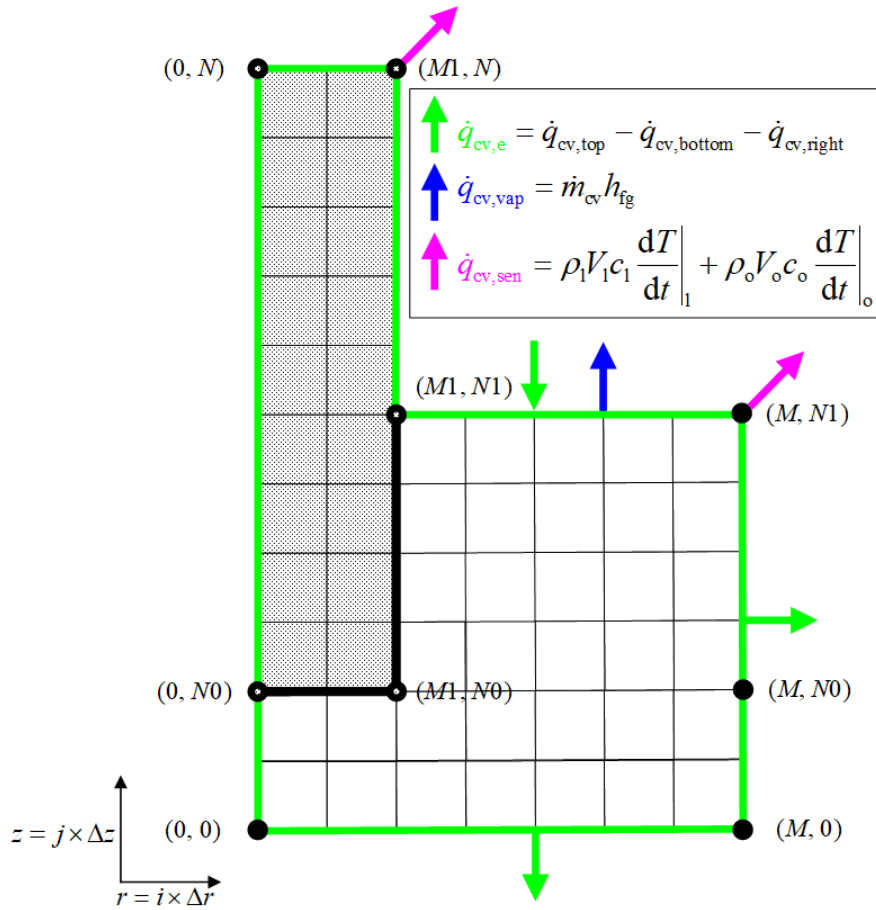


Figure 4.7: Schematic of the energy imbalance check applied to the whole CV, which consists of the external heat (green), the heat required to vaporize liquid at the saturation temperature (blue), and the sensible heat to raise the temperature of object and liquid (magenta) in time Δt .

The average temperature is calculated based on the values of each cell, for example, the average temperature in the object region at the time step n , $T_{avg}^n|_o$, is given by:

$$\begin{aligned}
T_{\text{avg}}^n \Big|_o &= \frac{\sum_{i,j} (T_{\text{cell}} \times V_{\text{cell}}) \Big|_o}{V_o} \\
&= \frac{\sum_{i=0}^{i=M-1} \sum_{j=N_0}^{j=N-1} \left\{ \left(\frac{T_{i,j}^n + T_{i+1,j}^n + T_{i,j+1}^n + T_{i+1,j+1}^n}{4} \right) \times [2\pi(i+0.5) dr \times dr \times dz] \right\}}{\frac{\pi(D_o)^2(L_H + L_C)}{4}}, \quad (4.72)
\end{aligned}$$

Similarly, the ratio of the energy imbalance to the total energy input is evaluated for further discussions, which is given by:

$$\begin{aligned}
\Phi_{\text{cv}} &= \frac{|I_{\text{cv}}|}{\dot{q}_{\text{total}}} \times 100\% = \frac{|I_{\text{cv}}|}{\dot{q}_o + \dot{q}_l} \times 100\% \\
&= \frac{|I_{\text{cv}}|}{\dot{q}_g'' \Big|_{j=N} \times A_{o,\text{top}} + \dot{q}_g'' \Big|_{j=N_1} \times A_{l,\text{top}}} \times 100\% , \quad (4.73) \\
&= \frac{|I_{\text{cv}}|}{\dot{q}_g'' \Big|_{z=L_C+L_L} \times \left[\frac{\pi(D_o)^2}{4} \right] + \dot{q}_g'' \Big|_{z=L_L} \times \left\{ \frac{\pi[D^2 - (D_o)^2]}{4} \right\}} \times 100\%
\end{aligned}$$

4.7 Validation

In this work, three stages of validations are systematically performed based on the experiments [17,75]. In general, the computational domain replicates the experimental setup with necessary assumptions. Hexane and water are used as the liquid, and aluminum and copper are used as the object's material, whose properties are provided in Table 4.4.

Table 4.4: Properties of the liquid and objects (at 1 atm) [72,82,85-88].

Property	Unit	Hexane	Water	Aluminum	Copper
Density, ρ	kg/m ³	634.34	998	2600	8978
Specific heat, c	J/kg · K	2348	4182	1080	381
Thermal conductivity, k	W/m · K	0.1189	0.6	185	387.6
Heat of combustion, ΔH_c	J/kg	44700000	--	--	--
Heat of vaporization, ΔH_{vap}	J/kg	335000	2260000	--	--
Saturation temperature, T_{sat}	K	342	373.15	--	--

Based on experimental conditions, it needs to be pointed out that the properties [72,82,85-88] in Table 4.4 are taken at different temperatures, depending on the manners of heating and the temperature variation. Properties of water and copper are obtained at about 298 K (ambient temperature), those of hexane are obtained at about 320 K (average of the ambient temperature and the saturation temperature), and those of aluminum are obtained at about 773 K (average of the ambient temperature and the estimated flame temperature).

4.7.1 First-stage validation

As illustrated in Figure 4.8, for the first-stage validation [75], no objects are immersed in the center of a water pool, whose liquid level is maintained at a constant height by using a gravity feedback device. A radiant heat panel providing a constant heat flux of \dot{q}_g'' heats the liquid pool from the top. Details of the setup are shown in Table 4.5.

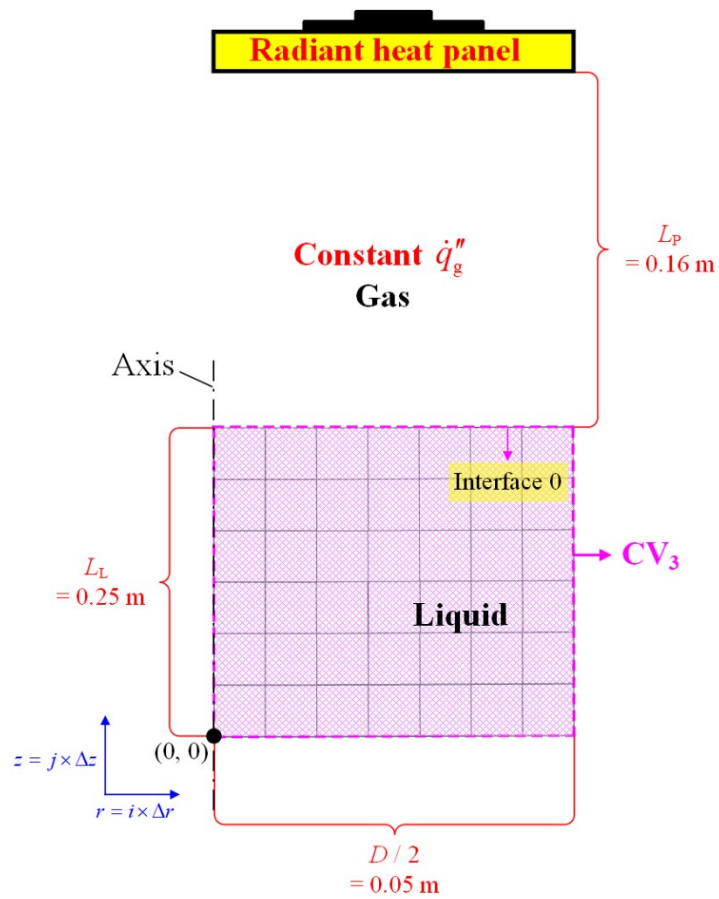


Figure 4.8: Schematic of the first-stage validation (not to scale), where no objects are immersed in a water pool having a constant height. The domain is heated by a radiant heat panel having a constant heat flux, \dot{q}_g'' , from the top.

Table 4.5: Detailed information of the setup for the first-stage validation.

Name	Unit	Value/description
Object	--	No
Liquid	--	Water
Heat input	--	Radiant heat panel
Heat flux, \dot{q}_g''	W/m ²	$70000 \times \zeta$
Distance between the radiant heat panel and liquid surface, L_P	m	0.16
Depth of liquid, L_L	m	0.25
Diameter of pool, D	m	0.1

It is noticed that the calculation of the effective heat flux received by the liquid pool, \dot{q}_g'' , includes a heat input coefficient, ζ , whose value is discussed in Section 5.1.

4.7.2 Second-stage validation

As illustrated in Figure 4.9, for the second-stage validation [75], a copper cylindrical object is immersed in a water pool, whose liquid level is maintained at a constant height by using a gravity feedback device. A radiant heat panel having a constant heat flux, \dot{q}_g'' , heats the liquid pool from the top. Details of the setup are shown in Table 4.6.

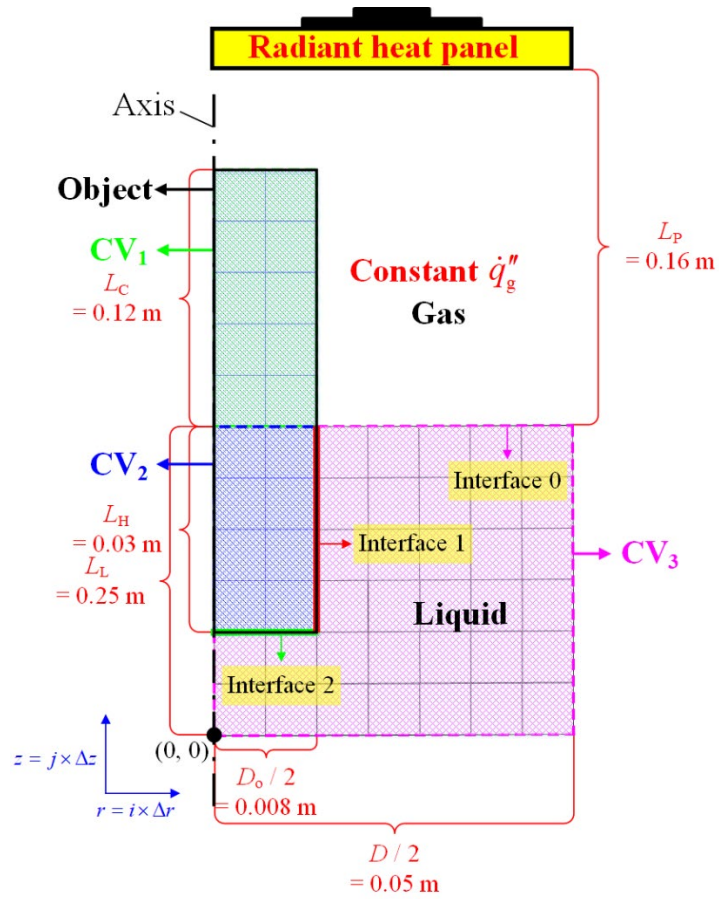


Figure 4.9: Schematic of the second-stage validation (not to scale), where a copper cylinder object is immersed in a water pool having a constant height. The domain is heated by a radiant heat panel having a constant heat flux, \dot{q}_g'' , from the top.

Table 4.6: Detailed information of the setup for the second-stage validation.

Name	Unit	Value/description
Object	--	Copper
Length of the collector, L_C	m	0.12
Length of the heater, L_H	m	0.03
Diameter of the collector, D_o	m	0.016
Liquid	--	Water
Heat input	--	Radiant heat panel
Heat flux, \dot{q}_g''	W/m ²	$70000 \times \zeta$
Distance between the radiant heat panel and liquid surface, L_P	m	0.16
Depth of liquid, L_L	m	0.25
Diameter of the pool, D	m	0.1

4.7.3 Third-stage validation

As illustrated in Figure 4.10, for the third-stage validation [17], an aluminum cylindrical object is immersed in the center of a hexane pool, whose liquid level is maintained at a constant height by using a gravity feedback device. Instead of using radiant heat panels, the hexane pool is ignited, such that the object is engulfed by a pool fire. Details of the setup are shown in Table 4.7.

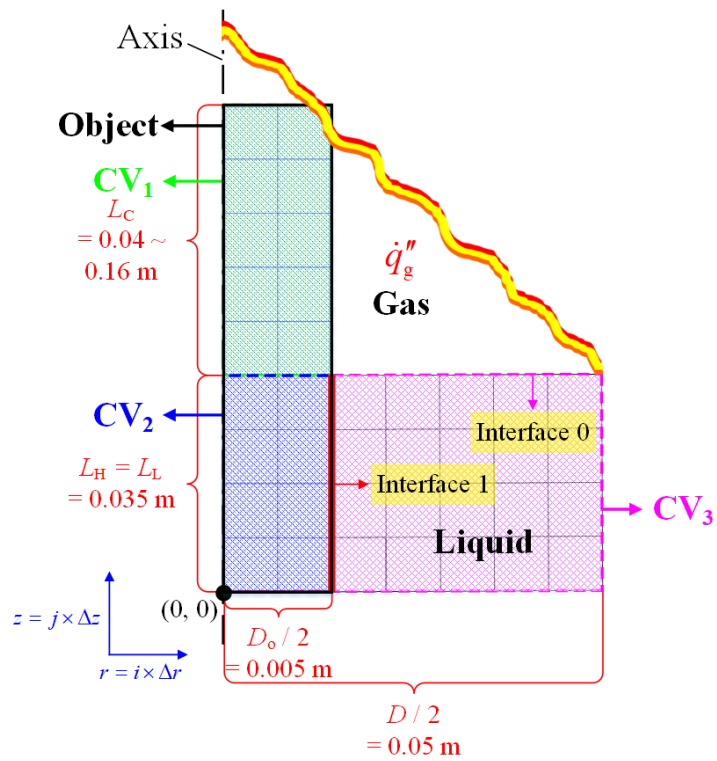


Figure 4.10: Schematic of the third-stage validation (not to scale), where an aluminum cylinder object is immersed in a hexane pool having a constant height. The domain is heated by the pool fire.

Table 4.7: Detailed information of the setup for the third-stage validation.

Name	Unit	Value/description
Object	--	Aluminum
Length of the collector, L_C	m	0.04-0.16
Length of the heater, L_H	m	0.035
Diameter of the collector, D_o	m	0.01
Liquid	--	Hexane
Heat input, \dot{q}_g''	--	Pool fire
Depth of liquid, L_L	m	0.035
Diameter of the pool, D	m	0.1

It is noticed that the object is immersed till the bottom surface of the container, and therefore, the boundary condition at interface 2 is absent, as discussed in Section 4.2.

Parametric studies have been conducted [17] by varying the length of collector, L_C , from 0.04 to 0.16 m in experiments; in accordance with this, the corresponding numerical simulations are performed for the validation, whose results are discussed in **Chapter 5**.

5 Numerical model results

This chapter discusses the results of stages of studies, including model verification (checking on convergence by analyzing the residues at interfaces and energy imbalance) and model validation (comparison of mass loss rate and temperature with experimental data). Subsequently, parametric studies exploring the effects of geometrical parameters of the immersed cylindrical object on pool fire burning rate are discussed by varying the object's length and diameter.

5.1 First-stage validation

The first-stage validation is conducted in a water pool having a constant liquid height, where no objects are immersed in the pool. The pool is heated using a constant heat flux heater as shown in Figure 4.8. The simulation time, $t = 2000$ s, is used based on the experimental data when the mass loss rate of liquid reaches a steady state. The model is verified and validated by comparing the mass loss rate of liquid and temperature in the liquid with experimental data.

5.1.1 Mass loss rate

In the initial stage, the mass loss rate of liquid is validated after checking the model input parameters, including grid size, time step, and heat input coefficient.

1. Grid size

As illustrated in Figure 4.8, the grid size is uniform and equal in radial and axial directions ($\Delta r = \Delta z$). In general, as the grid spacing is refined, the discretization errors are reduced for the diffusion terms, while the computational time is increased. Therefore, a convergence study is conducted to decide the optimal grid spacing to be used for further validations and parametric studies.

By taking the total time duration, $t = 2000$ s, time step, $\Delta t = 0.01$ s, and heat input coefficient, $\zeta = 0.55$, the influence of grid spacing on model results are investigated, where Δr (and Δz) = 0.0005 m, 0.001 m, 0.005 m, and 0.001 m. Variations of mass loss rate (MLR) and energy imbalance ratio along the grid spacing (Δr and Δz) are reported in Figure 5.1, indicating the grid convergence as for refined grid spacing. MLR on the left y-axis decreases for larger grid spacing of 1 cm, while the plot converges when the grid spacing is smaller than 0.001 m.

The energy imbalance ratio, Φ_{cv} , reported on the right y-axis is based on the whole CV, whose calculation is provided in Section 4.6.2. Values of energy imbalance ratio are small (around the magnitude of 10^{-6}) for all the cases, and so are their discrepancies at different grid spacing. However, it is to be noted that the imbalance is much lower for finer grids. The current model is thus verified, and convergence is noticed when the grid spacing is no larger than 0.001 m. In terms of this, grid spacing, Δr (and Δz) = 0.001 m is used for the following first-stage validation.

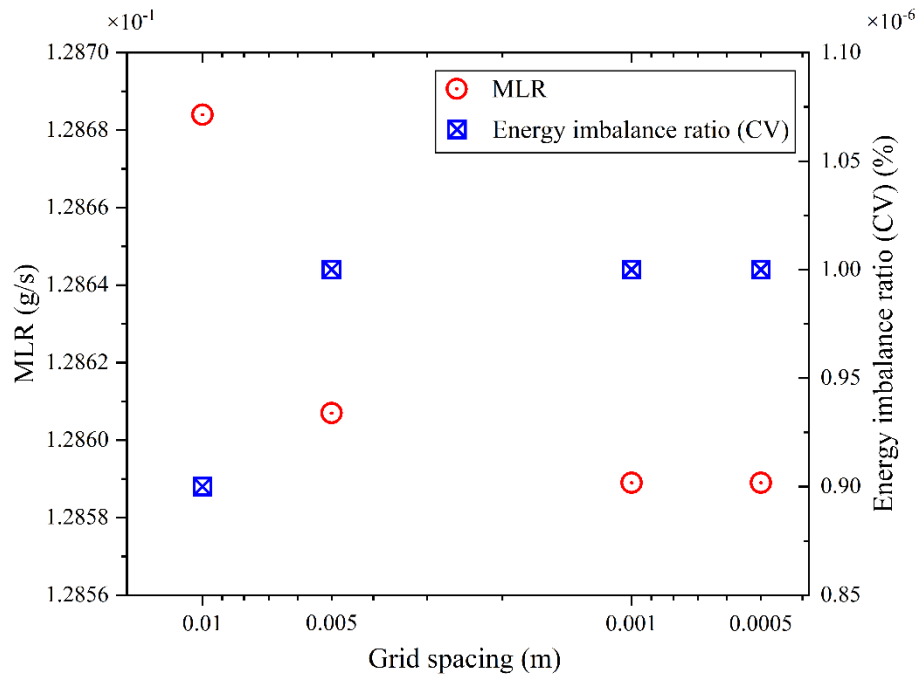


Figure 5.1: The influence of grid spacing on the model convergence, where the x-axis (in log10 scale) denotes the decreasing grid spacing, the left y-axis and blue square notations denote the mass loss rate, and the right y-axis and red circle notations denote the energy imbalance ratio applied to the whole CV.

2. Time step

The time step, Δt , is kept constant throughout the simulation. In general, as the time step is reduced, the discretization errors are reduced for the time evolution term, while the computational time is increased. Therefore, a time step effectiveness study is conducted to decide the optimal time step to be used for further validations and parametric studies.

By taking the duration, $t = 2000$ s, grid spacing, Δr (and Δz) = 0.001 m, and heat input coefficient, $\zeta = 0.55$, the influence of time step on model results are investigated, by varying Δt as 0.05 s, 0.01 s, and 0.002 s. Variations of MLR and energy imbalance ratio as a function of time

step are reported in Figure 5.2. MLR on the left y-axis is constant for the cases investigated. Values of energy imbalance ratio, Φ_{cv} , are small (around the magnitude of 10^{-6}) throughout the cases, indicating proper convergence. Φ_{cv} decreases with reducing Δt , and convergence is noticed when $\Delta t \leq 0.01$ s. In terms of this, time step, $\Delta t = 0.01$ s is used for the following first-stage validation.

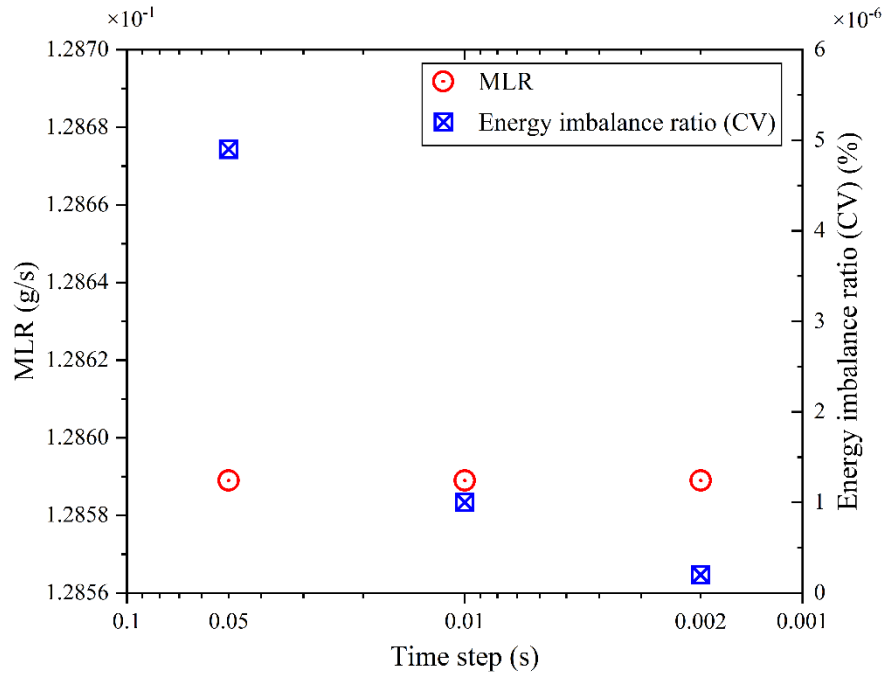


Figure 5.2: The influence of time step on the model convergence, where the x-axis denotes the decreasing time step (in log10 scale), the left y-axis and blue square notations denote the mass loss rate, and the right y-axis and red circle notations denote the energy imbalance ratio applied to the whole CV.

3. Heat input Coefficient

The traditional method to obtain the heat input coefficient, ζ , is complex. This requires the coupling of heat convection and radiation mechanisms. For example, the evaluation of the radiation view factor between the heat panel and the fuel surface should be conducted. To simplify this, ζ is

considered as a constant to be used for the first- and second-stages validations. This is reasonable because the heat input provided by the radiant heat panel is constant. Further, the setup and the environment are almost identical except for the immersed object. Furthermore, the primary purpose of the preliminary validations is to ensure the model's robustness and model the physical behavior.

For this study, ζ is determined based on the experimental data [75], for a time duration, $t = 2000$ s, grid spacing, Δr (and Δz) = 0.001 m, and time step, $\Delta t = 0.01$ s. As depicted in Figure 5.3, the experimental MLR (black solid) increases sharply as time proceeds at the beginning; later on, it reaches a steady state at about $t = 900$ s. The numerical curves share a similar trend, while the corresponding steady state time instants are reached earlier at about $t = 300$ s. As the focus of the current study is on the steady state, the discussions are presented to the scenarios after $t = 900$ s. Different heat input coefficients are studied, including $\zeta = 0.45$ (red dashed), 0.55 (blue dash-dotted), and 0.65 (red dotted). MLR is noticed to increase with increasing ζ . It is noted that when $\zeta = 0.55$, the numerical MLR matches well with the experimental data. Therefore, the effective heat flux received by the liquid pool is written as: $\dot{q}_g'' = 0.55 \times 70 \text{ kW/m}^2$.

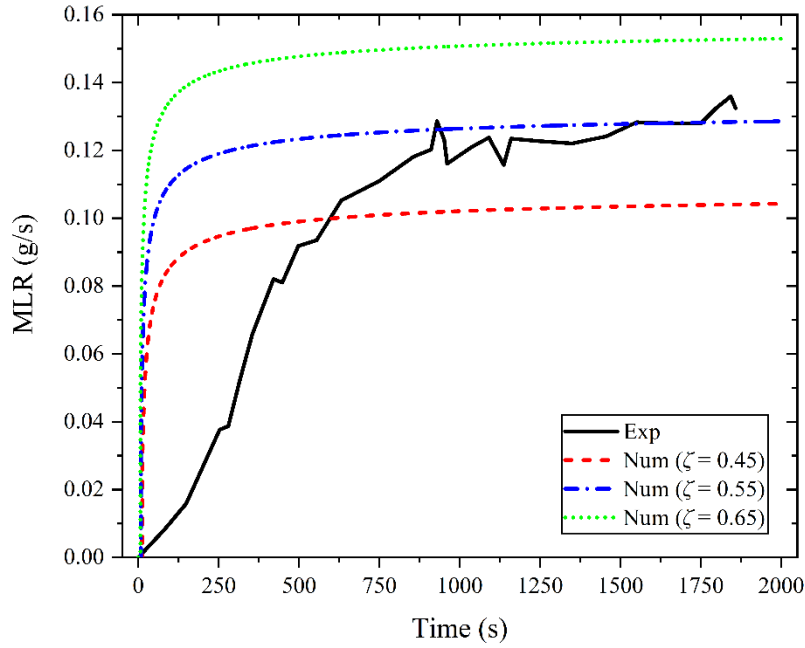


Figure 5.3: The variation of MLR with time, where heat input coefficient, $\zeta = 0.45$ (red dashed), 0.55 (blue dash-dotted), and 0.65 (green dotted). The experimental data (black solid) is digitized [75] by removing the initial 250 s with fluctuations.

Therefore, the first-stage model is validated by comparing mass loss rate, and the model inputs used for further discussions in this section are summarized in Table 5.1.

Table 5.1: Model inputs for the first-stage validation.

Name	Unit	Value
Grid size, Δr and Δz	m	0.001
Time duration, t	s	2000
Time step, Δt	s	0.01
Heat input coefficient, ζ	--	0.55

5.1.2 Temperature

Comparisons of the liquid temperature are shown in Figure 5.4, where the temperature is measured at the heights $z = 0.24$ m, 0.245 m, and 0.25 m from the bottom of the container [75]. The curvature of the numerical curve matches quite well with the experimental one, indicating similar values of the temperature gradient. The discrepancies between the two curves are probably caused by the liquid perturbation, model assumptions, and measurement deviations.

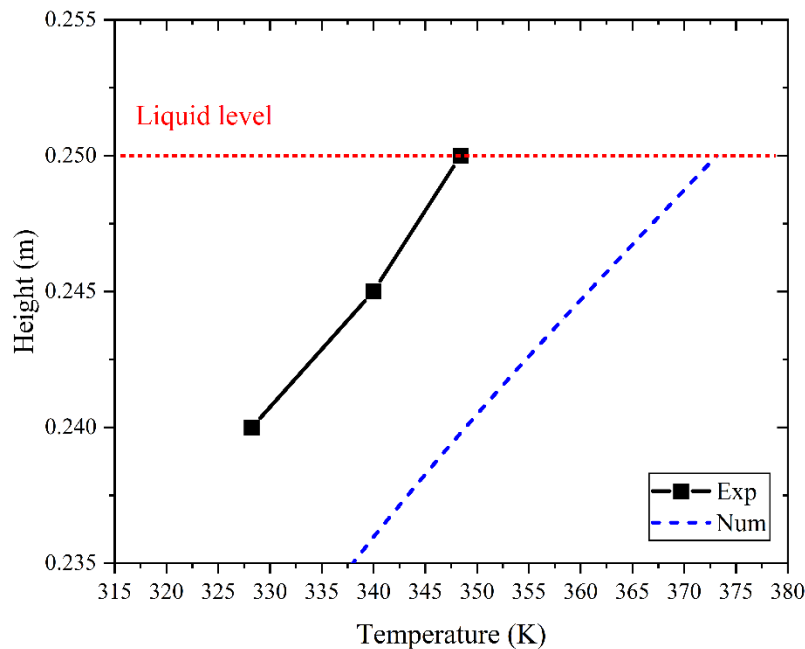


Figure 5.4: Liquid temperature along height at steady state, where the temperature is reported at $r = 0.03$ m, the black square denotes the experimental data from measurements, the blue dashed curve denotes the numerical results, and the red dotted line labels the liquid level.

The temperature contour plot in the liquid region is depicted in Figure 5.5. It is reasonable that the liquid temperature attains the saturation point, $T_{\text{sat}} = 373.15$ K at the liquid surface, and it

is the ambient temperature, $T_{\text{amb}} = 298.15 \text{ K}$ at the bottom. It is also intuitive that the temperature is identical at the same height, as the fuel surface is uniformly heated. Therefore, the temperature gradient is validated well with experimental measurements by assuming a constant value for heat input coefficient, $\zeta = 0.55$.

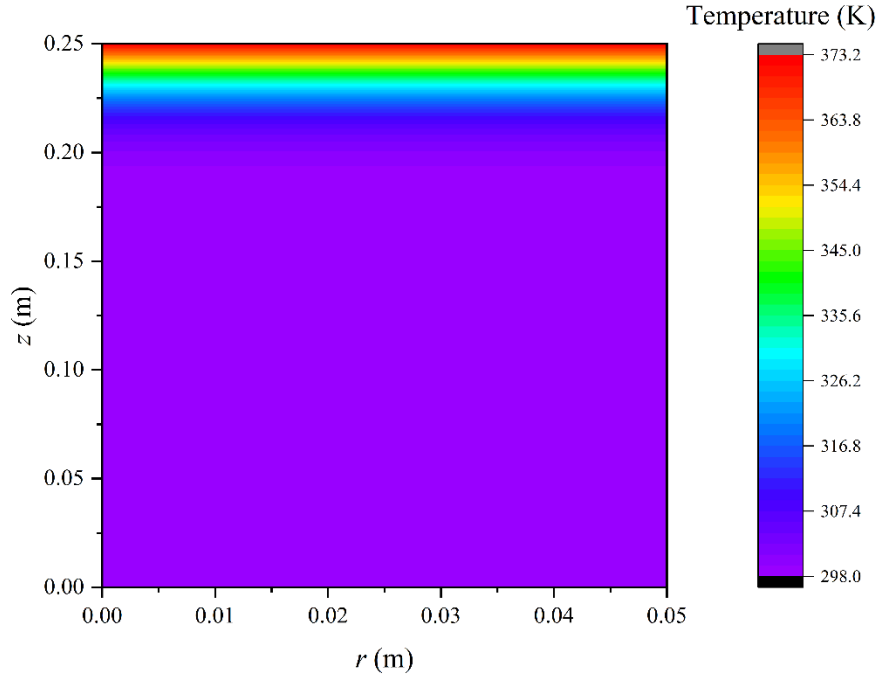


Figure 5.5: Temperature contour in liquid at $t = 2000 \text{ s}$, where the temperature ranges from 298.15 K to 373.15 K.

5.2 Second-stage validation

As shown in Figure 4.9, the second-stage validation is conducted in a water pool with a constant liquid height, where a copper cylindrical object is immersed. Based on the experimental data, the simulation time, $t = 2000 \text{ s}$, is used, when the mass loss rate of liquid reaches a steady state. Similarly, the model is verified and validated via discussions of mass loss rate of liquid and temperature in object and liquid.

Based on the results of Section 5.1, the model inputs used for this section are summarized in Table 5.2.

Table 5.2: Model inputs for the second-stage validation.

Name	Unit	Value
Grid size, Δr and Δz	m	0.0005
Time duration, t	s	2000
Time step, Δt	s	0.00025
Heat input coefficient, ζ	--	0.55

As indicated in Table 5.2, values of t and ζ are the same as those used for the first-stage validation, while Δr (and Δz) decreases slightly to accommodate enough cells in the immersed object that has a small diameter of $D_o = 0.016$ m. Δt is reduced accordingly to ensure the grid Fourier number of object, λ_o , to be used for the temperature calculation as explained in the Eq. (4.22).

5.2.1 Model verification

Model verification is discussed by implementing the model inputs shown in Table 5.2, including the residues at interfaces and energy imbalance.

The maximum residues at interfaces 1 and 2 are depicted in Figure 5.6, along with the corresponding locations. The information of interfaces is depicted in Figure 4.9, and the calculations of the residues are provided in Section 4.5. The residues indicate the error in evaluating the interface temperature from heat flux balance instead of the governing equation. Values are noticed to vary as time proceeds due to the temperature evolves in liquid and object. At

$t = 2000$ s, the maximum residue is $\gamma_o \approx 0.064\%$, which is the one located at (0.008,0.25), calculated at the object side of interface 1. Such a small residual value indicates that the procedure to evaluate the interface temperature using heat flux balance is justified.

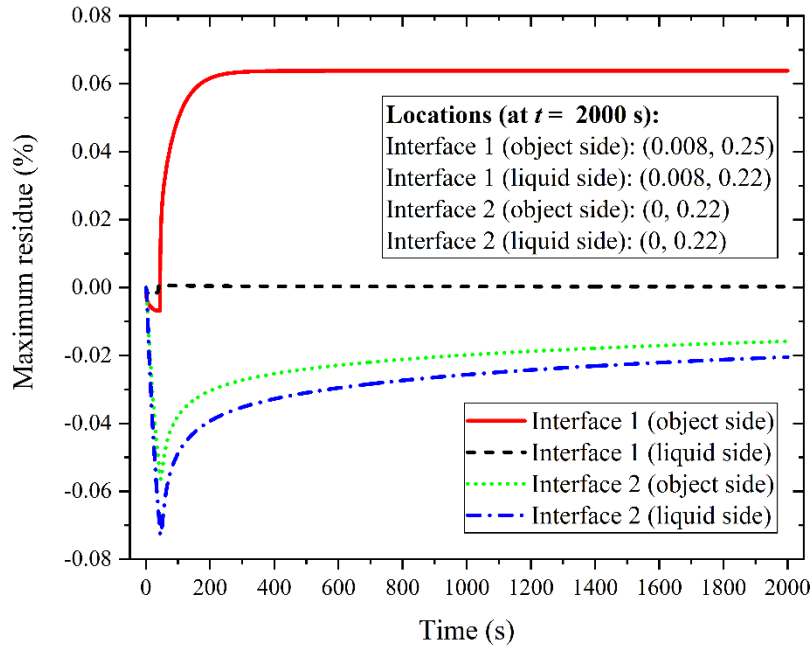


Figure 5.6: Maximum residues at interfaces 1 (red solid and black dashed) and 2 (green dotted and blue dash-dotted) calculated at the object and liquid sides as a function of time, whose locations (at $t = 2000$ s) are labeled.

The energy imbalance ratio as a function of time is depicted in Figure 5.7, including the values reported per the maximum among the cells and the whole CV, whose calculations are discussed in Section 4.6. The variation of imbalance ratios fluctuates at the beginning, while they become comparatively steady after about 600 s. The maximum imbalance ratio among individual cells is $\Phi_{\text{cell,max}} \approx 2.43\%$ located at (0.008, 0.25), which is a corner node in the domain. The imbalance

value of the whole CV is $\Phi_{cv} \approx 0.27\%$. These small values for imbalance show that energy is conserved in the CV.

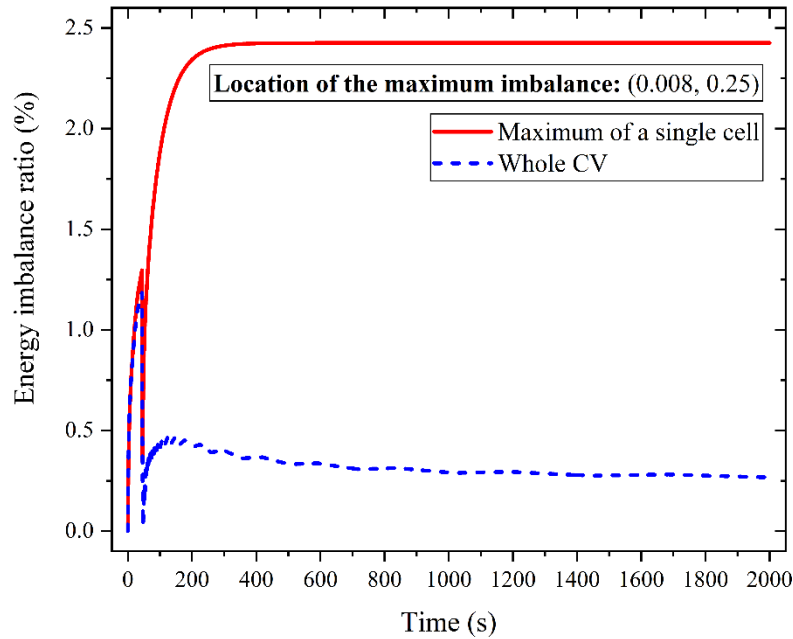


Figure 5.7: Energy imbalance ratio as a function of time, consisting of the maximum value among individual cells (red solid) and the one applied to the whole CV (blue dashed).

5.2.2 Mass loss rate

In this stage, the mass loss rate of liquid is validated by implementing the model inputs shown in Table 5.2.

As depicted in Figure 5.8, by using the same heat input coefficient, $\zeta = 0.55$, small discrepancies are observed in MLR at a steady state. It may be because of the variation of ζ after an object is immersed in the liquid. It may also be because the experimental MLR shows an increasing trend, as indicated towards the end of its curve. However, the overall effect of an immersed object in enhancing the mass loss rate by about 1.6 times as compared to the baseline

case is predicted well by using the model. Therefore, the second-stage validation can be assumed to be validated for mass loss rate.

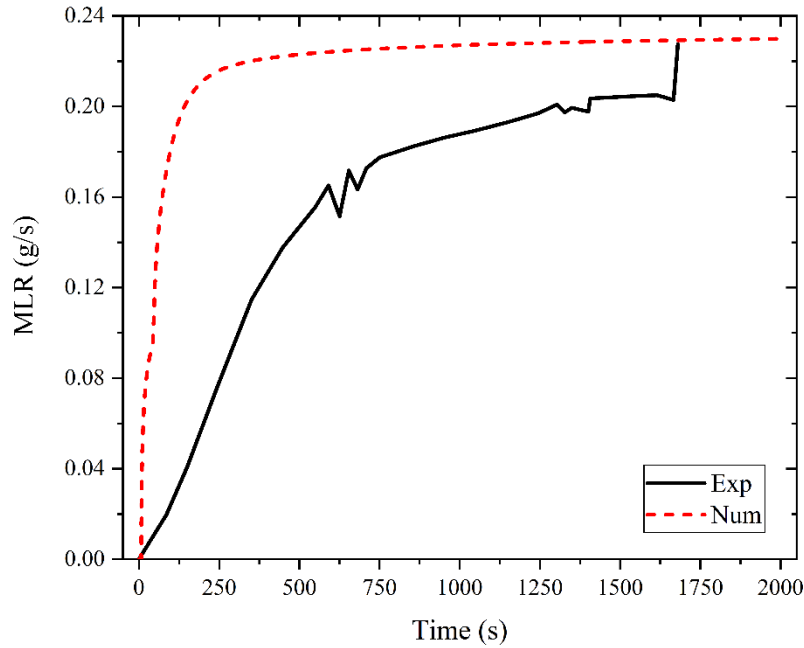


Figure 5.8: The variation of MLR as a function of time, consisting of the experimental data (black solid) digitized [75] by removing the initial 250 s with fluctuations and numerical data from the model.

Details of the MLR from interfaces are shown in Figure 5.9. It is observed that most of the vaporization mass generates from interface 0 at the liquid surface, while there is rare vaporization from interface 2 at the bottom of the object. This is because the bottom of the object is not as heated as the side of the object. Such results are reasonable because the object's size is much smaller than that of the liquid pool so that the liquid absorbs comparatively more heat via its larger surface. However, it is noticeable that the enhancement in the MLR due to the immersed object accounts for more than 36% of the total mass loss rate.

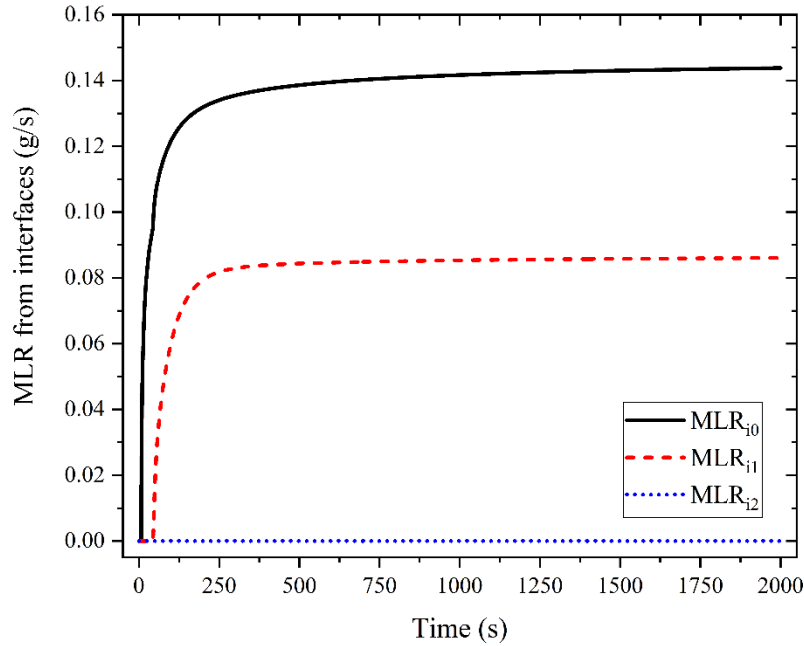


Figure 5.9: The variation of the MLR from interfaces as a function of time. For subscripts, “i0” denotes interface 0 representing the liquid surface (black solid), “i1” denotes interface 1 (red dashed), and “i2” denotes interface 2 (blue dotted).

5.2.3 Temperature

Comparisons of the liquid temperature are shown in Figure 5.10, where the temperature is measured at the heights, $z = 0.24$ m, 0.245 m, and 0.25 m from the bottom of the container [75]. By excluding the temperature measured at the height of 0.245 m considering the liquid perturbation and measurement deviations, the curvature of the numerical curve matches well with the experimental one, indicating similar values of the temperature gradient.

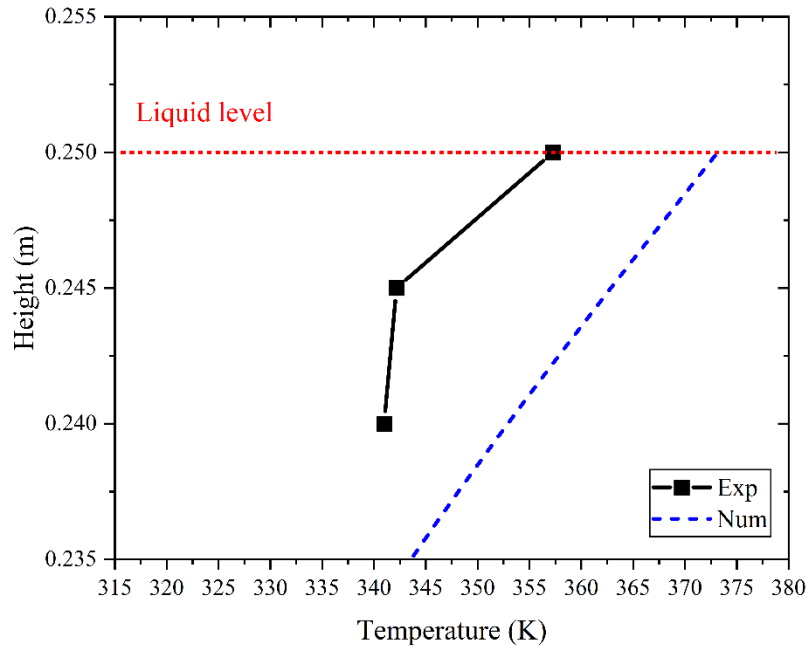


Figure 5.10: Liquid temperature along height at steady state, where the temperature is reported at $r = 0.03$ m, the black square denotes the experimental data from measurements, the blue dashed curve denotes the numerical results, and the red dotted line labels the liquid level.

The temperature contour plot in the liquid and object is depicted in Figure 5.11. The liquid surface reaches the saturation point, $T_{\text{sat}} = 373.15$ K. The bottom of the liquid almost keeps the ambient temperature, $T_{\text{amb}} = 298.15$ K. Temperature increases axially along with the object as it is heated from the top and the sides. In the radial direction, the temperature reduces away from the immersed object. In the object, the maximum temperature appears at the top of the collector, which is around 570.0 K. It should also be noted that the interface temperature is limited to the saturation temperature of the liquid. This limitation leads to heat flux imbalance at the interfaces and this

excess heat is used to evaluate the mass loss rate at interfaces (as discussed in Section 4.4.4). In general, the second-stage validation is validated via temperature.

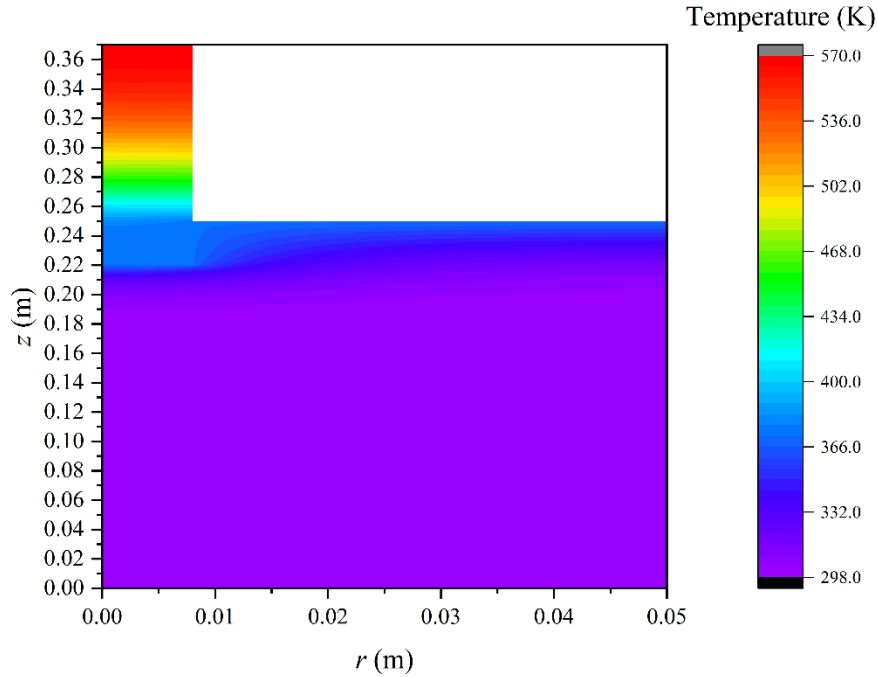


Figure 5.11: Temperature contour in liquid and object at $t = 2000$ s, where the temperature ranges from 298.15 K to 570.0 K.

5.3 Third-stage validation

As shown in Figure 4.10, the third-stage validation is conducted in a hexane pool maintaining a constant liquid height, where a cylindrical aluminum object is immersed in the liquid. The simulation time, $t = 600$ s, is chosen based on the experimental data when the mass loss rate of liquid reaches a steady state. Similar to the previous two stages, the model is verified and validated through discussions of mass loss rate of liquid and temperature in object and liquid.

Based on the results of Sections 5.1 and 5.2, the model inputs used for this section are summarized in Table 5.3.

Table 5.3: Model inputs for the third-stage validation.

Name	Unit	Value
Grid size, Δr and Δz	m	0.001
Time duration, t	s	600
Time step, Δt	s	0.002

As indicated in Table 5.3, Δr (and Δz) is slightly increased to 0.001 m to save the computational time, and hence, residue and imbalance need to be checked before the validation; Δt decreases accordingly, to ensure the grid Fourier number of object, λ_o , and meanwhile to save the computational time. The time duration t decreases according to the experimental design. It is noticed that ζ is no longer required because a pool fire is implemented as the heat input instead of a radiant heat panel, and model inputs in the flame region are discussed in Section 4.2.2.

5.3.1 Model verification

Model verification is discussed by implementing the model inputs shown in Table 5.3, including the residues at interface 1 (interface 2 is absent in this stage) and energy imbalance.

At $t = 600$ s, the maximum residues at interface 1 for different collector lengths, L_C , are depicted in Figure 5.12. The residues calculated at the object side, γ_o , are larger than those calculated at the liquid side, γ_l . However, all residues are quite small, indicating that the procedure to limit the temperature at interface 1 is applicable from the perspective of model stability. γ_o

increases with increased collector length, L_C , which could be due to higher heat collected by the domain through the elongated object.

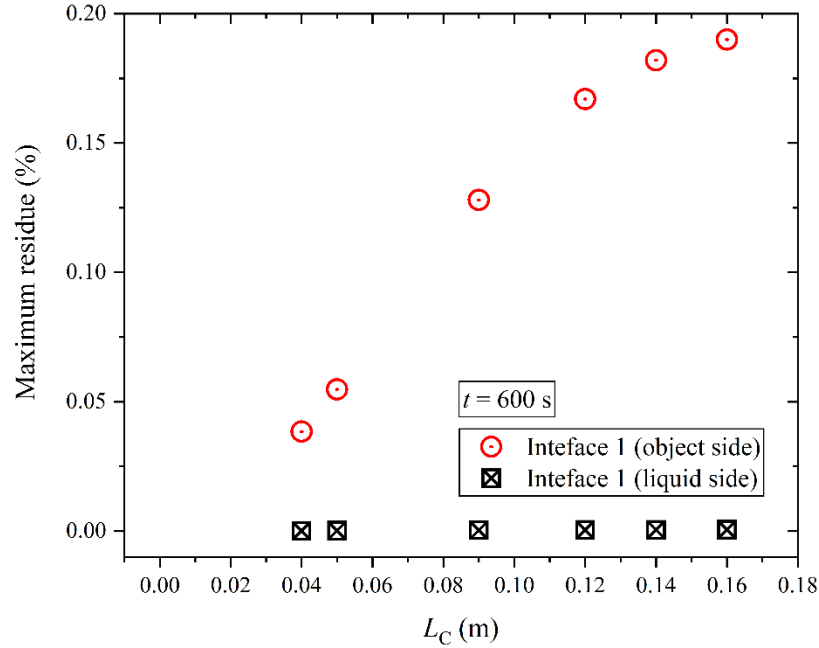


Figure 5.12: Maximum residue at different L_C at $t = 600$ s, which are calculated from object (red circle) and liquid (black square) sides.

At $t = 600$ s, the energy imbalance ratios at different L_C are depicted in Figure 5.13, including the values reported per the maximum among individual cells and in the whole CV. Both maximum imbalance ratio of a single cell, $\Phi_{\text{cell,max}}$, and that of the whole CV, Φ_{cv} increase with an increase in L_C , while such increase later tends to slow down at higher values of L_C . The maximum ratio, $\Phi_{\text{cell,max}} \approx 6.5\%$ is comparatively small, indicating that the current model is verified.

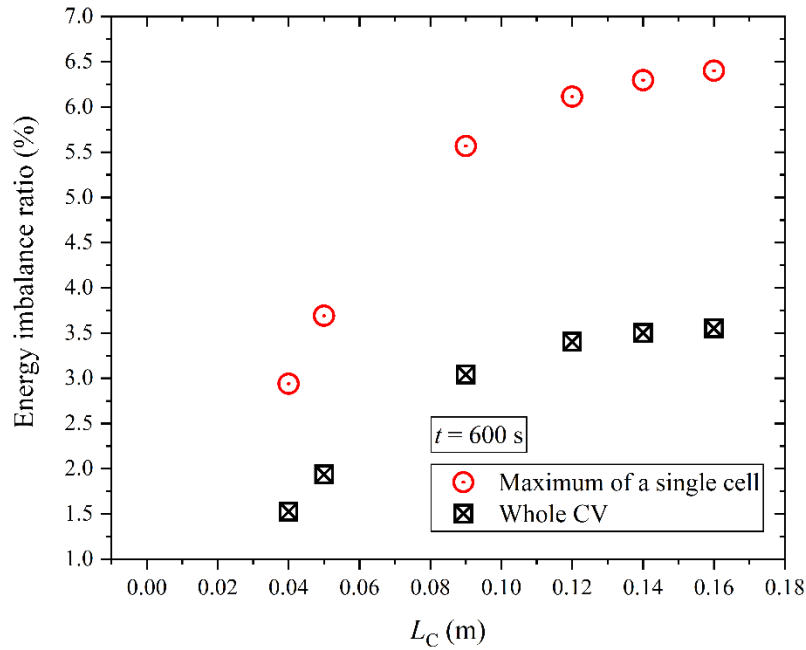


Figure 5.13: Energy imbalance ratio at different L_C at $t = 600$ s, including the maximum value among individual cells (red circle) and the one applied to the whole CV (black square).

5.3.2 Mass loss rate

In this stage, the mass loss rate of liquid is validated by implementing the model inputs shown in Table 5.3.

As depicted in Figure 5.14, predictions of MLR by the model generally match well with the experimental data. The experimental MLR first increases with an increase in L_C , and it reaches a local maximum at $L_C = 0.14$ m. However, the numerical MLR monotonically increases with the increase of L_C . The situation at $L_C = 0.16$ m needs further attention as explained in the following sections. But due to the small discrepancy at that point, the second-stage validation is validated via mass loss rate.

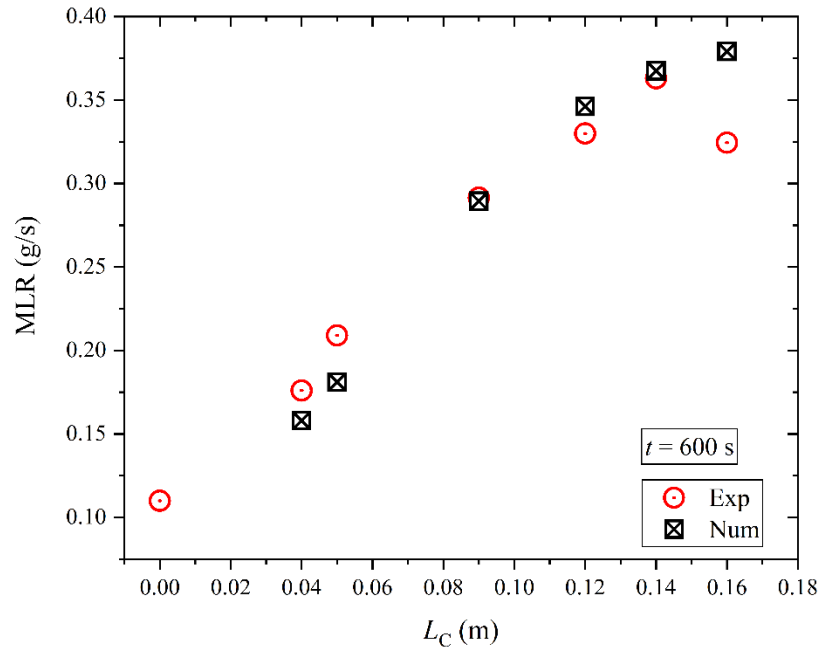


Figure 5.14: MLR at different L_C at $t = 600$ s, including the experimental data (red circle) from the reference [17] and numerical data (black square) from the model.

Details of the numerical MLR from interfaces are shown in Figure 5.15, for $L_C = 0.04$ m, 0.05 m, 0.09 m, 0.12 m, 0.14 m, and 0.16 m. When $L_C < 0.09$ m, MLR is dominated by the portion coming from interface 0 at the liquid surface. When L_C is larger, MLR is dominated by the portion coming from interface 1. This indicates that the immersed object plays a more important role when L_C is high enough to collect heat from the flame.

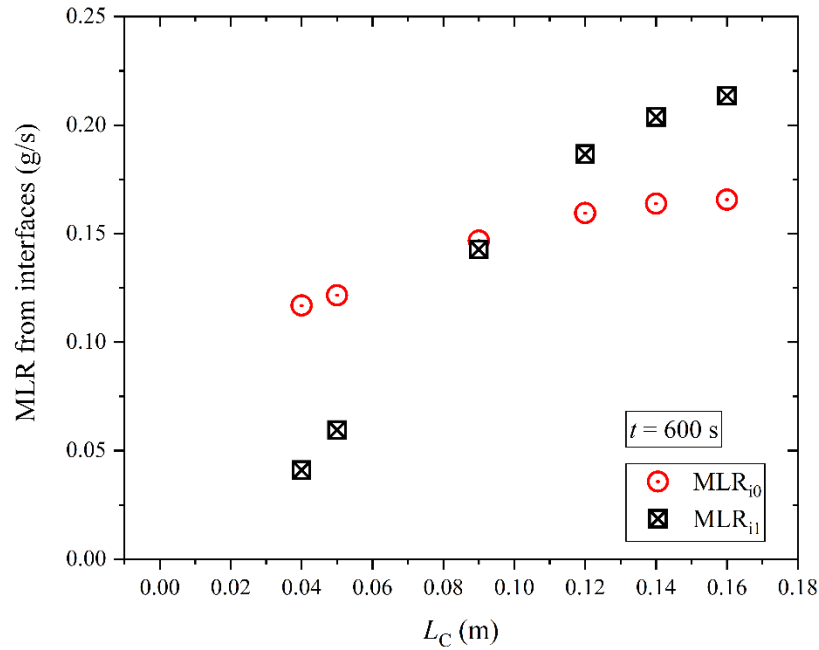


Figure 5.15: The variation of the MLR from interfaces at different L_C at $t = 600$ s. For subscripts, “i0” denotes interface 0 representing the liquid surface (red circle), and “i1” denotes interface 1 (black square).

5.3.3 Temperature

At $t = 600$ s, comparisons of the object surface temperature are shown in Figure 5.16, where discrepancies are noticed between the experimental and numerical data. This is because of the assumptions used for the model and the difficulties in measuring the object surface temperature. For example, 1. because of the temperature limit in the heater region, the numerical result of the lower object temperature is impacted; 2. the experimental temperature is measured by immersing the tip of the thermocouple in the object, therefore, proper calibrations are required; 3. the measurement is influenced by the surrounding flickering flame’s higher temperature.

Meanwhile, the flame temperature is reported, whose trend matches well with that of the object surface temperature with a given difference. Furthermore, recalling the physical structure of a flame, where the maximum temperature occurs in the flame region, it is seen that the object is fully engulfed by the flame when $L_C = 0.14$ m.

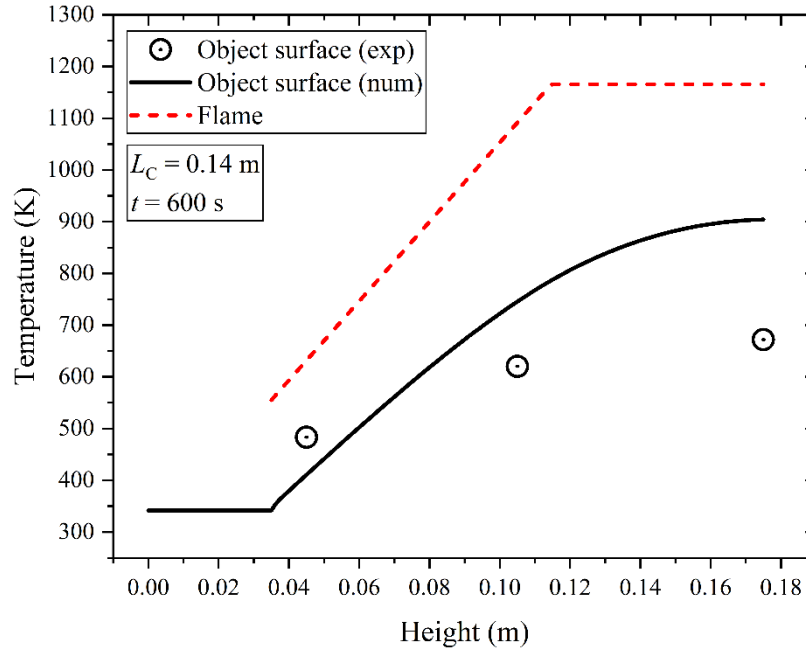
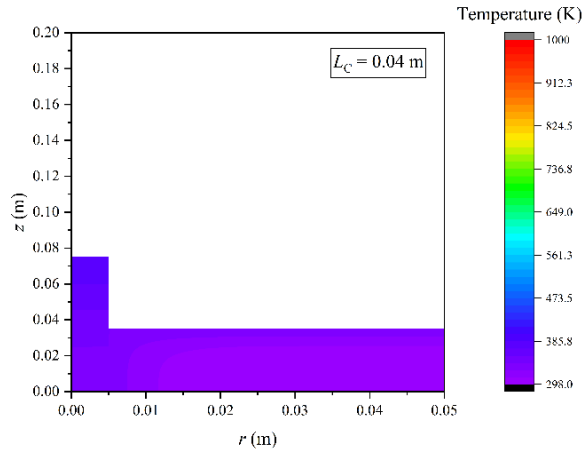
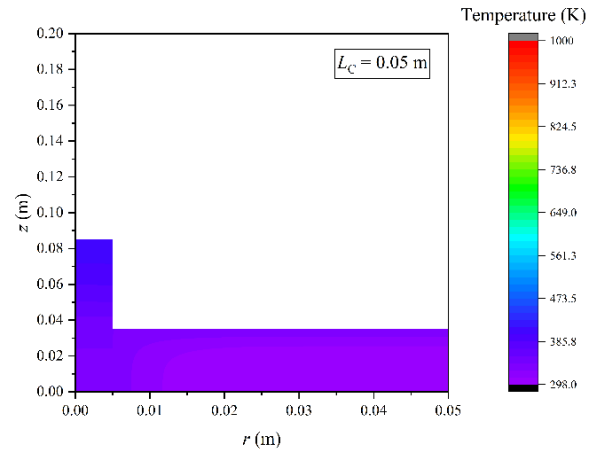


Figure 5.16: Temperature of the object surface ($r = 0.05$ m) and flame along the height, where $t = 600$ s, the length of the heater is $L_H = 0.035$ m, and the length of the object is $L_C = 0.14$ m.

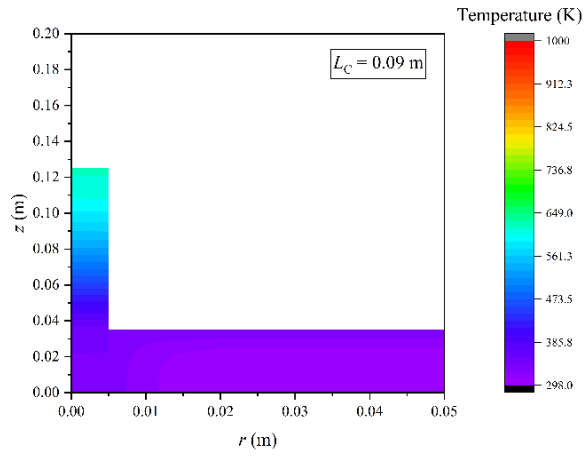
The temperature contour plots in liquid and object are depicted in Figure 5.17, where $L_C = 0.14$ - 0.16 m. The maximum temperature of the object increases with an increase in L_C , which corresponds to a monotonical increase of MLR. In general, the third-stage validation can be considered validated via temperature data.



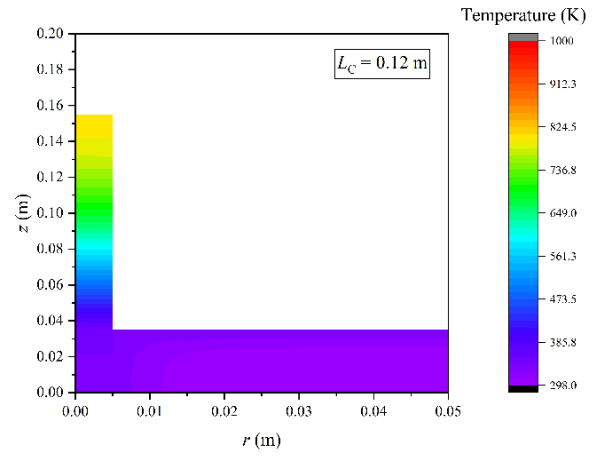
(a)



(b)



(c)



(d)

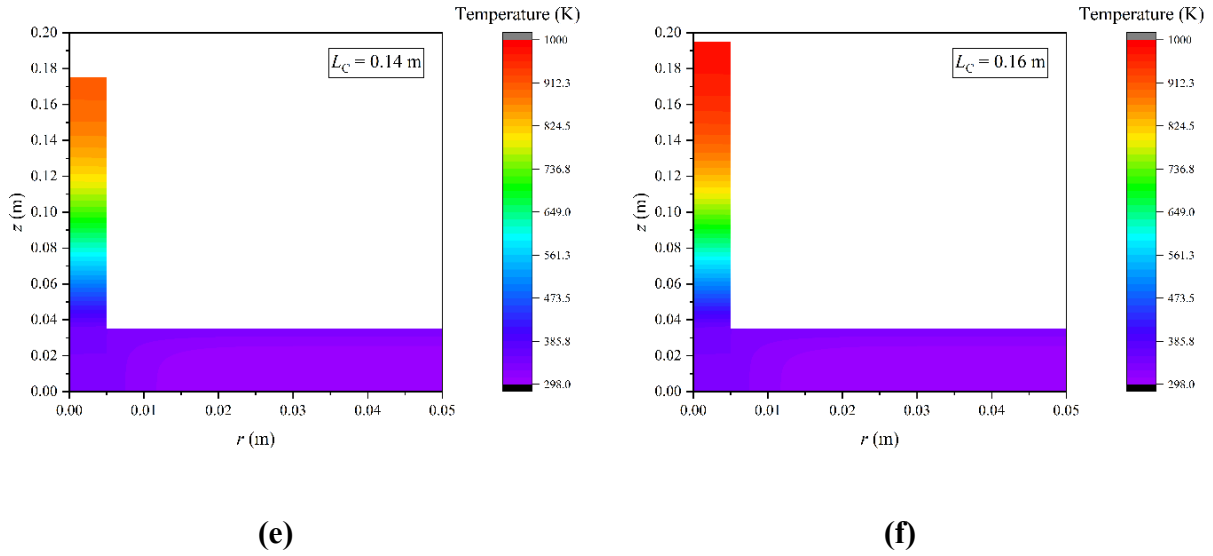


Figure 5.17: Temperature contour in liquid and object at $t = 600$ s, where $L_C = 0.04$ m, 0.05 m, 0.09 m, 0.12 m, 0.14 m, and 0.16 m, and the temperature bar ranges from 298.15 K to 1000.0 K.

5.3.4 Flame height

The flame height at different L_C is illustrated in Figure 5.18, where the tendency of the numerical data matches well with that depicted in the experimental images and the corresponding measurements [17]. Furthermore, the object is fully engulfed by the flame for all cases investigated. Such phenomena support the previous finding that the numerical MLR and maximum temperature monotonically increase as L_C increases from 0.04 to 0.16 m. During experiments, the flame tilts because of the implementation of the ventilation hood, which would have slight discrepancies in the measured MLR and temperature for the tallest collector case. Therefore, it is possible to have small differences between the experimental and numerical data. Thus, the third-stage validation can be considered as validated via flame height.

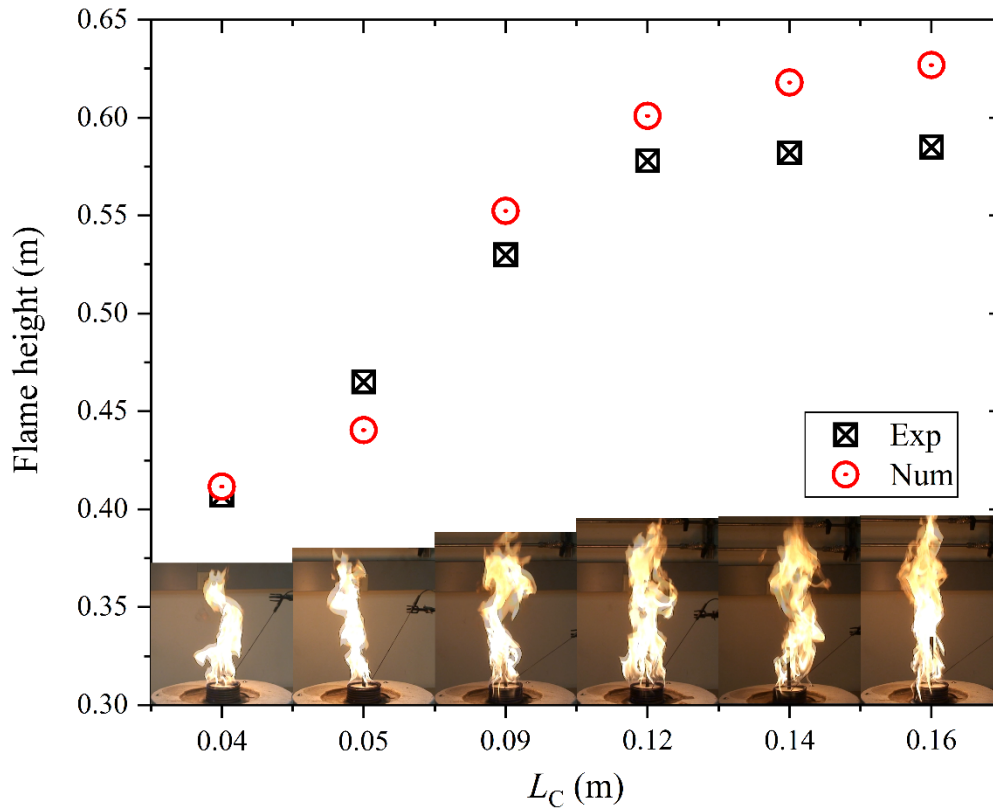


Figure 5.18: Flame height at different L_C , where the numerical data is obtained at $t = 600$ s, and the corresponding images are taken during experiments.

5.4 First-stage parametric study (L_C)

Similar to the experimental works exploring the influence of the object configurations on fires, two stages of parametric studies are performed using numerical simulations. The first parametric study is on the influence of the object length, L_C , on a liquid hexane pool fire. The primary purpose of this study is to estimate an optimal collector length, L_C , that facilitates faster and more efficient burning.

According to the numerical results presented in Figure 5.14, MLR monotonically increases as L_C increases from 0 to 0.16 m, which indicates that an optimal L_C does not exist in the range. Also, the value of L_C is much smaller compared to the flame height (about 0.6 m), as reported in Figure 5.18. Therefore, the range of L_C is expanded to that from 0 to 1 m. Other model inputs are kept the same as used in Section 5.3, including the grid size, Δr , Δz , the time duration, t , and the time step, Δt .

5.4.1 Model verification

As reported in Figure 5.19, the maximum residues at interface 1 are shown for different L_C at $t = 600$ s. The residues are calculated at the object side, γ_o , as well as at the liquid side, γ_l . As L_C increases, γ_o first increases to the maximum around $L_C = 0.25$ m, after that, the values are almost constant at around 0.195% till $L_C = 1$ m. The variable γ_l remains almost constant and has a small value (around 0%) compared to γ_o . As the maximum residue is approximately 0.2%, all residues are considered relatively small, indicating that the procedure to limit the temperature at interface 1 is applicable.

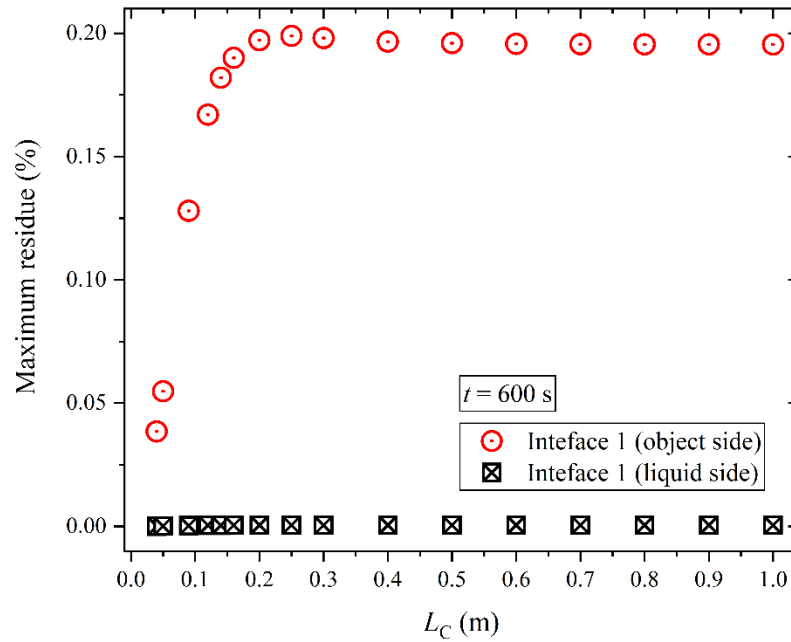


Figure 5.19: Maximum residue at different L_C at $t = 600$ s, where values of residue are calculated from object (red circle) and liquid (black square) sides, respectively, and $L_C = 0.04$ m, 0.05 m, 0.09 m, 0.12 m, 0.14 m, 0.16 m, 0.2 m, 0.25 m, 0.3 m, 0.4 m, 0.5 m, 0.6 m, 0.7 m, 0.8 m, 0.9 m, and 1 m.

The energy imbalance ratios at different L_C are presented in Figure 5.20, including the ratios calculated from the maximum among individual cells and that from the whole CV. The tendency of the two scatter plots is similar to each other: at first, ratios increase rapidly with the increase of L_C up to around 0.25 m, and subsequently, ratios decrease gradually as L_C further increases from 0.25 to 1 m. The maximum values are obtained at $L_C = 0.25$ m, where the maximum ratio among individual cells, $\Phi_{\text{cell,max}}$, is about 6.5%, and the ratio from the whole CV, Φ_{cv} , is about 3.6%. All

the ratios reported are quite small, and it is reasonable that $\Phi_{\text{cell,max}}$ is larger than Φ_{cv} at each L_C .

The model can therefore be considered as verified.

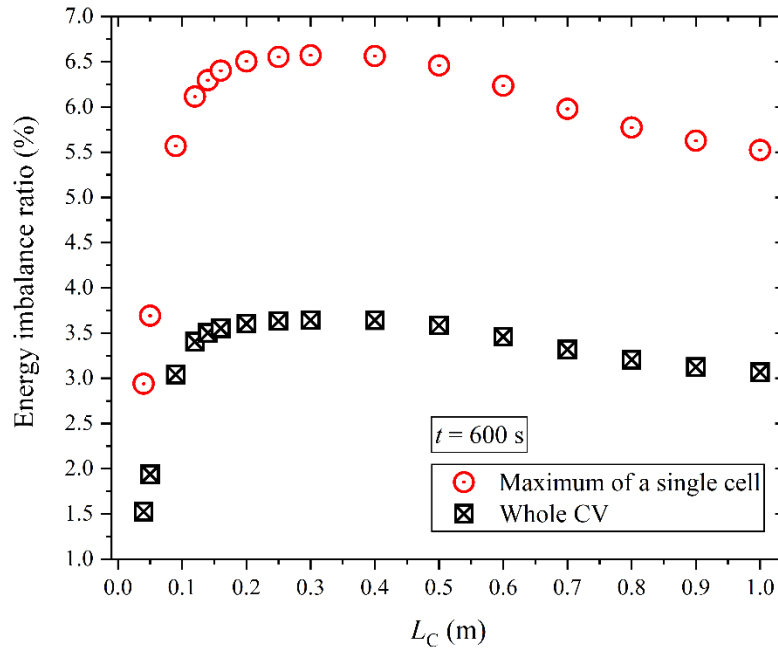


Figure 5.20: Energy imbalance ratio at different L_C at $t = 600$ s, including the maximum value among individual cells (red circle) and the one applied to the whole CV (black square).

5.4.2 Mass loss rate

Comparisons of the MLR from experiments and numerical models are shown in Figure 5.21, where $L_C = 0$ m denotes the baseline case without immersed objects. When L_C is kept in the range of 0.04-0.16 m, the numerical data generally matches well with the experimental ones as discussed in Section 5.3.2. When L_C is varied in a range of 0.2-1 m, the corresponding experimental data is not available. The numerical MLR first increases to reach the maximum value (about 0.39 g/s) at $L_C = 0.25$ m, and it saturates at around 0.37 g/s for higher L_C values. Therefore, there can be about

a 3.5 times increase in MLR over the baseline case (0.11 g/s), when an immersed object is utilized. The configuration of $L_C = 0.25$ m relates to the maximum in the residue, imbalance ratio, and MLR, indicating its potential importance to the practical design.

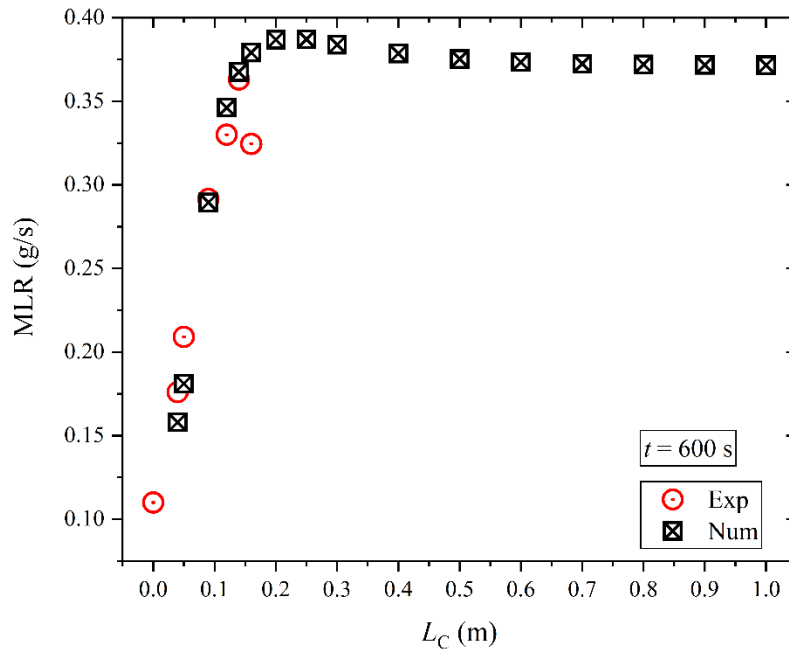


Figure 5.21: MLR at different L_C at $t = 600$ s, including the experimental data (red circle) from the reference [17] and numerical data (black square) from the model.

Numerical MLR results from interfaces are shown in Figure 5.22, where L_C is in the range of 0.04-1 m. MLR is initially dominated by its value at the liquid surface (interface 0), when $L_C < 0.09$ m. It is later dominated by its value at interface 1, when $L_C \geq 0.12$ m. This indicates that the immersed object plays a significant role when L_C is increased to a threshold height. The MLR at interface 1 keeps increasing as an increase in L_C , and attains the maximum MLR is at $L_C = 0.25$ m, indicating the optimal length for L_C .

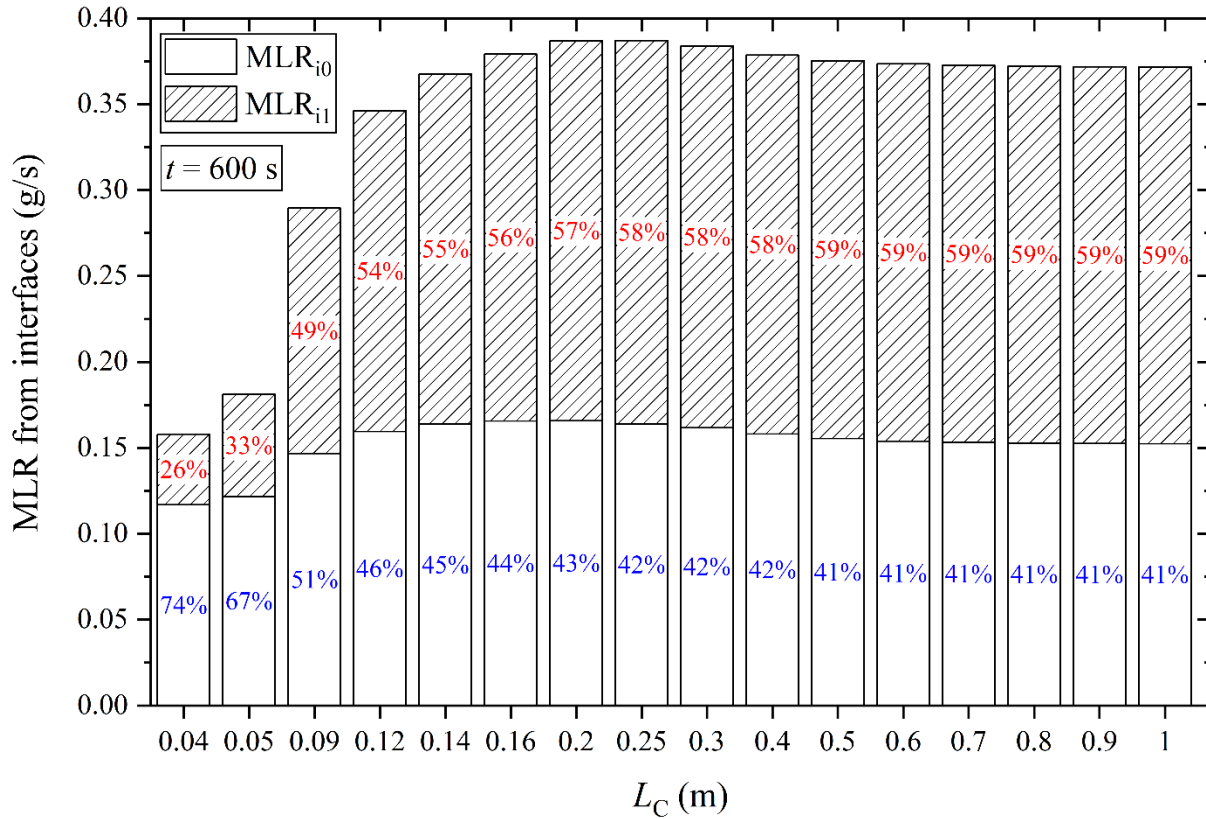


Figure 5.22: A bar plot showing the MLR from interfaces at different L_C at $t = 600$ s, where the x-axis represents L_C , and the y-axis represents MLR. For subscripts, “i0” denotes interface 0 representing the liquid surface (blank box with blue words), and “i1” denotes interface 1 (shaded box with red words) representing the solid-liquid interface. The percentage denotes the ratio of the MLR from the corresponding interface to the total MLR.

5.4.3 Temperature

At $t = 600$ s, the temperatures of the object surface and flame are presented in Figure 5.23. The flame temperature varies as discussed in Section 4.2.2, with values almost overlapping with each other, except for the one at $L_C = 0.04$ m. It is because the flame temperature is low when it is near

the liquid surface, such that a smaller amount of heat can be transferred to the object at the corresponding height. The temperature of the object's surface varies according to the variation of L_C . It is noticed that the maximum temperature (about 1130 K) at $L_C = 0.25$ m is the highest among all the cases investigated, which corresponds to the largest MLR as discussed in Section 5.4.2. The tendency of the object surface temperature matches that of the flame temperature, which indicates a reasonable temperature prediction over the object surface that is heated up a hot flame region.

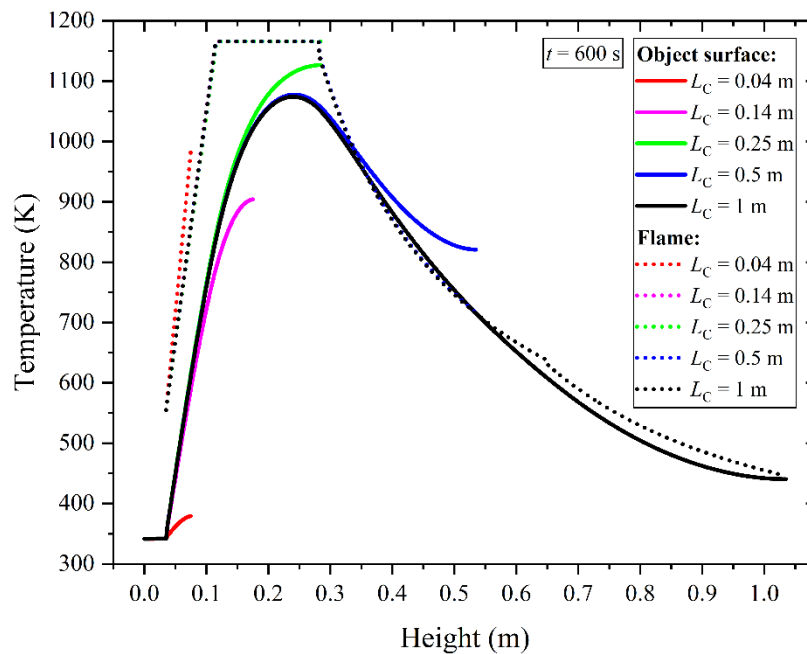
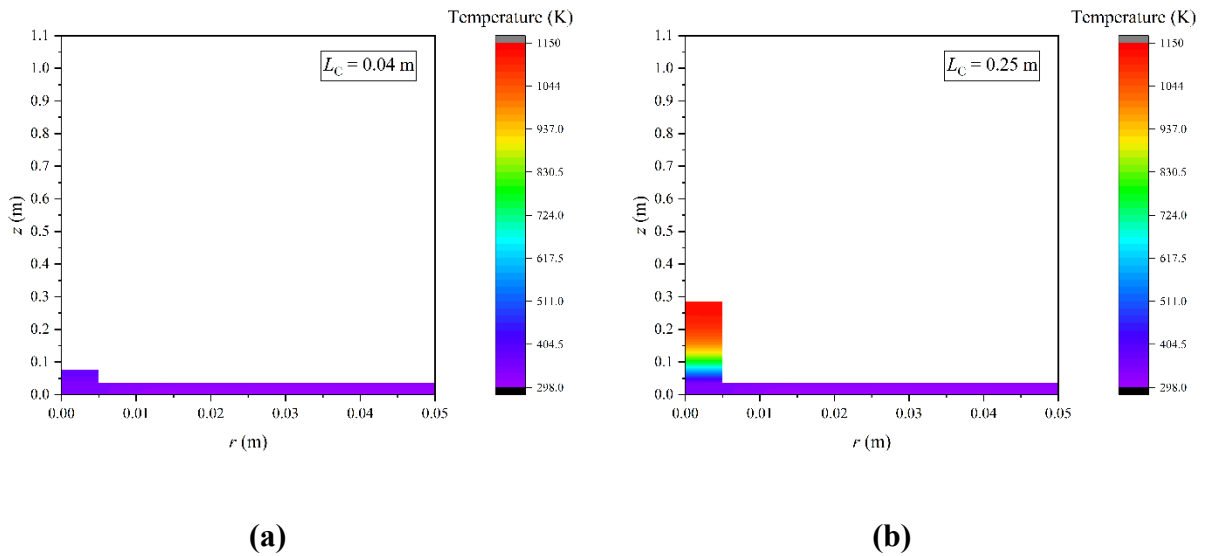
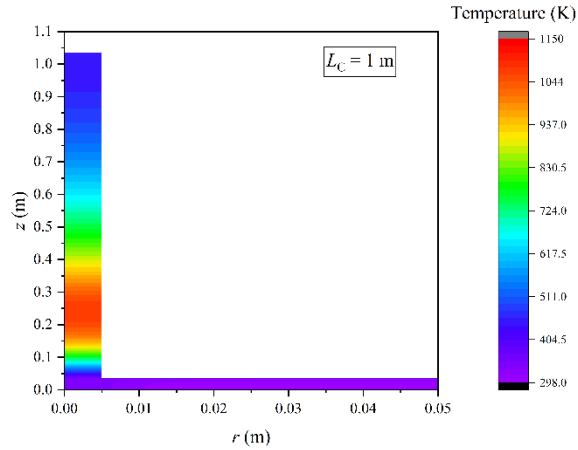


Figure 5.23: Temperature of the object surface ($r = 0.05$ m) (solid) and flame (dotted) along height, where $t = 600$ s, and the lengths of collectors are: $L_C = 0.04$ m, 0.14 m, 0.25 m, 0.5 m, and 1 m.

Typical L_C cases ($L_C = 0.04$ m, 0.25 m, and 1 m) are selected to show the temperature contour plot in liquid and object as depicted in Figure 5.17. When $L_C = 0.04$ m, the maximum temperature in the object is around 380 K, which is much less than the general flame temperature. The

maximum temperature is observed at the top of the object when L_C increases to 0.25 m, which means the flame temperature at such elevated heights is much higher. When L_C further increases to 1 m, the temperature distribution in the object varies along the height. The maximum temperature is found at around 0.25 m above the liquid surface. However, this value is lower than that in the $L_C = 0.25$ m case. Liquid temperature is similar in all these cases since its maximum value cannot exceed the saturation temperature.





(c)

Figure 5.24: Temperature contour in liquid and object at $t = 600$ s, where $L_C = 0.04$ m (a), 0.25 m (b), and 1 m (c), and the temperature bar ranges from 298.15 K to 1150.0 K.

The coupled behavior of thermal and mass transport is ascertained by the above analysis.

5.5 Second-stage parametric study (L_C and D_o)

Based on Section 5.4, L_C impacts both MLR of liquid and temperatures in liquid and object. More importantly, $L_C = 0.25$ m can be considered as the optimal length based on the pool size, fuel type, and fuel depth used in this study. It should be noted that such optimal configuration may probably only be valid for the given input parameters. For example, besides L_C , the diameter of an object, D_o , is another essential geometric parameter of the object that requires analysis. Further, the combination of L_C and D_o can provide mathematical expressions capable of predicting MLR for a range of these parameters.

In terms of this, 81 cases are investigated for the second-stage parametric study, by varying the values of both L_C and D_o . Details are summarized in Table 5.4, where D_o is varied in the range of 0.0025-0.01 m and L_C is varied in the range of 0.04-1 m. Accordingly, Δr (and Δz), as well as

Δt are varied to ensure enough grids are present in the slender object, resulting in appropriate grid Fourier numbers, and affordable simulation times. It should also be noted that to ensure the steady state, the time duration, t , is increased to 3000 s in numerical simulations.

Table 5.4: Model inputs for the second-stage parametric study.

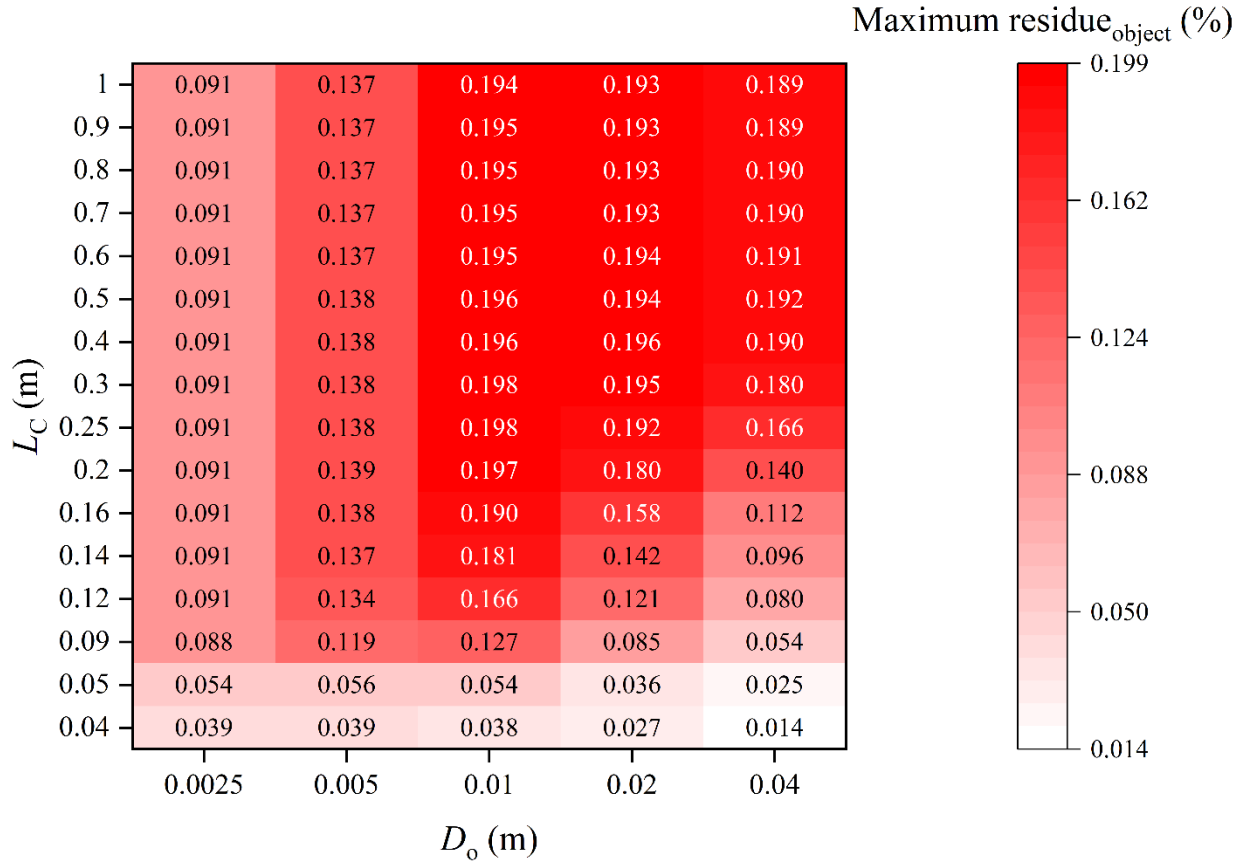
No. of cases	D_o (m)	L_C (m)	Δr (and Δz) (m)	Δt (s)	t (s)
1 (baseline, experiment only)	0	0	--	--	600
2-17	0.0025	0.04-1	0.00025	0.000125	3000
18-33	0.005	0.04-1	0.0005	0.0005	3000
34-49	0.01	0.04-1	0.001	0.002	3000
50-65	0.02	0.04-1	0.001	0.002	3000
66-81	0.04	0.04-1	0.001	0.002	3000

5.5.1 Model verification

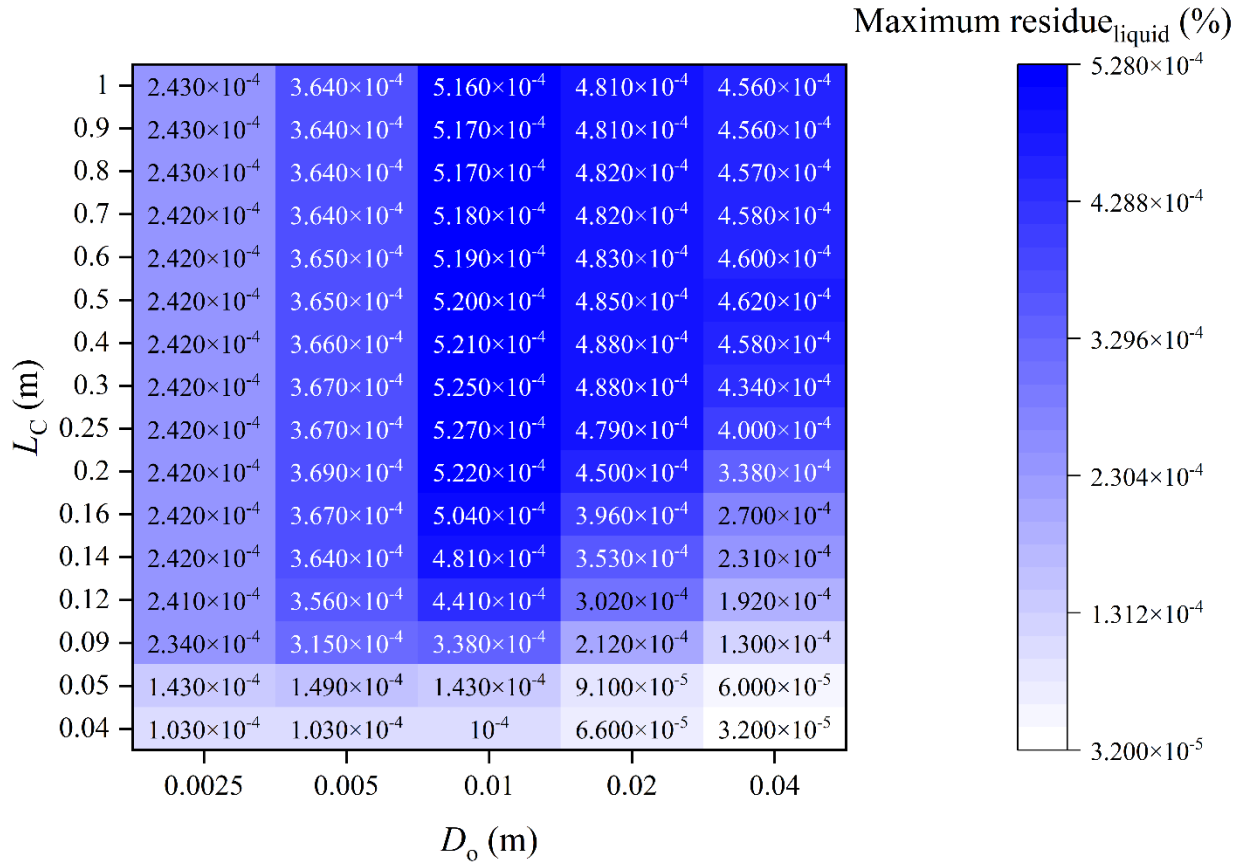
Heatmaps presenting the maximum residues at interface 1 are shown in Figure 5.25, where L_C is in the range of 0.04-1 m, D_o is in the range of 0.0025-0.04 m, and $t = 3000$ s. The residues are calculated from (a) object side, γ_o , as well as from (b) liquid side, γ_l .

As L_C increases from 0.04 to 1 m, for a certain D_o , γ_o first increases to a maximum value and then slightly decreases, while γ_l monotonically increases. As D_o increases from 0.0025 to 0.04 m, for a certain L_C , both γ_o and γ_l reach their maximum values at around $D_o = 0.01$ m for most cases. It can also be observed that as D_o increases, the maxima of γ_o and γ_l correspond to comparatively

larger L_C . In summary, all residues are quite small ($< 0.2\%$), indicating that the procedure to limit the temperature at interface 1 is applicable.



(a) γ_o .

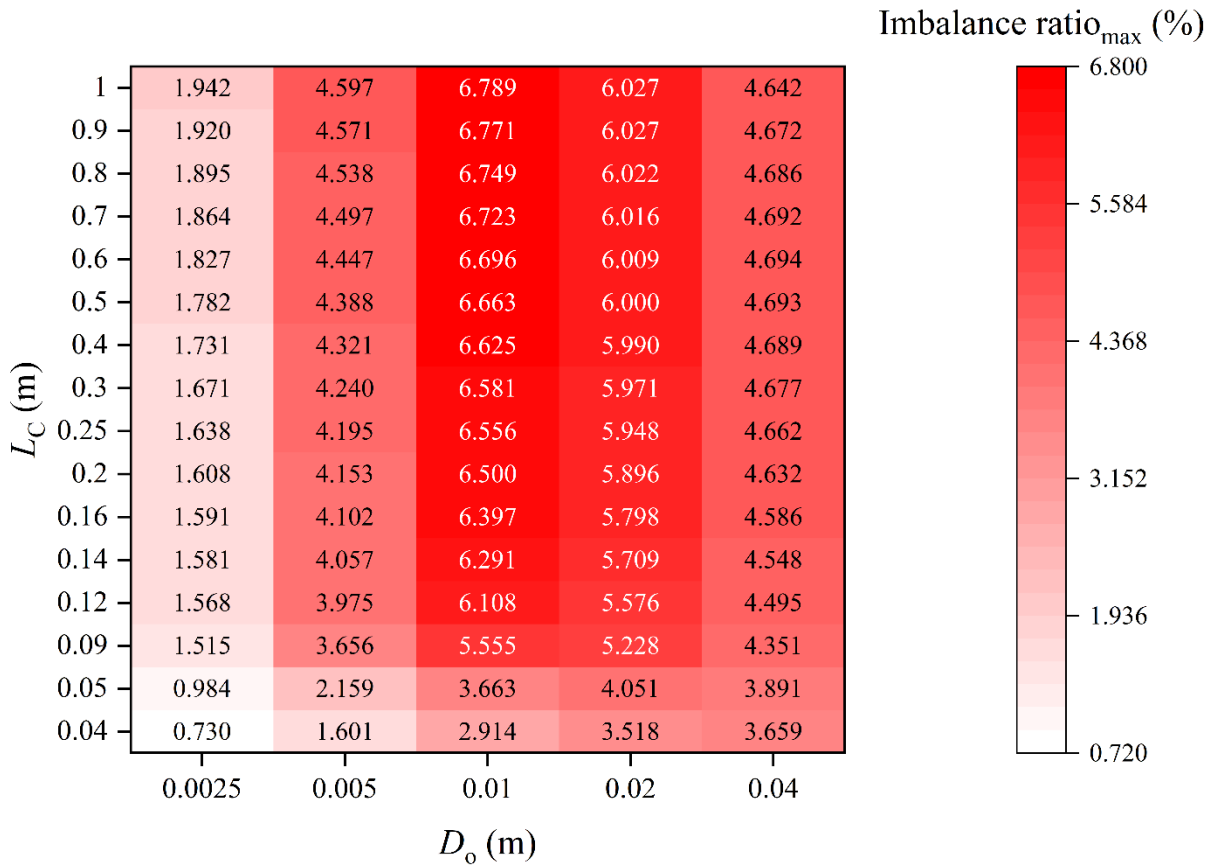


(b) γ_1 .

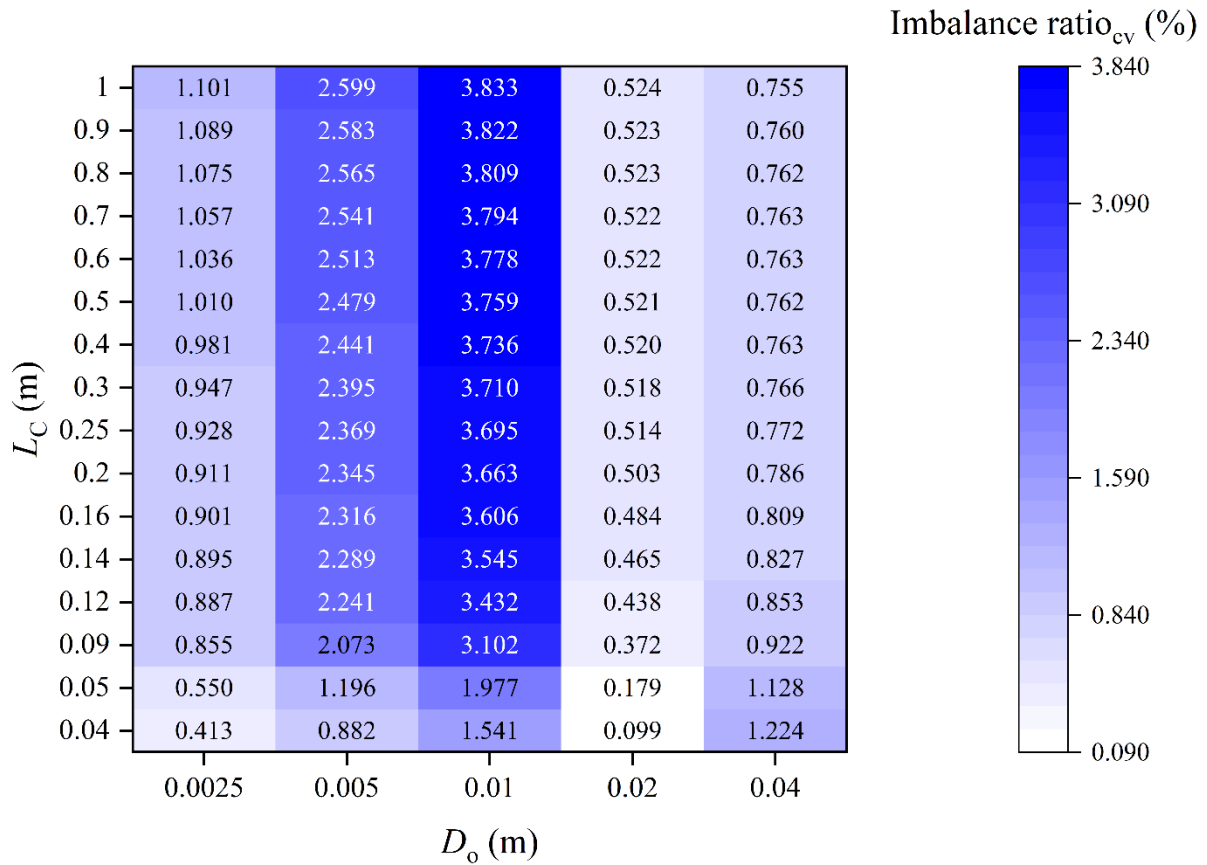
Figure 5.25: Maximum residue at different L_C and D_o at $t = 3000$ s, including the values calculated from object (a, red) and liquid (b, blue) sides, where $D_o = 0.0025$ – 0.04 m and $L_C = 0.04$ – 1 m.

The energy imbalance ratios at various L_C and D_o are displayed in Figure 5.26, including those calculated from the maximum among individual cells, $\Phi_{\text{cell,max}}$, and from the whole CV, Φ_{cv} . Parameters are varied as: $L_C = 0.04$ – 1 m, $D_o = 0.0025$ – 0.04 m, and $t = 3000$ s. For a certain D_o , both $\Phi_{\text{cell,max}}$ and Φ_{cv} increase as L_C increases; however, such finding is slightly different from that reported in Section 5.4.1, where t is fixed as 600 s to match the experimental duration.

However, when L_C and D_o increase, it would be ideal to extend t accordingly, because it generally requires more time to reach a steady state, when the heat penetrates a larger domain. Similar to residues, as D_o increases from 0.0025 to 0.04 m, for a certain L_C , both $\Phi_{\text{cell,max}}$ and Φ_{cv} reach the maximum at $D_o = 0.01$ m for most cases, which is impacted by the variation of temperature distribution, as well as different model inputs. All ratios reported are quite small ($< 6.8\%$), and it is reasonable that $\Phi_{\text{cell,max}}$ is larger than Φ_{cv} at the corresponding L_C and D_o . The model is considered verified, after updating $L_C = 0-1$ m and $D_o = 0.0025-0.04$ m.



(a) $\Phi_{\text{cell,max}}$



(b) Φ_{cv} .

Figure 5.26: Energy imbalance ratio at $t = 3000$ s, including the maximum value among individual cells (a, red) and the one applied to the whole CV (b, blue) sides, where $D_o = 0.0025\text{--}0.04$ m and $L_C = 0.04\text{--}1$ m.

5.5.2 Mass loss rate

Based on preceding discussions, MLR is noticed to increase after immersing an object in a liquid pool fire. Therefore, as shown in Figure 5.27, MLR is reported by calculating the ratio of MLR to the MLR from the baseline experiment (0.11 g/s) for different L_C and D_o values. Among all cases investigated with varying D_o , MLR is noticed to increase for as much as about 20 times for $D_o =$

0.04 m, which is meaningful to practical applications. Ratios also vary with the variation of L_C at a given D_o . As L_C increases, the ratio first increases considerably and later slightly decreases and attains an almost constant value, suggesting the existence of an optimal L_C at given D_o . The optimal L_C is meanwhile noticed to vary at different D_o . With an increase in D_o , the ratio generally increases, indicating that more heat is available for liquid vaporization.

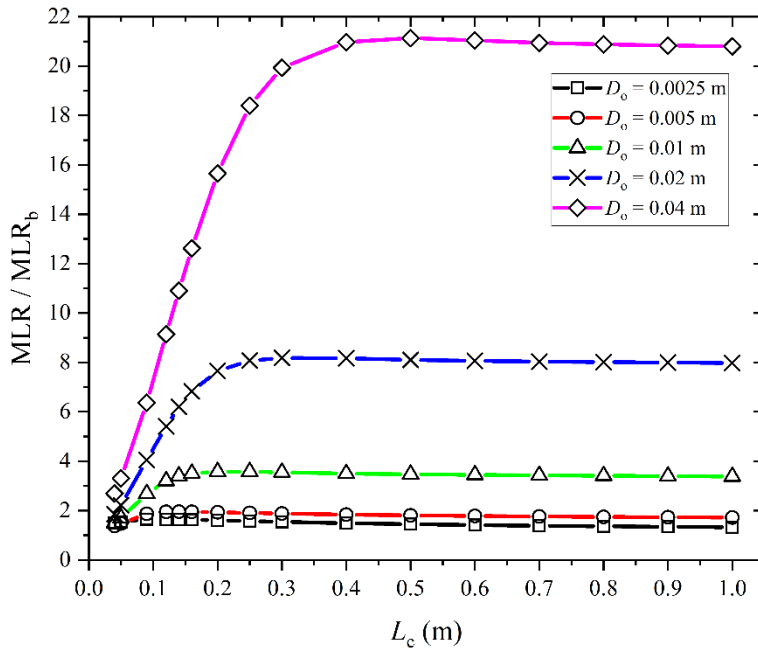


Figure 5.27: The ratio of MLR to MLR_b at $t = 3000$ s, where $D_o = 0.0025-0.04$ m and $L_C = 0.04-1$ m. MLR_b denotes the MLR from the baseline experiment, whose value is 0.11 g/s.

To better explore the influence of the immersed object on MLR, the ratio of MLR from interface 1 to the total MLR at different L_C and D_o is presented in Figure 5.28. As discussed, MLR includes the mass vaporization from interfaces 0 and 1. For the cases having larger L_C and D_o , MLR from interface 1 plays a more significant role than MLR from interface 0. For most D_o , when $L_C < 0.15$ m, the ratio shows a significant increase as L_C increases.

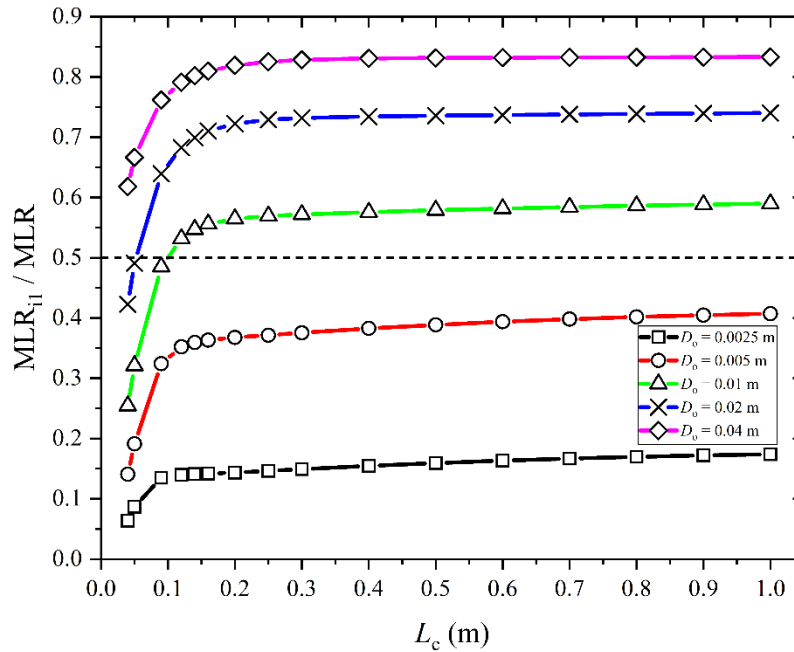


Figure 5.28: The ratio of MLR_{i1} to MLR at $t = 3000$ s, where $D_o = 0.0025\text{--}0.04$ m and $L_C = 0.04\text{--}1$ m. MLR consists of MLR_{i0} and MLR_{i1} , which denotes the mass vaporization coming from interface 0 and 1, respectively. The black dashed line points out the situation when $MLR_{i0} = MLR_{i1}$.

5.5.3 Mass loss rate prediction

Even though the results from experiments and numerical simulations are quite comparable, their implementation needs requirements, which some users do not favor. Instead, correlations capable of providing immediate solutions under certain configurations (for example, L_C and D_o) would be more valuable. In terms of this, two correlations are proposed to predict MLR of a hexane pool as a function of L_C and D_o by taking advantage of experiments and validated numerical simulations.

5.5.3.1 2D plot method

At first, for normalizing the varying net liquid surface area exposed to the gas phase, the mass flux, \dot{m}'' , is obtained as:

$$\dot{m}'' = \frac{\dot{m}}{A_1}, \quad (5.1)$$

where \dot{m} (kg/s) is the mass loss rate, A_1 (m²) is the net liquid surface area, which is calculated as:

$$A_1 = A_p - A_s, \quad (5.2)$$

where A_p (m²) is the area of the pool surface, and A_s (m²) is the cross-sectional area of the object.

Next, the geometry of the object is considered as: P_c/A_c , where P_c and A_c are the perimeter and surface area of the cylindrical collector, respectively, and they are calculated as:

$$P_c = 2(\pi D_o + L_c), \quad (5.3)$$

$$A_c = \frac{\pi D_o^2}{4} + \pi D_o L_c, \quad (5.4)$$

Plots depicting the relationship between \dot{m}'' and P_c/A_c are shown in Figure 5.29, where scatters denote numerical data from simulations, indicating an exponential function distribution. The red dashed plot is generated by implementing a nonlinear curve fit, with adjusted $R^2 \approx 0.98148$, showing a satisfactory match with the numerical data. The curve fitting is expressed as:

$$\dot{m}'' = 1.218 \exp \left[\frac{\left(-\frac{P_c}{A_c} \right)}{14.20072} \right] + 0.02649, \quad (5.5)$$

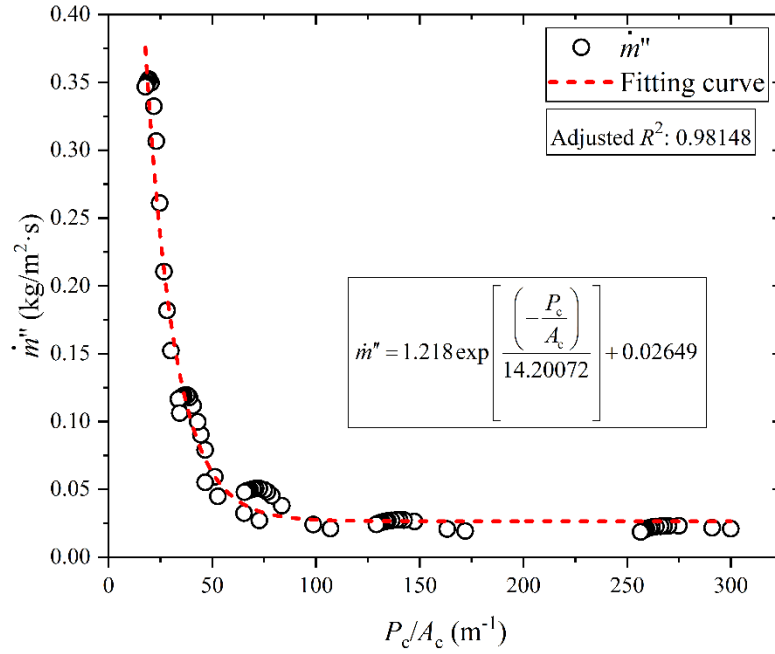


Figure 5.29: Relationship between \dot{m}'' and P_c/A_c depicted by numerical data (black circle) and a non-linear curve fitting plot (red dashed), where adjusted $R^2 \approx 0.98148$.

5.5.3.2 3D plot method

It is impossible to include the baseline experiment data while using the 2D plot method. Therefore, a 3D plot method is proposed, where the baseline case is also included, and a relationship among \dot{m}'' , L_C and D_o is proposed.

First, it is noticed that the range of L_C and D_o differs a lot, and hence, a technique named min-max normalization [89] is applied to rescale the range of values to [0,1]. For L_C , the normalized value, L_C^* , is given by:

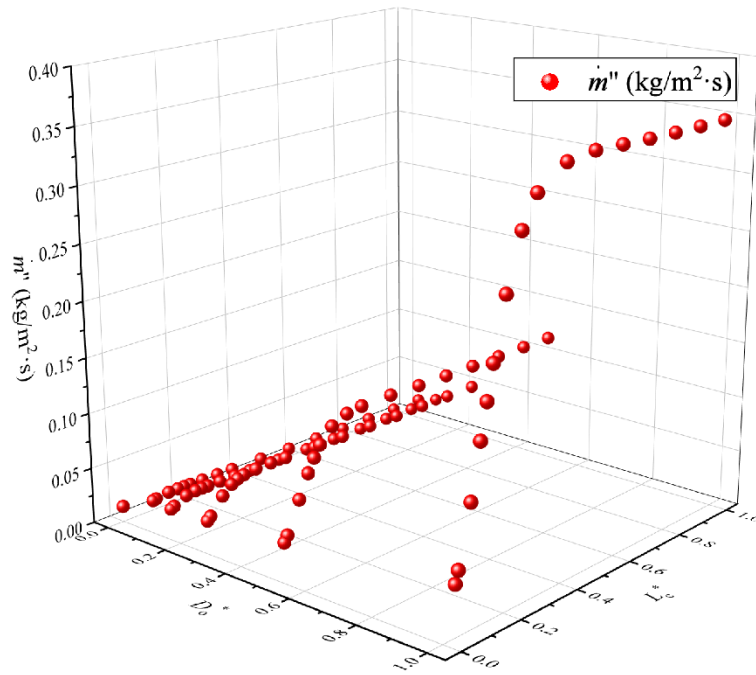
$$L_C^* = \frac{L_C - L_{C,\min}}{L_{C,\max} - L_{C,\min}}, \quad (5.6)$$

where L_C is the give length of collector, $L_{C,\min} = 0$ m (baseline), $L_{C,\max} = 1$ m, $D_{o,\min} = 0$ m (baseline), and $D_{o,\max} = 0.04$ m.

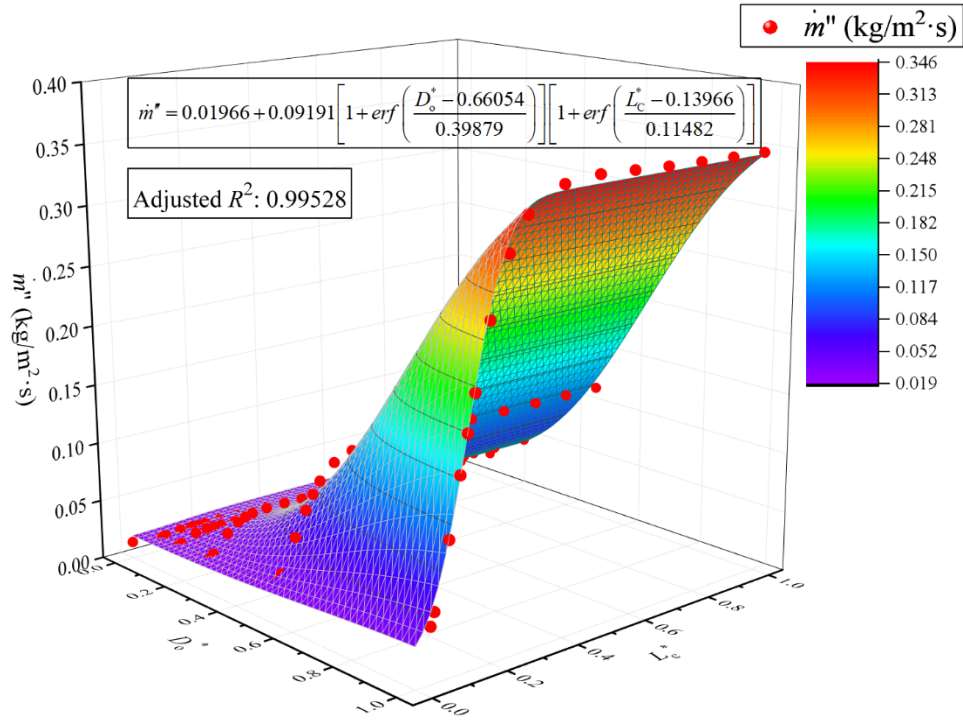
By using the results from all 81 cases (including the baseline experiment), a 3D scatter plot is generated, as shown in Figure 5.30(a). \dot{m}'' is seen to be dependent on both L_C^* and D_o^* . Accordingly, a non-linear surface fitting method may be suitable to fit the data. Based on the data distribution, a non-linear Gaussian cumulative function is used, whose general formula is expressed as:

$$z = z_0 + 0.25B \left[1 + \operatorname{erf} \left(\frac{x-C}{\sqrt{2D}} \right) \right] \left[1 + \operatorname{erf} \left(\frac{y-E}{\sqrt{2F}} \right) \right], \quad (5.7)$$

where x , y , and z denote D_o^* , L_C^* , and \dot{m}'' , respectively; z_0 , B , C , D , E , and F are coefficients that need to be determined based on the fitting.



(a) Numerical data.



(b) Numerical data and a surface fitting plot.

Figure 5.30: The variation of \dot{m}'' along L_c^* and D_o^* , denoted by (a) numerical data (red sphere) and (b) a non-linear surface fitting plot (rainbow palette), where adjusted $R^2 \approx 0.99528$.

The fit is shown in Figure 5.30(b), by implementing a nonlinear surface fit, with adjusted $R^2 \approx 0.99528$, showing a satisfying match with the numerical data. The fitting surface is expressed as:

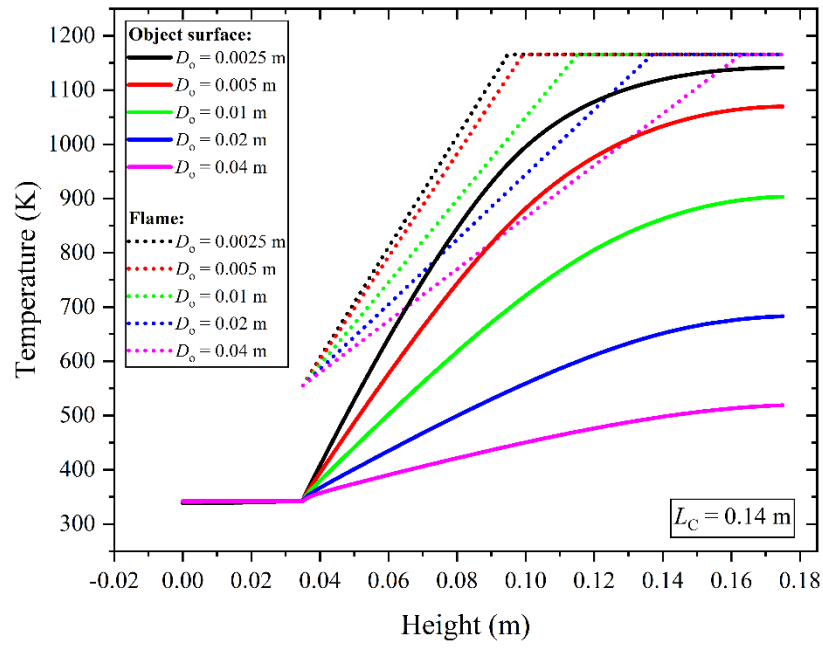
$$\dot{m}'' = 0.01966 + 0.09191 \left[1 + \operatorname{erf} \left(\frac{D_o^* - 0.66054}{0.39879} \right) \right] \left[1 + \operatorname{erf} \left(\frac{L_c^* - 0.13966}{0.11482} \right) \right], \quad (5.8)$$

5.5.4 Temperature

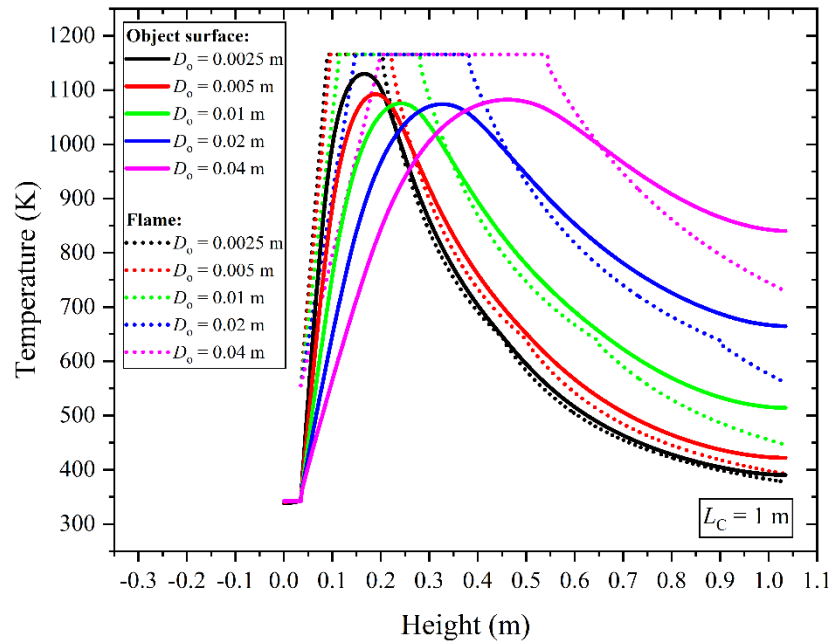
Before discussions, it is important to point out that the time duration used in Figure 5.31(a) and (b) is $t = 3000$ s, while it is $t = 600$ s in Figure 5.23, which causes slight discrepancies when being compared with each other. As the influence of L_C is discussed in Section 5.4, only two typical L_C values are presented in this section, which are $L_C = 0.14$ m (lower than the flame height) and $L_C = 1$ m (higher than the flame height).

When D_o is small, the variation of object surface temperature along the axial direction is large, indicating an easier thermal penetration and dissipation in a slender object. Because of the interactions among different regions, the flame temperature distribution is altered accordingly, manifesting in the elongation of the flame region with an increase of D_o .

When L_C is small, the top of the object is located within the flame region, and hence, the surface temperature of the object increases with an increase of height. When L_C exceeds the height of the flame region, both temperature decreases, and the temperature gradient along the axial direction is dependent on D_o .



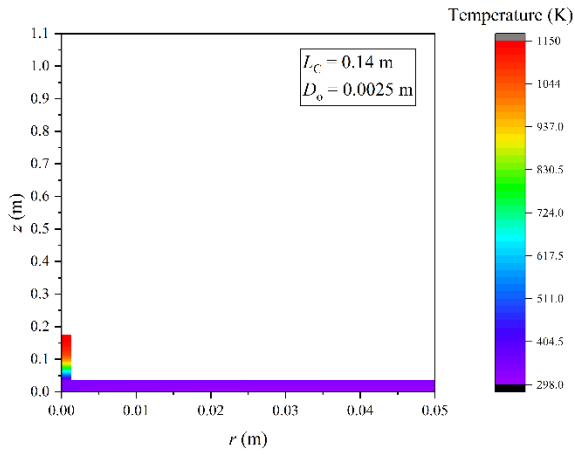
(a) $L_C = 0.14$ m.



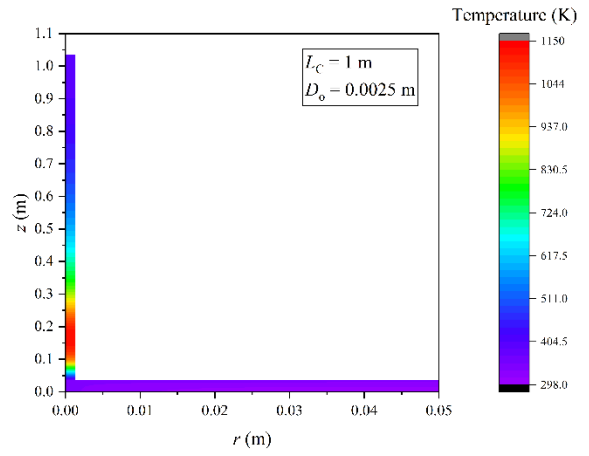
(b) $L_C = 1$ m.

Figure 5.31: Temperature of the object surface (solid) and flame (dotted) at different L_C and D_o , where $t = 3000$ s, L_C is (a) 0.14 m and (b) 1 m, and $D_o = 0.0025$ m, 0.005 m, 0.01 m, 0.02 m, and 0.04 m.

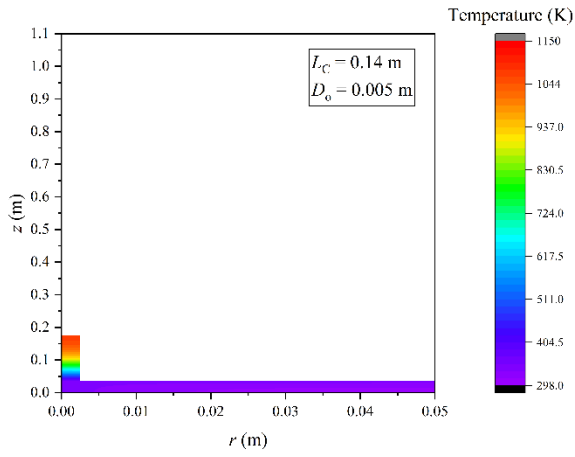
Such distribution is displayed in Figure 5.32. Interestingly, the temperature at the top of the object decreases as the D_o increases, when $L_C = 0.14$ m, while it increases with an increase in D_o , when $L_C = 1$ m. This is because when L_C is small, there is insufficient heat used to heat the object, and hence, the increase of D_o causes more thermal dissipation from the object. When L_C is large, it takes advantage of being in the flame region having high temperature, and hence, the increase of D_o facilitates thermal penetration and storage in the object.



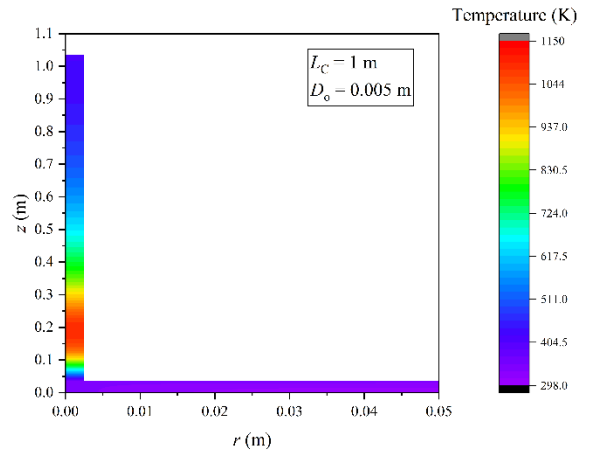
(a)



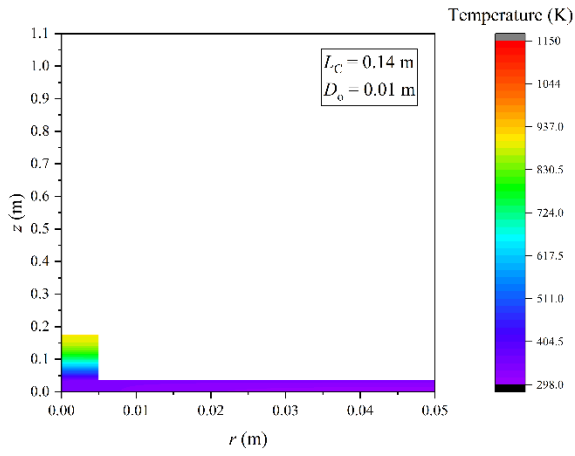
(b)



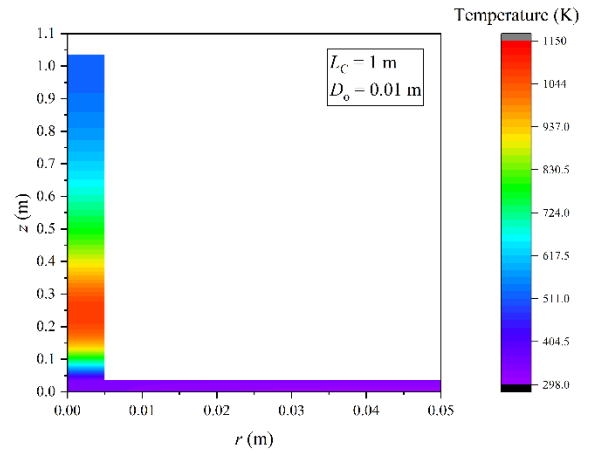
(c)



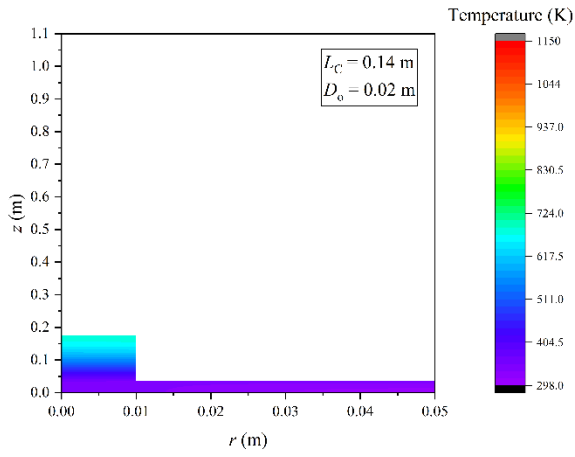
(d)



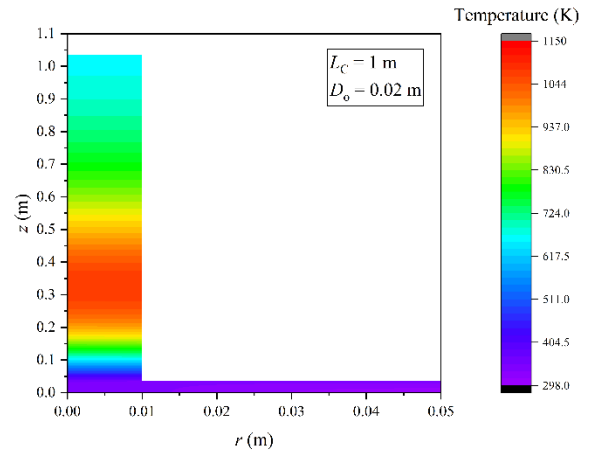
(e)



(f)



(g)



(h)

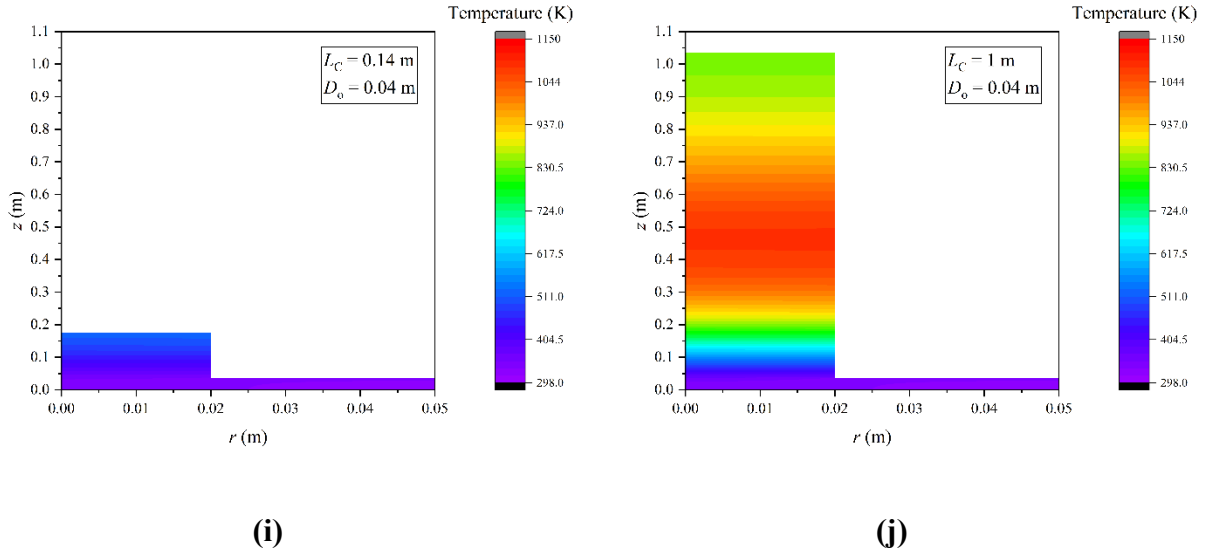
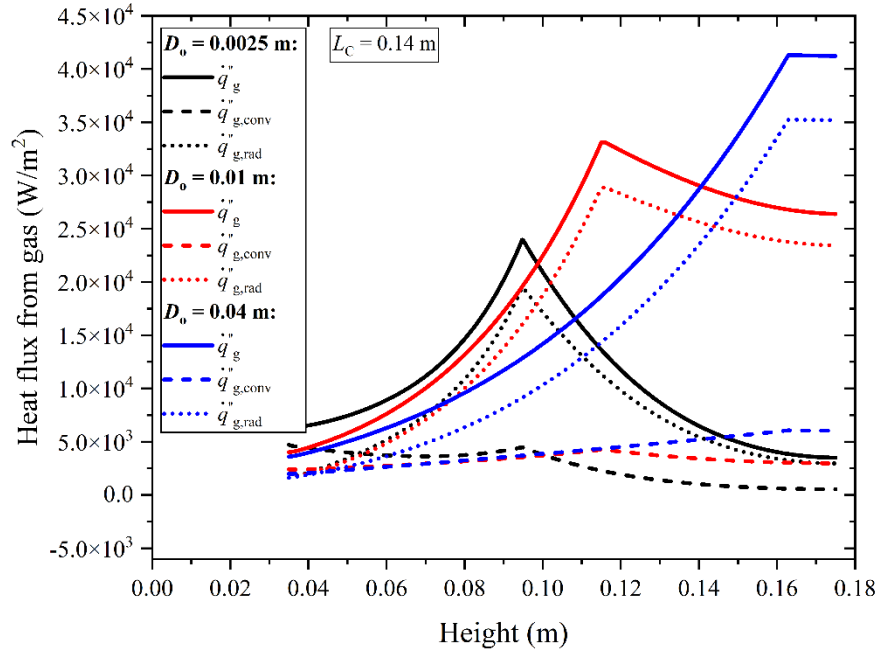


Figure 5.32: Temperature contour in liquid and object at $t = 3000$ s, where $L_C = 0.14$ m and 1 m, $D_o = 0.0025$ m, 0.005 m, 0.01 m, 0.02 m, and 0.04 m, and the temperature bar ranges from 298.15 K to 1150.0 K.

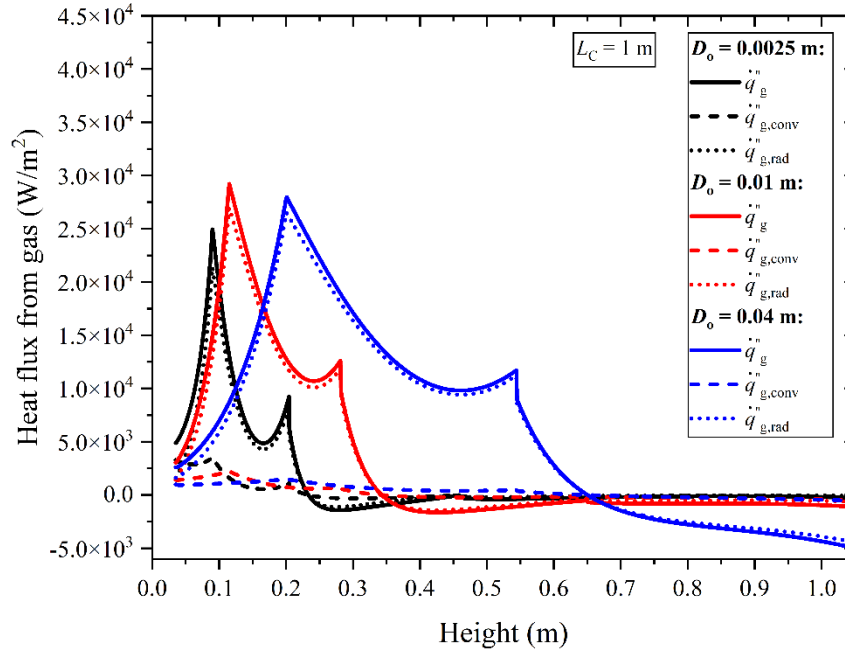
5.5.5 Heat flux from the hot gas

Heat flux from the flame to the object along height is shown in Figure 5.33, with input parameters as: $t = 3000$ s, $L_C = 0.14$ m and 1 m, and $D_o = 0.0025$ m, 0.01 m, and 0.04 m. Recalling the discussion in Section 4.2.2.3, the total heat flux, \dot{q}_g'' , consists of convection, $\dot{q}_{g,\text{conv}}''$, and radiation,

$$\dot{q}_{g,\text{rad}}''.$$



(a) $L_C = 0.14 \text{ m}$.



(b) $L_C = 1$ m.

Figure 5.33: Temperature of the object surface (solid) and flame (dotted) at different L_C and D_o , where $t = 3000$ s, L_C is (a) 0.14 m and (b) 1 m, and $D_o = 0.0025$ m, 0.01 m, and 0.04 m.

At the height not very close to the liquid surface, $\dot{q}_{g,rad}''$ dominates due to the distinct temperature difference between the hot gas (flame) and object surface. When L_C is small, the increase of D_o from 0.0025 to 0.04 m facilitates higher total heat flux on the object, as shown in Figure 5.33(a). However, when L_C is large, the increase of D_o may not contribute to the increase of the peak heat flux.

It is also interesting to note that the heat flux becomes negative when the collector height exceeds the flame height. Such finding corresponds to the temperature difference between the object surface and hot air at the same height, as shown in Figure 5.31. Besides the present model

setup, it is also reasonable to develop the situation due to the different thermal properties between the object and gas.

5.6 Summary

A computational model is developed, including interactions among all three phases (gas, liquid, and solid). The outputs are capable of predicting the MLR of the liquid and temperature distribution in object and liquid. After the model construction, three stages of validations are conducted, where the convergence is verified by checking the residue at interfaces and the energy imbalance for the domain. Meanwhile, the outputs are validated by comparing the results with the experimental data from the literature [17,75]. The model is considered verified because of small values, and the model is considered validated because of small discrepancies with the experimental data. After the model is verified and validated, two parametric studies are conducted to explore the influence of the object configurations on the pool fire. Results indicate the existence of the optimal length provided with the current model setup. Further analyses show that the MLR of liquid can be increased over 20 times, which is meaningful to the practical design. Furthermore, possible correlations are proposed based on the experimental data and numerical results to provide immediate solutions under specific configurations.

6 Conclusions

6.1 Summary

The present work investigates pool fire burning facilitated by subcooled nucleate boiling heat and mass transfer processes. Experimental and numerical approaches are both implemented, whose analyses prove that the pool fire burning rate is increased because of the additional thermal loop, allowing the interactions among gas (fire), liquid (fuel), and solid (object) regions. Especially after the immersed object surface temperature exceeds the saturation temperature of bulk liquid, the boiling initiates at the solid-liquid interfaces, further increasing the heat and mass transfer in liquid, the liquid vaporization rate, and the burning rate. More importantly, the pool fire burning is noticed to vary at different object configurations, and therefore, particular designs are considered to benefit the industrial applications.

Experiments are conducted to study the interactions among regions:

- Primary measurements include heat flux from the heated object to liquid, pool fire burning rate/mass loss rate (MLR) of liquid, and temperature of the surface of an object.
- Meanwhile, such processes are characterized by various bubble phenomena dependent on heat flux, excess temperature, location, etc.
- Qualitative and quantitative methods are used to diagnose the images of flame and bubbles. For flame images, the flame height at a steady state is determined by applying a threshold to binarize images based on visual observation. For bubble images captured by the cameras equipped at different locations, multiple information can be collected from the processed images, including departure frequency, distribution, number, size, velocity, etc. Analyses also suggest performing the bubble quantification in different regions.

- Furthermore, three stages of experiments are conducted to examine the object's different configurations (inclination, immersion depth, and surface condition). Analyses show the existence of the optimal inclination angle because of the comparatively higher heat transfer coefficient and more efficient cooling effect. Subsequent analyses point out the inconsistency in MLR, as the increase of the immersion depth and the introduction of holes modify the surface condition.
- In general, bubble diagnostic results match the measured data from several aspects:
 1. More vigorous bubble phenomena are found with higher heat fluxes and excess temperature cases.
 2. After introducing an immersed object, the appearance of bubbles and their corresponding behaviors are found to facilitate the heat and mass transfer processes and the liquid perturbation, which causes the increase in MLR.
 3. The inconsistency in MLR at different object configurations corresponds to bubble phenomena and bubble quantification results.

A numerical model is built up and developed to predict the MLR of liquid and temperature distribution in object and liquid.

- During the model construction, necessary assumptions and simplifications are required. The Finite Difference Method (FDM) discretizes the governing equations and boundary conditions.
- Interactions among the three phases are coupled. The flame region is simulated as a hot gas phase region by specifying a temperature distribution according to empirical correlations, and it is coupled with the MLR of liquid. Unsteady energy equations in cylindrical polar coordinates are solved for the object and the liquid regions by following the procedures that

all heat from the heated interfaces is transferred to heat the liquid. After the liquid attains saturation, the extra heat is all used for vaporization.

- Next, three stages of validations are performed, where the model is verified by checking the energy imbalance and is validated by comparing model outputs with the experimental data.
- Furthermore, two parametric studies are conducted to explore the potential optimal designs by varying the object configurations (length of the collector and diameter of the object). According to the MLR of liquid and the temperature distribution in the object and flame, as the length of the collector increases, the influence of the object is initially found to increase. After that, it attains the maximum, where the optimal length exists. Further analyses show that the MLR of liquid can ideally be increased over 20 times if provided with appropriate object configurations.
- In addition, by using the experimental and numerical data, two types of empirical correlations are proposed, which are capable of providing immediate solutions under specific configurations.

Different **configurations** of the object are explored in this work:

- Optimal designs are reported while varying inclinations of the object and lengths of the collector. Meanwhile, variations are noticed in the MLR, temperature distribution, and bubble phenomena by varying immersion depth, surface condition, and diameter of the object.
- Such findings can be implemented in the practical design. More importantly, by following the techniques and procedures in this work, more potential optimal designs can be sought and examined, whose outcomes will improve the Flame RefluxerTM technique and effectively solve real-world oil spills issues.

6.2 Future works

Based on the summary of the present work, selected future works are summarized as follows:

- More configurations are expected to be examined via both experimental and numerical methods to further the investigation of the thermal loop and provide more comprehensive solutions to the optimal design in complex scenarios.
- Systematically temperature measurements in fire, object, and liquid during experiments would provide additional data for validating the numerical model.
- A more precise cell load would be helpful to eliminate the error, especially for the cases having small immersed objects.
- Instead of solely focusing on the particular region, bubble quantification techniques need to be developed to diagnose the bubble phenomena in multiple regions.
- The simplified numerical model needs further examination to ensure it can be validated by future experiments where different object configurations are varied.
- In the flame region, gas properties are currently based on the air in the current model. Therefore, it would also be reasonable to consider the mixture properties of the combustion products.
- The numerical model requires further development from different aspects. For example, the temperature at the solid-liquid interface is currently limited to the saturation temperature of the liquid. Even though the heat flux caused by such limitation is used to evaluate the mass loss rate, there should still be discrepancies at the interface due to the variation of the liquid properties. Therefore, to better explore the scenarios at the interface, the temperature limit (at the object side) needs to be re-evaluated. As a result of this, it is also reasonable to consider

the variation of liquid thermal properties at the interface influenced by the vaporization and the boiling curve.

- Current correlations need to be further developed for better uses in complicated scenarios based on the data from future experiments and numerical models.

Appendices

Appendix A temperature-resistance calibration

The direct temperature measurement on the wire surface using thermocouples is not easy, because of the small contact area and the additional electrical impact. To handle this, an alternative method proposed by Nukiyama [34] is implemented. This technique relates the surface temperature of wire with its electrical resistance via measurements.

A calibration experiment is performed, by immersing a test wire in a canola oil bath. The oil is gradually heated using a thermal plate placed at the bottom, and the oil is gently and intermittently stirred to ensure a uniform distribution of temperature. The oil temperature, T , is recorded via a thermocouple, and the wire resistance, R , is reordered via a multimeter. As the heating process is comparatively steady, the oil temperature can be regarded as the wire temperature, T .

The relationship between the wire temperature and its resistance is depicted in Figure A.1, where two trials are included. According to the linear fitting, when the oil temperature lies between 50 °C and 150 °C, the temperature-resistance calibration can be expressed as:

$$R = \omega T + R_0, \quad (\text{A.1})$$

where $\omega \approx 0.00235 \text{ } \Omega/\text{ }^\circ\text{C}$ is the slope, representing the temperature-resistance coefficient, and R_0 is the y-intercept, representing the resistance at $T = 50 \text{ }^\circ\text{C}$.

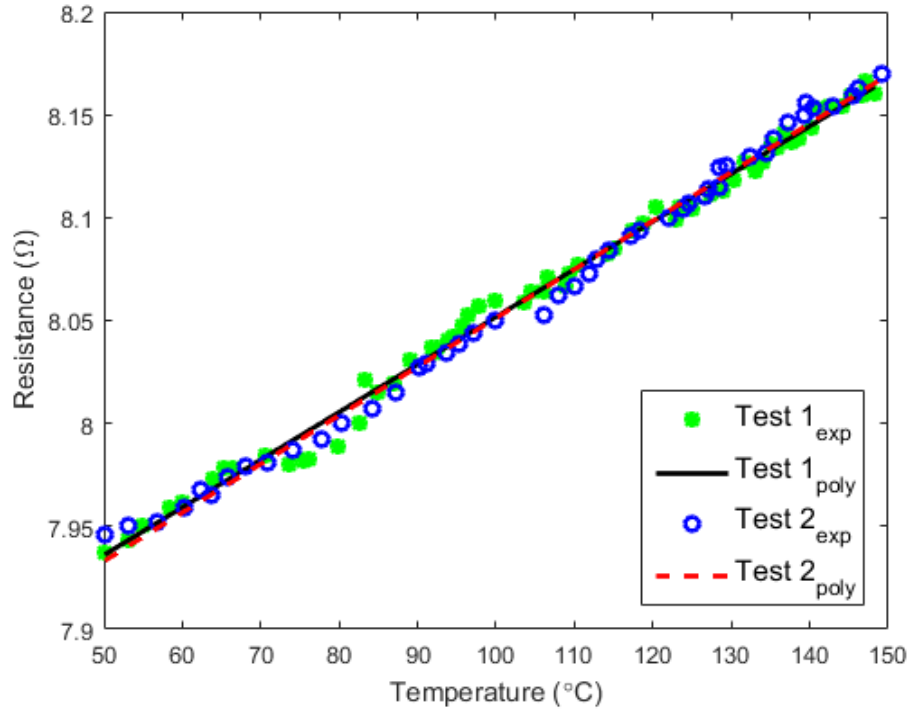


Figure A.1: The temperature-resistance calibration, where circular symbols denote experimental data, and lines represent their corresponding linear fitting. The liquid temperature ranges from 50 to 150 °C.

Furthermore, two important points need to be followed when determining the wire temperature:

1. Due to the temperature difference in the interior of the wire, ΔT_w , the surface temperature of a wire, T_s , needs to be further corrected by considering the thermal conduction, which is given by:

$$\Delta T_w = T - T_s = \frac{UI}{4\pi l k_w}, \quad (\text{A.2})$$

where k_w is the thermal conductivity of nichrome.

2. Before each experiment, the wire surface is carefully cleaned to remove potential residues.

Appendix B Energy imbalance at interfaces

As discussed in Section 4.5, derivations of the $T_{i,j}^{n+1}|_{GE}$ summarized in Table 4.2 and Table 4.3 are shown below.

B.1 Solid side

1. Interface 2: $i = 1$ to $M1 - 1, j = N0$

For the discretization at interface 2, the central difference method is implemented in the radial direction, and the forward difference method is implemented in the axial direction. The temperature at node (i, j) is given by:

$$\begin{aligned}
 \frac{T_{i,j}^{n+1} - T_{i,j}^n}{\Delta t} &= \frac{\alpha_o}{i(\Delta r)} \frac{T_{i+1,j}^n - T_{i-1,j}^n}{2(\Delta r)} + \alpha_o \frac{T_{i+1,j}^n - 2T_{i,j}^n + T_{i-1,j}^n}{(\Delta r)^2} + \alpha_o \frac{2T_{i,j}^n - 5T_{i,j+1}^n + 4T_{i,j+2}^n - T_{i,j+3}^n}{(\Delta z)^2} \\
 \Rightarrow T_{i,j}^{n+1} &= T_{i,j}^n + \lambda_o \left(\frac{T_{i+1,j}^n - T_{i-1,j}^n}{2i} \right) + \lambda_o (T_{i+1,j}^n - 2T_{i,j}^n + T_{i-1,j}^n) + \lambda_o (2T_{i,j}^n - 5T_{i,j+1}^n + 4T_{i,j+2}^n - T_{i,j+3}^n) \\
 &= (1 - 2\lambda_o + 2\lambda_o) T_{i,j}^n + \lambda_o \left(\frac{T_{i+1,j}^n - T_{i-1,j}^n}{2i} \right) + \lambda_o (T_{i+1,j}^n + T_{i-1,j}^n) + \lambda_o (-5T_{i,j+1}^n + 4T_{i,j+2}^n - T_{i,j+3}^n) \\
 &= T_{i,j}^n + \lambda_o \left(\frac{T_{i+1,j}^n - T_{i-1,j}^n}{2i} \right) + \lambda_o (T_{i+1,j}^n + T_{i-1,j}^n - 5T_{i,j+1}^n + 4T_{i,j+2}^n - T_{i,j+3}^n)
 \end{aligned}$$

(B.1)

Therefore, the ratio of residue for the object side, γ_o , at the interface 2 is given by:

$$\gamma_o = \frac{T_{i,j}^n + \lambda_o \left(\frac{T_{i+1,j}^n - T_{i-1,j}^n}{2i} \right) + \lambda_o (T_{i+1,j}^n + T_{i-1,j}^n - 5T_{i,j+1}^n + 4T_{i,j+2}^n - T_{i,j+3}^n) - T_{i,j}^{n+1}}{T_{i,j}^{n+1}} \times 100\%, \quad (B.2)$$

2. Node $(M1, N0)$

For the discretization at the corner node ($M1, N0$), the backward difference method is implemented in the radial direction, and the forward difference method is implemented in the axial direction.

The temperature at the node ($M1, N0$) is given by:

$$\begin{aligned}
\frac{T_{i,j}^{n+1} - T_{i,j}^n}{\Delta t} &= \frac{\alpha_o}{i(\Delta r)} \frac{3T_{i,j}^n - 4T_{i-1,j}^n + T_{i-2,j}^n}{2(\Delta r)} + \alpha_o \frac{2T_{i,j}^n - 5T_{i-1,j}^n + 4T_{i-2,j}^n - T_{i-3,j}^n}{(\Delta r)^2} + \alpha_o \frac{2T_{i,j}^n - 5T_{i,j+1}^n + 4T_{i,j+2}^n - T_{i,j+3}^n}{(\Delta z)^2} \\
\Rightarrow T_{i,j}^{n+1} &= T_{i,j}^n + \lambda_o \left(\frac{3T_{i,j}^n - 4T_{i-1,j}^n + T_{i-2,j}^n}{2i} \right) + \lambda_o (2T_{i,j}^n - 5T_{i-1,j}^n + 4T_{i-2,j}^n - T_{i-3,j}^n) + \lambda_o (2T_{i,j}^n - 5T_{i,j+1}^n + 4T_{i,j+2}^n - T_{i,j+3}^n) \\
&= \left(1 + \frac{3}{2i} \lambda_o + 2\lambda_o + 2\lambda_o \right) T_{i,j}^n + \lambda_o \left(\frac{-4T_{i-1,j}^n + T_{i-2,j}^n}{2i} \right) + \lambda_o (-5T_{i-1,j}^n + 4T_{i-2,j}^n - T_{i-3,j}^n) \\
&\quad + \lambda_o (-5T_{i,j+1}^n + 4T_{i,j+2}^n - T_{i,j+3}^n) \\
&= \left(1 + \frac{3}{2i} \lambda_o + 4\lambda_o \right) T_{i,j}^n + \lambda_o \left(\frac{-4T_{i-1,j}^n + T_{i-2,j}^n}{2i} \right) + \lambda_o (-5T_{i-1,j}^n + 4T_{i-2,j}^n - T_{i-3,j}^n - 5T_{i,j+1}^n + 4T_{i,j+2}^n - T_{i,j+3}^n)
\end{aligned}$$

(B.3)

Therefore, the ratio of residue for the object side, γ_o , at the node ($M1, N0$) is given by:

$$\begin{aligned}
\gamma_o &= \frac{\left(1 + \frac{3}{2i} \lambda_o + 4\lambda_o \right) T_{i,j}^n + \lambda_o \left(\frac{-4T_{i-1,j}^n + T_{i-2,j}^n}{2i} \right) + \lambda_o (-5T_{i-1,j}^n + 4T_{i-2,j}^n - T_{i-3,j}^n - 5T_{i,j+1}^n + 4T_{i,j+2}^n - T_{i,j+3}^n) - T_{i,j}^{n+1}}{T_{i,j}^{n+1}} \times 100\%,
\end{aligned}$$

(B.4)

3. Node (0, N0)

By applying the L'Hospital rule [84], the Eq. (4.56) is developed as:

$$\frac{\partial T}{\partial t} = 2\alpha_o \frac{\partial^2 T}{\partial r^2} + \alpha_o \frac{\partial^2 T}{\partial z^2}, \text{ when } r \rightarrow 0,$$

(B.5)

For the discretization at the corner node ($0, N0$), the central difference method is implemented in the radial direction, and the forward difference method is implemented in the axial direction.

The temperature at the node ($0, N0$) is given by:

$$\begin{aligned}
\frac{T_{i,j}^{n+1} - T_{i,j}^n}{\Delta t} &= 2\alpha_o \frac{T_{i+1,j}^n - 2T_{i,j}^n + T_{i-1,j}^n}{(\Delta r)^2} + \alpha_o \frac{2T_{i,j}^n - 5T_{i,j+1}^n + 4T_{i,j+2}^n - T_{i,j+3}^n}{(\Delta z)^2} \\
\Rightarrow T_{i,j}^{n+1} &= T_{i,j}^n + 2\lambda_o (T_{i+1,j}^n - 2T_{i,j}^n + T_{i-1,j}^n) + \lambda_o (2T_{i,j}^n - 5T_{i,j+1}^n + 4T_{i,j+2}^n - T_{i,j+3}^n) \quad , \quad (\text{B.6}) \\
&= (1 - 4\lambda_o + 2\lambda_o)T_{i,j}^n + 2\lambda_o (T_{i+1,j}^n + T_{i-1,j}^n) + \lambda_o (-5T_{i,j+1}^n + 4T_{i,j+2}^n - T_{i,j+3}^n) \\
&= (1 - 2\lambda_o)T_{i,j}^n + 4\lambda_o (T_{i+1,j}^n) + \lambda_o (-5T_{i,j+1}^n + 4T_{i,j+2}^n - T_{i,j+3}^n)
\end{aligned}$$

where $T_{i-1,j}^n = T_{i+1,j}^n$, because $\left. \frac{\partial T}{\partial r} \right|_{r=0} = \frac{T_{i+1,j}^n - T_{i-1,j}^n}{2(\Delta r)} = 0$ at the axis.

Therefore, the ratio of residue for the object side, γ_o , at the node $(0, N0)$ is given by:

$$\gamma_o = \frac{(1 - 2\lambda_o)T_{i,j}^n + 4\lambda_o (T_{i+1,j}^n) + \lambda_o (-5T_{i,j+1}^n + 4T_{i,j+2}^n - T_{i,j+3}^n) - T_{i,j}^{n+1}}{T_{i,j}^{n+1}} \times 100\% \quad , \quad (\text{B.7})$$

B.2 Liquid side

1. Interface 1: $i = M1, j = N0 + 1$ to $N1$

For the discretization at interface 1, the forward difference method is implemented in the radial direction, and the central difference method is implemented in the axial direction. The temperature at node (i, j) is given by:

$$\begin{aligned}
\frac{T_{i,j}^{n+1} - T_{i,j}^n}{\Delta t} &= \frac{\alpha_1}{i(\Delta r)} \frac{-3T_{i,j}^n + 4T_{i+1,j}^n - T_{i+2,j}^n}{2(\Delta r)} + \alpha_1 \frac{2T_{i,j}^n - 5T_{i+1,j}^n + 4T_{i+2,j}^n - T_{i+3,j}^n}{(\Delta r)^2} + \alpha_1 \frac{T_{i,j+1}^n - 2T_{i,j}^n + T_{i,j-1}^n}{(\Delta z)^2} \\
\Rightarrow T_{i,j}^{n+1} &= T_{i,j}^n + \lambda_1 \left(\frac{-3T_{i,j}^n + 4T_{i+1,j}^n - T_{i+2,j}^n}{2i} \right) + \lambda_1 (2T_{i,j}^n - 5T_{i+1,j}^n + 4T_{i+2,j}^n - T_{i+3,j}^n) + \lambda_1 (T_{i,j+1}^n - 2T_{i,j}^n + T_{i,j-1}^n) \\
&= \left(1 - \frac{3}{2i} \lambda_1 + 2\lambda_1 - 2\lambda_1 \right) T_{i,j}^n + \lambda_1 \left(\frac{4T_{i+1,j}^n - T_{i+2,j}^n}{2i} \right) + \lambda_1 (-5T_{i+1,j}^n + 4T_{i+2,j}^n - T_{i+3,j}^n) + \lambda_1 (T_{i,j+1}^n + T_{i,j-1}^n) \\
&= \left(1 - \frac{3}{2i} \lambda_1 \right) T_{i,j}^n + \lambda_1 \left(\frac{4T_{i+1,j}^n - T_{i+2,j}^n}{2i} \right) + \lambda_1 (-5T_{i+1,j}^n + 4T_{i+2,j}^n - T_{i+3,j}^n + T_{i,j+1}^n + T_{i,j-1}^n)
\end{aligned} \quad , \quad (\text{B.8})$$

Therefore, the ratio of residue for the liquid side, γ_1 , at the interface 1 is given by:

$$\begin{aligned} & \left(1 - \frac{3}{2i}\lambda_1\right)T_{i,j}^n + \lambda_1\left(\frac{4T_{i+1,j}^n - T_{i+2,j}^n}{2i}\right) \\ \gamma_1 = & \frac{+ \lambda_1\left(-5T_{i+1,j}^n + 4T_{i+2,j}^n - T_{i+3,j}^n + T_{i,j+1}^n + T_{i,j-1}^n\right) - T_{i,j}^{n+1}}{T_{i,j}^{n+1}} \times 100\%, \end{aligned} \quad (\text{B.9})$$

2. Interface 2: $i = 1$ to $M1 - 1, j = N0$

For the discretization at interface 2, the central difference method is implemented in the radial direction, and the backward difference method is implemented in the axial direction. The temperature at node (i, j) is given by:

$$\begin{aligned} \frac{T_{i,j}^{n+1} - T_{i,j}^n}{\Delta t} &= \frac{\alpha_1}{i(\Delta r)} \frac{T_{i+1,j}^n - T_{i-1,j}^n}{2(\Delta r)} + \alpha_1 \frac{T_{i+1,j}^n - 2T_{i,j}^n + T_{i-1,j}^n}{(\Delta r)^2} + \alpha_1 \frac{2T_{i,j}^n - 5T_{i,j-1}^n + 4T_{i,j-2}^n - T_{i,j-3}^n}{(\Delta z)^2} \\ \Rightarrow T_{i,j}^{n+1} &= T_{i,j}^n + \lambda_1 \left(\frac{T_{i+1,j}^n - T_{i-1,j}^n}{2i} \right) + \lambda_1 (T_{i+1,j}^n - 2T_{i,j}^n + T_{i-1,j}^n) + \lambda_1 (2T_{i,j}^n - 5T_{i,j-1}^n + 4T_{i,j-2}^n - T_{i,j-3}^n) \\ &= (1 - 2\lambda_1 + 2\lambda_1)T_{i,j}^n + \lambda_1 \left(\frac{T_{i+1,j}^n - T_{i-1,j}^n}{2i} \right) + \lambda_1 (T_{i+1,j}^n + T_{i-1,j}^n) + \lambda_1 (-5T_{i,j-1}^n + 4T_{i,j-2}^n - T_{i,j-3}^n) \\ &= T_{i,j}^n + \lambda_1 \left(\frac{T_{i+1,j}^n - T_{i-1,j}^n}{2i} \right) + \lambda_1 (T_{i+1,j}^n + T_{i-1,j}^n - 5T_{i,j-1}^n + 4T_{i,j-2}^n - T_{i,j-3}^n) \end{aligned} \quad (\text{B.10})$$

Therefore, the ratio of residue for the liquid side, γ_1 , at the interface 2 is given by:

$$\gamma_1 = \frac{T_{i,j}^n + \lambda_1 \left(\frac{T_{i+1,j}^n - T_{i-1,j}^n}{2i} \right) + \lambda_1 (T_{i+1,j}^n + T_{i-1,j}^n - 5T_{i,j-1}^n + 4T_{i,j-2}^n - T_{i,j-3}^n) - T_{i,j}^{n+1}}{T_{i,j}^{n+1}} \times 100\%, \quad (\text{B.11})$$

3. Node $(M1, N0)$

For the discretization at the corner node $(M1, N0)$, the forward difference method is implemented in the radial direction, and the backward difference method is implemented in the axial direction.

The temperature at the node $(M1, N0)$ is given by:

$$\begin{aligned}
\frac{T_{i,j}^{n+1} - T_{i,j}^n}{\Delta t} &= \frac{\alpha_1}{i(\Delta r)} \frac{-3T_{i,j}^n + 4T_{i+1,j}^n - T_{i+2,j}^n}{2(\Delta r)} + \alpha_1 \frac{2T_{i,j}^n - 5T_{i+1,j}^n + 4T_{i+2,j}^n - T_{i+3,j}^n}{(\Delta r)^2} + \alpha_1 \frac{2T_{i,j}^n - 5T_{i,j-1}^n + 4T_{i,j-2}^n - T_{i,j-3}^n}{(\Delta z)^2} \\
\Rightarrow T_{i,j}^{n+1} &= T_{i,j}^n + \lambda_1 \left(\frac{-3T_{i,j}^n + 4T_{i+1,j}^n - T_{i+2,j}^n}{2i} \right) + \lambda_1 (2T_{i,j}^n - 5T_{i+1,j}^n + 4T_{i+2,j}^n - T_{i+3,j}^n) + \lambda_1 (2T_{i,j}^n - 5T_{i,j-1}^n + 4T_{i,j-2}^n - T_{i,j-3}^n) \\
&= \left(1 - \frac{3}{2i} \lambda_1 + 2\lambda_l + 2\lambda_l \right) T_{i,j}^n + \lambda_1 \left(\frac{4T_{i+1,j}^n - T_{i+2,j}^n}{2i} \right) + \lambda_1 (-5T_{i+1,j}^n + 4T_{i+2,j}^n - T_{i+3,j}^n) + \lambda_1 (-5T_{i,j-1}^n + 4T_{i,j-2}^n - T_{i,j-3}^n) \\
&= \left(1 - \frac{3}{2i} \lambda_1 + 4\lambda_l \right) T_{i,j}^n + \lambda_1 \left(\frac{4T_{i+1,j}^n - T_{i+2,j}^n}{2i} \right) + \lambda_1 (-5T_{i+1,j}^n + 4T_{i+2,j}^n - T_{i+3,j}^n - 5T_{i,j-1}^n + 4T_{i,j-2}^n - T_{i,j-3}^n)
\end{aligned}$$

(B.12)

Therefore, the ratio of residue for the liquid side, γ_1 , at the node (M1, N0) is given by:

$$\begin{aligned}
&\left(1 - \frac{3}{2i} \lambda_1 + 4\lambda_l \right) T_{i,j}^n + \lambda_1 \left(\frac{4T_{i+1,j}^n - T_{i+2,j}^n}{2i} \right) \\
\gamma_1 &= \frac{+ \lambda_1 (-5T_{i+1,j}^n + 4T_{i+2,j}^n - T_{i+3,j}^n - 5T_{i,j-1}^n + 4T_{i,j-2}^n - T_{i,j-3}^n) - T_{i,j}^{n+1}}{T_{i,j}^{n+1}} \times 100\%, \quad (B.13)
\end{aligned}$$

4. Node (0, N0)

By applying the L'Hospital rule [84], the Eq. (4.56) is developed as:

$$\frac{\partial T}{\partial t} = 2\alpha_1 \frac{\partial^2 T}{\partial r^2} + \alpha_1 \frac{\partial^2 T}{\partial z^2}, \text{ when } r \rightarrow 0, \quad (B.14)$$

For the discretization at the corner node (0, N0), the central difference method is implemented in the radial direction, and the backward difference method is implemented in the axial direction.

The temperature at the node (0, N0) is given by:

$$\begin{aligned}
\frac{T_{i,j}^{n+1} - T_{i,j}^n}{\Delta t} &= 2\alpha_1 \frac{T_{i+1,j}^n - 2T_{i,j}^n + T_{i-1,j}^n}{(\Delta r)^2} + \alpha_1 \frac{2T_{i,j}^n - 5T_{i,j-1}^n + 4T_{i,j-2}^n - T_{i,j-3}^n}{(\Delta z)^2} \\
\Rightarrow T_{i,j}^{n+1} &= T_{i,j}^n + 2\lambda_1 (T_{i+1,j}^n - 2T_{i,j}^n + T_{i-1,j}^n) + \lambda_1 (2T_{i,j}^n - 5T_{i,j-1}^n + 4T_{i,j-2}^n - T_{i,j-3}^n) \quad , \quad (B.15) \\
&= (1 - 4\lambda_1 + 2\lambda_l) T_{i,j}^n + 2\lambda_1 (T_{i+1,j}^n + T_{i-1,j}^n) + \lambda_1 (-5T_{i,j-1}^n + 4T_{i,j-2}^n - T_{i,j-3}^n) \\
&= (1 - 2\lambda_1) T_{i,j}^n + 4\lambda_1 (T_{i+1,j}^n) + \lambda_1 (-5T_{i,j-1}^n + 4T_{i,j-2}^n - T_{i,j-3}^n)
\end{aligned}$$

where $T_{i-1,j}^n = T_{i+1,j}^n$, because $\left. \frac{\partial T}{\partial r} \right|_{r=0} = \frac{T_{i+1,j}^n - T_{i-1,j}^n}{2(\Delta r)} = 0$ at the axis.

Therefore, the ratio of residue for the liquid side, γ_1 , at the node $(0, N0)$ is given by:

$$\gamma_1 = \frac{(1-2\lambda_1)T_{i,j}^n + 4\lambda_1(T_{i+1,j}^n) + \lambda_1(-5T_{i,j-1}^n + 4T_{i,j-2}^n - T_{i,j-3}^n) - T_{i,j}^{n+1}}{T_{i,j}^{n+1}} \times 100\%, \quad (\text{B.16})$$

Bibliography

- [1] M. Fingas, Handbook of oil spill science and technology, John Wiley & Sons, 2014.
- [2] A. Jernelöv, The threats from oil spills: now, then, and in the future, AMBIO (2010) 39 353-366.
- [3] P.F. Kingston, Long-term environmental impact of oil spills, Spill Science & Technology Bulletin 7.1-2 (2002) 53-61.
- [4] E.R. Gundlach, O.H. Miles, Vulnerability of coastal environments to oil spill impacts, Marine technology society Journal 12.4 (1978) 18-27.
- [5] P. Sebastião, C.G. Soares, Modeling the fate of oil spills at sea, Spill Science & Technology Bulletin 2.2-3 (1995) 121-131.
- [6] M. Fingas, Oil Spill Science and Technology, Gulf professional publishing, 2016.
- [7] M.B. Tahir, A. Batool, COVID-19: Healthy environmental impact for public safety and menaces oil market, Science of the Total Environment 740 (2020) 140054.
- [8] K.M. Magalhães, K.V. Souza Barros, M.C.S. Lima, C. Almeida Rocha-Barreira, J.S.R. Filho, M. Oliveira Soares, Oil spill + COVID-19: A disastrous year for Brazilian seagrass conservation, Science of The Total Environment 764 (2021) 142872.
- [9] J.V. Mullin, A.C. Michael, Introduction/overview to *in situ* burning of oil spills, Spill Science & Technology Bulletin 8.4 (2003) 323-330.
- [10] D.E. Fritz, *In situ* burning of spilled oil in freshwater inland regions of the United States, Spill Science & Technology Bulletin 8.4 (2003) 331-335.
- [11] M. Fingas, In-Situ Burning for Oil Spill Countermeasures, CRC Press, 2018.

- [12] H. Koseki, H. Hayasaka, Estimation of thermal balance in heptane pool fire, *Journal of Fire Sciences* 7 (1989) 237-250.
- [13] A.S. Rangwala, K.S. Arsava, G. Mahnken, X. Shi, A novel experimental approach to enhance burning of oil-water emulsions by immersed objects, Worcester Polytechnic Institute, Worcester, 2015.
- [14] A.S. Rangwala, X. Shi, K.S. Arsava, G. Mahnken, Methods and systems for clean-up of hazardous spills, U.S. Patent No. 9,772,108 B2, 26th September 2017.
- [15] H. Sezer, K.S. Arsava, A.S. Rangwala, Oil spill clean-up using immersed metal wool, *Journal of environmental chemical engineering* 5 (2017) 5196-5206.
- [16] H. Sezer, K.S. Arsava, S.P. Kozhumal, A.S. Rangwala, The effect of embedded objects on pool fire burning behavior, *International Journal of Heat and Mass Transfer* 108 (2017) 537-548.
- [17] K.S. Arsava, G. Mahnken, A.S. Rangwala, Use of immersed conductive objects to enhance the burning rate of hydrocarbon pool fires, *Cold Regions Science and Technology* 146 (2018) 133-141.
- [18] K.S. Arsava, V. Raghavan, A.S. Rangwala, Enhanced oil spill clean-up using immersed thermally conductive objects, *Fire Technology* 54 (2018) 1745-1758.
- [19] B.D. Ditch, J.L. de Ris, T.K. Blanchat, M. Chaos, R.G. Bill, Jr., S.B. Dorofeev, Pool fires - An empirical correlation, *Combustion and flame* 160 (12) (2013) 2964-2974.
- [20] J.G. Quintiere, *Fundamentals of fire phenomena*, John Wiley & Sons, 2006.
- [21] D. Drysdale, *An Introduction to Fire Dynamics*, John Wiley & Sons, 2011.

- [22] J. Fang, S. Zheng, J. Wang, K. Wang, H.R. Shah, J. Wang, An analysis of heat feedback effects of different height embedded plates on promotion of pool fire burning using a variable B number, *International Journal of Thermal Sciences* 145 (2019) 106041.
- [23] V. Babrauskas, Estimating large pool fire burning rates, *Fire technology* 19.4 (1983) 251-261.
- [24] A. Nakakuki, Heat transfer mechanisms in liquid pool fires, *Fire safety journal* 23 (1994) 339-363.
- [25] A. Nakakuki, Heat transfer in small scale pool fires, *Combustion and flame* 96 (1994) 311-324.
- [26] A. Hamins, T. Kashiwagi, R.R. Burch, Characteristics of pool fire burning, *Fire resistance of industrial fluids*, ASTM International, 1996.
- [27] P. Joulain, The behavior of pool fires: state of the art and new insights, *Symposium (International) on Combustion*, Elsevier, (1998) 2691-2706.
- [28] L. Hu, A review of physics and correlations of pool fire behaviour in wind and future challenges, *Fire safety journal* 91 (2017) 41-55.
- [29] L.H. Russell, J.A. Canfield, Experimental measurement of heat transfer to a cylinder immersed in a large aviation-fuel fire, (1973) 397-404.
- [30] C.J. Pry, A Consideration of Some Simple Models for Assessing Heat Transfer to Objects Engulfed in Pool Fires, AEEW-M-2321, UKAEA Atomic Energy Establishment, Winfrith, U.K, 1985.
- [31] L.A. Gritzo, V.F. Nicolette, Coupling of large fire phenomenon with object geometry and object thermal response, *Journal of Fire Sciences* 15.6 (1997) 427-442.
- [32] J.P. Holman, *Heat Transfer*, McGraw-Hill, 2010.

- [33] T.L. Bergman, A.S. Lavine, Fundamentals of Heat and Mass Transfer, John Wiley & Sons, 2017.
- [34] S. Nukiyama, The maximum and minimum values of heat transmitted from metal to boiling water under atmospheric pressure, International Journal of Heat and Mass Transfer 9 (12) (1934) 1419-1433.
- [35] S.G. Kandlikar, M. Shoji, V.K. Dhir, Handbook of phase change: boiling and condensation, CRC Press, 1999.
- [36] J.W. Westwater, Boiling of liquids, Advances in Chemical Engineering 1 (1956) 1-76.
- [37] L.S. Tong, Y.S. Tang, Boiling Heat Transfer and Two-Phase Flow, Taylor & Francis, 1997.
- [38] L. Lee, B.N. Singh, The influence of subcooling on nucleate pool boiling heat transfer, Letters In Heat and Mass Transfer 2 (4) (1975) 315-323.
- [39] H. Wang, X. Peng, B. Wang, D.J. Lee, Bubble sweeping and jet flows during nucleate boiling of subcooled liquids, International Journal of Heat and Mass Transfer 46 (5) (2003) 863-869.
- [40] F. Lu, X. Peng, B. Bourouga, Nucleate boiling modes of subcooled water on fine wires submerged in a pool, Experimental Heat Transfer 19 (2) (2006) 95-111.
- [41] Y. Fujita, M. Tsutsui, Nucleate boiling of two and three-component mixtures, International Journal of Heat and Mass Transfer 47 (21) (2004) 4637-4648.
- [42] G.V. Rao, A.R. Balakrishnan, Nucleate pool boiling heat transfer of multicomponent mixtures, Chemical Engineering Research and Design 82 (1) (2004) 43-52.
- [43] B.A. Abid, A.J. Sultan, Heat transfer of single and binary systems in pool boiling, Al-Khwarizmi Engineering Journal 6 (1) (2010) 14-23.

- [44] H. Peng, G. Ding, H. Hu, W. Jiang, D. Zhuang, K. Wang, Nucleate pool boiling heat transfer characteristics of refrigerant/oil mixture with diamond nanoparticles, *International Journal of refrigeration* 33 (2) (2010) 347-358.
- [45] M.L. Roesle, F.A. Kulacki, An experimental study of boiling in dilute emulsions, part A: Heat transfer, *International Journal of Heat and Mass Transfer* 55 (7) (2012) 2160-2165.
- [46] M.L. Roesle, F.A. Kulacki, An experimental study of boiling in dilute emulsions, part B: Visualization, *International Journal of Heat and Mass Transfer* 55 (7) (2012) 2166-2172.
- [47] J.N. Addoms, Heat transfer at high rates to water boiling outside cylinders, Ph.D. Dissertation, Chemical Engineering Department, Massachusetts Institute of Technology, MA, 1948.
- [48] P.J. Berenson, Experiments on pool-boiling heat transfer, *International Journal of Heat and Mass Transfer* 5 (10) (1962) 985-999.
- [49] R. Siegel, J.R. Howell, Critical heat flux for saturated pool boiling from horizontal and vertical wires in reduced gravity, National Aeronautics and Space Administration, 1965.
- [50] I.P. Vishnev, Effect of orienting the hot surface with respect to the gravitational field on the critical nucleate boiling of a liquid, *Journal of Engineering Physics and Thermophysics* 24 (1) (1973) 43-48.
- [51] J.Y. Chang, S.M. You, Heater orientation effects on pool boiling of micro-porous-enhanced surfaces in saturated FC-72, *Journal of Heat Transfer* 118 (4) (1996) 937-943.
- [52] M.G. Kang, Effect of surface roughness on pool boiling heat transfer, *International journal of heat and mass transfer* 43 (22) (2000) 4073-4085.
- [53] S.G. Kandlikar, A theoretical model to predict pool boiling CHF incorporating effects of contact angle and orientation, *Journal of Heat Transfer* 123 (6) (2001) 1071-1079.

- [54] H. Wang, X. Peng, B. Wang, W. Lin, C. Pan, Experimental observations of bubble dynamics on ultrathin wires, *Experimental heat transfer* 18 (1) (2005) 1-11.
- [55] P. Zhang, X. Ren, R.Z. Wang, Experimental investigation of the heat transfer characteristics of liquid nitrogen in the capillary tubes, *IEEE transactions on applied superconductivity* 16 (2) (2006) 449-452.
- [56] J.M.S. Jabardo, G. Ribatski, E. Stelute, Roughness and surface material effects on nucleate boiling heat transfer from cylindrical surfaces to refrigerants R-134a and R-123, *Experimental Thermal and Fluid Science* 33 (4) (2009) 579-590.
- [57] B.J. Jones, J.P. McHale, S.V. Garimella, The influence of surface roughness on nucleate pool boiling heat transfer, *Journal of Heat Transfer* 131 (12) (2009).
- [58] M.S. El-Genk, A. Suszko, Effects of inclination angle and liquid subcooling on nucleate boiling on dimpled copper surfaces, *International Journal of Heat and Mass Transfer* 95 (2016) 650-661.
- [59] J.W. Westwater, J.G. Santangelo, Photographic study of boiling, *Industrial & Engineering Chemistry* 47 (8) (1955) 1605-1610.
- [60] M.A. Johnson, Jr., J. De La Peña, R.B. Mesler, Bubble shapes in nucleate boiling, *AIChE Journal*, 12 (2) (1966) 344-348.
- [61] A. Sakurai, M. Shiotsu, K. Hata, K. Fukuda, Photographic study on transitions from non-boiling and nucleate boiling regime to film boiling due to increasing heat inputs in liquid nitrogen and water, *Nuclear Engineering and Design* 200 (2000) 39-54.

- [62] D. Qiu, G. Son, V.K. Dhir, D. Chao, K. Logsdon, Dynamics of single and multiple bubbles and associated heat transfer in nucleate boiling under low gravity conditions, *Annals of the New York Academy of Sciences* 974 (1) (2002) 378-397.
- [63] J. Straub, Johannes, Boiling heat transfer and bubble dynamics in microgravity, *Advances in Heat Transfer*, Vol. 35, Academic Press, 2001, 57-172.
- [64] A. Coulibaly, X. Lin, J. Bi, D.M. Christopher, Bubble coalescence at constant wall temperatures during subcooled nucleate pool boiling, *Experimental thermal and fluid science* 44 (2013) 209-218.
- [65] X. Pi, A.S. Rangwala, The influence of wire orientation during nucleate pool boiling in subcooled dodecane, *International Journal of Heat and Mass Transfer* 137 (2019) 1247-1257.
- [66] X. Pi, L. Chang, A.S. Rangwala, The influence of an immersed heater on pool fire burning behaviors, 11th US National Combustion Meeting, 2019, Pasadena, CA, United States.
- [67] X. Pi, L. Chang, A.S. Rangwala, The burning rate of a pool fire increased by bubble behaviors during nucleate boiling, *Fire Safety Journal* 120 (2021) 103097.
- [68] X. Pi, K. Twarog, L. Chang, C.J. Sung, A.S. Rangwala, The influence of surface configuration of an immersed metal element to pool fire burning, 35th American Society for Gravitational and Space Research (ASGSR) Meeting, 2019, Denver, CO, United States.
- [69] J. Tellinghuisen, Statistical error propagation, *The Journal of Physical Chemistry A*, 105 (15) (2001): 3917-3921.
- [70] A.J. Wheeler, A.R. Ganji, *Introduction to engineering experimentation*, Prentice Hall, New Jersey, 1996.

- [71] D.M. Christopher, H. Wang, X. Peng, Heat transfer enhancement due to Marangoni flow around moving bubbles during nucleate boiling, *Tsinghua Science and Technology* 11 (5) (2006) 523-532.
- [72] M.J. Hurley, D.T. Gottuk, J.R. Hall, Jr., K. Harada, E.D. Kuligowski, M.T. Puchovsky, J.L. Torero, J.M. Watts Jr., C.J. Wieczorek, *SFPE Handbook of Fire Protection Engineering*, fifth ed., Springer, 2016.
- [73] <https://www.ansys.com/>.
- [74] <https://pages.nist.gov/fds-smv/>.
- [75] N.G. Sauer, H. Ho, S. Nair, G. Mahnken, M. Kottalgi, A.S. Rangwala, K.S. Arsava, K. Stone, C. Laikin-Credno, *Advancing the Maturity of the Flame Refluxer Technology*, Worcester Polytechnic Institute, Worcester, 2021.
- [76] G. Heskestad, Luminous heights of turbulent diffusion flames, *Fire safety journal* 5 (2) (1983) 103-108.
- [77] B.J. McCaffrey, Purely buoyant diffusion flames: some experimental results, NBSIR 79-1910, National Bureau of Standards, Washington, D.C., 1979.
- [78] S. Sudheer, S.V. Prabhu, Characterization of hexane pool fires using infrared thermography, *Journal of fire sciences* 31 (2) (2013) 143-165.
- [79] S. Sudheer, S.V. Prabhu, Measurement of flame emissivity of hydrocarbon pool fires, *Fire Technology* 48 (2) (2012) 183-217.
- [80] C.O. Popiel, J. Wojtkowiak, K. Bober, Laminar free convective heat transfer from isothermal vertical slender cylinder, *Experimental Thermal and Fluid Science* 32 (2) (2007) 607-613.

- [81] C.O. Popiel, Free convection heat transfer from vertical slender cylinders: a review, *Heat Transfer Engineering* 29 (6) (2008) 521-536.
- [82] <https://www.engineeringtoolbox.com/>.
- [83] E. Planas-Cuchi, J.M. Chatris, C. L'opez, J. Arnaldos, Determination of flame emissivity in hydrocarbon pool fires using infrared thermography, *Fire Technology* 39 (3) (2003) 261-273.
- [84] D.A. Anderson, J.C. Tannehill, R.H. Pletcher, R. Munipalli, V. Shankar, *Computational Fluid Mechanics and Heat Transfer*. CRC Press, 2020.
- [85] B. Le Neindre, G. Lombardi, P. Desmarest, M. Kayser, A.N. Sabirzianov, F.R. Gabitov, F. Gumerov, Y. Garrabos, Thermal conductivity of gaseous and liquid n-hexane, *Fluid Phase Equilibria* 474 (2018) 60-75.
- [86] <https://webbook.nist.gov/chemistry/>.
- [87] A.E. Cote, C.C. Grant, J.R. Hall, Jr., R.E. Solomon, P.A. Powell, *Fire Protection Handbook*, twentieth ed., National Fire Protection Association, Quincy, MA, 2008.
- [88] P.T. Summers, Y. Chen, C.M. Rippe, B. Allen, A.P. Mouritz, S.W. Case, B.Y. Lattimer, Overview of aluminum alloy mechanical properties during and after fires, *Fire Science Reviews* 4 (1) (2015) 1-36.
- [89] A. Jain, K. Nandakumar, A. Ross, Score normalization in multimodal biometric systems, *Pattern recognition* 38 (2005) 2270-2285.